Fabrication and Characterisation of DLC-graphene Nanocomposite Coatings for Tribological Application

Nik Roselina binti Nik Roseley

Submitted in accordance with the requirements for the degree of
Doctor of Philosophy

The University of Leeds

School of Mechanical Engineering

Leeds, UK

Jan, 2019

The candidate confirms that the work submitted is his own and that appropriate credit has been given where reference has been made to the work of others.

This copy has been supplied on the understanding that it is copyright material and that no quotation from the thesis may be published without proper acknowledgement.

Works related to the thesis

Patent

Nik Roselina N.R, T. Liskiewicz, A. Neville, Effect of post-treatment of the fabrication of DLC-GNP nanocomposite coating, *patent application in preparation*

Conferences

Nik Roselina N.R, T. Liskiewicz, A. Neville, Effect of DLC deposition time on adhesion of DLC-graphene composite nanocoating, TriboUK2017, Poster Presentation, April 2017

Nik Roselina N.R, T. Liskiewicz, A. Neville, Fabrication of DLC-graphene nanocomposite coating for tribological application, Winter Tribology Fair, Poster presentation, Jan 2017

Acknowledgement

I would like to express my greatest gratitude to my supervisors Assoc. Prof Dr Tomasz Liskiewicz and Prof Anne Neville for their endless supports since the first day I started my PhD until today. This thesis will not be here without their guidance.

This journey would not be complete without these people who have been really helpful: kind-hearted Andrew, who always there with me in the PVD room and lab; friendly Mick, who never say no when I ask a favour; cheerful Jordan, who always been there when I needed him, not to forget Tony who is always willing to help. I am also in debt to Dr Chun Wang who has provided advice and helping me with Raman spectroscopy and nanoindentation. Also, thank you to Dr Vishal and Dr Huang Zhang who has been helping me a lot with the PECVD process. I would also thank everybody in IFS who have made this journey smooth and possible.

My sincere thanks also go to all my colleagues and friends, Doris, Mohammad, Sherry, Sam, Frank, Frederick, Taufiq, Leo, and many others to mention here, who have not only technically helped me in the lab, but have always been around to cherish my days especially during the 'down-day'. I specifically would like to thank Sam for helping me with the thesis proofreading.

I would like to convey my appreciation to the Malaysian Government and Universiti Teknologi MARA (UiTM) for the financial support and the precious opportunity that has been given to do my PhD at the University of Leeds.

Last but not least, I would like to thank my greatest support system; husband, Mohd Najib, daughter, Damia Qistina and son, Danish Qasyri. Thank you for the endless support and sacrifice that have been made for me since the day I decided to do my PhD until today. Not to forget my parents, in-laws and siblings who have been sending their thoughts and prayers.

Abstract

This work presents the development and characterisation of single and multilayer Diamond-Like Carbon (DLC)-graphene nanoplatelet (GNP) nanocomposite coatings. This study opens up a new challenge in the fabrication of carbon composites using DLC and GNP with enhanced mechanical and tribological properties. The purpose of the composite is to exploit the advantages of the excellent mechanical and tribological properties of graphene that have been reported by many works.

The objectives of this thesis are to develop a method to fabricate DLC and GNP nanocomposite coatings, to prepare the nanocomposite coatings and to investigate their physical, mechanical and tribological properties. The fabrication of DLC-GNP nanocomposite coatings was carried out using the combination of spin coating of GNP and DLC deposition using PECVD. The two types of DLC-GNP that have been prepared are single-layer and multilayer.

The surface morphology and microstructure of DLC-GNP was characterised using optical microscopy and Scanning Electron Microscopy (SEM). Focused Ion Beam (FIB) SEM was used to observe the layers in the composite and measure the thickness of the multilayer DLC-GNP nanocomposite coating. The coating comprises the interlayer, spin-coated GNP and DLC film.

This study shows that an optimised post-treatment is required to substantially improve the adhesion strength of spin-coated GNP and thus that of the whole nanocomposite coating. It was observed that columnar structure was generated in-situ during a wear tests on coatings post-treated for more than 180 minutes. The results were unintentionally found after three hours of sliding test. The columnar structure contributed to the significant reduction of the coefficient of friction (CoF) to 0.06, and the wear rate compared to other samples.

According to Raman spectroscopy analysis, both single and multilayer DLC-GNP nanocomposite coatings have typical spectra similar to that of pure DLC. However, DLC-GNP has a broad range of I_D/I_G ratio values compared to pure DLC due to the dispersion of spin-coated GNP. The observation though cross-

section FIB also proved that DLC film covered the spin-coated GNP by creating a bonding layer during DLC film deposition.

The multilayer DLC-GNP demonstrated major improvements in adhesion strength of almost doubling the value obtained by single-layer DLC-GNP. The wear resistance also increased remarkably which can be related to the enhancement of adhesion strength. It is proposed that the GNP in the composite is released during the running-in period and acted as a slider between the counterpart and coating.

Table of Contents

List of Figures

xxi

List of Tables

List of Abbreviations

a-C	Amorphous carbon
a-C:H	Hydrogenated diamond-like carbon
CNT	Carbon nanotube
CVD	Chemical Vapour Deposition
CoF	Coefficient of friction
DLC	Diamond-like Carbon
DMF	Dimethylformamide
DOF	Degree of freedom
E	Elastic Modulus
EDX	Energy dispersive X-ray
EHD	Elastohydrodynamic
FIB	Focus ion beam
FSP	Friction stir processing
FWHM	Full width at half maximum
GLC	Graphite-like carbon
GNP	Graphene nanoplatelet
H	Hardness
HSS	High Speed Steel
IL	Ionic liquid
MWCNT	Multiwalled carbon nanotube
NMP	N-Methyl-2-pyrrolidone
PCD	Polycrystalline diamond
PECVD	Plasma enhanced chemical vapour deposition
PLD	Pulsed laser deposition
PVD	Physical vapour deposition
S/N	Signal-to-noise
SEM	Scanning electron microscopy

ta-C   Tetrahedral amorphous carbon

W-C:H   Hydrogenated tungsten carbide

WLI   White light interferometry

EELS   Electron energy loss spectroscopy

RF-PECVD   Radio-frequency plasma enhanced chemical vapour deposition

HF-PECVD   High-frequency plasma enhanced chemical vapour deposition

XPS   X-ray photoelectron spectroscopy

Chapter 1

Introduction

1.1 Background of Study

The growth of the human population to 99 billion by 2050, as well as the economic growth at that time is expected to substantially increase the demand for energy [2]. It is foreseen that the world will be facing the age of energy deficiency should we fail to tackle the issue efficiently. One of the ways to reduce the global energy consumption other than substituting the energy source is by improving the efficiency of energy usage in our systems. Generally, energy efficiency means using less energy to produce the same amount of services of output, or it can also be defined as the ratio of a useful output of a process and energy input into a process [3].

Holmberg et al. [4] reported that in 2009 one car passenger uses an average of 340 litres/year of fuel to overcome friction. While for heavy-duty vehicles, in 2012 about 180, 000 million litters were consumed when the fuels were used for the same purpose [5]. A huge portion of energy is being wasted to overcome friction in a moving system which does affect not only the economy but also increases CO_2 emissions. Hence, it is vital to reduce/eliminate friction in a mechanical system for a greener and sustainable future. Figure 1.1 shows the trend of reduction of friction for different lubrication mechanisms predicted by Holmberg which include boundary lubrication, mixed lubrication, elastohydrodynamic (EHD) and hydrodynamic. Holmberg has also presented a similar review on friction in trucks and buses, and paper machines in the perspective of tribological contact and friction mechanism [5, 6].

Industry 4.0 is the Fourth Industrial Revolution that converges industrial production, and information and communication technologies [7]. Every industrial revolution in the past has shown the need for improved energy efficiency, and the fourth revolution should be no different in that respect. One

of the potentials of energy efficiency is through the management of surface technology to reduce friction and resist wear, which in return provides energy efficiency and a prolonged lifetime of devices. Application of smart coatings that are capable of not only reducing friction and resisting wear but also with the ability to adapt to the environment, self-repair and self-lubrication are in current demand.
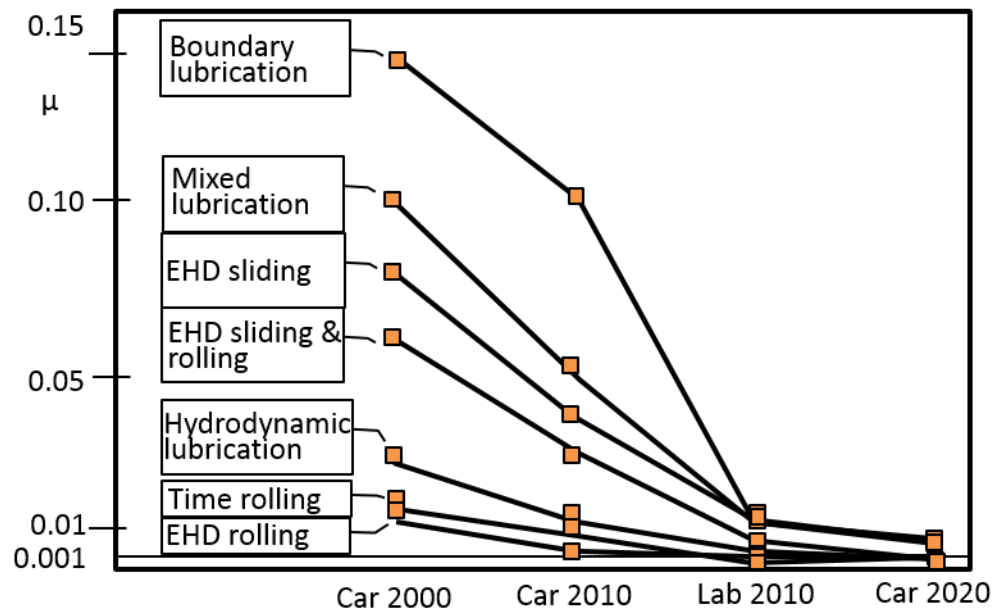
Figure 1.1 Predicted trend of reduction in friction for four different types of passenger car as a function of the main lubrication mechanisms. Adapted from [4].

Application of coatings as solid lubricants is one solution to improve surface function. It has been proven to improve the surface capability to reduce friction and resist wear which in return provides energy efficiency and prolonged lifetime of devices. DLC coatings represent one of the most outstanding coatings for low friction and wear especially for high load applications. It has been long known in various applications including automotive, aerospace and biomedical. DLC also has a wide range of characteristic values depending on the method of preparation and doping or composite. DLC can be considered as one of the best candidates to be tailored in the form of a smart surface to be further improved and optimised to get the best performance.

Many proven works and attempts have been reported in incorporating new elements in amorphous DLC to improve the mechanical and tribological properties. In this work, graphene nanoplatelets (GNP) are introduced to the DLC film structure to produce a new composite coating of DLC-GNP. Graphene, on the one hand, is currently the most trending carbon material with remarkable bloom in numbers of research and patents. This strongest 2D material ever known to science and found by a human is believed to have better performance compared to other types of carbon material with the same lattice structure as CNT. Incorporation of GNP in DLC matrix is believed to supplement each other which resulted in overall improvement of the mechanical and tribological properties of the composite coating.

1.2 Objectives of the Thesis

The overall aim of this study was to develop a novel composite coating of Diamond-Like Carbon (DLC) and graphene nanoplatelet (GNP) that is tough and capable of reducing wear and friction. Hence, the objectives of the study are as follows:

(a) To develop a new coating design of DLC-GNP nanocomposite coating that can be applied in various tribological applications.

(b) To develop a process to deposit DLC and GNP as a nanocomposite coating while maintaining the adhesion and increasing the robustness.

(c) To investigate the mechanical and tribological properties of the nanocomposite coating.

1.3 Thesis Outline

This thesis is composed of eight chapters, and the structure is shown in Figure 1.2. Details of the results' chapter are also presented in Figure 1.3. It is divided into

- **Chapter 1**: discusses the background of this work that comprises about global energy efficiency and world trend on the reduction of friction. This chapter ends with the outline of this whole report.

3

- **Chapter 2**: presents the theory on tribological coating and a review of thin film coatings, composite coatings of carbon-based and DLC-based is given. Review on graphene as a potential dopant in the composites is also discussed. Characteristic of film coatings are discussed at the end of this chapter.

- **Chapter 3**: describes research methodology of this study. This includes the experimental procedure and setup for each of the processes from sample preparation, graphene coating, and DLC coating. The fundamental principles and characterisation techniques are also described.

- **Chapter 4**: presents optimisation of GNP deposition which includes a selection of the solvent and dispersion times using ultrasonication. This chapter also presents the results of optimisation of spin-coated GNP using Taguchi method.

- **Chapter 5**: presents experimental results on production and characterisation of single-layer DLC-GNP nanocomposite coating. In this chapter, results of an experimental parameter of DLC deposition time, the effect of post-treatment and GNP concentration are presented. Each test in the subsection is characterised separately to study the physical, mechanical their tribological properties.

- **Chapter 6**: presents experimental results on production and characterisation of multilayer DLC-GNP nanocomposite coating. Each test in the subsection is characterised separately to study the physical, mechanical their tribological properties.

- **Chapter 7**: discusses the results obtained in chapter 4, 5 and 6. Discussion focuses on the structure of as-prepared DLC-GNP nanocomposite coating, the mechanical, the chemical structure and tribological behaviour of the nanocomposite coating.

- **Chapter 8**: gives the conclusions of the work in this thesis. This last chapter also discusses the future plan of this work.
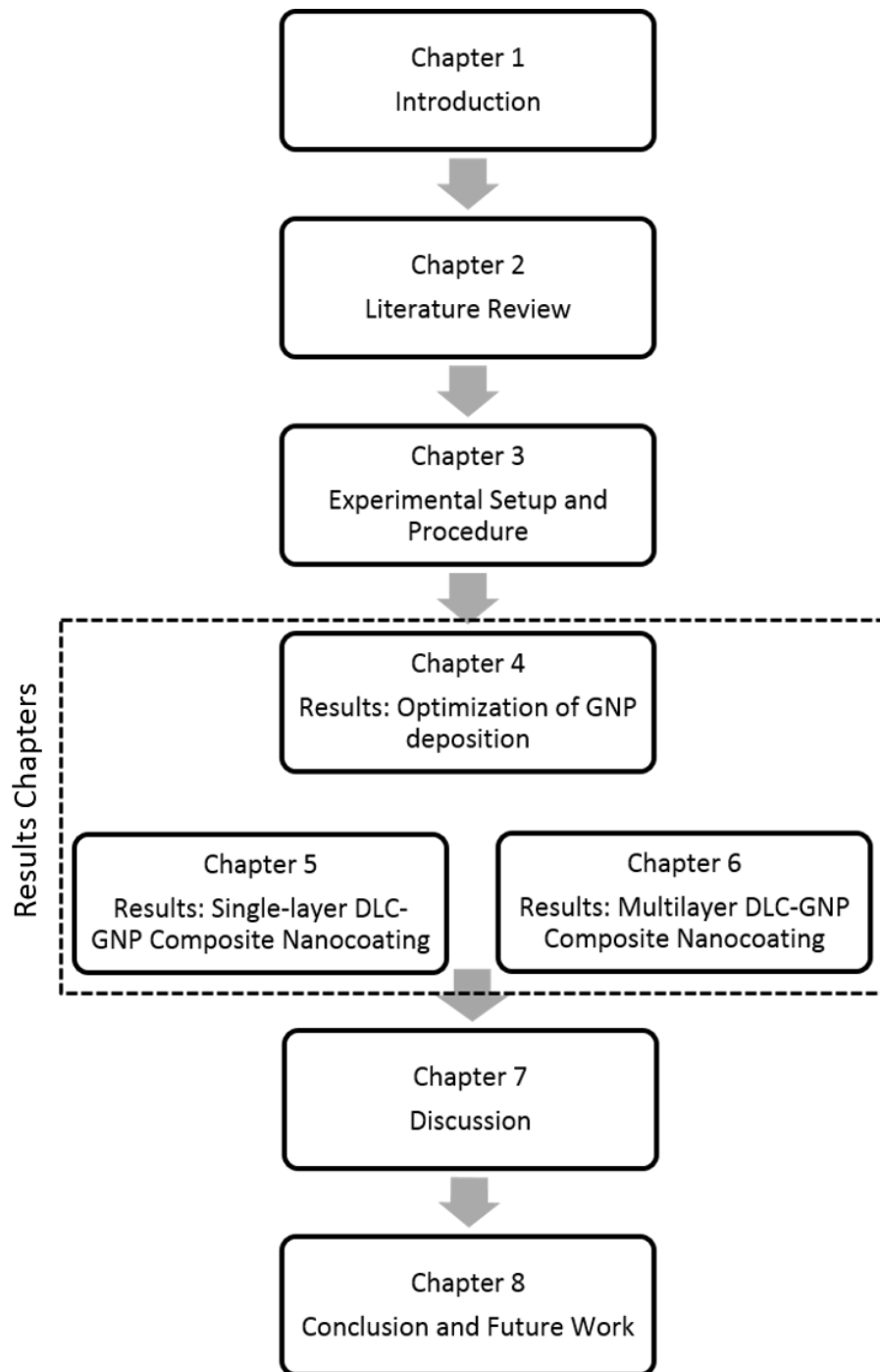
Figure 1.2 Flowchart of the thesis
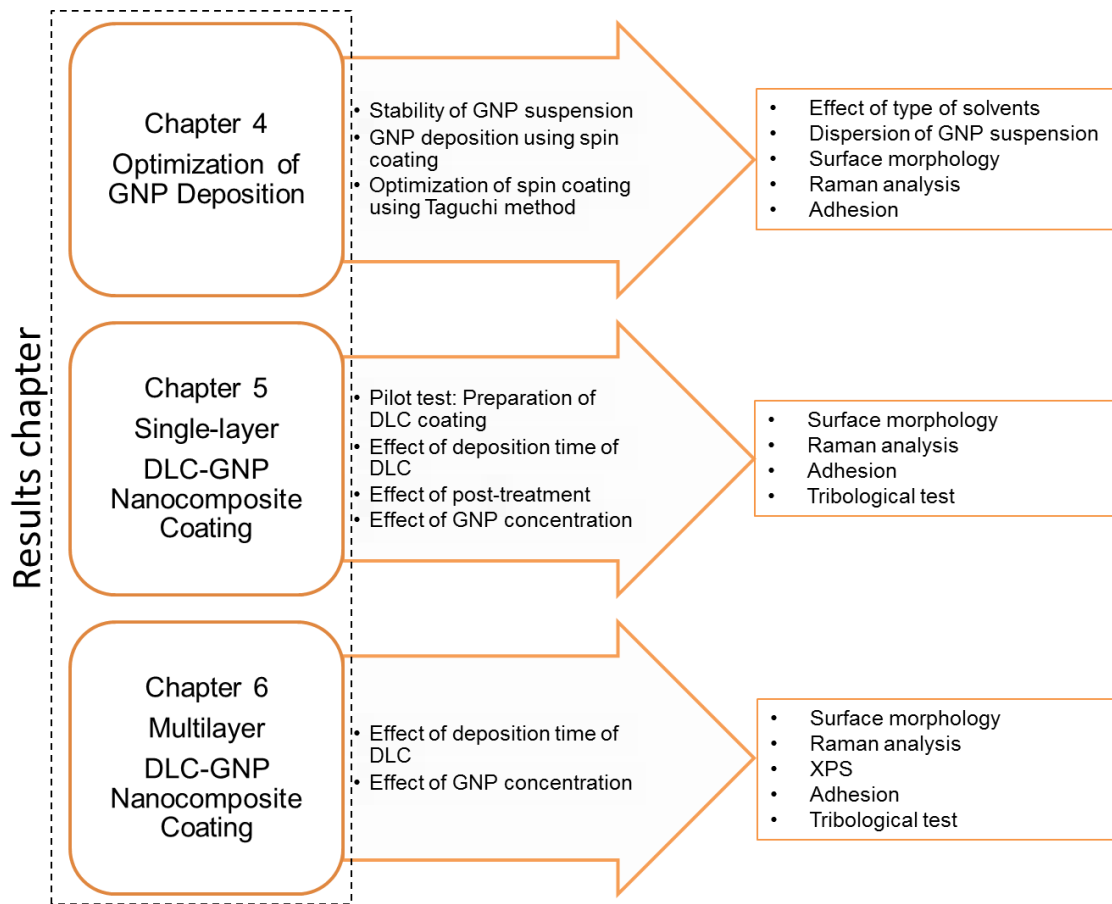
Figure 1.3 The structure of results chapter

Chapter 2
Theory and Literature Review

2.1 Introduction

This chapter gives theory and a thorough review of thin film coatings for tribological applications; composite coatings; carbon-based composite coatings; DLC-based nanocomposite coatings and usage of graphene as an additive in composite coating. This chapter also reviews the characterisation techniques for nanocomposite coating. The motivation of the work, problem statement, objectives of this study and scope of work will conclude the chapter.

This literature review aims to identify the type of carbon-based composite coatings that have been reported focusing on DLC and graphene for tribological applications. It is also to recognise various experimental methodologies that have been used. Table 2.1 shows the main section of this chapter and the relevant keywords that have been used to search related publications.

Table 2.1 Keywords used for each main section of the literature review

Main section	Keywords
Thin film coating	Tribology, deposition, coating
DLC Composite	Chemical structure, DLC composite, tribological properties, deposition, PECVD, adhesion, critical load, surface roughness, hardness, elastic modulus, friction and wear, Raman, chemical structure, toughness
Graphene Composite	Graphene composite, dispersion, solvents, deposition, graphene nanoplatelets, tribological properties, friction, wear, hardness, elastic modulus, adhesion, critical load, hardness, Raman, toughness

2.2 Theory

2.2.1 Coating: state of the art

For many years, thin film coatings have been used for many technological applications such as automotive, aerospace, food technology, construction and many others. It is known that most component failures in industry occur due to the failure of the surface. The rapid growth of industries such as automotive and machinery has driven the demand for smart coatings with excellent mechanical and tribological performance, environmentally-friendly and cost-effective. In tribology, application of coatings is generally to reduce friction and wear resistance. Friction and wear have become important especially since the era of the first industrial revolution. Until today, moving towards Industry 4.0, friction and wear are still relevant issues. The application of surface engineering for energy efficiency is seen as one the hallmarks of the new industrial revolution of Industry 4.0.

Matthews and group [8] illustrated the timeline of tribology from unitribology in the year of 1800, which relates to the overall performance of the device, to nanotribology in Figure 2.1. Enhancement of surface analysis methods enables us to investigate tribology in as small as atomic scale. It allows us to have a further understanding of tribological mechanisms hence provide a better solution to reduce friction and wear in the system. In future, we would expect to have a robust coating that could offer lubrication effect to control friction and at the same time tough enough to resist wear. The recent terms such as self-lubricated and self-repair are the advanced functionality that is expected for future tribological coatings.

Unitribology
Machinery tribology
Performance, efficiency, reliability, lifetime

Decitribology
Component tribology
Torque, forces, vibrations, clearance, alignment

Macrotribology
Contact tribology
Hertz contact pressure, elastohydrodynamic, pitting, scuffing, scoring

Microtribology
Asperity tribology
Fracture, elastic and plastic deformation, debris, surface layers

Nanotribology
Molecular tribology
Molecules, atoms, van der Waal's forces, single crystals, strings

1 — m
10^{-1} — dm
10^{-3} — mm
10^{-6} — µm
10^{-9} — nm

1800   1850   1900   1950   2000   2050   Year

Figure 2.1 Illustration of the timeline of tribology. Adapted from [8]

2.2.2 Design of coating for tribological application

Several factors play a vital role in designing a coating. Holmberg et al. [9] names these four zones to be critically considered when designing a tribological coating. There are fabricated surfaces, the coating itself, the interface between coating and substrate and the substrate as illustrated in Figure 2.2. Some of the critical properties of a good tribological coating given are the surface roughness and chemical reactivity, hardness and thermal stability of, adhesion between coating and substrate, and fracture toughness and hardness of substrate.
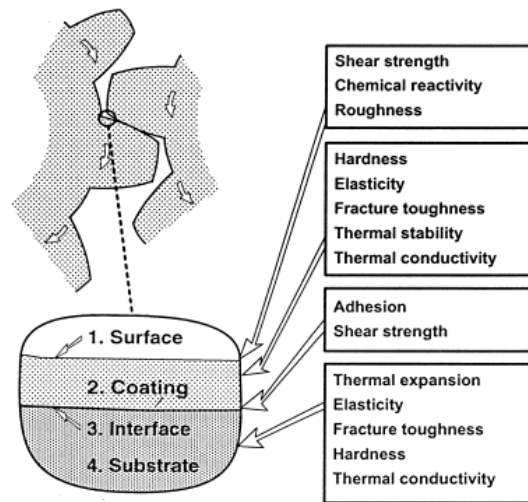
Figure 2.2 Important tribological properties in different zones of the coated surface [9]

Surface roughness of substrate is essential in determining the final surface roughness of coating. According to the model suggested by Salvadori et al. [10], in the early stage of the deposition process on rough surfaces, the tops of the hills grow faster than the valleys are filled thus increase the roughness of DLC film. As the DLC film grows thicker, the roughness growth decreases as illustrated in Figure 2.3. It is likely that surface roughness of a coating can be reduced by selecting a substrate with low surface roughness and increasing the thickness of coating up to certain level. However, Ohana et al. [11] reported that rough surfaces of 263 nm showed better adhesion compared to smooth surfaces with a surface roughness of 1.4 nm. Therefore, when selecting the surface roughness of the substrate, there may not be any specific range of surface roughness that can be considered as the best choice. The suitable value of surface roughness may depend on methods of deposition, type of coating and application of the coating.
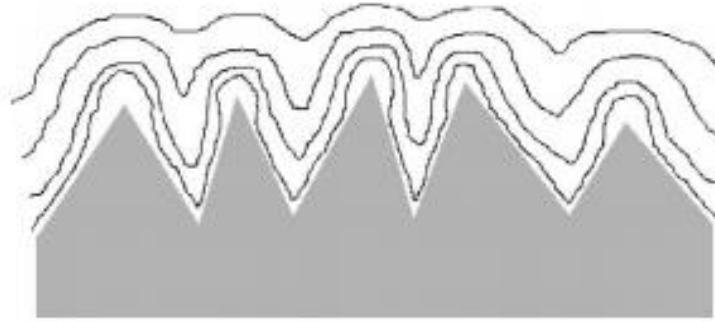
Figure 2.3 Diagram of a rough substrate with successive DLC deposition [10]

Ensuring adhesion of a coating is one the most vital and challenging tasks in surface engineering. Weak adhesion of a coating to substrate restricts the real performance of the coating. Several parameters that may influence the adhesion of coating are surface treatment before coating process, types of substrates, methods of processing, roughness of the surface etc. Waseem et al. [12] found that harder substrates show better adhesion properties with DLC.

2.2.3 Composite coating

Composites combine two or more materials which improve the functionality of the new composite material. They offer more advantages over conventional engineering materials. Composite materials can be classified into a few types as shown in Figure 2.4. For tribological applications, the most effective type of composite layer is the surface layer composite. The recent fabrication of advanced tribological coatings combines the improved function composite with a tribological layer that gives rise to better mechanical properties with excellent tribological performance. Additionally, Zhang et al. [13] described the term 'nanocomposite coating' as a coating composed of at least two phases of either a nanocrystalline phase and an amorphous phase, or two nanocrystalline phases. In other words, any incorporation of nanosize element in a coating is known as a nanocomposite coating.
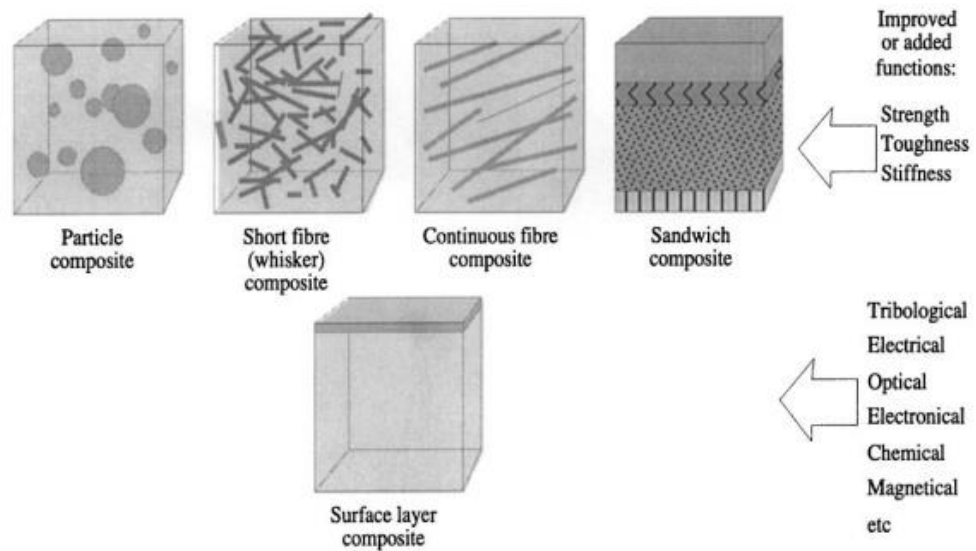
Figure 2.4 Various type of composite materials and the properties improvement [14]

2.2.4 Correlation between mechanical properties of coatings and their tribological properties.

The ratio of hardness (H) and elastic modulus (E) defines the plasticity index of a material which is the ability of materials to deform plastically in the face of an abrasive [15]. Hardness is the ability of material to withstand deformation, while elastic modulus is the quantity that measures a material's resistance to being deformed elastically when stress is applied to it. It is an important parameter to explain elastic-plastic and wear-resisting properties on thin films [16]. The plastic/ elastic properties depend on both hardness, H and the elastic modulus, E. It is reported that plastic deformation is reduced in materials with high hardness and low modulus E* [17].

Musil [18] proposed the dependences of stress vs strain for brittle, tough and resilient hard coatings in Figure 2.5. Musil reported that hard and tough materials exhibit both elastic and plastic deformation and materials that can withstand strain between ε_1 and ε_{max} without cracking exhibit a higher toughness.
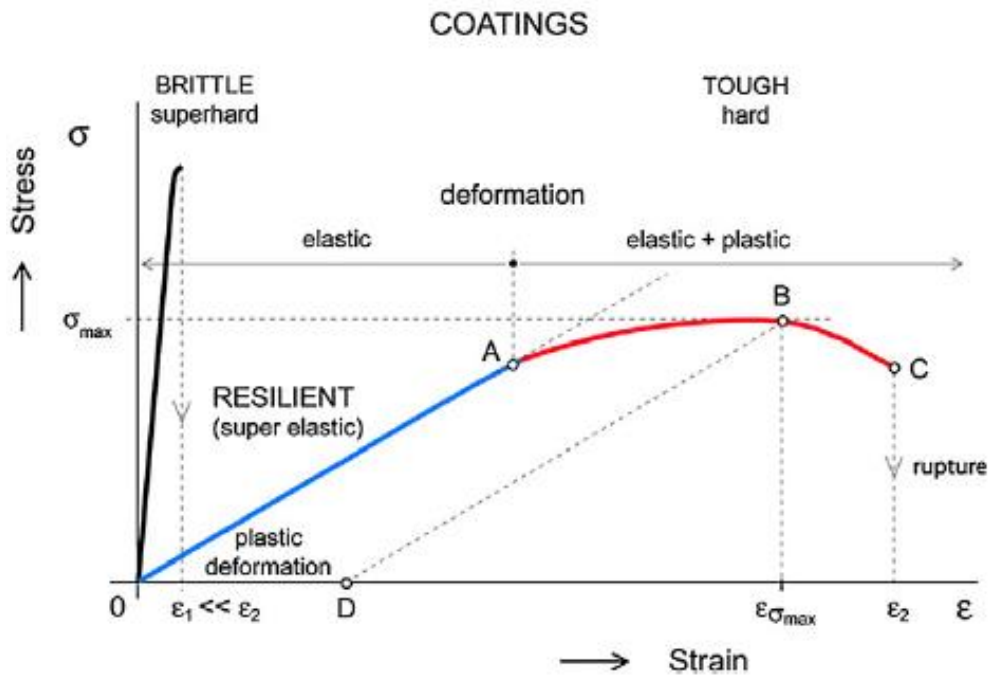
Figure 2.5 Schematic of coating behaviour vs strain and stress [18]

The higher the value of H/E, the higher resistance towards wear. Dwivedi and Kumar [16] suggested that for wear resistant coatings, a high hardness coating with H/E ratio over 0.1 is preferable. However, it has also been reported that hard coatings with the same value of H/E ratios, but different elastic modulus will perform differently. The wear performance of those with a lower value of elastic modulus outperforms those with higher elastic modulus [19].

Musil et al. [19] successfully produced ~3000 nm thick TiC/a-C composite films, a combination of crystalline and amorphous film with a good lubricating and wear-resistant behaviour. The films demonstrated low values of E^* satisfying the condition of $H/E^* >0.1$. This is also supported by their earlier finding on Ti-C coating which possessed low friction with decreasing value of E^* [19].

2.3 Carbon-based Composite Coatings

2.3.1 Introduction

By mass, carbon is the fourth most abundant element in the creation. It is recognised as the hardest substance ever found by human. This fascinating chemical element has the ability to form different hybridisation of sp^3, sp^2 and sp^1. Carbon allotropes can exist in varies structural forms such as diamond, graphite, fullerene, nanotube. A significant number of works have been made on using carbon materials in various application including tribology. Discoveries and development of novel and unique allotropes of carbon have presented a noteworthy contribution to the research world and industries.

To satisfy the demands from many industries, investigations on advanced coatings such as composite coatings has become one of the favourite topics of interest among researchers. Composite coatings have been proven to be more superior compared to conventional single element coatings.

2.3.2 Structure of carbon-based composite coating

Carbon-based composite coatings can be in the form of a mix of elements in specific matrixes for instant incorporation of carbon fibre in polymer. Multilayered coatings are also another type of carbon-based composite where a few layers of elements are combined and can usually be distinguished easily through a microscope. The advantage of a composite coating is that we may have more than one desired characteristic with the addition to the existing, or the character may also be altered to preferred performance according to the needs.

An example of multilayered carbon-based composite films can be seen in Figure 2.6. Chen and group [20] produced a composite coating consisting of polycrystalline diamond (PCD)/ Ti/tetrahedral amorphous carbon (ta-C) by a two-step process of CVD and filtered cathodic vacuum arc growth. The existence of layers can be seen clearly in the cross-sectional observation. Another common type of carbon-based composite coating is particle reinforced composite. Sarmadi et al. [21] fabricated copper (Cu)-graphite surface

composite using friction stir processing (FSP) method. Graphite particles in the size of 5 μm were dispersed and embedded into the surface of Cu that has been grooved earlier. Figure 2.7 shows the optical image of Cu-graphite composite surface. Black areas in the figure represent graphite particles.
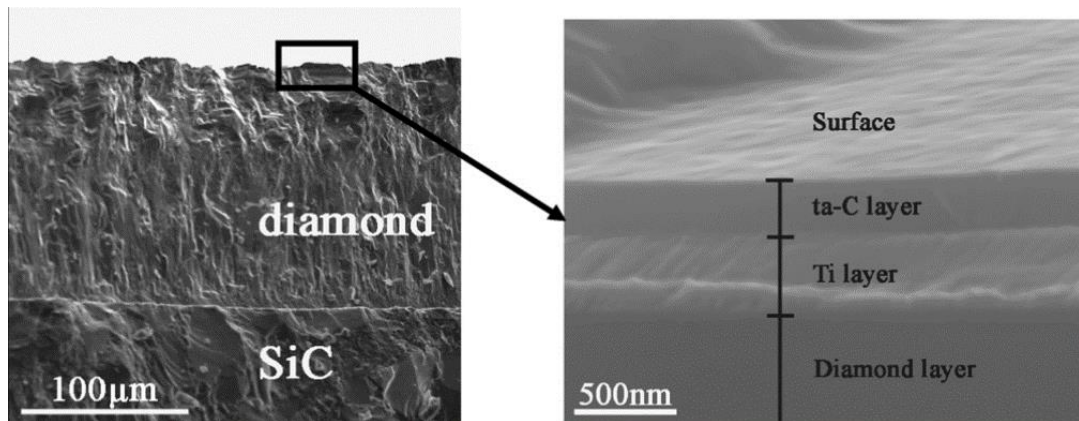
Figure 2.6 SEM micrographs of (PCD)/Ti/ta-C composite film cross section [20]
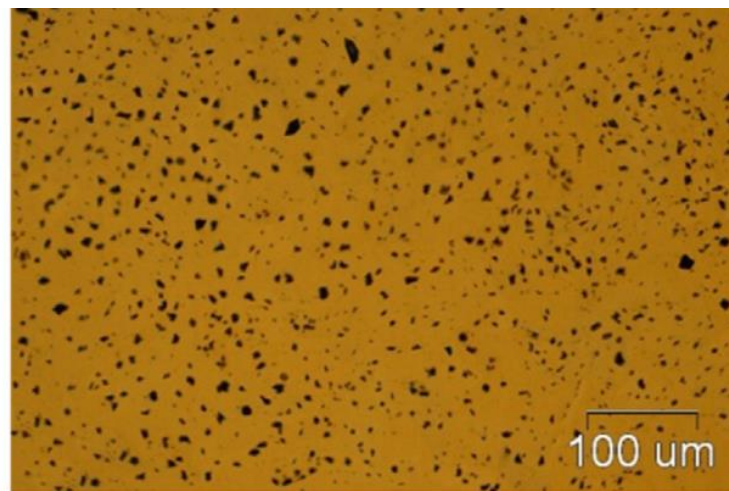
Figure 2.7 Optical image of Cu-graphite composite [21]

2.3.3 Mechanical and tribological performance of composite coating

Table 2.2 summarises several fascinating features of the carbon family of diamond, tetrahedral DLC (ta-C) and hydrogenated DLC (a-C:H). The

properties of the carbon vary significantly depending on their hydrogen content and sp^3 bonding.

Table 2.2 Typical properties of diamond, amorphous carbon and graphite. Adapted from [22, 23]

Crystal system	Diamond	ta-C	a-C:H
	Diamond cubic	Amorphous	Amorphous
Density (kg/m^3)	3515	3260	2350
sp^3 content (%)	~100	>80	<50
Hydrogen content (at%)	<0.1	0	30
Hardness (GPa)	45	>20	<15
Elastic Modulus (GPa)	1050	757	300
Residual stress (GPa)	0	8-10	1-2

Deaquino et al. [24] reported that incorporation of graphite increased the hardness of Al-graphite composite coating and the resistance of wear improved as the hardness increased. The experimental results of the hardness and wear rate are shown in Figure 2.8. Incorporation of more graphite up to 1.5wt% in the Al matrix seems to enhance the mechanical and tribological properties of the composite coating.
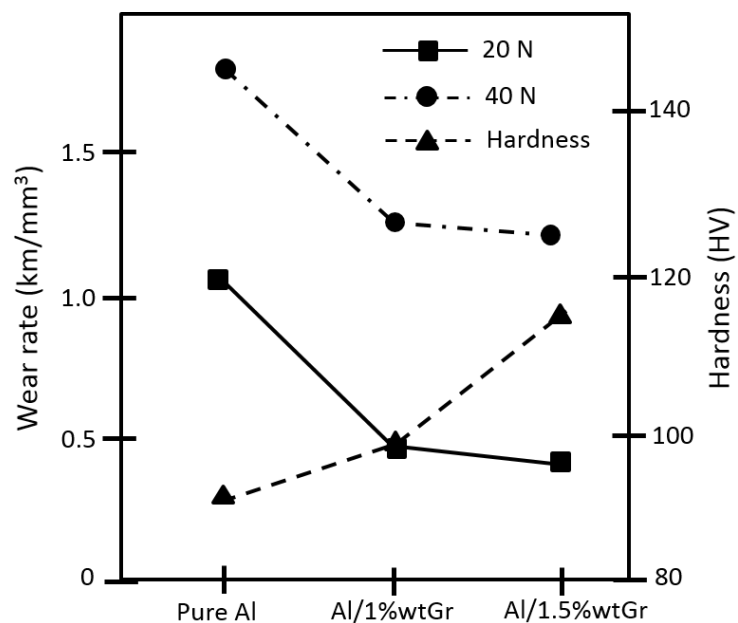
Figure 2.8 Hardness and wear rate of Al-graphite composite coating. Adapted from [24, 25]

Figure 2.9 illustrates the benefit of having a composite of multilayers to prevent fracture. It shows how elastic layers allow the brittle layers to slide over each other under load thus allow deformation of the surface. This type of composite coating combines both hardness and elasticity to avoid failure due to the bending stress generated [26]. The review on the mechanical and tribological behaviour of a carbon-based composite of DLC and graphene will be presented in the following section.
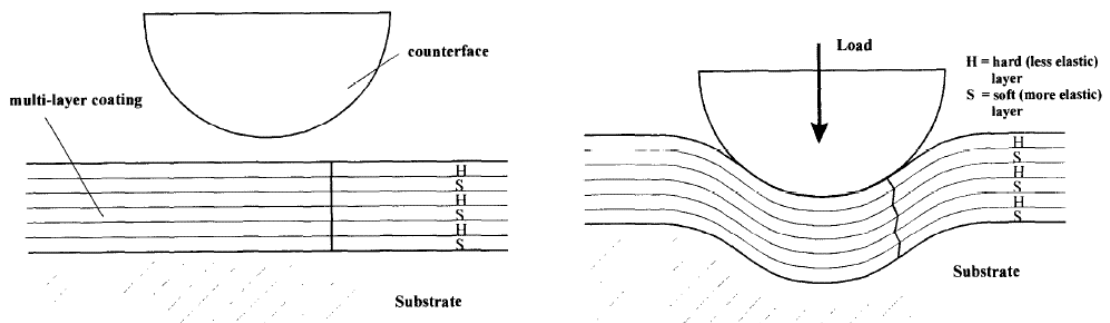
Figure 2.9 Schematic representing an illustration of alternating elastic properties of multilayer coating that allow deformation without fracture [26]

2.3.4 Application of the carbon-based coating

Table 2.3 summarises various types of carbon-based coatings and their potential applications. The carbon-based coatings are found to have potential to be applied in the areas such as electronics, machinery, aerospace, optical, tribological. Most of the applications relate to machinery or moving parts. This indicates the importance of composite coatings that can control friction and wear.

17

Table 2.3 A selection of carbon-based materials as coatings and their potential applications

Coating	Substrate	Potential Application	Ref
CNT grown on DLC	Si (100) wafers coated with Ti	Electrochemical sensing	[27]
Graphene on DLC	P-type Si (100) coated with 300 nm SiO2 wafers	Electronic material	[28]
Aluminium/graphite (Al/Gr) composites		Tribological application	[25]
Si-DLC	Si	Magnetic storage disks.	[29]
Transition metal [30] doped DLC (TM = Ag, Ti and Ni) thickness ~500 nm	AISISS304	Tribological	[31]
DLC/MWCNT hybrid composite	AISI F138 stainless steel plates (20 mm × 10 mm)	Electrode for detection of chemicals in aqueous solutions.	[32]
W doped DLC	AISI 52100 bearing steel plate	Engine components	[33]
DLC/IL/graphene composite	Stainless steel	Space applications	[34]
Copper-graphite surface composite	Pure copper plates	Bearing materials	[21]
Surface modification of insulated DLC film to graphene	Single crystal (100) Si wafer	Electronics application	[35]
Diamond/tetrahedral amorphous carbon composite films	Silicon carbide (SiC) wafers	Cutting tool protection	[20]
CNT doped with DLC	Silicon	Optics, micro-electronics, tooling, automobile industry	[36]
Ti-doped graphite-like carbon (GLC) films	Si (100) and stainless steel	Water hydraulic system	[37]
CNT grown on DLC	p-type (100) silicon wafer	Field emission displays, transistors, and sensors.	[38]
DLC doped MWCNT	Single crystal silicon wafer (100)	Tribological and optical	[39]
DLC coating deposited on CNT films	H-terminated Si(001) SiO2 layer = 30 nm thick	Mechanical	[40]

2.4 Diamond-Like Carbon (DLC) and DLC-based Nanocomposite Coating

2.4.1 Introduction

The history of DLC began in 1971 when Aisenberg and Chabot [41] first prepared the film. Nevertheless, Schmellenmeier [22] was actually the first to mention hard amorphous carbon films in 1953. The chemical structure, physical and mechanical properties have been extensively studied since then. It also has been applied in numerous of application in industries. In a way, DLC coatings can now be said as a mature research topic. Figure 2.10 represents the rough numbers of publication on DLC from the year of 1977 to 2016 which have been extracted from the Web of Science using search word of 'diamond-like-carbon'. It is apparent that the number of works done on DLC increased tremendously since 1990. However, the figure seems to be almost not changing since the year 2007.
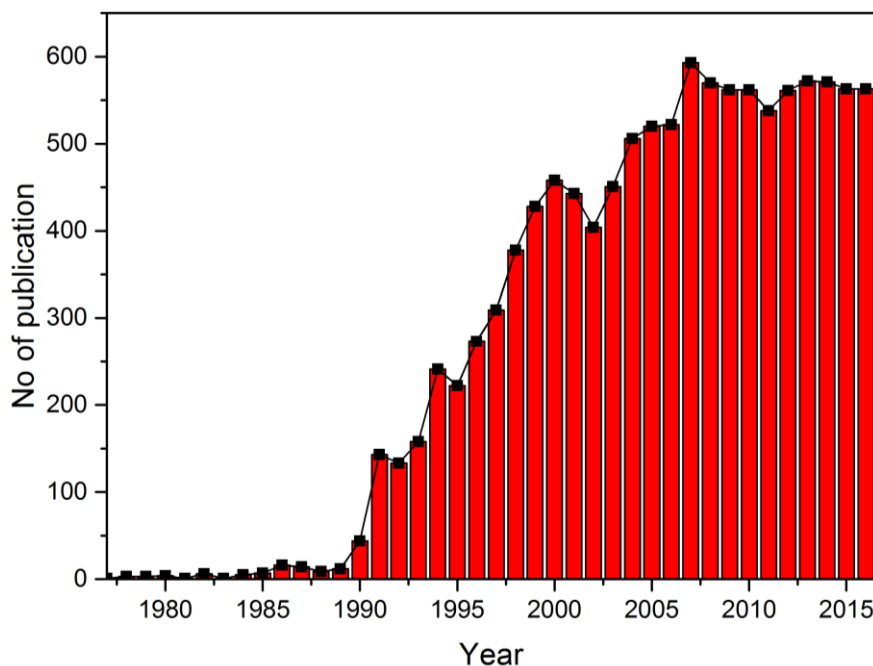
Figure 2.10 Number of publication of DLC since the year 1977 to 2016

2.4.2 Chemical structure of DLC

The term of DLC usually refers to the hydrogenated form of diamond-like carbon (a-C:H) [42]. Typical amorphous DLC will consist of sp^2 and significant sp^3 carbon structures [43]. Sp^2-bonded is graphite-like clusters embedded in an amorphous sp^2-bonded carbon matrix, while sp^3 have diamond-like behaviour. Robertson [43] categorised amorphous carbon-hydrogen alloys into the ternary phase diagram as shown in Figure 2.11. The top corner of sp^3 represents diamond, lower left corner (sp^2) is graphite, and the lower right corner is hydrogen. He also proposed specific domains of carbon-based films with regard to their sp^3 and sp^2 hybridised carbon and hydrogen content. Figure 2.12 shows the structure of amorphous DLC film [44].
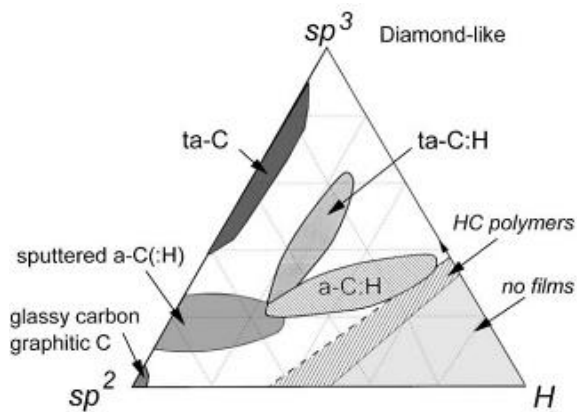
Figure 2.11 Ternary phase diagram of bonding in amorphous carbon-hydrogen alloys [43]
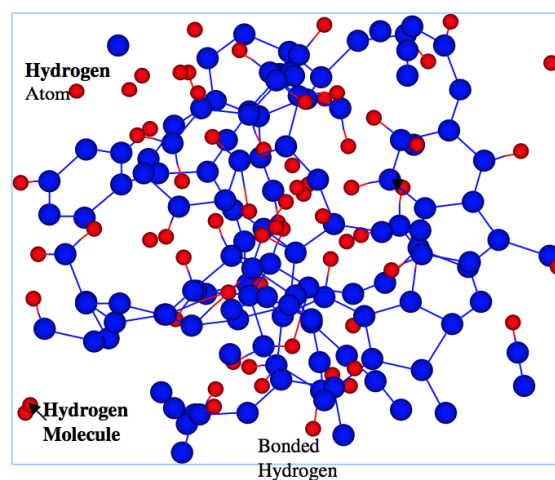
Figure 2.12 Structure of amorphous DLC films [44]

2.4.3 Application of DLC

The unique properties of DLC films, such as high hardness and low friction coefficient, chemical inertness, infrared transparency, and high electrical resistivity, combined with smoothness and low deposition temperatures, making them suitable for a large number of applications especially related to its tribological behaviour. It has shown extraordinary performance and been proven to have potential to be applied in engineering application such as biomedical, aerospace [45]. Table 2.4 summarises some of the industrial sector and potential application of DLC coating.

Table 2.4 Review of the application and potential application of DLC coating

Industrial Sector	Application	Ref
Automotive	Automotive engine components	[46]
Production	Pump of electro-hydrostatic actuators	[47]
Biomedical	Wear and corrosion resistance for artificial joint	[48]
Renewable energy	Solar cell	[49]
Renewable energy	Photovoltaic (PV) technology	[50]
Oil & Gas	Corrosion protection in off-shore	[51]
Manufacturing	Micro forming	[52]
Medical	Medical implant	[53]
Aerospace	Vacuum and space devices	[54]
Aerospace	Solar cells	[55]
Sensor	Pressure sensors	[56]
Electronic	Microelectronic devices	[57]
Hard disk	Magnetic recording media	[58]

2.4.4 Deposition technique

2.4.4.1 Overview

In 1971, Aisenberg and Chabot [41] produced the first DLC thin film using ion beam deposition method. Since then, it has been a bloom of studies in preparing and investigating its properties. Review on DLC by Erdemir and Donnet [44] more than ten years ago shows that production of an excellent and robust system of DLC had now become more facile and economical. To date,

DLC has successfully been synthesised using PVD, pulse laser deposition, CVD and PECVD [59]. DLC can be prepared at as low as sub-zero to 400°C [60]. The next section will explain roughly the deposition process of DLC in several selected methods.

2.4.4.2 Physical Vapour Deposition (PVD)

PVD is a vaporisation coating technique that involves the transfer of material at the atomic level. In PVD, coating is formed by evaporation or sputtering of atoms from the target in a low-pressure environment. Ionized gas atoms collide with the target materials and eject metal ions which are then attracted to the substrate by a negative bias voltage that is applied to the table. The atoms will then condense, nucleate and form a film. Figure 2.13 shows the basic principle of the sputtering technique in PVD. PVD commonly operates at lower temperature than CVD process.
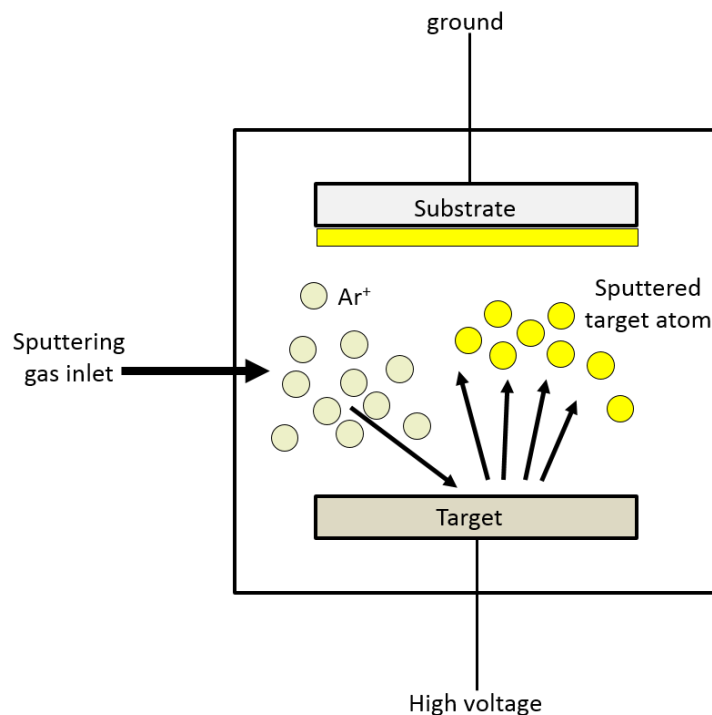
Figure 2.13 Schematic of sputtering in PVD

Xiao et al. [61] prepared DLC coating using PVD with argon as the sputtering gas. Carbon phase was grown from plasma, comprising acetylene and argon on AISI 52100 steel balls as substrate. Nanohardness and elastic modulus

were measured to be 21 and 140 GPa respectively. Table 2.5 listed selected works on DLC film deposition using PVD technique. The thickness varies between from 63 nm to more than 1.0 µm.

Table 2.5 Deposition methods of DLC using PVD technique coating from literature

Temperature (°C)	Thickness (µm)	Substrate	Ref
• 400-600	1.5-2.0	Plasma nitride AISI 4140 steel	[62]
• Max: < 250	0.063	316L stainless steel	[59]
• -	1.6	TiC coated bearing rings	[63]
• 0.26 – 2.10		Low alloy working steel	[64]
• 35 - 500	0.3	Glass, alumina, Si, ZrO_2, molybdenum, $CoSb_3$	[65]
• 100	0.5	440°C stainless steel	[66]

2.4.4.3 Chemical Vapour Deposition (CVD) and Plasma Enhanced Chemical Vapour Deposition (PECVD)

In contrast to the PVD technique, in CVD, the chemical reaction is in the vapour phase of the constitutive elements to form a material precursor. Figure 2.14 illustrates the theory of film deposition by the CVD method. CVD involves thermally induced reaction of metal-containing molecules on a heated surface. The first process is the transportation of volatile precursor into the reactor and to the substrate. The precursor will adsorb and reacts to release the supporting ligands which are subsequently desorbed and moved out of the reactor. The metal atoms will then diffuse and form a stable nucleus followed by further growth. Growth will take place once a continuous film is formed on the metal being deposited.

The principle of the PECVD is the same with CVD. PECVD technique is typically used for the deposition of elemental materials (Al, a-C, C-Si), nitrides (AlN, Si_3N_4) and carbides (BCN, SiC). Earlier work on DLC deposition using CVD requires a very high temperature of more than 1000°C. This is a great limitation for thermally sensitive substrates, and it also promotes the generation of defect on either the substrate or depositing layer. It is also the reason why it is hard to find DLC film deposition using only CVD method without the

assistance of plasma enhance technique. In PECVD the temperature of deposition could be lowered by creating an electric discharge or glow discharge plasma. Plasma promotes chemical reactions, and it also provides energy to the substrate surface to enhance the process of nucleation, part migration and kinetics. There are several methods to generate plasmas. One of the most common methods is by electrical discharge in gaseous. Adding techniques such as radio frequency and microwave source help to sustain the plasma in PECVD [12].
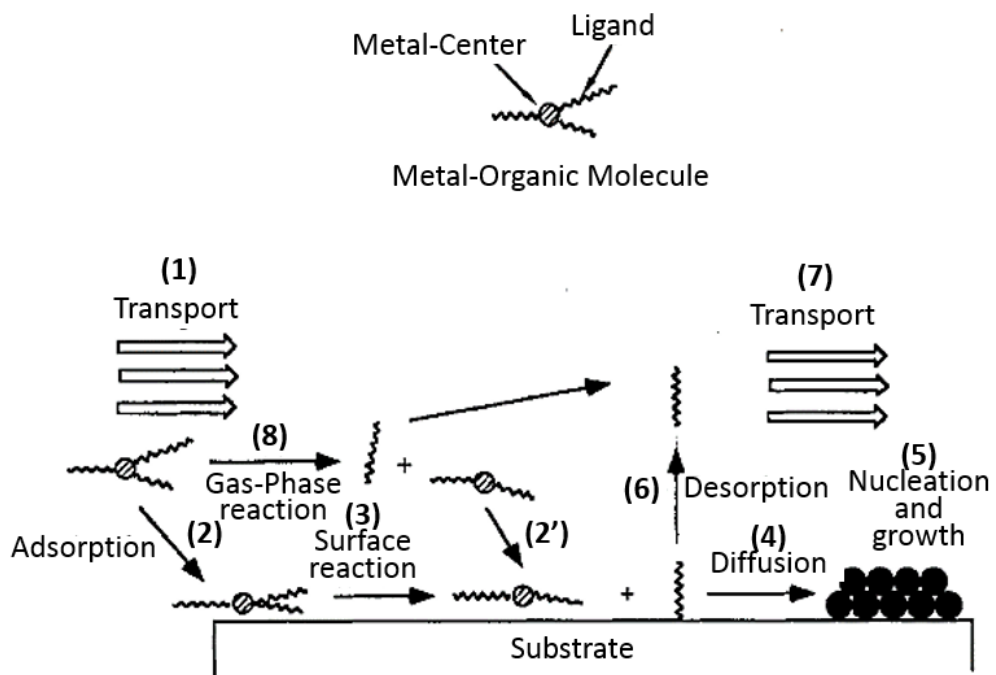
Figure 2.14 Deposition steps in CVD process [67]

Table 2.6 Deposition methods of DLC coating using PECVD technique from literature

Temperature (°C)	Thickness (µm)	Substrate	Ref
• -	1.5	M2 HSS	[68]
• <200	Max 2.6	Si	[69]
• -	2	Ti_6Al_4V substrates	[70]
• 200	0.2 -0.87	Si and glass	[71]
• 150	1.50 - 2	Si wafer	[72]
• Max 150	0.04	Si, quartz and polycarbonate CD	[73]

2.4.4.4   Other deposition methods

Other than PVD and CVD, DLC films have also been reported to be produced by Pulsed Laser Deposition (PLD), cathodic vacuum arc discharge etc [74-78]. Magnetron Sputtering is another well-known deposition technique of DLC coatings that have been used for centuries [79].

2.4.5   DLC-based composite Coating

Recent advances in DLC coatings have also brought us numerous types of DLC-based composite coatings which have been demonstrated to overcome the drawbacks reported before. DLC composites involve the incorporation of new phase/ element into the amorphous carbon matrix to modify and enhance the intrinsic properties. Incorporation of another element in DLC coating can either be in the form of multi-layered, matrices or nanostructures. It has been proven to improve the performance of conventional DLC coating, especially on its mechanical and tribological properties.

Figure 2.15 depicts the TEM micrograph of a Ti-DLC coating. Bharathy et al. [80] used an approach of incorporating Ti nanoparticles in the matrix of amorphous DLC. By using TEM, Ti particles in DLC matrix and particles distribution can be observed while density and size can be measured. Using EELS, crystallite structure of Ti has been confirmed.

Figure 2.16 shows the schematic of the fabrication process of DLC-CNT coating and the SEM image after fabrication by Kinoshita and group [40]. CNT was first grown by PECVD process before deposition of DLC in the same chamber using RF-PECVD technique. The coating has improved toughness and reduction of the elastic modulus and dynamic hardness with the increase of CNT concentration in the composite. Another similar work of DLC-CNT coating was carried out by Wei and group [36]. Wei used spin coating method to deposit a CNT film on substrate before deposited DLC coating on the CNT film via PECVD technique. On the other hand, Zanin et al. [32] used a slightly different approach to produce DLC-CNT composite coatings. The DLC and CNT were deposited in the same CVD chamber at the same time. While DLC

films were being deposited, CNT was incorporated by spraying it into the chamber.
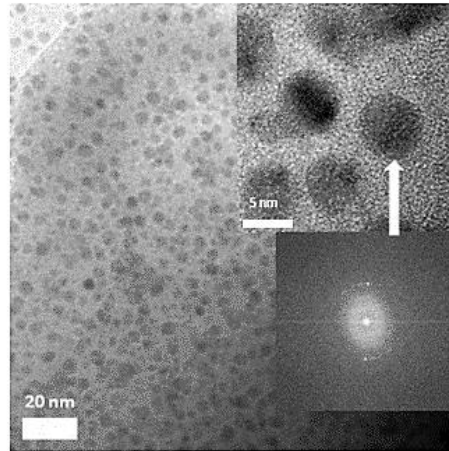
Figure 2.15 TEM micrograph of particles reinforced nanocomposite of Ti-DLC coating [80]
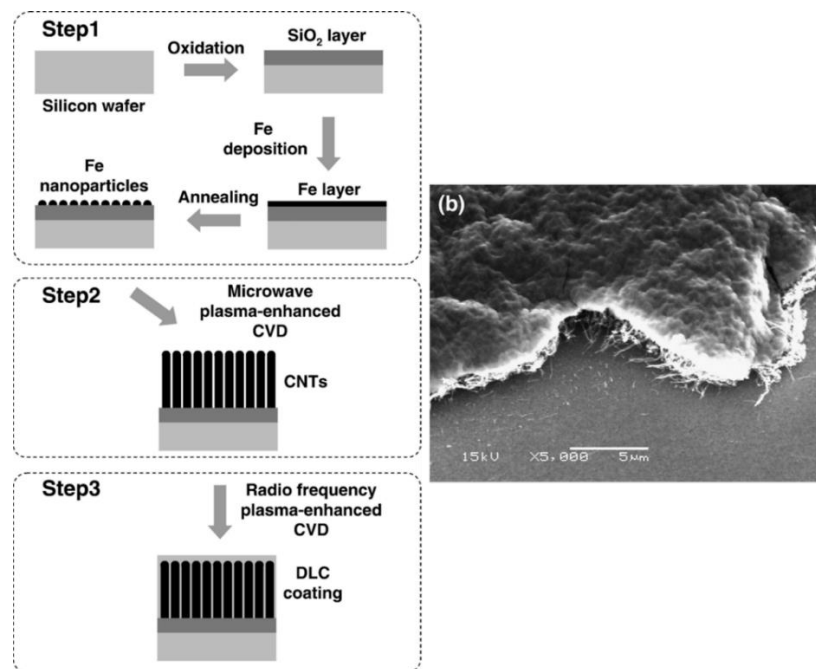
Figure 2.16 Schematic representing the fabrication of DLC-CNT composite coating (left) and the SEM image of the coating(right) [40]

Table 2.7 summarises a review of various types of DLC-based composite coatings and their fabrication methods. The methods to fabricate DLC-based composite coatings can be divided into two approaches which are; one-pot deposition, where both DLC and other phases are deposited in the same

26

chamber without the need of another process, and the two-step procedure is when two different methods of depositing are used. Most of the process for one-pot deposition is carried out using the CVD technique including the PECVD and RF-PECVD. This suggests CVD is the most possible and facile technique to fabricate another type of DLC-based composite coating. The review also showed that DLC-based composite coating could be classified into three main groups which are DLC-transition metal, DLC-non-metallic and DLC polymer/ceramic.

Table 2.7 A review of specific DLC-based composite coatings

Coating types	Fabrication Method	Type of deposition
CNT-DLC [40]	CNT: microwave PECVD DLC: RF-PECVD	One-pot
MWNT-carbon film [39]	DLC: electrochemical deposition	One-pot
CNT-DLC [38]	DLC: RF-PECVD CNT: HF-PECVD	One-pot
CNT-DLC [36]	spinning coating DLC: PECVD	Two-step
Ti-DLC [81]	Hybrid ion beam	One-pot
DLC-graphene [35]	a-C:H film: PECVD	One-pot
DLC-IL-graphene [34]	spinning at 2000 rpm for 30 s DLC: unbalanced magnetron sputtering technique	Two-step
W-DLC [33]	PVD	One-pot
DLC-MWCNT [32]	PECVD	One-pot
Transition metal-DLC [31]	nanosecond pulsed laser deposition (PLD)	One-pot
Si-DLC [29]	radio-frequency PECVD	One-pot
Graphene-DLC [28]	DLC: RF-plasma PMMA	Two-step
DLC-CNT [27]	CVD	One-pot

2.4.6 Mechanical and tribological properties of DLC and DLC-based composite

Among other tribological coatings, DLC films provide the broadest range of mechanical and tribological behaviours. It is well known to have high hardness and unique tribological properties. The properties widely vary as the amount of sp^2 and sp^3 bonded carbon atoms change. As shown in Figure 2.17, DLC with high sp^2 bonded carbon atoms are relatively soft and have graphite behaviour in tribological tests, while high sp^3 DLC behaves more like a diamond which is super hard thus showing outstanding tribological properties [44]. However, according to Erdemir and Donet [44], although DLC is also known to have super hardness but it has lack of lubricity ability and friction reducer. Liu et al. [34] reported graphitisation of DLC resulting high friction when applied in long duration, high load and sliding speed. In Figure 2.18, Erdemir and Donnet [44] suggested that there is no straightforward relationship between hardness and coefficient of friction values for DLC film. DLC can be as hard as 90 GPa, gives low friction and high wear resistant film ever known.
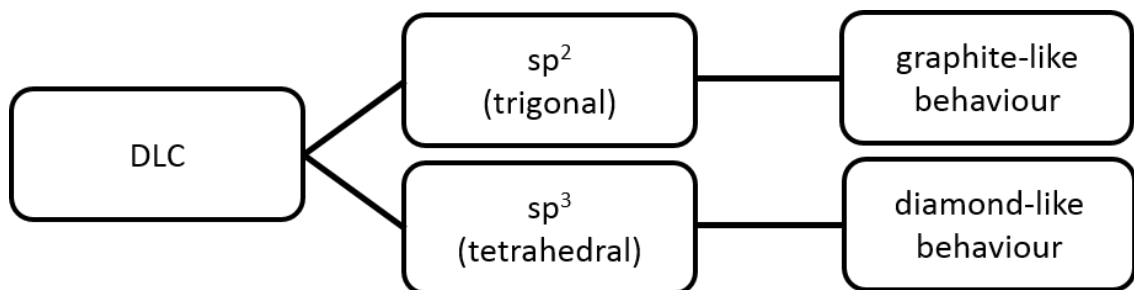
Figure 2.17 Behaviour of sp^2 and sp^3 in DLC
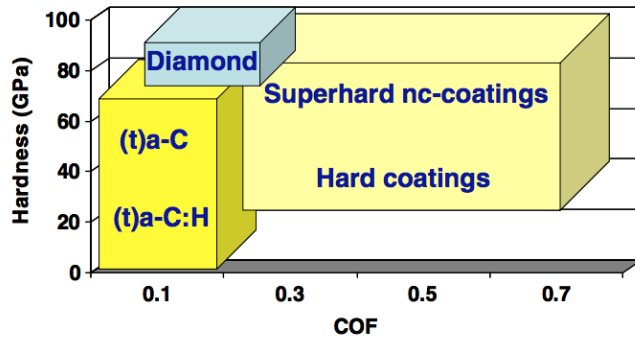
Figure 2.18 Hardness and coefficient of friction (CoF) of carbon-based and other hard coatings [44]

Kinoshita et al. [40] reported that the elastic modulus and dynamic modulus of fabricated DLC-CNT composite coating reduced as the concentration of CNT increased with measured values of 1227 and 230 GPa respectively (Figure 2.19). The fibrous structure of CNT seems to make the coating softer than conventional DLC coating. Interestingly, observation of the indentation showed that the toughness of coating increased by the addition of CNT.
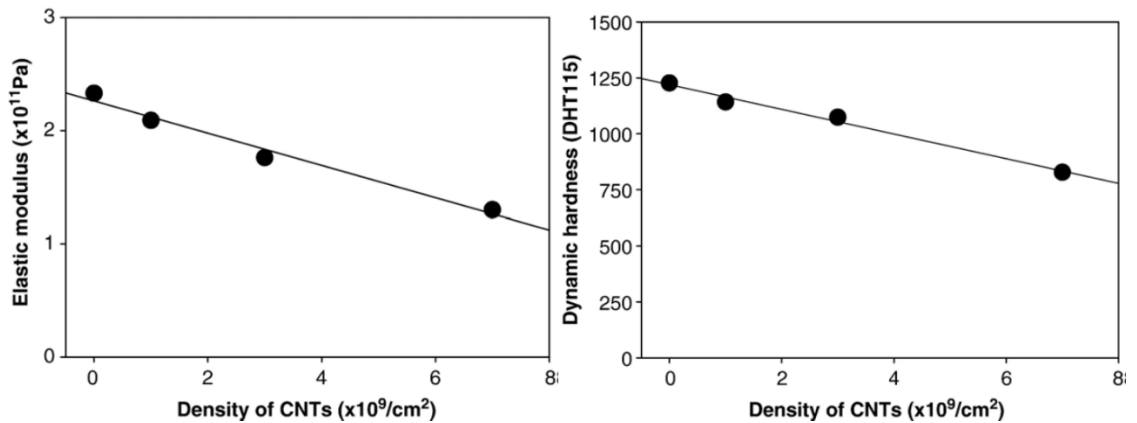
Figure 2.19 Elastic modulus and dynamic hardness of DLC-CNT composite coating [40]

Table 2.8 summarises the values of elastic modulus, hardness, residual stress, the ratio of hardness (H) and elastic modulus (E), the coefficient of friction and the thickness from various works done on DLC and their composite. Elastic modulus and hardness of DLC-based composite coating vary in a wide range from 55 to 280 GPa and 6 to 40 GPa respectively. Most of the reported DLC composite coating showed low values of elastic modulus and hardness as compared to pure DLC coating. It is worth noting that the mechanical property

of DLC coating can easily be tailored by incorporation of a new phase to its system.

Table 2.8 Review of published values of elastic modulus, hardness, residual stress, measured H/E ratio, friction coefficient and thickness of DLC and DLC-based composite coatings

Coating	Elastic Modulus, E (GPa)	Hardness, H (GPa)	Residual stress (GPa)	H/E	Friction coefficient	Thickness (nm)
DLC-CNT [36]	113-127	10.8-13	2.15-2.35	0.09-0.10	0.025-0.11	NA
W/Ti-DLC[82]	55- 120	6 – 12.5	0.3–0.9	≈ 0.1	NA	~600 ± 15
Cu/DLC [16]	209-280.9	14.2–26.2	NA	~ 0.093	NA	NA
DLC DLC/C DLC/Ti [83]	>200 180-225	40 25 25	NA	~0.125 0.129-0.111	NA	400-600

2.5 Graphene and Graphene-based Nanocomposite Coating

2.5.1 Graphene nanomaterials

Graphene can be defined as a monolayer of sp^2 bonded carbon atoms with two-dimensional (2D) honeycomb lattice and is also a building block for 0D buckyballs, 1D nanotubes and 3D graphite [84, 85]. It has all of its carbon atoms on the surface; therefore, the properties may be altered easily with the material contacting the surface [86]. Monolayer graphene was first experimentally observed by Boehm-Hofman in 1962 [87]. In 2004, Sir Professor Andrei Geim and Sir Professor Kostya Novoselov isolated graphene unambiguously and in 2010, they won the Noble Prize in Physics for the discovery [88]. It is the first truly 2D material ever discovered in the universe. Since then graphene has been produced in various sizes and thickness. Figure 2.20 shows the graphene flake image with a thickness of ~ 3 nm captured by the group in 2004 [89].
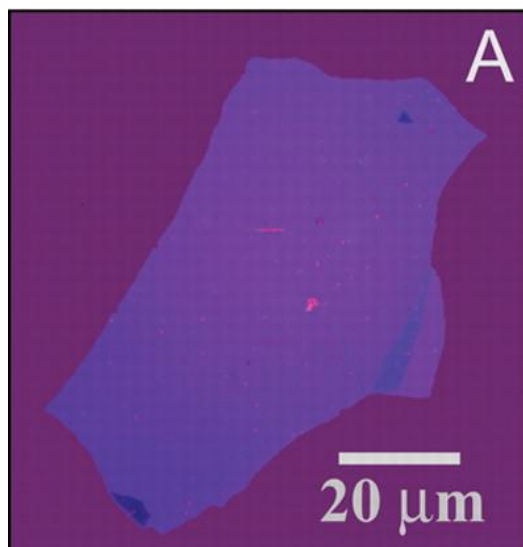
Figure 2.20 Graphene flake image captured by Novosolov and group prepared by mechanical exfoliation [89].

Generally, graphene can be distinguished between single-layer, bilayer and few-layer graphene with a layer number of less than ten [88]. Figure 2.21 represents the two layers graphene which each carbon is bonded to the four nearest neighbours [90]. Table 2.10 shows the mechanical properties of

graphene reported in few selected literature. As we can see, compared to steel, graphene has more than 100 times the strength by weight and the highest tensile strength of any material ever tested. Experimental and computer simulation on graphene by Lee et al. [91], showed that graphene could be easily bent and exhibit extremely large Young modulus, E of 1.0 TPa.
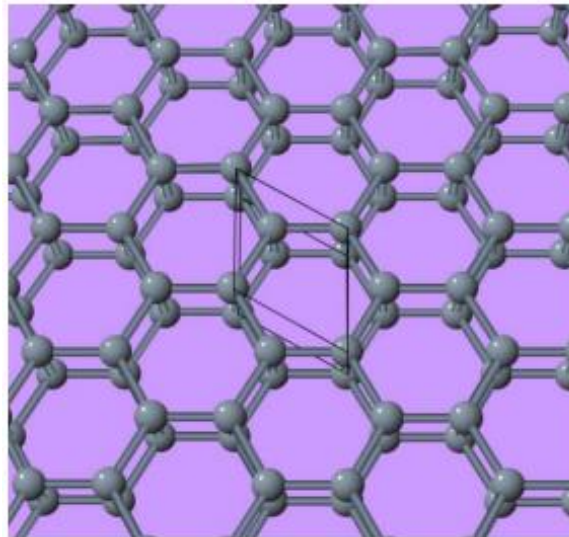
Figure 2.21 2D Carbon allotrope formed by two graphene layers [90]

Since graphene can be produced in different chemical structure and size, numerous terms have been used to describe graphene. Table 2.9 shows the term for graphene and graphene-related materials that have been proposed by Bianco et al. (2013) [92]. The list also includes the chemical structure, thickness and lateral dimensions of the proposed term. These terms may be beneficial to be used as a guide to differentiate different types of graphene.

Table 2.9 Nomenclature of 2D carbon sheets (graphene/ graphene oxide) [92]

	Chemical structure	Thickness	Lateral dimensions
Graphene layer	Hexagonal organization of sp2 bonded carbons	Single-atom thick sheet	From several nanometers to macroscale
Bilayer graphene, trilayer graphene	Stacked graphene	2 or 3 well-defined layers	Extended lateral dimension
Few layers of graphene (FLG)	Stacked graphene	From 2 to about 5 well-defined layers	Extended lateral dimension
Multilayers of graphene	Stacked graphene	From 2 to about 5 well-defined layers	Extended lateral dimension
GNP/ nanosheets/ nanoflakes	2D graphite material	< 100 nm	< 100 nm
Graphene nanosheet	Graphene layer	Single-atom thick sheet	< 100 nm
Graphene microsheet	Graphene layer	Single-atom thick sheet	From 100 nm to 100 µm
Graphene oxide	Chemically modified graphene by oxidation of the basal plane	Single layer	Extended lateral dimension
Reduced graphene oxide	Graphene oxide which has been reduced	Single layer	Extended lateral dimension

Table 2.10 A selection of mechanical properties of graphene from the literature

	Mechanical Properties	Value	Reference
Graphene	Young modulus	E = 1.0 TPa	[91]
	breaking strength	42 Nm^{-1}	[91]
	Adhesion energy	0.45 ± 0.02Jm^{-2} (monolayer graphene) 0.31 ± 0.03Jm^{-2} (2 - 5 graphene sheet)	[93]
Graphene oxide	Young's modulus	207.6 ± 23.4 GPa	[94]

Research carried out on graphene has significantly increased since its discovery. Based on the search conducted on numbers of publications using Web of Science, there is a drastic rise of works on graphene since 2007 until today (Figure 2.22). Data in Figure 2.22 was obtained when using the word "graphene" as a keyword search in the title in Web of Science (By Sept 2017). The number of publication in year 2016 increased more than 300% compared to year 2000. Up to year 2016, more than 27,000 manuscripts with "graphene" as their topic can be found in the search engine of Web of Science. This enormous sudden interest may be due to its wide range of potential application including electrical, electronic, mechanical and tribological. When the scale of the search was reduced to using the keyword of "graphene", "friction" and "wear", the trend of research on the related topic can be seen as in Figure 2.23. However, the number of publication in this area is comparatively low compared to the total number of publication as in Figure 2.22.
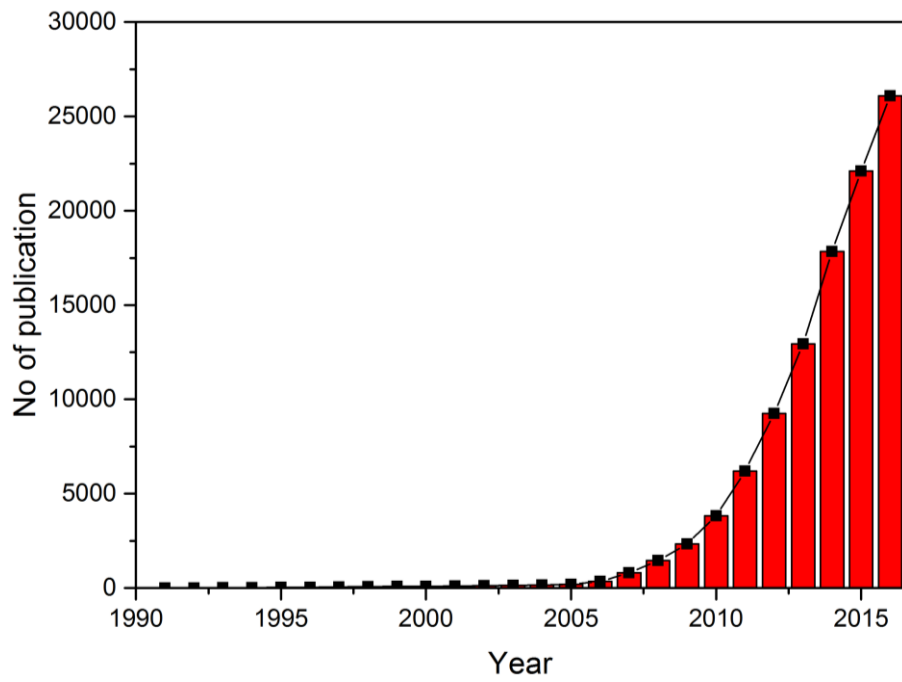
Figure 2.22 Number of publications on graphene from 1991 to 2016
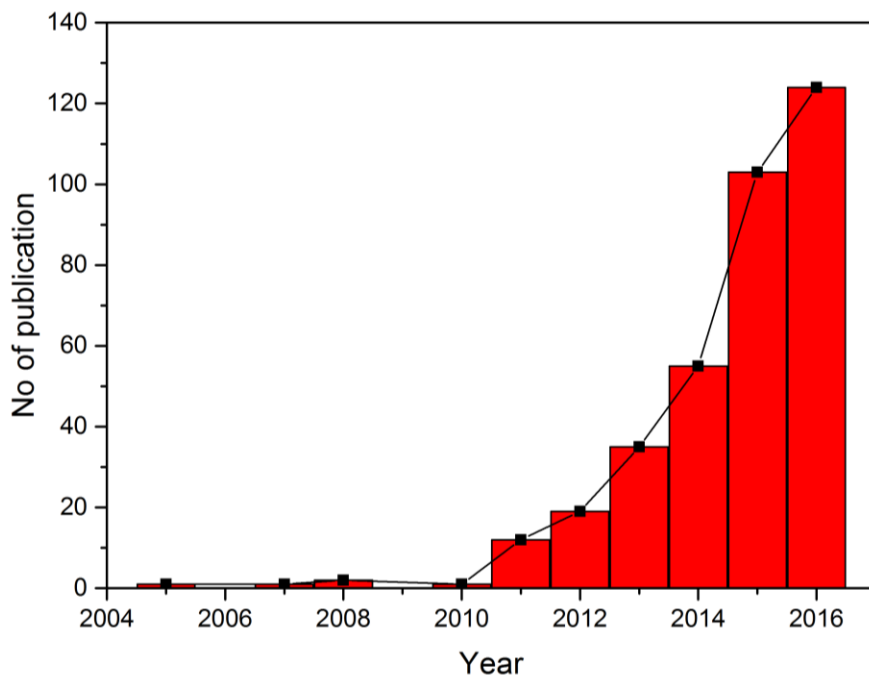
Figure 2.23 Number of publications on graphene from 2005 to 2016 related to friction and wear

2.5.2 Production of graphene

Graphene was first produced by Novoselov et al. [95] by sticking a flake of graphite to tape which was then exfoliated to separate the graphite layers, and have repeatedly been done to reduce the number of layers until only a few layers of graphene sheets was isolated. However, this process will only produce a small amount of graphene and make it almost impossible to use for further studies.

Many research efforts have been made in an attempt to produce graphene. Like most of the other nanomaterials, fabrication of graphene may involve both bottom-up and top-down approaches. Table 2.11 summarises the methods to produce graphene in various morphology such as nanowalls and film, since 2004 until recently. One of the most commonly used technique to produce graphene is CVD. Compared to thermal exfoliation method, CVD method has the capability to produce larger size of graphene with the ability to control its size [1].

Table 2.11 A review of methods of preparation for graphene nanomaterials

Types of graphene	Method of preparation
Graphene nanowalls [96]	RF-PECVD
Graphene film [97]	CVD on copper foils and films using methane
Large and by-layer graphene [98]	Ex situ on 6H-SiC
Mono to trilayer graphene [99]	CVD on molybdenum foils
Ultra-thin graphene sheet [100]	Thermal exfoliation
Graphene film [85]	CVD
Graphene nanowalls [101]	PECVD
Graphene films [102]	MWPCVD
Graphene nanosheet [103]	microwave PECVD
Graphene film [84]	Mechanical exfoliation
Graphene film [104]	Thermal decomposition
Graphene film [89]	Mechanical exfoliation
Graphene sheet [105]	Solution-based approach using hydrazine

Graphene can be synthesised as either loose graphene powder or film depending on its applications and needs. Extensive works carried out to produce graphene, has made it possible for the industry and scientific world to obtain graphene in a large quantity with good quality and at a low-cost. BCC research has estimated that graphene-based product will continue to grow up to $2.1 billion by 2025 [106]. Figure 2.24 depicts the global market trend of graphene-based product from 2011 to 2022. This has been projected based on huge numbers of potential applications of graphene being investigated.
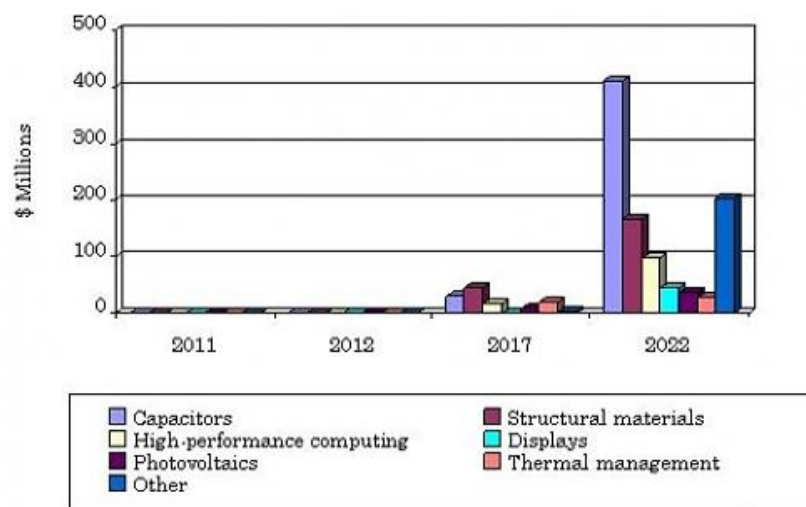
Figure 2.24 Global market trend for graphene-based product [106]

2.5.3 Types of graphene materials and their composite

With the discovery of graphene, large numbers of works have been carried out to investigate its potential application as a composite. Extensive researches have been ventured on integrating graphene into existing coexist coatings to produce graphene-based composite coating. Most of the works are in polymer or metal matrix composites. Table 2.12 summarises selected literature on the composite coating containing graphene. A review of the tribological performance of graphene-based composite is given in Section 2.5.5.

Table 2.12 Work reported in the literature on graphene-based nanocomposite materials

Composite coating	Ref
Polyurethane (PU)-functionalized FG and FGO composite	[107]
Polytetrafluoroethylene (PTFE) filled with graphene platelets	[108]
CNT-GO hybrid/epoxy composite	[109]
Composite based GO and IL	[110]
DLC-graphene	[28]
Al-GNP	[111]
Al-GNP and Al-GO	[112]
Graphene/CNT/Al2O3	[113]
TiAl/multilayer graphene	[114]
Silica-graphene nanoplatelet	[115]
Graphene/Copper	[116]

2.5.4 Performance of graphene and graphene-based nanocomposite in tribological application

The tribological properties of graphene has been widely studied and reported in the literature. One of the tribological applications of graphene is as an additive in lubricating oil. Nano graphene modified lubricant was first patented in 2012 by Zhamu et al. [117]. According to the work, nano graphene platelets with the average thickness of 10 to 50 nm have a good lubricity at elevated temperature, and the wear volume was less than one half of that lubricated with graphite or CNT. Good lubricity performance of graphene at elevated temperature was due to its high chemical reactivity and nanoscale size that enable graphene to penetrate wear gaps.

Compared to graphite nanoparticles or carbon nanotube-modified lubricants, nano graphene platelets modified lubricant was reported to have a better thermal conductivity, friction-reducing capability, anti-wear performance and viscosity stability [118, 119]. Lin and group [120] reported the improvement of

wear resistant and load-carrying capacity of machine when 0.075 wt% of graphene was added as additives. Figure 2.25 shows the reduction of wear rate and friction coefficient when graphene nanoplatelets are added as an additive in base oil. These few studies show that graphene at specific amount can act as an excellent functional additive in lubricating oils compare to other carbon materials. The tribological behaviour is attributed to their small size and extremely thin laminated structure.
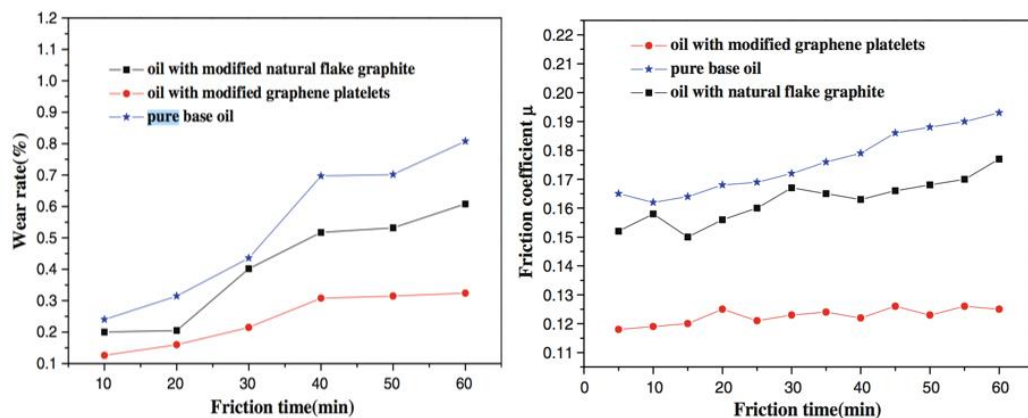
Figure 2.25 Wear rate and friction coefficient of graphene platelets compared to graphite and pure base oil [120]

Graphene has also been studied as a potential solid lubricant for various application in the tribological application. Won and co-workers [1] investigated the tribological performance of graphene on Cu substrate under dry condition (Figure 2.26). The performance of graphene improves as the deposition time increase which demonstrates graphene as a solid lubricant. They also noticed that degradation of graphene coating after numbers of sliding cycles was due to the transformation of graphene to amorphous carbon.

Another example is the attempt by Kim et al. [85] to study the adhesion and frictional characteristics of graphene grown different metal catalyst using CVD. The results showed that interaction between graphene and substrate is an essential factor for friction and wear reduction. They suggested a more in-depth study of graphene-substrate interaction to improve the performance of graphene film.
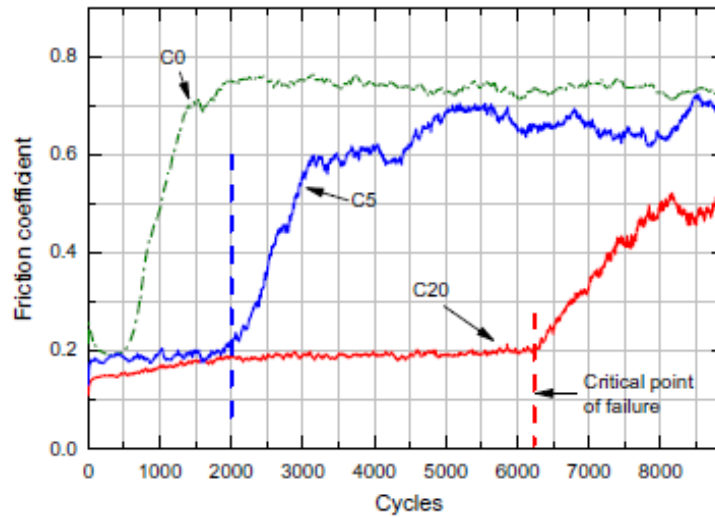
Figure 2.26 Typical friction coefficient of Cu substrate (C0), graphene-Cu grown for five minutes (C5) and graphene-Cu grown for 20 minutes (C20) [1]
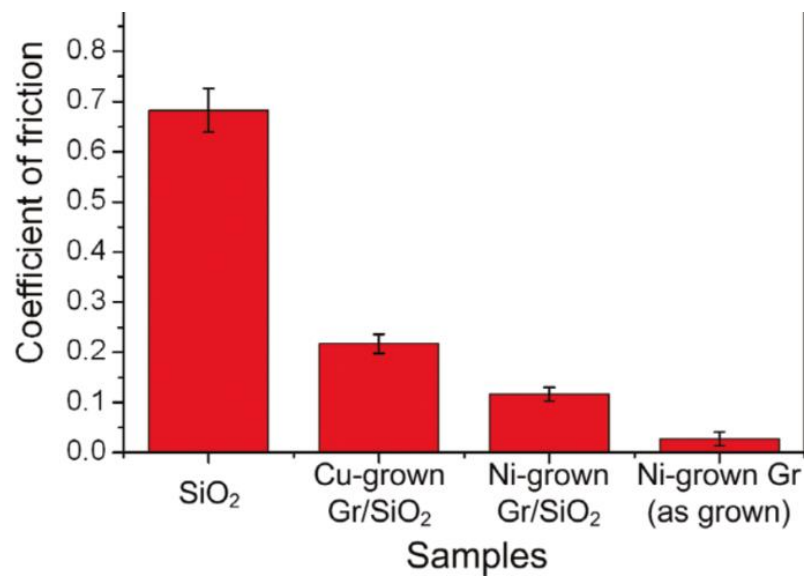
Figure 2.27 Coefficient of friction for graphene grown on different substrates [85]

Mo et al. [107] on the other hand reported the wear rate of polyurethane (PU) composite reinforced with graphene in dry and seawater conditions. The wear rate of the PU composite decreased as 0.25 wt% of graphene were added, before increased with concentration of graphene. This was attributed to balancing reinforcement and lubrication of filler and crack generated by the graphene. The results demonstrate that dispersion of filler (graphene) and

proper concentration are essential to improve tribological performance of PU composite coating.
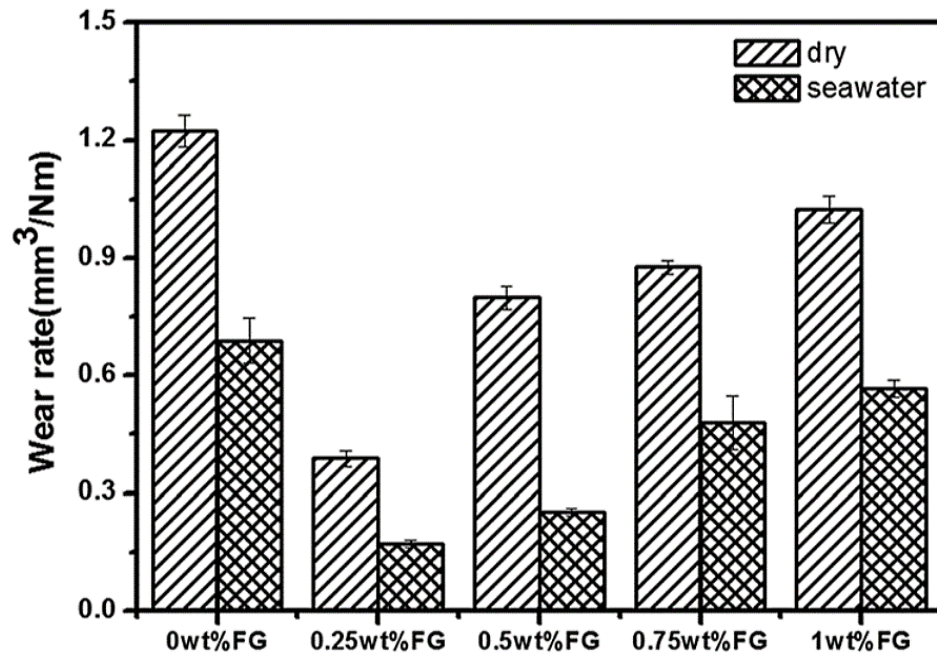
Figure 2.28 Wear rate of polyurethane (PU) composite reinforced with functionalized graphene [107]

Listed in Table 2.13 are some of the selected literature on the value of friction for graphene as a solid lubricant. As can be seen, most of the studies were in nano/micro scale when graphene served as an individual coating. Due to weak adhesion to the substrate as well as the puckering effect, it can be proposed that it is almost impossible for graphene to act only by itself in macro scale. It is therefore important that development of graphene as solid lubricant should be either in multilayers, epoxy composite or mix matrices.

Table 2.13 A review of the performance of graphene as solid lubricant from selected literature

Materials	COF/friction force	Substrate	Tribometer
Graphene [91]	*0.35 – 1 nN *friction force		AFM
Graphene [121]	NA	SiO_2/Si	FFM
Graphene [85]	~0.03	SiO_2/Si	Home-built microtribometer
Multi-layer graphene films [84]	*0.36 to *0.62 nN * friction force		AFM
Composite based GO and IL [110]	~0.09	Si	AFM
CNT-GO hybrid/epoxy composite [109]	~0.4	-	Pin-on disc
Polyurethane (PU)-based composite coatings reinforced with various content of functionalized FG and FGO [107]	0.1	White cast iron	UMT-3 tribometer
Polytetrafluoroethylene (PTFE) filled with graphene platelets [108]	0.185	-	Pin-on-plate
Graphene [122]		SiO_2/Si	FFM
Graphene with nanodiamond [123]	~ 0.04 (dry) ~0.27 (humid)	SiO_2	

2.6 Coating Characteristic of DLC and Graphene-based Nanocomposite

2.6.1 Surface morphology

Surface morphology and structure of coating can be characterised by optical microscopy, Scanning Electron Microscopy (SEM), Transmission Electron Microscopy (TEM), Profilometry and Atomic Force Microscopy (AFM). Figure 2.29 shows the AFM and SEM images of biocompatible Ag-DLC coating, produced using radio frequency plasma-assisted chemical vapour deposition (RF PACVD) and magnetron sputtering (MS) methods by Bociąga et al. [124]. SEM gives qualitative information while AFM provides both qualitative and quantitative data about the surface morphology. Micrographs from the SEM show that the surface of DLC is smooth compared to AG-DLC coating that is rough and nonhomogeneous. The surface was also found to be smoother after deposition of DLC, due to DLC filling into the scratches area on the substrate thus lowering the surface roughness. Surface topography examined in a tapping mode by AFM, revealed more clear 3D images of the surface of each sample. It was found that the increased of surface roughness after the addition of Ag, owed to the irregular granular structure of Ag which increase the surface roughness Sa to 2.21 nm.
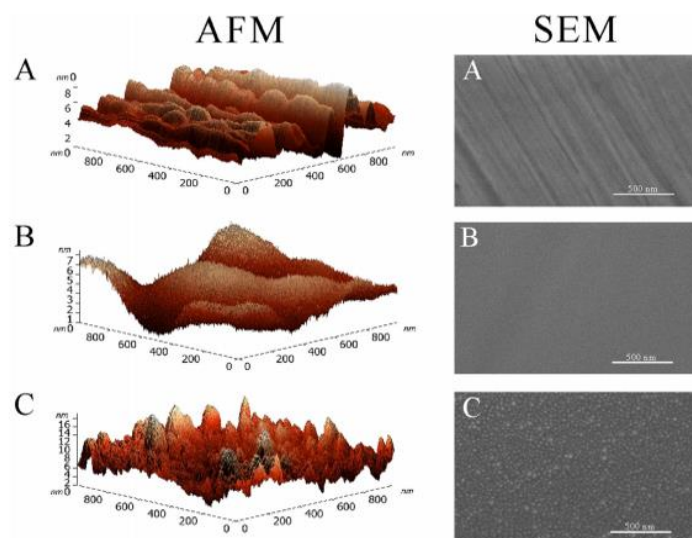
Figure 2.29 AFM and SEM characterisations of (A) AISI3 16LVM steel, (B) DLC and (C) Ag-DLC coating [124]

44

Paul and group [125] did a microstructural studies of Au/DLC composite coating by using TEM. Figure 2.30 shows the TEM micrographs of Au/DLC composite coating produced at different gas mixture parameter. By using TEM, nanoscale size of the particles which range between 2- 5 nm have been able to be measured. The density of Au in the composite was estimated through the images. Diffraction patterns confirmed the existence of Au nanocrystallite arisen from DLC matrix.
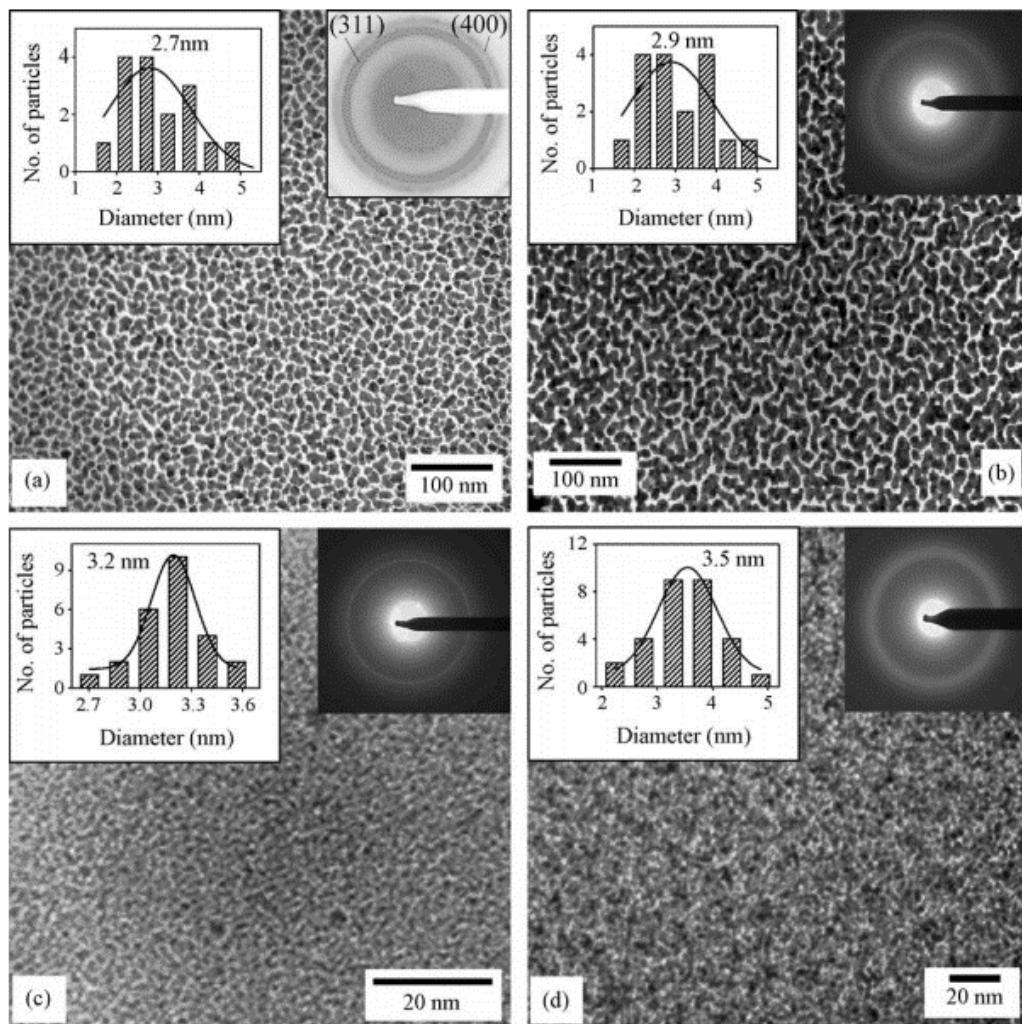
Figure 2.30 TEM micrographs of Au/DLC composite film deposited using CVD at different amount of argon in methane+argon gas mixture [125]

2.6.2 Structural arrangement of carbon atoms

Raman spectroscopy is an easy and non-destructive tool in characterising carbon materials. All carbon commonly shows features of G and D-peaks in Raman spectra which lie at around 1560 and 1360 cm^{-1} respectively [126]. Zanin et al. [127] deposited vertically aligned multiwalled carbon nanotubes (VACNT) on the DLC surfaces and found D, G and D'-peaks appeared centred at 1357 cm^{-1}, 1585 cm^{-1} and 1622 cm^{-1} respectively (Figure 2.31). Combination of narrow D-peak of VACNT and broader for DLC seem to combine and produced broad D and G-peak for VACANT-DLC coating. This has proven that DLC is not replacing VACNT but exist as two different phases as a composite coating.
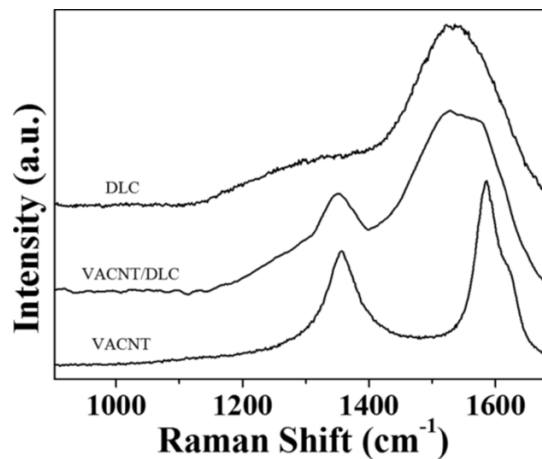
Figure 2.31 Raman spectrum of VACNT-DLC composite coating [127]

Hu et al. [39] fabricated CNT-DLC composite films by means of electrochemical deposition of an organic compound as a carbon source. Figure 2.32 shows the Raman spectrum of CNT-DLC composite films compared with the spectra of DLC films and CNTs individually. The range of G-peak for CNT-DLC composite coating at 1500 -1600 cm^{-1} is due to the existence of a graphite-like layer of sp^2 microdomains. The shift at G-peak after incorporation of CNT may be attributed to the strained or curved graphite plane within the film. Table 2.14 and

Table 2.15 summarised a selection of works on the D, G-peaks of DLC-based composite and graphene-based composite coating respectively. The values

may be used as a reference when identifying the bonding type that exists within the fabricated DLC-graphene composite.
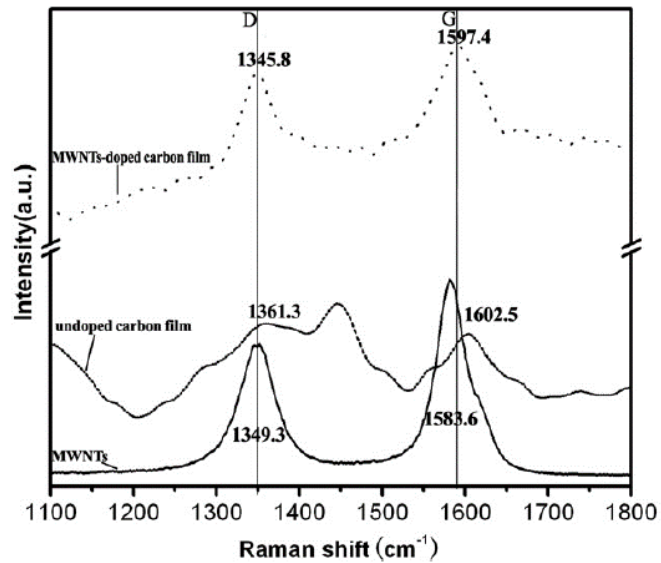
Figure 2.32 Raman analysis of CNT-DLC and DLC films, and CNT [39]

Table 2.14 Selection of the position of D and G-peaks for DLC-based composite coating

Ref	Materials	D band position (cm^{-1})	G band position (cm^{-1})	D' band position (cm^{-1})
[36]	DLC/CNT/Si	1350.0 (wide)	1580.0	-
	DLC Si	-	1530.0	
	CNT/Si	1350.0 (narrow)	1590.0	-
[39]	CNT- DLC	1345.8	1597.4	-
	DLC	1361.3	1602.5	
	CNT	1349.3	1583.6	
[32]	DLC	1345.0	1541.0	
	MWCNT	1345.0	1525.0	1610
	DLC/MWCNT	1350.0	1540.0	1610

Table 2.15 Selection of D and G-peaks for graphene-based composite coating

Ref	Materials	D band position (cm^{-1})	G band position (cm^{-1})	2D band position (cm^{-1})
[35]	Virgin DLC film	~1365	~1500	-

	Graphene/DLC	~1365	~1540	2714, 2848 (wide)
[28]	Graphene-DLC	1360	1560	2700

2.6.3 Chemical bonding of coating

XPS is a common method used to confirm the existence of chemical bonding in one coating. Huang et al. [128] compared the XPS spectra of mechanically mixed and chemically bonded TiO_2-graphene nanocomposite. It was found that C-Ti bond has been observed at two weak peaks centred at 4551.1 and 461.1 eV that relates to Ti $2p_{3/2}$ and $2p_{1/2}$ from the chemically bonded TiO_2-graphene sample, which confirms the chemical bonding present between graphene and TiO_2. These peaks do not exist in the mechanically mixed sample.

For carbon-based materials, it is usually used to estimate the sp^2 sp^3-fraction [39]. Figure 2.33 shows the XPS spectra of CNT-DLC film and undoped DLC film. The intensity of sp^3 is higher for CNT-DLC film compared to DLC film. Fitted C1s spectra for both films show four distinct features which assigned to sp^3-C, sp^2-C, C-O and C=O. The C1s spectra for CNT-DLC film has shifted to higher binding energies. The sp^3 peak slightly shifted from 284.1 to 284.4 eV for CNT-DLC film, while for sp^2, the peak shift from 284.9 for DLC film to 285.2 eV for CNT-DLC film.
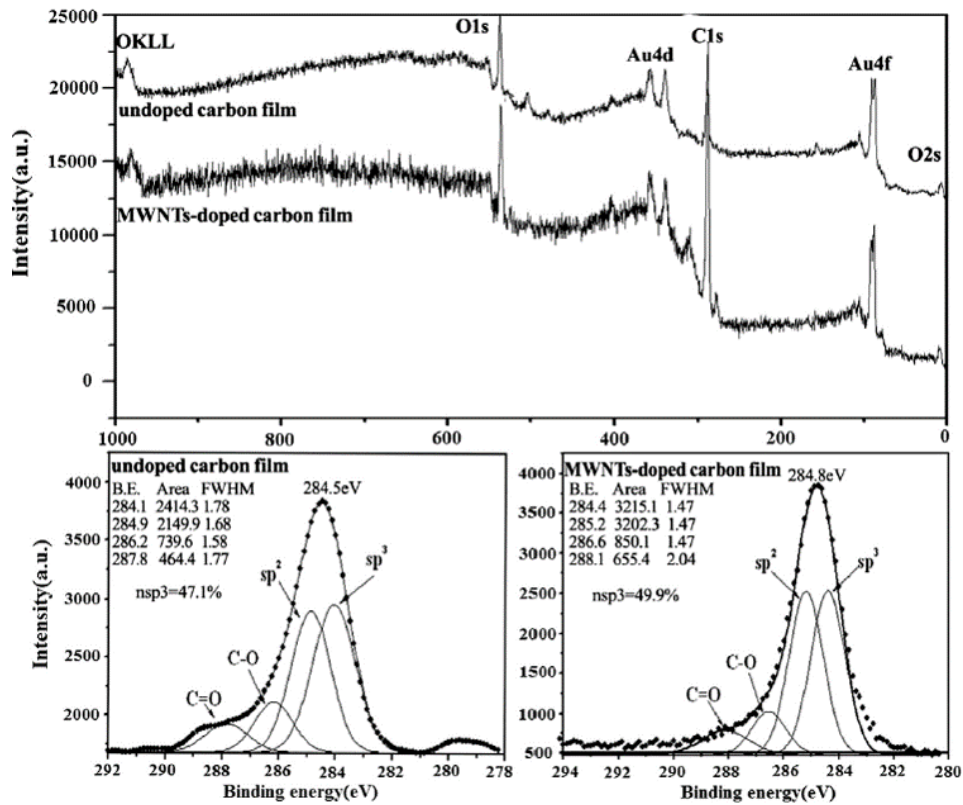
Figure 2.33 XPS spectra of CNT-DLC composite film [39]

2.6.4 Adhesion

Excellent adhesion of the coating to the substrate is essential to ensure functionality of the coating. One of the major issues that have been addressed during the early study of DLC coatings is their adhesion with substrate. High internal stress that benefits the hardness of DLC makes it relatively difficult to adhere to the substrate. Few methods have been suggested to improve the adhesion of DLC. Mori and group [129] suggested that surface treatments may improve the adhesion of the coating.

The scratch tester provides a common quantitative method to measure adhesion for thin film coating. Figure 2.34 shows the example of the scratch track of DLC coated on die steel prepared by Waseem et al. [12]. The first micrograph indicates the region of first critical load where initial cracking appears. The next two micrographs show the first adhesive failure and the end of the scratch respectively. This is an example of a coating with good adhesion without any significant wear being observed. Acoustic emission curve can also be used to predict critical load. Figure 2.35 depicts the acoustic emission DLC coating and other samples produced by Waseem and group [12]. The high

acoustic emission may demonstrate the brittleness of the substrate when the coating is delaminated.
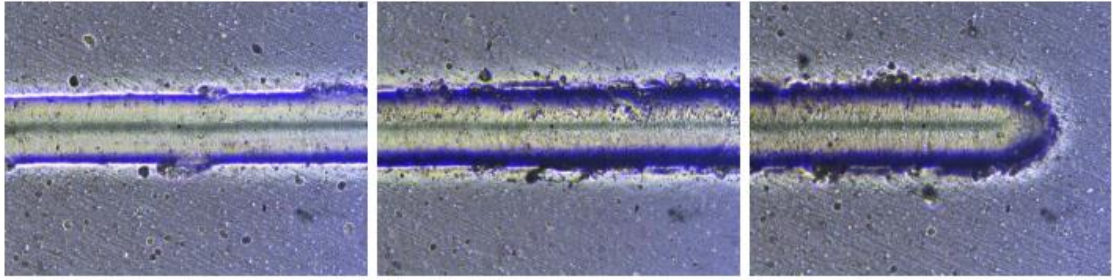
Figure 2.34 Scratch track of DLC coated die steel at 20N [12]

Wang et al. [130] described plastic deformation as the main reason for the failure of the coating in the DLC-Zr coating on Ti substrate. Figure 2.36 shows the scratch tracks of DLC-Zr deposited on a different type of substrate. Fine-grained Ti and Ti alloy demonstrated higher critical load, where coating failure happened at higher load compared to coarse-grained Ti substrate.
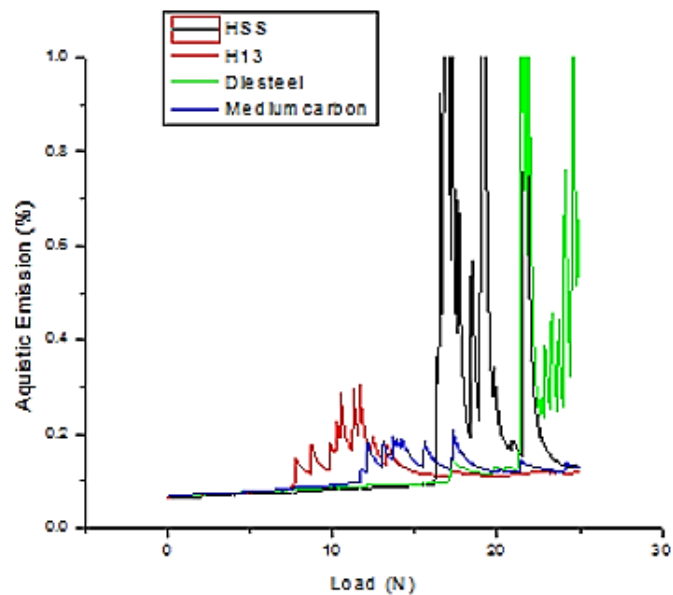
Figure 2.35 Load vs acoustic emission of DLC coating[12]
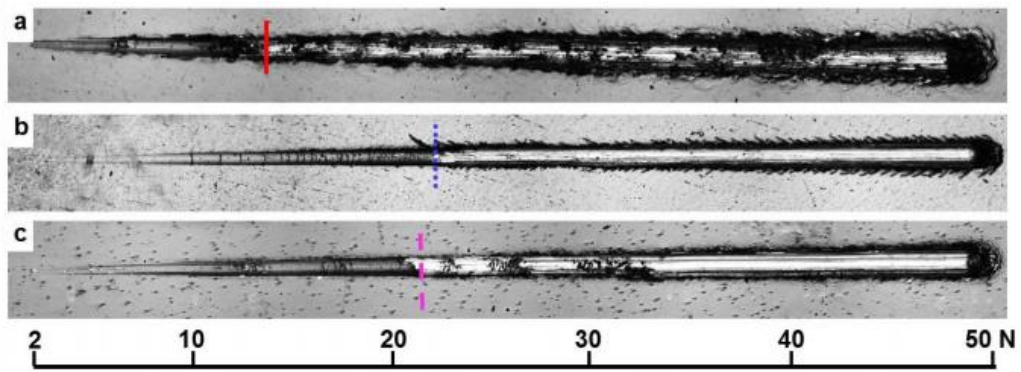
Figure 2.36 Scratch track of DLC-Zr coating on Ti substrates [130]

2.6.5 Hardness and elastic modulus

The hardness of thin film coating can be measured in either macro or micro/nanoscale. Vicker hardness is the most common method used to measure macro scale hardness. Measurement of hardness using Vicker hardness is used when coating hardness influence by the substrate is desired. Nanoindentation is normally use to measure micro/nanoscale hardness of thin film coating. Value of hardness using nanoindentation usually is the real hardness of coating itself without any influence of the substrate hardness. Nanoindentation has been used to investigate the mechanical properties of the surface from micro-level down to sub-micron level [131].

Chockalingam et al. [132] investigated the mechanical properties of DLC coating deposited on SiAlON ceramic. They suggested that hard or superhard behaviour of the coating can be estimated based on the load-displacement curve as can be seen in Figure 2.37. The sample with superhard behaviour showed small hysteresis between the loading and unloading curves with drastic recovery during unloading. While for hard coating, hysteresis was fairly large with smaller recovery during unloading. The coating showed the maximum hardness of 43.4 GPa.
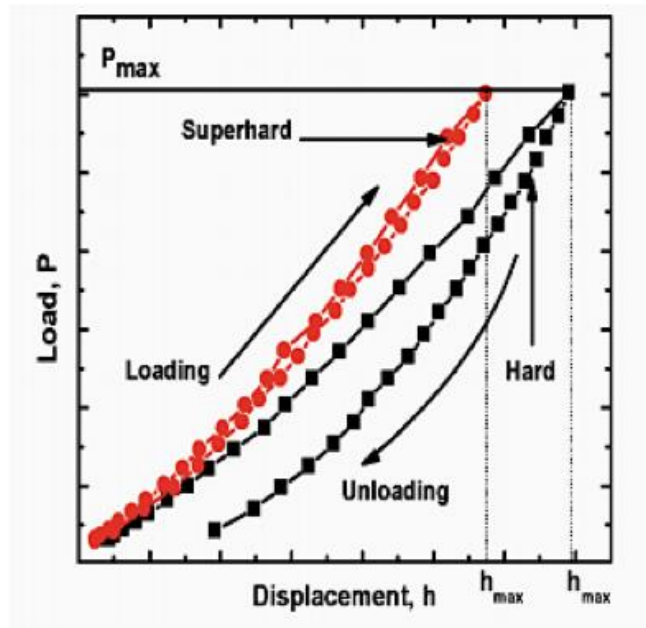
Figure 2.37 Typical load vs displacement of DLC coating on SiAlON substrate [132]

Table 2.16 represents a selection of literature for nanoindentation parameters of loading and unloading rate, and thickness parameters used for various type of DLC coatings. The value of load varies from as small as 1.0 mN to as big as 600 mN for several types of DLC and DLC composite coatings. Lower load applied for coating Cu/DLC and DLC with interlayers in Table 2.16 may be due to lower thickness of the coating.

Table 2.16 The values of nanoindentation load, coating thickness and types of the substrate for selected DLC and DLC-based composite coating from the literature

Coating	Nanoindentation load (N)	Thickness (µm)	Substrate	Ref
Cu/DLC	5 - 20	0.337-0.376	Si (100)	[16]
DLC	1 - 600	1.3-2.1	M2 steel	[131]
DLC with metallic interlayers	5-20	0.280-0.337	Si (100)	[133]

2.7 Summary

52

2.7.1 Advantages and limitations of DLC and graphene as a solid lubricant

A thin coating of DLC is one of the promising solutions that has been applied to provide the optimal performance in both mechanical and tribological aspects. DLC has a wide range of characteristic values depending on the method of preparation and the doping material. This makes DLC among the most reported coatings for tribological purposes among researchers. Modification of DLC thin films by incorporating other elements was introduced since the 2000s to improve and enhance its multifunctional performance.

Graphene, on the other hand, is currently the most trending carbon material with remarkable bloom in the number of researches and patents. It is foreseen to have tremendous potential application in many applications including tribology. This strongest 2D material ever known to science and found by the human is believed to have better performance compared to another type of carbon materials with same lattice structure such as CNT. Other than reports on using graphene as a stand-alone coating, this literature review also reveals few efforts on integrating graphene in conventional coatings for tribological applications. The works describe graphene as a coating that can reduce friction and wear in numerous conditions, both in macro and micro/nanoscale. Table 2.17 summarises the advantages and the limitations of using graphene as solid lubricant reported. It can be summarised that despite having extraordinary mechanical and tribological properties, limitations such as listed in Table 2.17 have made it very challenging for graphene to be functionally used as a coating in real life.

Table 2.17 Advantages and limitation of graphene as a solid lubricant

Advantages	Limitation
• Low friction • High wear resistance • Ultra-high strength • Lightweight and nanoscale thickness • Heat resistance	• Need to be closely bonded with the substrate to achieve low friction • Loosely-bound • Low adhesion to the substrate layer • Puckering effect

| • Corrosion resistance | • Difficulty to disperse |

2.7.2 The motivation of the work

In an effective tribological system, a mechanical device with low friction and high wear resistance surface is vital for energy efficiency and sustainability. Literature review proved that fabrication of DLC-based composite coatings can provide beneficial mechanical and tribological properties that retain the benefits of a DLC coating and the filler (e.g. CNTs). The resulting properties of the composite coating depend on the type of the material that was incorporated into the coating and the method of preparation. Since the 2000s, numerous studies have been devoted to processing of various types of DLC-based composite coatings. CNTs have been reported to have a broad application as the filler for DLC-based composite coating [28, 36]. However, one of the drawbacks is the agglomeration and entanglement of CNT structure during processing. It has been also shown that the composite coating structure does not always retain desired tribological properties [40].

Although graphene has a similar lattice structure to CNT, it is characterised by a higher surface area. Graphene also has stronger interfacial bonding between each individual sheet. Another advantage is that it is relatively inexpensive. Graphene has been used successfully as a solid lubricant and additive in a lubricated system [117]. The literature review showed that there was a number of attempts of introducing graphene at the surface of sliding interface where it would act as a low shear layer between the surfaces, thus reducing the friction [1, 85]. However, most of the studies done were fundamental in nature and were done in micro/nanoscale rather than full tribological scale corresponding to the industrial applications.

To date, there is no reported work on the development and fabrication of DLC/ graphene composite coating. The hypothesis of this work is that mechanical properties of the DLC /graphene nanocomposite coating can be enhanced using an optimised DLC/graphene nanocomposite coating architecture for improved tribological performance.

2.7.3 Research gaps

Reviews on the performance of graphene as an additive and solid lubricant have testified its superior performance in mechanical and tribological properties. Nevertheless, limitations such as weak adhesion or bonding with substrates and puckering effect seem to have hindered further commercialisation in the real application. Composite is an alternative route to trigger the commercialisation of graphene-based material in the real-world application. With the combination of DLC and graphene, a robust composite coating with low CoF and manageable wear can be developed.

Chapter 3
Experimental Setup and Procedure

3.1   Introduction

In this chapter, the experimental setup and procedure for fabrication of DLC-graphene nanoplatelet (GNP) nanocomposite coatings, characterisation and test methodologies are explained. Figure 3.1 shows the experimental flowchart of the work. The work involves preparation of the GNP suspension, GNP spin coating and DLC film deposition to produce single-layer DLC-GNP nanocomposite coating. In the case of multilayer DLC-GNP, the process of GNP deposition using spin coating method will be repeated after the first layer of DLC film was deposited. Coatings were then investigated for its chemical and physical, mechanical and tribological properties.
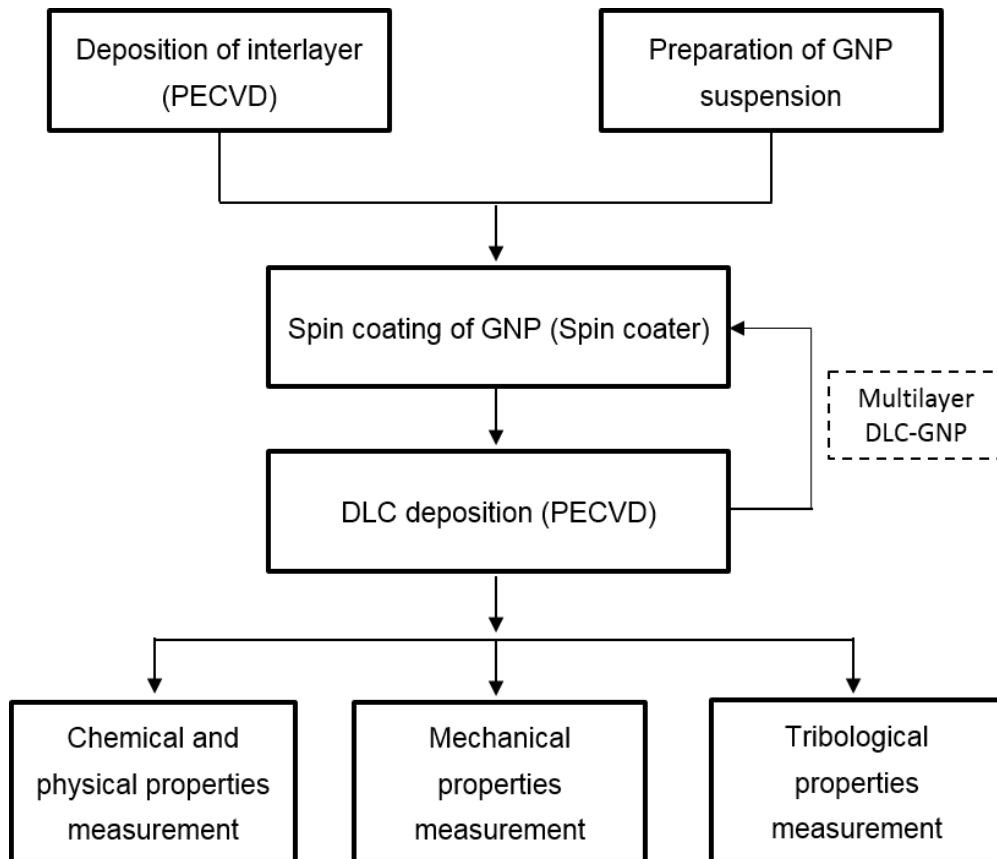
Figure 3.1 Experimental flow of the work

3.2 Materials

3.2.1 Substrate and graphene

Substrate used for coating throughout this work is M2 grade high-speed steel (HSS). Graphene used in this work is commercial purchased graphene nanoplatelets (GNP) (ACS Material, >99.0%, thickness 2 -10 nm). The GNP was used without any modification. Table 3.1 summarised the type of substrate and materials, specification used in this work.

Table 3.1 Specification of substrates and materials used

Materials	Specification	Maker
M2 High Speed Steel (HSS)	Surface roughness 0.01-0.02 μm	Paterson-precision
Graphene nanoplatelets (GNP)	Thickness 2-10 nm, powder form	ACS Material, LLC
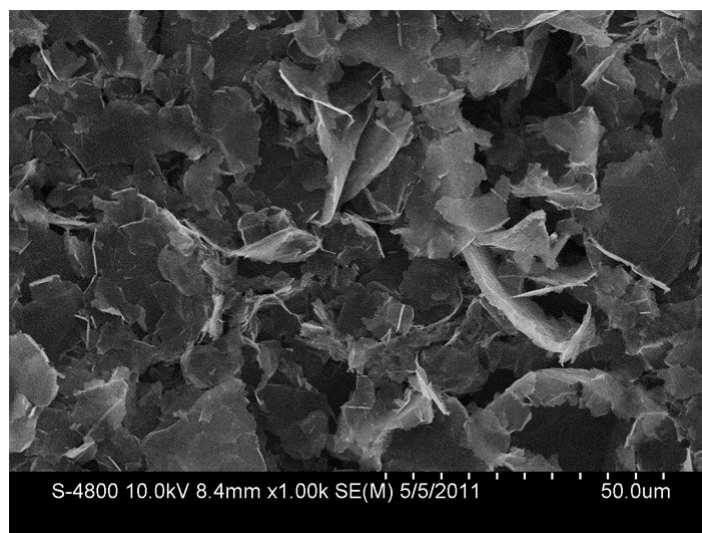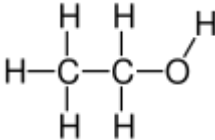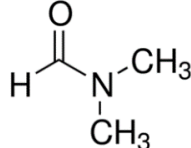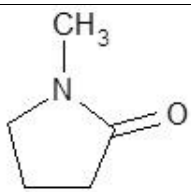
Figure 3.2 SEM micrograph of graphene nanoplatelets (GNP) produced by ACS Material which were used in this work [134]

3.2.2 Solvents

Stability and good dispersion of GNP are important for its final application. In order to achieve this condition, appropriate selection of dispersion methods and solvents is crucial. In this work, three type of solvents were selected which are ethanol, Dimethylformamide (DMF) and N-Methyl-2-pyrrolidone (NMP). DMF and NMP are among the typical organic solvents that have been used in previous work for graphene and Carbon Nanotubes (CNT) [135-138]. Ethanol, on the other hand, is a common solvent used for many nanomaterials for dispersion and storage. Table 3.2 tabulates the type of solvents and its specification.

Table 3.2 Product specification of solvents used [139]

Solvent	Chemical structure	Molecular formula	Product description
Ethanol		C_2H_6O	• Colourless liquid • Boiling point: 78.2°C • Flash point: 16.6°C
Dimethylformamide (DMF)		C_3H_7NO	• Colourless liquid • Boiling point: 153°C • Flash point: 58°C
N-Methyl-2-pyrrolidone (NMP)		C_5H_9NO	• Colourless liquid • Boiling point: 204°C • Flash point: 91°C

3.3   Graphene Dispersion with Solvents

Prior to spin coating of graphene solution on a substrate, graphene nanoplatelets (GNP) were mixed and dispersed in the three solvents of ethanol, DMF and NMP. Well-dispersed graphene solution is vital to avoid aggregation of GNP when deposited on the surface. To study the effect of sonication time on the dispersibility, 1.0 mg/mL concentration of GNP suspensions were prepared and sonicated using ultrasonic method for a duration from one to ten hours. Ultrasonic is a well-known and one of the efficient way to separate agglomerated nanomaterials such as Carbon Nanotubes (CNT) and nanoparticles

Mixing of GNP and solvent	→	Sonication (1 - 6 hours)	→	GNP suspension
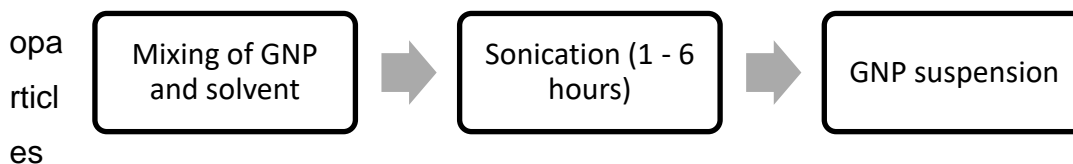
for a stable suspension.

Figure 3.3 Schematic diagram showing steps in the preparation of graphene dispersion

The dispersibility of GNP was assessed by observing the sedimentation of GNP dispersed in the three solvents. GNP dispersions which have been sonicated for one to ten hours were placed in borosilicate glass vials. Observations at one, two, five and 168 hours (one week) were photographed. The photographs were then analysed using ImageJ to measure the greyscale level. To measure the greyscale in ImageJ, Plot Profile was used to create a plot of intensity values across features in the image. Details of greyscale level measurement are attached in Appendix A.

3.4   Preparation of Graphene Coatings

Figure 3.4 shows the flowchart of the preparation process of graphene coating. High-Speed Steel (HSS) M2 substrates were first deposited with an interlayer of Cr/WC using PECVD method. The spin coating process was performed at room temperature by flooding the substrate surface with GNP suspensions on the interlayer coated substrates. This work applied the dynamic dispense method where the solution was dynamically deposited during spinning. All samples were dried at room temperature for further process and characterisations.

For the investigation on the effect of solvent, a fixed parameter of 1.0 mg/mL concentration of GNP suspensions; 1500 rpm of spinning speed and spinning time of 30 seconds. In this work, a home-made spin coater was used to deposit GNP. Figure 3.5 shows the experimental setup using the spin-coater for GNP spin coating process. As can be seen in the figure, the spin coater is equipped with substrate holder at the centre of the spin coater body. The substrate holder is also attached to the magnet used for the substrate spinning. A lid covering the spin coater during spinning has a hole in the middle that is used to insert the pipette for GNP deposition.
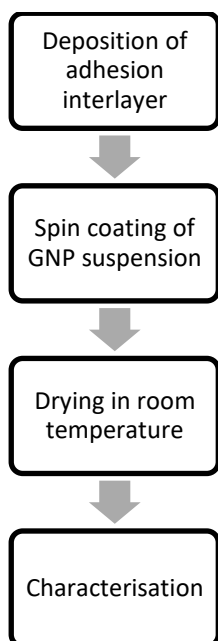
Figure 3.4 Flow chart of the procedure of graphene coating using a spin coater
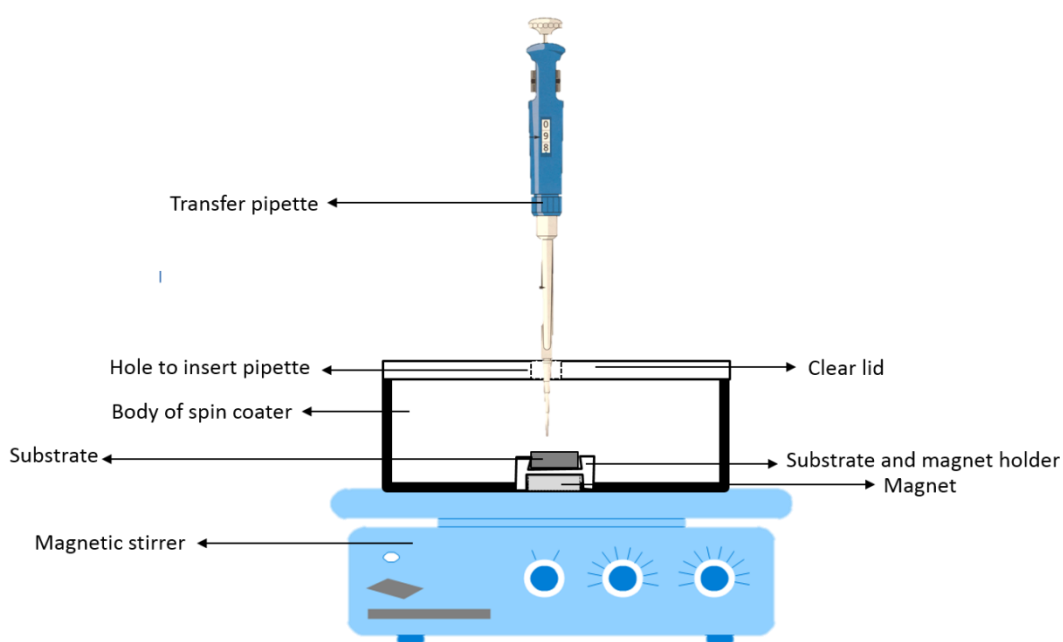
Figure 3.5 Schematic of GNP spin-coating process using a spin-coater

For the other set of experiments in this work, spinning speeds, time, amount of suspension were varied from 500 to 1500 rpm, 10 to 30 seconds and 0.25 to 1.00 mL respectively. The spinning speed and time were selected based on the few preliminary tests on the suitability of the speed and the home-made spin-coater. 1500 rpm is the limitation of speed that the spin-coater could reach.

Concentrations of GNP suspensions were various between 0.25 to 2.00 mg/mL for the study on the effect of concentration. The selected concentration is reasonable range used in previous studies of carbon nanotube (CNT) and GNP [140-143].

3.5 Optimisation of Graphene Coating using a Spin Coating with Taguchi Method

Spin coating with speed range of 500 to 1500 rpm and spinning duration of 10 to 30 seconds were used in this work. In the present work, Taguchi method was used to determine the effect of variables of spinning speed (A), spinning duration (B) and volume of solution (C) to investigate the optimum condition of GNP dispersion on a substrate. Each factor has equally three levels. To find the optimum deposition conditions, the factors and levels considered for graphene spin coating are shown in Table 3.3.

Table 3.3 Factors and levels for GNP spin coating process

| Level | Factor | | |
	Spinning speed (rpm) A	Spinning duration (sec) B	Volume of graphene solution (mL) C
1	500	10	0.25
2	1000	20	0.50
3	1500	30	1.00

Table 3.4 shows the plan of experiment prepared according to the Taguchi orthogonal Table L_9. The total degree of freedom (DOF) for this four-factor three-level experiment considering the individual factor and their interaction is seven. Therefore the total number of experiment needs to be equal or more than seven. In this work, L_9 orthogonal array is chosen as satisfies all the DOF condition. Optimisation of measured values was determined by comparing the means values. The magnitude of variation of design quality in response to changes in the control factors is quantified by using signal-to-noise (S/N) ratio.

DOF = 1 x (no of variables) * (no of levels -1)

    = 1 + (3 x (3-1))

    = 1 + 6

    =7

Table 3.4 Design of Taguchi $L_9(3^4)$ orthogonal array for graphene coating

Exp No	Factor			S/N ratio
	A (rpm)	B (sec)	C (mL)	
1	500 (L_1)	10 (L_1)	0.25 (L_1)	S/N_1
2	500 (L_1)	20 (L_2)	0.50 (L_2)	S/N_2
3	500 (L_1)	30 (L_3)	1.00 (L_3)	S/N_3
4	1000 (L_2)	10 (L_1)	1.00 (L_3)	S/N_4
5	1000 (L_2)	20 (L_2)	0.25 (L_1)	S/N_5
6	1000 (L_2)	30 (L_3)	0.50 (L_2)	S/N_6
7	1500 (L_3)	10 (L_1)	0.50 (L_2)	S/N_7
8	1500 (L_3)	20 (L_2)	1.00 (L_3)	S/N_8
9	1500 (L_3)	30 (L_3)	0.25 (L_1)	S/N_9

The details of the Taguchi method are explained elsewhere [144]. A higher value of S/N ratio indicates a higher quality of characteristic. In this work, the experimental results of surface roughness of spin-coated GNP and GNP distribution were used as the response to improve GNP deposition. The results were analysed by measuring the S/N ratio for the three levels of each factor by a method of statistical calculation. The factor level that yields the highest value will be the optimal levels. S/N formulation was used to minimize the surface roughness value where:

$$S/N = -10 \log \left(\sum_{i=1}^{n} y_i^2 / n \right)$$ 3.1

On the other hand, in order to maximize the GNP distribution, the following S/N formulation was used:

$$S/N = -10 \log \left(\sum_{i=1}^{n} (1/y_i^2)/n \right) \qquad 3.2$$

where y_i is the measured value in each test and n is the number of samples per trial.

3.6   Deposition of DLC coating

After GNP deposition using spin coating method, DLC film was deposited via PECVD process in the PVD Lab in School of Mechanical Engineering, University of Leeds, using a Hauzer Flexicoat 850 deposition system (Figure 3.6). Figure 3.7 shows the schematic of Hauzer Flexicoat 850 used in this work. The system is equipped with Microwave, Magnetron, High Power Impulse Magnetron Sputtering (HiPIMS), Filtered Arc Deposition, Cold Finger and Plasma Etching capabilities. The front side of the system function as a door and housing for target. The magnetron sources are located at the opposing walls. The final deposition source is located at the back of the chamber which also has a double function as a door and can be opened for cleaning purpose.

Substrates were affixed to cylindrical columns inside the deposition chamber. Figure 3.8 represents the layout of the cylindrical columns at the substrate table in the vacuum chamber for the Hauzer Flexicoat 850 deposition system. The columns allow for a twofold rotation, dummies will be rotating independently from the table, while the holders can achieve a threefold rotation that allows the samples to be rotated separately from the table and dummies.

Figure 3.6 The Hauzer Flexicoat 850 deposition system

The system is controlled by a unique software design by Hauzer installed to the system. The water system, control units and power supplies are located behind the deposition chamber. For cooling down the system, chilled water must always be available when using the deposition system.
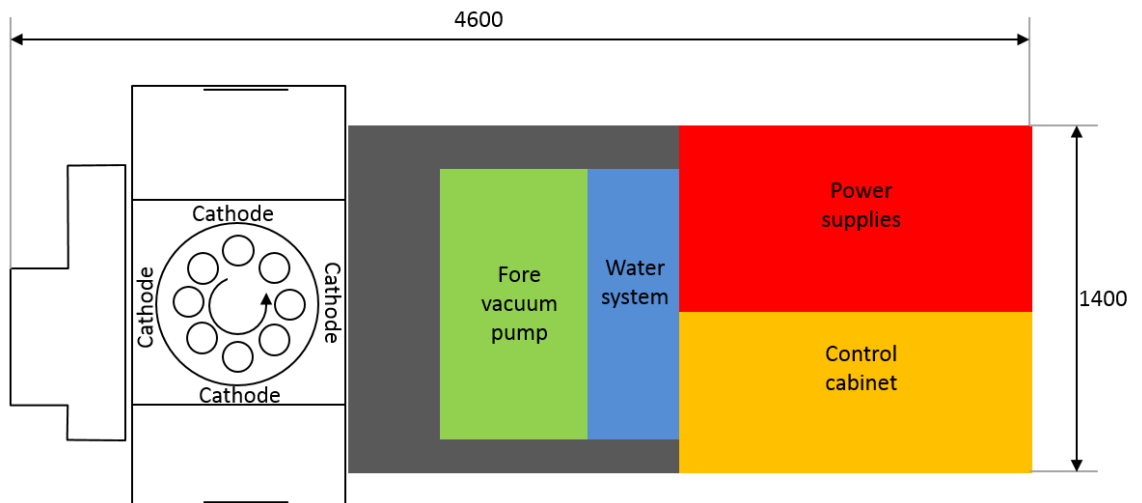
Figure 3.7 Schematic of Hauzer Flexicoat 850
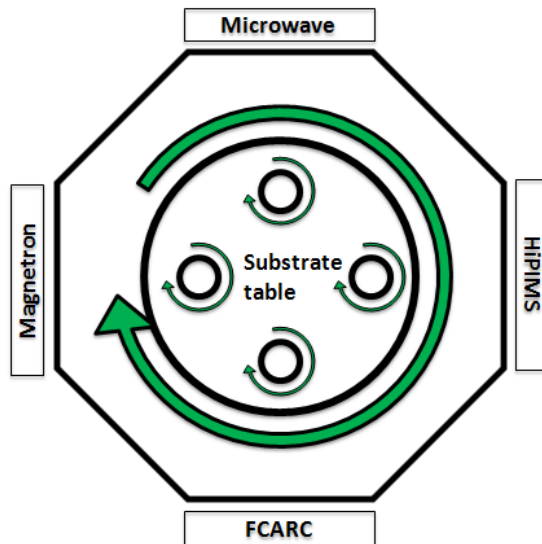
Figure 3.8 Schematic view of the vacuum chamber in Hauzer Flexicoat 850 system [69].

3.7 Characterisation of Coating

3.7.1 Coverage distribution and size of spin-coated GNPs

A Leica optical microscope DM6000 was employed to capture the morphology of spin-coated GNP on substrates. Five measurements were taken from each sample as in Figure 3.9 and the images were then analysed with ImageJ to measure the coverage distribution and size of the spin-coated GNP. Detail measurement using ImageJ is attached at Appendix B.
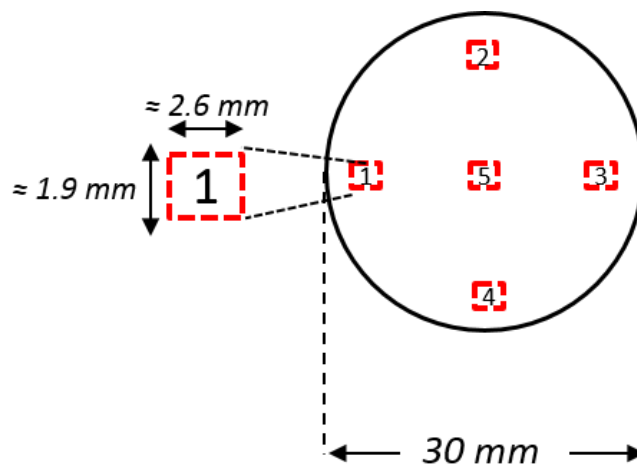
Figure 3.9 Schematic of the areas on samples for measurement of coverage distribution and size of spin-coated GNP

3.7.2 Thickness of coating

In this work, the thickness of coatings was either been measured by a Calo tester or White Light Interferometry (WLI) by measuring the step height. In some cases, the thickness of coating has also been investigated using Scanning Electron Microscopy (SEM) [145]. Calo tester is a micro-scale abrasion testing using a rotating ball and abrasive medium. Figure 3.10 shows the schematic of position for the sample, rotating ball and abrasive medium. Abrasive medium that was introduced is 1.0 μm diamond suspension. This was used to lubricate the interface. A 25 mm diameter stainless steel ball was rotated for three minutes at speed of 200 rpm. A crater was form on the coating surface and can be calculated using equation 3.3.

$$e = \frac{a.b}{d}$$

3. 3

Where e is the coating thickness and d is the ball diameter. Value of *a* and *b* have been measured using an optical microscope (shown in Figure 3.10).
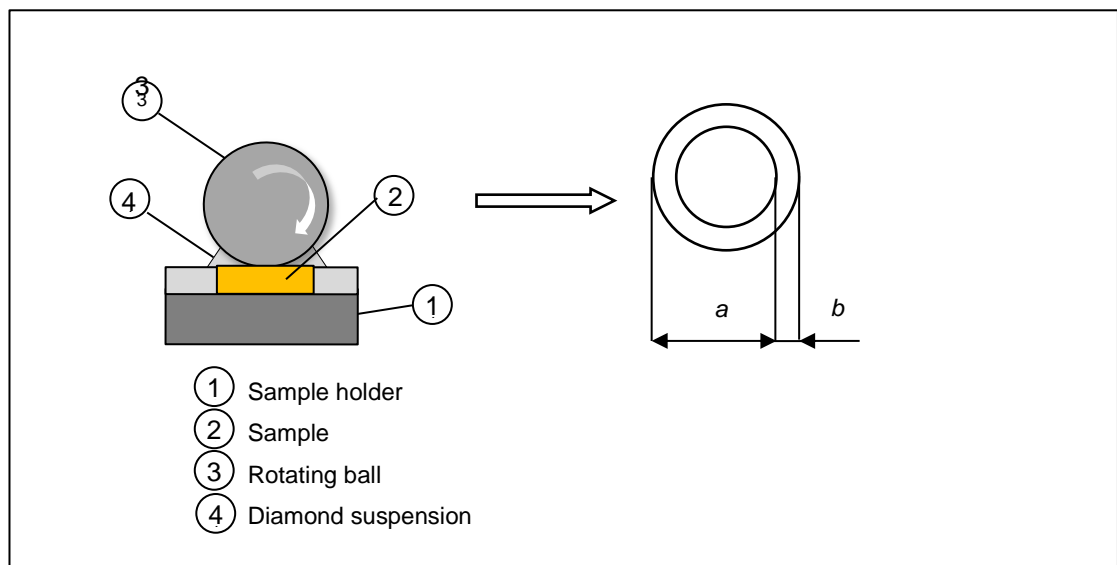
Figure 3.10 Schematic of Calo-tester and the measurement of *a* and *b* values.

Coating thickness has also been confirmed using White-light Interferometry (WLI). In this work, measurement has been performed using Veeco White Light Interferometer. A step was created on the surface by masking a portion of the substrate and removing it after coating deposition. Coating thickness was

directly measured as the height of the step contour trace as shown in Figure 3.11. WLI is a non-contact profilometry technique. Figure 3.12 represents the typical schematic of measurement of surface roughness using white-light [146]. It combines waves from a source, and the light source reflected from a specimen surface to presume the surface morphology of specimen by the constructive and destructive wavelength superposition. WLI provides advantages over the other types of optical and stylus profilers due to its ability to scan the entire field rather than point to point scanning which greatly accelerates the measurement process. Furthermore, it is non-contact, therefore non-destructive to the specimen.
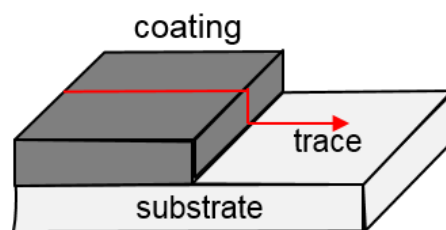
Figure 3.11 Schematic diagram of topography tracing of coating-substrate system
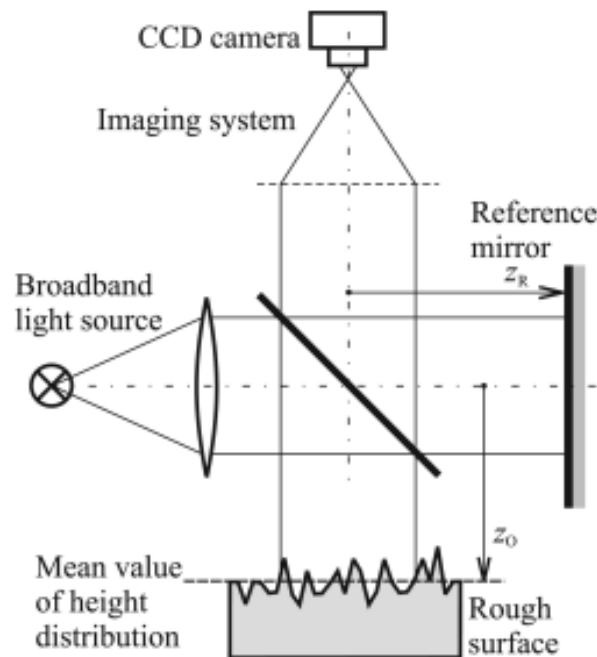
Figure 3.12 Schematic of surface topography measurement using WLI [146]

3.7.3 Surface roughness measurements and surface profile

White light interferometry (WLI) on Veeco WYKO (NT3300S Model) Bruker NPFlex instrument also was used to obtain the surface roughness and surface profile of every coating. WLI is non-contact surface metrology that is beneficial to give images of a real topography including shape, waviness and roughness without physically damaging the sample. In WLI, an optical device splits a beam of light exiting a single source into two beams. The beams are then recombined to create an interference pattern. This combined pattern is analysed to measure the difference in paths the two beams have travelled.

In this work, mean surface roughness was obtained by measuring the surface roughness at five different areas on the sample as shown in Figure 3.13. Figure 3.13 represents the schematic drawing of areas on samples where measurements are conducted on every sample. Interference images obtained were analysed using Vision64 software from Bruker. Surface roughness is analysed to the least square line with Gaussian regression filter.
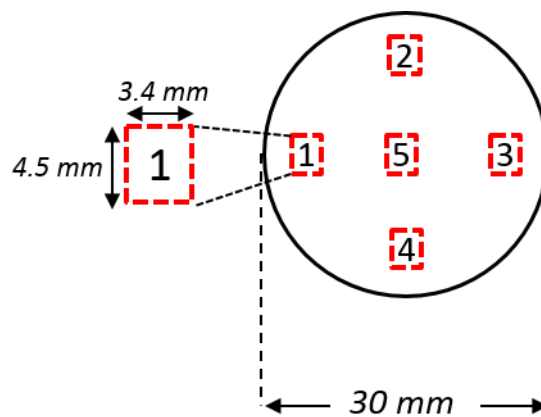
Figure 3.13 Schematic of areas on samples for surface roughness measurement

3.7.4 Scanning Electron Microscope (SEM)

In a typical Scanning Electron Microscope, the sample surface is bombarded by a focused electron beam (Figure 3.14) [145]. Electrons are emitted from an electron gun. By applying an acceleration voltage, the electron will be

accelerated through the anode and passes through magnetic lenses. The objective lens focuses the electron beam and then directed over the sample. Several numbers of scattering processes occur when the electron probe hits the sample surface. This will give rise to different signals which can be detected individually and used to create various types of images. Secondary electrons are commonly used to image a surface, while backscattered electrons are used to improve topographic or compositional images.
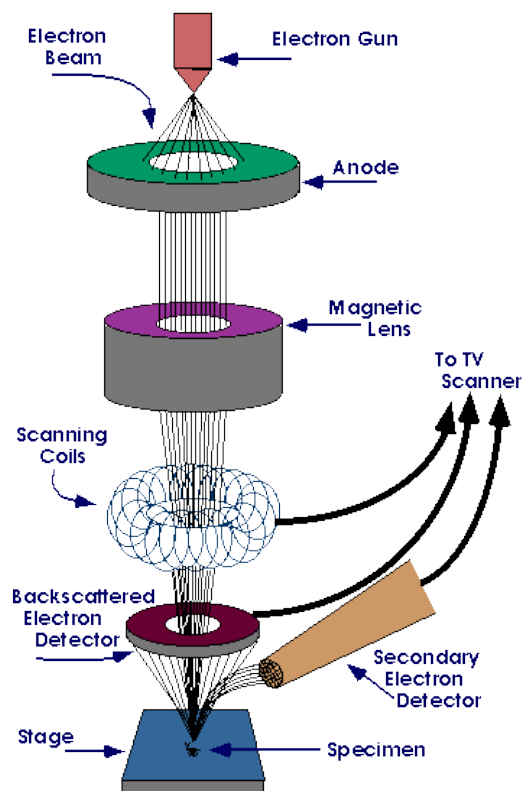
Figure 3.14 Schematic illustration of the principle of SEM

There are two types of SEM used in this work. They are Hitachi SU8230 Scanning Electron Microscope and FEI Helios G4 CX model. Hitachi SU8230 is used to give virtual information on the surface morphology after coating deposition and the fractional cross-section of the single layer DLC-GNP nanocomposite coating. FEI Helios G4 CX with a precisely focused ion beam (FIB) was used to analyse the cross-section of the multilayer DLC-GNP nanocomposite coating.

3.7.5 Energy Dispersive X-Ray Analysis (EDX)

Elemental composition analysis of samples is measured with Energy dispersive X-ray (EDX) analysis which is equipped with the SEM (Hitachi SU8230). Quantitative and qualitative analyses of elements present were analysed using Aztec software. EDX scan area and mapping were used to detect elemental species present at the specific target area. In EDX, a high energy electron beam will reach the sample and interact with local atoms where inner shell electrons are excited to higher energy states and create an electron-hole which is filled by an outer shell electron.

3.7.6 Raman Spectroscopy

Raman Spectroscopy is based on inelastic scattering of monochromatic light where the light interacts with the molecules in the sample creating a quantitative shift in the energy of protons and yields information about the vibrational and rotational modes within a material. Inelastic scattering occurred if the excited molecular vibration does not return to its initial energy level which can be either lower energy (Stokes) or higher energy (anti-Stokes) than the absorbed photon. Stokes peaks are easier to observe. The detected scattering intensity is then plotted against a range of wavenumbers, $1/\lambda$ (cm^{-1}) that is equivalent to the shift in energy relative to the excitation source. Different chemical structure of certain substance will have specific chemical shift or fingerprints. It is a standard characterisation method for most carbon materials.

In this study, Raman spectroscopy invia Qontor from Renishaw was used to analyse the types of GNP and chemical bonding within the DLC and DLC-GNP nanocomposite coating. A wavelength of the incident laser beam of λ = 488 nm was used for all Raman Spectra characterisation under the ambient condition as it is commonly used for both graphene and DLC. The Raman spectroscopy is equipped with 5x, 10x and 50x short distance objectives and 50x long-distance objective. Two scan range of 800-2000 cm^{-1} and 2000-3000 cm^{-1} was applied to identify carbon peaks of GNP and DLC-GNP nanocomposite coating. All measurements were conducted in air at room temperature (RT). Samples are placed on motorised stage and laser is focused through the objective lenses. The excitation power was kept at the lowest to avoid local heating and

damage to GNP and DLC. A linear baseline subtraction and intensity normalisation were performed for all spectrum obtained. Peak positions and full width at half maximum (FWHM) data were identified using the Gaussian and Lorenz fit.

For DLC and DLC-GNP nanocomposite coating, the variations in intensities of the main peak of D and G were analysed using I_D/I_G ratio. I_D/I_G is believed to relate to the size of the graphite planes in DLC films [147, 148]. On the other hand, for graphene, I_G/I_{2D} or I_{2D}/I_G ratio is usually used to evaluate the defect and number of layer.

3.7.7 X-ray Photoelectron Spectroscopy (XPS)

XPS is a surface characterisation technique. It is a common non-destructive tool for chemical composition analysis and for investigation of the character of the carbon bonding in DLC coatings. It can reveal the binding energy of carbon atoms and determine the sp^2 and sp^3 hybridisation in DLC coatings. A schematic diagram of emission process of photoelectrons by X-rays due to photoelectric and Auger effects is shown in Figure 3.15. Each element has a unique set of binding energies, therefore XPS can be used to determine the concentration of electrons in the near surface region. The kinetic energy of the emitted photoelectrons is given by Eq. 3.4 [149].

$$E_K = hv - E_b - W_s \hspace{3cm} 3.4$$

Where hv is the energy of the photon, E_b is the binding energy of the atomic orbital from which the electron originates, and W_s is the spectrometer work function.
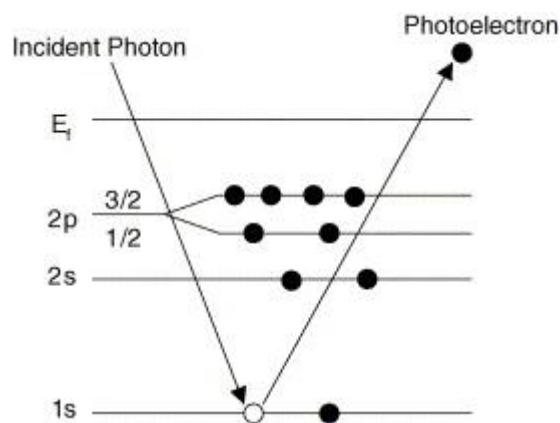
Figure 3.15 Schematic of emission process of photoelectrons by X-rays [150]

The binding energy of carbon atoms in DLC-GNP nanocomposite coatings were determined using XPS. In this work, XPS surface analysis was carried out by SPECS EnviroESCA using Al K-alpha monochromatic X-ray source. To investigate the chemical state of the carbon atoms, high resolution peak spectra were extracted. The data analysis was performed using XPSPeak software. The sp^2 and sp^3 content were calculated based on the areas of the peaks.

3.7.8 Nanoindentation

In this work, hardness is defined as a measure of the resistance to localised plastic deformation introduced by mechanical indentation [151]. Hardness relates closely to elastic modulus which is the resistance of a material to being deformed elastically when stress is applied. The ratio of hardness to elastic modulus (H/E) known as a plasticity index, can also be derived from the obtained results.

Nanoindentation is a tool widely used to measure the mechanical properties of coating such as hardness and elastic modulus at smaller scale. In nanoindentation test, the indenter will penetrate the surface of the coating until the maximum load, creating both elastic and plastic deformation. Indentation parameters such as loading and unloading rates can significantly affect the measured values from the test. Therefore, few parameters need to be considered and further compared with available literature data. The maximum

penetration depth is fixed to be 10% of the coating thickness to avoid any influence from substrate hardness. Therefore, it is necessary to determine the thickness of coating before the test is carried out.

Figure 3.16 represents a typical load/displacement curve by nanoindentation. F_{max} is the maximum applied force, h is the indentation depth under applied test force, h_p is the permanent indentation depth after the removal of the test force, h_{max} is the maximum indentation depth at F_{max}.
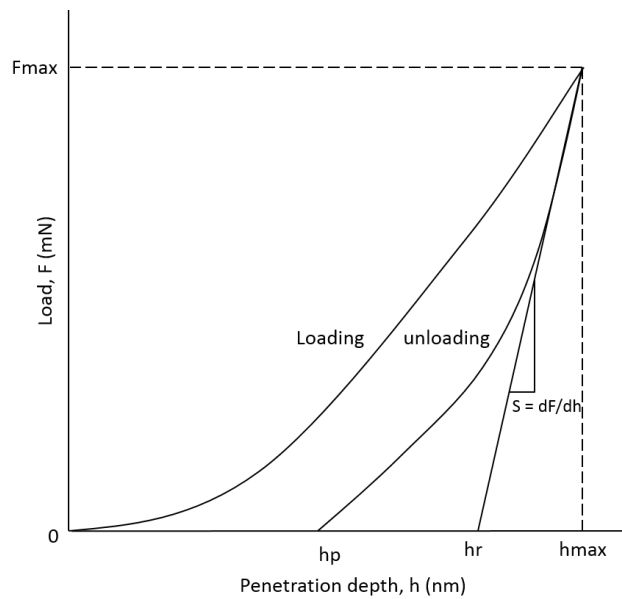
Figure 3.16 A typical load/displacement curve

Hardness was calculated using the classical hardness definition shown in Eq. 3.5 and of Eq. 3.6 was used to calculate the elastic modulus.

$$H = \frac{P}{A'}$$
3.5

Where P is the load being applied and A' is the projected contact area of the indenter tip measured through the depth of the indentation. Reduced modulus is measured using a power law fitting, and the elastic modulus can be calculated using the Oliver and Pharr method as in Eq. 3.6 [152].

$$\frac{1}{E_r} = \frac{(1 - v^2)}{E} + \frac{(1 - v_i^2)}{E_i}$$
3.6

where E_r is the reduced modulus, v and E are the Poisson's ratio and the reduced modulus of the specimen respectively, v_i and E_i are the Poisson's ratio and Young's modulus of the indenter tip respectively. The plasticity index of H/E ratio will be calculated and compared.

In this work, surface hardness (H) and elastic modulus (E) of the nanocomposite coatings were investigated by mean of a Berkovich nano-indenter using Micro Materials indentation platform with shaving triangular pyramid diamond Berkovich indenter tip. The penetration depth and applied load are used to compute the modulus of the coatings. All tests were carried out in noise and vibration free environment. Ten indentations were made for each maximum load and loading/unloading time. The final measured hardness and elastic modulus of the coating were the averages of the 20 individual indentations.

3.7.9 Adhesion

There have been several methods developed to investigate the adhesion of coating on the substrate. Table 3.5 shows the methods reported from literature to measure the adhesion of coating on the substrate. This data is edited from the works carried out by Chalker et al. [153] and Rickerby [154]. Scratch test is classified as quantitative of methods to measure adhesion (from Table 3.5).

Despite the difficulties to interpret the failure more from the resulted scratch track, scratch test is one of the most common methods that has been used to investigate the adhesion of coating on the substrate. Scratch test is a test where a loaded diamond stylus (generally a Rock-well C diamond with a tip of 200 µm radius) is drawn across a coating under increasing load until some clear failure occurs at a load which is known as critical load Lc [155]. Figure 3.17 represents the schematic of the typical scratch tester.

Table 3.5 Qualitative and quantitative methods to measure thin film adhesion [153]

Qualitative	Quantitative
Mechanical methods	
Scotch tape test	Direct pull-off method
Abrasion test	Laser spallation test

Bend and scratch test	Indentation test
	Ultracentrifuge test
	Scratch test
Non-mechanical methods	
X-ray diffraction	Thermal method
	Nucleation test
	Capacity test
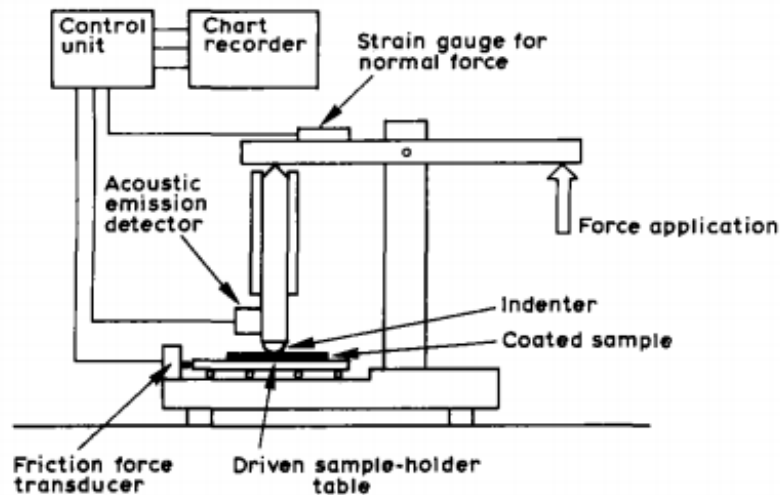
Figure 3.17 Schematic of typical scratch tester [156]

Bull et al. [157] described that failure mode in scratch test relies firmly on substrate and coating hardness. Bull presented the outcome from various scratch test as in Figure 3.18. A coating having a low hardness of coating and substrate tend to have plastic deformation which lessens the potential for failure of the coating. While high hardness coating potentially has failure and fracture of either through its thickness, interfacial or bulk. Figure 3.19 represents the rating of various failure modes in the scratch test for brittle and ductile materials. The failure that can be observed in a particular type of coating might be a combination of several types of failure modes such as tensile cracking and spallation [155].
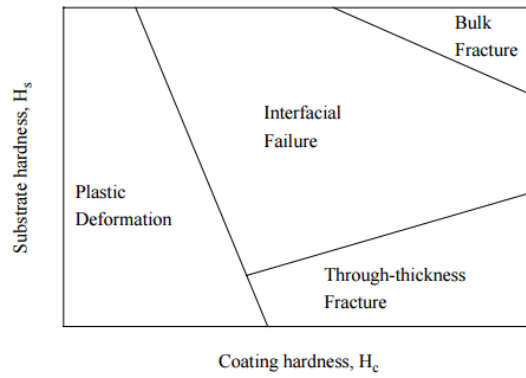
Figure 3.18 Schematic showing failure modes from the various scratch test as a function of coating and substrate hardness [157]
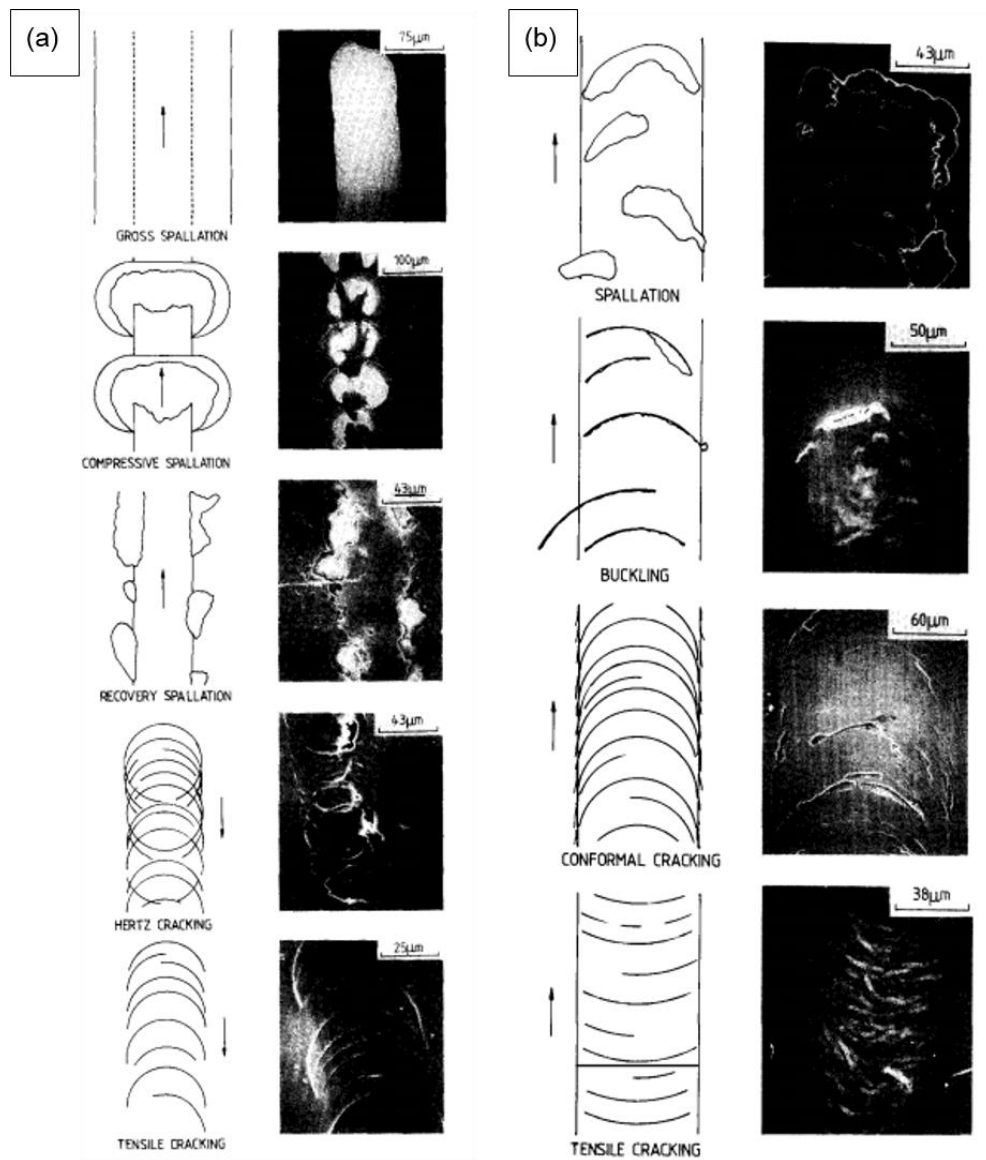
Figure 3.19 Failure modes in the scratch test for (a) brittle and (b) ductile coating [155]

The adhesion can be considered as weak if the coating peeled off from the substrate while tip passed over it. On the other hand, if the coating only cracks in a roughly semi-circular arc along the scratch without peeling off, then the adhesion can be considered as good. Critical load is the load when the coating stripped from the substrate [32].

In this work, a scratch test was performed to probe the adhesion strength of the deposited DLC-GNP nanocoatings on the M2 HSS substrates. The test was carried out using a CSM micro scratch tester, using a progressive load from 1 to 50 N at a loading rate of 100 N/min and a speed of 10 mm/min. The indenter is a Rockwell C diamond indenter with a tip radius of 200 µm. Critical load Lc was determined by optical microscopy. In this work, L_{C1} is noted as the critical load that identifies the first adhesive failure of the coating.

3.8   Biceri Pin-on-Reciprocating Plate Tribometer

3.8.1   Test condition

Friction and wear of coatings were studied using a Biceri pin-on-reciprocating-plate tribometer. This tribometer has an electric motor that drives a rotating disk on which an eccentrically places connecting rod has been attached. The connecting road is coupled to a table on a linear bearing. The load is applied by putting the weight at the end of the arm. A schematic image of pin-on-reciprocating plate test is shown in Figure 3.20. A thermocouple is attached to the lubricant bath to control the temperature throughout the test. In this work, all tribological test was conducted at a temperature of 100 °C.
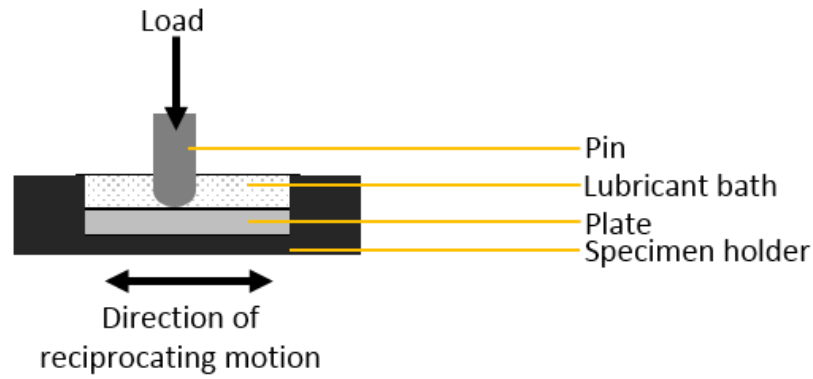
Figure 3.20 Schematic of Biceri pin-on-reciprocating plate tribometer

Tests were conducted in the air with relative humidity. The plate samples were 30 mm in diameter. The counterpart pin was 20 mm in length and 6 mm diameter with 40 mm radius of curvature on one end. Material properties of the discs and pin used to carry out the test are given in Table 3.6.

Table 3.6 Material properties of plates (substrate/ coatings) and counterpart

| | Plate/ Coating | | Pin |
	Substrate	Coating	
Material	HSS M2 Grade steel	DLC and DLC-GNP nanocomposite coating	Cast iron
Dimension	D = 30 mm		D = 6 mm L = 20 mm 40 mm radius curvature
Roughness	~ 10 – 20 nm	~ 30 – 250 nm	70 – 90 nm
Hardness	8.0 GPa	~ 20-21 GPa	4.0 – 4.5 GPa
Reduced Elastic Modulus	218 GPa	~ 187-194 GPa	134 GPa

The pressure exerted on the plate from the pin was calculated using Hertzian contact pressure equations using the normal load and the weight hanging from

the pivoted beam. The Hertzian contact pressure calculated to be 750 MPa which corresponded to 281 N normal load with 11.5 kg hanging weight at the pivoted beam resembling a pressure condition in cam tappet environment. The stroke length was 10 mm at a frequency at 1 Hz. The experimental running conditions are summarised in Table 3.7. Prior to experimental setup, all samples and pins were sonically cleaned with acetone for ten minutes.

Table 3.7 Test condition of Biceri pin-on reciprocating test

Test condition	Parameter
Lubricants	Base oil Group III
Temperature (° C)	100
Contact pressure (MPa)	750
Average entrainment speed (cm/s)	2
Test duration (hour)	3

3.8.2 Characterisation after tribological testing

A Leica optical microscope DM6000 was used to observe the morphology of the wear after wear test. Figure 3.21 shows the example of images of the wear track on disk and wear scar on the counterpart pin after the test. The wear tracks and scars generated on the discs and pins were analysed to investigate the morphology and chemical structure.
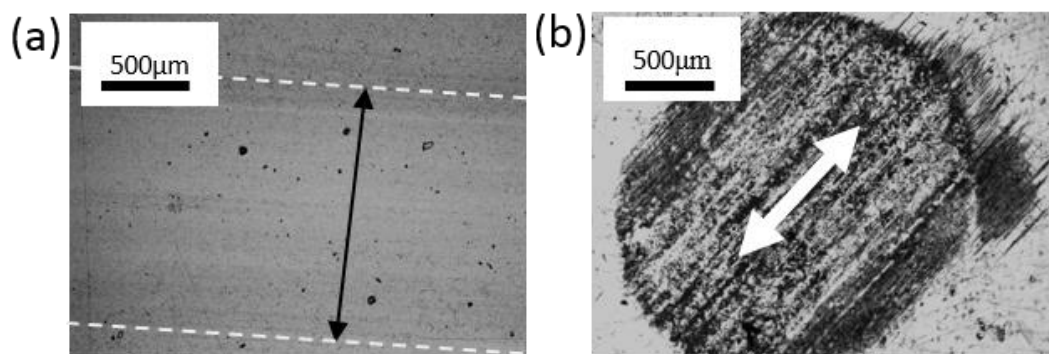
Figure 3.21 Examples of (a) wear track on the disc and (b) wear scar on counterpart pin after test on Biceri pin-on-disc reciprocating-plate tribometer

Measurement of the wear scar depth, cross-sectional areas and the surface topography were carried out using WLI. Raman analysis was performed on the

wear tracks and scars after each tribological test to investigate any formation of tribo film and change of structure after the test. All samples and pins were cleaned with heptane ultrasonically for few minutes before any surface characterisation was done.

3.8.3 Measurement of volumetric wear and wear coefficients

In the present study, volumetric wear of the wear tracks was measured directly using Vision64 software package due to the irregular shape of wear tracks. As for counterpart pins, since the shape of the pin is not flat but have 40 mm curvatures, wear volume were estimated manually using Eq. 3.6 and 3.7 [158],

$$V = \frac{1}{3}\pi h^2(3R - h) \qquad\qquad 3.6$$

$$h = R - \sqrt{\left(R^2 - \frac{D^2}{4}\right)} \qquad\qquad 3.7$$

where V is the volume of material, R is the pin radius, and D is the wear scar diameter. Finally, the specific wear rate was calculated using Archard relationship as follows:

$$K_i = \frac{V_i}{F \times S} \qquad\qquad 3.8$$

Chapter 4

Results: Optimisation of GNP Deposition

4.1 Introduction

Graphene is well acknowledged to have poor colloidal stability owing to strong Van der Waals forces between each graphene plane [159, 160]. It must be able to disperse well over a reasonable period of time to be beneficial for any fabrication process. There is no standard method to disperse graphene. The choice of solvent and sonication time are among the parameters that need to be optimised to achieve optimal graphene dispersion. In this work, DMF, ethanol and NMP were selected as types of solvent to be tested as they are well-known for solvent dispersion for carbon nanostructure [161, 162]. Sonication time varies depending upon the method used as well as the solvents selected. Sonication time of stable carbon nanomaterials such as graphene and carbon nanotube (CNT) suspension can be varied as low as ten minutes up to two hours [163]. In this section GNP suspensions in DMF, ethanol and NMP will be denoted as GNP/DMF, GNP/ethanol and GNP/NMP respectively.

The main experimental results in this chapter are shown in Figure 4.1. Figure 4.1 summarises the topic, the test parameters and the findings of each section. The results include dispersibility of GNP in solvents, GNP deposition using spin coating, followed by optimisation of spin coating process based on GNP distribution and surface roughness using Taguchi Method. A summary of the outcomes of this chapter will also be summarised.
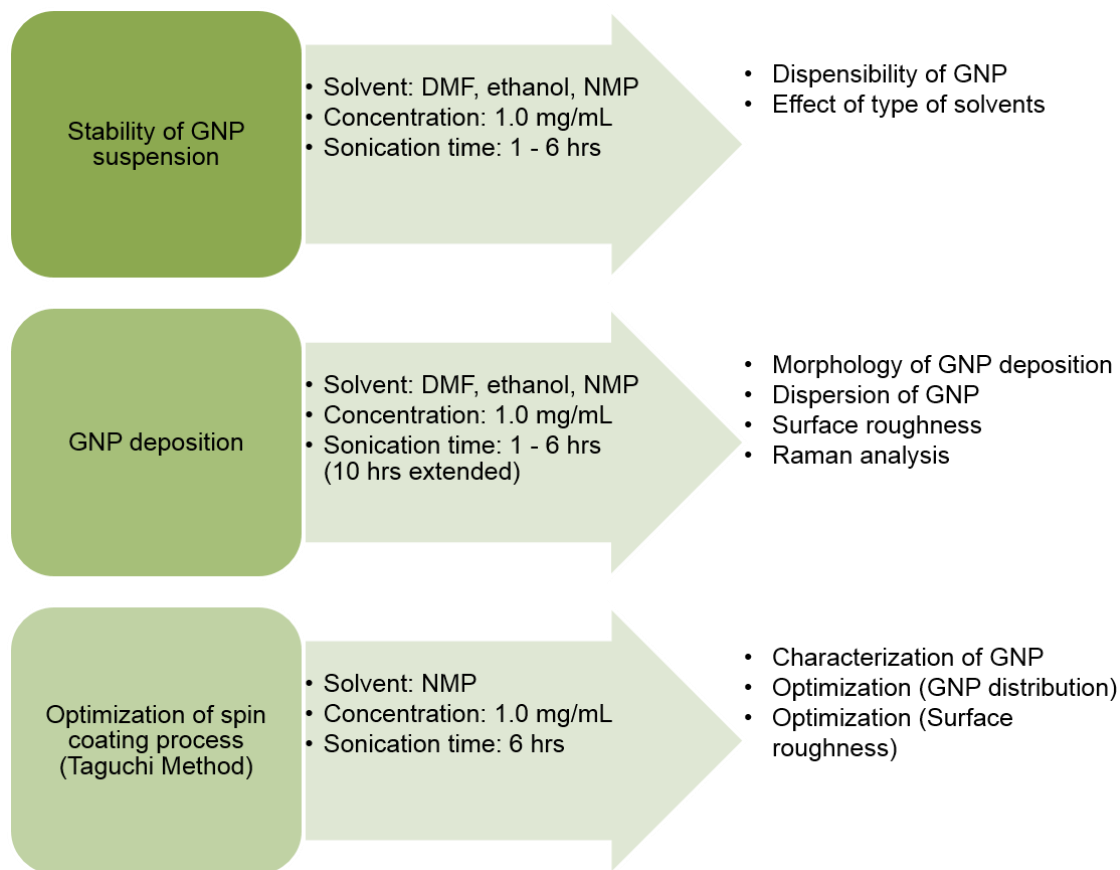
Figure 4.1 The experimental procedures in this chapter

4.2   Aim

Driven by the literature review and the goal of this project, which is the design of a DLC-GNP nanocomposite coating, the main aim of this section is to attain optimal uniform graphene distribution. The objectives of the work are as follows:

i.   To optimise the dispersion condition of GNP using solvents by a sonication method.

ii.   To evaluate the effect of GNP dispersion on spin-coated GNP.

iii.   To investigate the effect of spin coating parameters on spin-coated GNP.

This chapter can be divided into two main works which are: 1. The stability of GNP suspensions and 2. Deposition of GNP using spin coating method. The

aim is to select one solvent for GNP that can produce the optimum condition of GNP deposition. GNPs were dispersed in three types of solvents at different sonication times. The GNP suspensions were then deposited on M2 HSS substrates that have been coated with an interlayer of Cr/W.

4.3   Stability of Graphene Nanoplatelets (GNP) Suspension

4.3.1   Dispersibility of GNP in solvents as a function of sonication time

To investigate the effect of sonication time on GNP dispersibility, GNP suspensions were ultrasonicated for a duration from one to six hours. Observations immediately after sonication (zero hour), one, five and 168 hours (one week) were recorded. This sedimentation experiment is a semi-quantitative method to characterise the stability of GNP in each solvent. The photographs of sedimentation tests are attached in Appendix D1, D2, and D3.

A grayscale level applied to the suspension was used as a tool to quantitatively measure the change of suspension over time. To see the change of dispersion quantitatively, the grayscale of the top view of the suspensions has been measured using ImageJ analysis software. The measurement method is explained in Section 3.3 and Appendix A. Typically, the lowest value of grayscale (0) represents complete black colour, while the highest value (255) is taken to be white (Figure 4.2).

Lowest   Grayscale   Highest

0 $\longrightarrow$ 255

Black   White

Figure 4.2 Interpretation of grayscale value

Figure 4.3 shows the grayscale of GNP dispersion in ethanol, DMF and NMP sonicated for one to six hours. The grayscale was measured from recorded images of sedimentation tests in Appendix C right after dispersion and also was aged for one, five hours and one week respectively.

Sonication time seems to have less influence on GNP dispersion in ethanol (Figure 4.3(a)). Grayscale values increased as the ageing time increased for all six GNP dispersions. As been seen in Appendix D, total precipitation has been observed for all six dispersions after one week which was shown by high grayscale level in Figure 4.3(a).

Figure 4.3(b) shows that the grayscale values of GNP/DMF at different sonication times displaying changes for all six dispersions. No noticeable increase of grayscale values was observed as ageing time was increased from one hour to five hours. There is quite a distinct trend of grayscale decrements as sonication time increased. This indicates that the longer sonication time is, the less precipitation occurred. Six hours of sonication time showed the best dispersibility of GNP/DMF.

As for GNP/NMP in Figure 4.3(c), no visible increment of grayscale values can be observed as the ageing time increased to five hours, for all one to six hours dispersions. Grayscale level remains constant even after one week, except for the GNP/NMP sonicated for only one hour. After one hour, longer sonication yields no significant difference of GNP stability.

After one week, both GNP/ethanol and GNP/DMF dispersions have high level of grayscale value which show high precipitation of GNP. GNP/NMP dispersion, on the other hand, has a lower value of grayscale compared to the other dispersions and remained almost stable. The results demonstrate that sonication time does influence the dispersion of GNP suspension to a certain extent. It is also in agreement with the finding reported by other researchers on dispersibility of GNP and other carbon materials such as CNT [164].
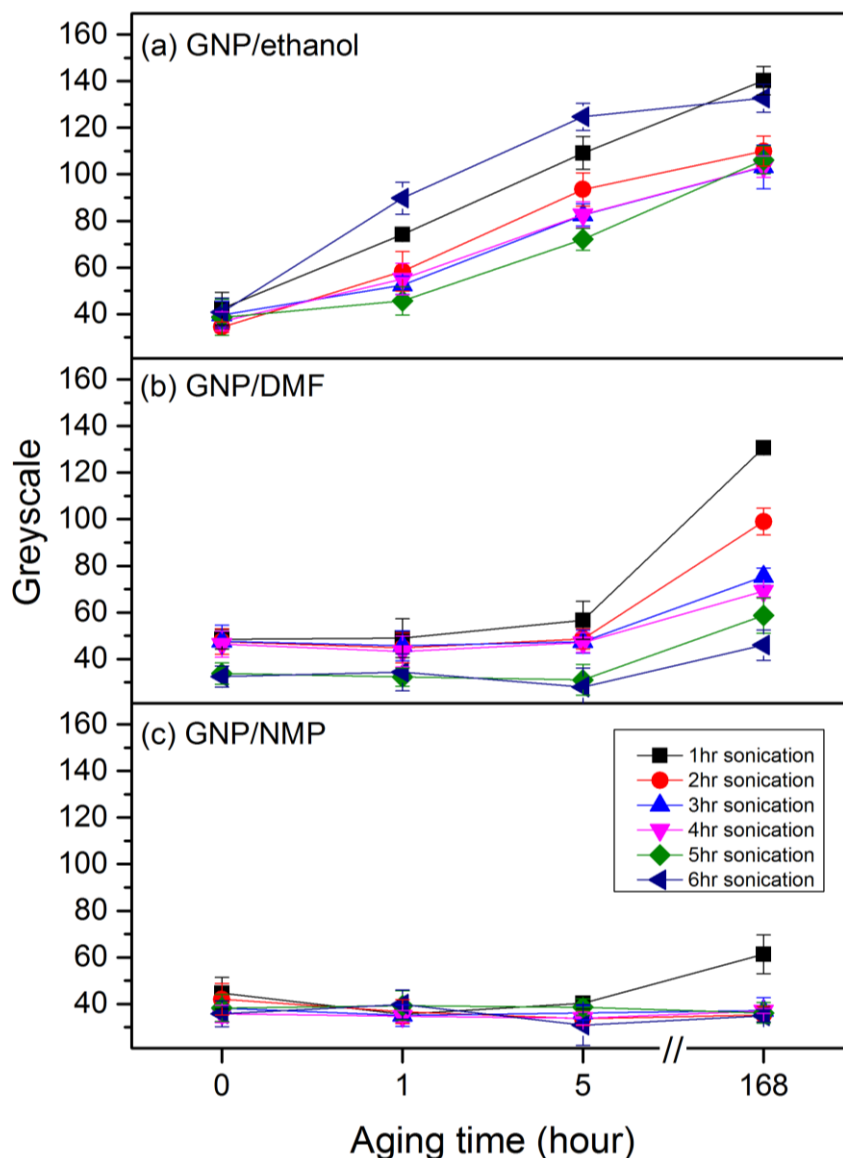
Figure 4.3 Grayscale of suspension (a) GNP/ethanol, (b) GNP/DMF and (c) GNP/NMP sonicated for one to six hours by a function of ageing time. Grayscale was measured by images captured at the ageing time of zero, one and five and 168 hours (one weeks)

4.3.2 Effect of type of solvents on GNP dispersion

GNPs were dispersed using ultrasonic methods in three types of solvents which are ethanol, DMF and NMP. Ethanol, DMF and NMP are the types of solvents that are commonly used to disperse GNP. GNP solutions have been sonicated for six hours and its stability over time were observed. GNP sonicated in DMF, ethanol and NMP will be named as GNP/DMF, GNP/ethanol and GNP/NMP onwards. As a reference, Table 4.1 shows the values of

dynamic viscosity of ethanol, DMF and NMP at 25°C. NMP has the highest followed by ethanol and DMF.

Table 4.1 Dynamic viscosity of solvents used in the work

Solvent	Dynamic Viscosity at 25°C (mPas)
Ethanol	1.040
Dimethylformamide (DMF)	0.802
N-Methyl-2-pyrrolidone (NMP)	1.650

Figure 4.4 displays the comparison of optical images for GNP dispersion in (a) ethanol, (b) DMF and (c) NMP. The first column is the image of the dispersion after sonication and the next following columns are the dispersions after one, two hours and one week respectively. Observation immediately after ultrasonication showed that GNPs disperse well in all the polar solvents of ethanol, DMF and NMP. However, GNP solution in ethanol (GNP/ethanol) started to settle down from solution even before one hour after sonication. Complete precipitation can be observed after five hours of sonication (Figure 4.4(a)). Little sediments can be observed for graphene solution in DMF after five hours. Complete precipitation did not happen even one week after sonication. However visible separation of precipitated GNP from the solution can obviously be seen at this stage (Figure 4.4(b)). While graphene solution in NMP can be stabled with only little occurrence of sediments or visible particles for even after one week (Figure 4.4(c)). However, simple manual agitation is enough to re-disperse the settled GNP in all type of solvents. Manual agitation was performed by moderately shaking each vial for few seconds with hand. The grayscale of the dispersions were plotted in Figure 4.5
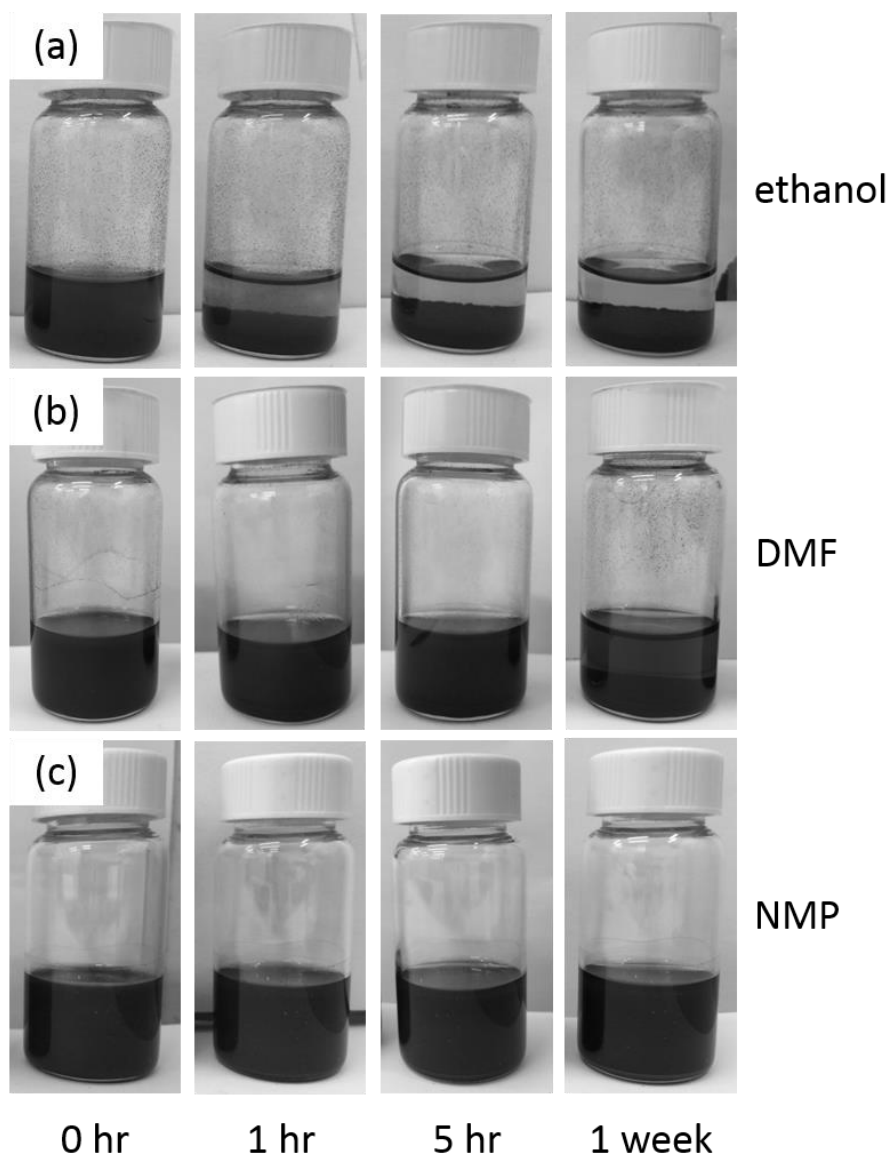
Figure 4.4 Images of GNP dispersed in (a) ethanol, (b) DMF and (c) NMP through ultrasonication (six hours). From left, 1st column: dispersion after sonication. 2nd column: dispersion after one hour. 3rd column: dispersion after five hours. 4th column: dispersion after one week

Measured grayscale for results in Figure 4.4 is plotted in Figure 4.5. As can be seen, GNP/ethanol has the highest grayscale of all, and the value increased with time which can be seen as complete sedimentation after one week (168 hours) in Figure 4.4. While for GNP/NMP, the grayscale remained almost unchanged over the period of one week.
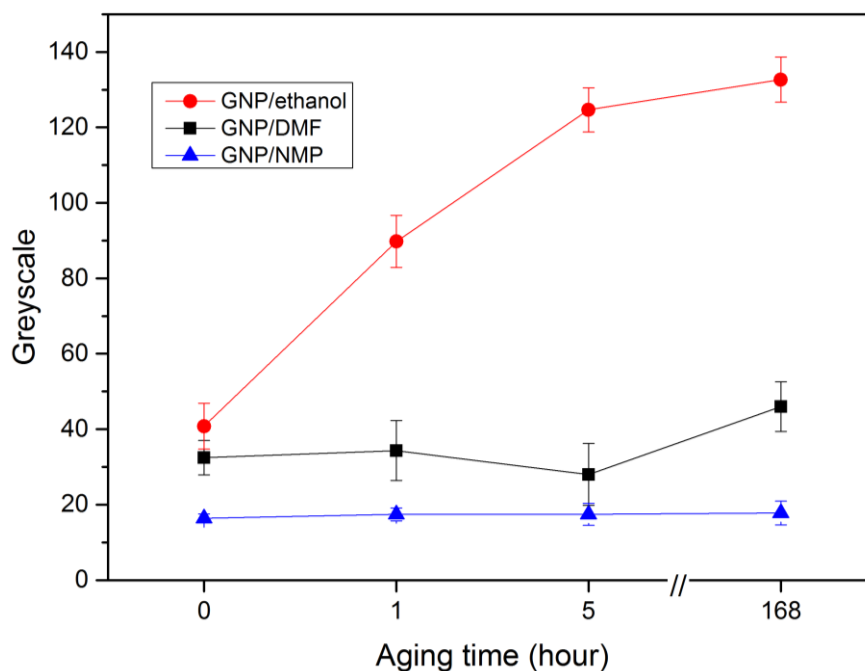
Figure 4.5 Comparison of grayscale of GNP/ethanol, GNPDMF and GNP/NMP
sonicated for six hours by a function of ageing time

4.3.3 Summary of stability of GNP dispersion

As a summary, these semi-qualitative results show that:

i. Although graphene showed good dispersibility with all three solvents after sonication, GNP/NMP suspension displayed lesser sedimentation of GNP over storage time followed by DMF and graphene. Stability rank of the three suspensions is as follows:

GNP/NMP > GNP/DMF > GNP/ethanol

ii. Sonication time of the suspension does give a substantial effect on the stability of GNP, especially for DMF and ethanol solvents.

iii. Stability of GNP in NMP was easily achieved after two hours of sonication time.

4.4 GNP Deposition using Spin Coating Method as a Function of the Solvent type and Sonication Time

This section characterizes the effect of each solvent on the GNP deposition using spin coating method. GNP was deposited using 0.25mL drop of GNP

suspension in DMF, ethanol and NMP solvents at a concentration of 1.0 mg/mL with a fixed non-optimised spin coating method of 1500 rpm spinning speed for 30 seconds.

4.4.1 Morphology of GNP deposition

Figure 4.6 shows the morphology of spin-coated graphene on interlayer using solvents of ethanol, DMF and NMP sonicated for six hours. Micrographs on the right side demonstrate the higher magnification the coating. The images show numbers of GNP distributed reasonably uniform over the substrates. Size of GNPs was noticeably smaller for GNP/NMP (Figure 4.6 (c)) compared to GNP/ethanol and GNP/DMF in Figure 4.6 (a) and (b). There were more bright areas in GNP/NMP, while samples of GNP/DMF and GNP/ethanol have more dark areas. Dark areas are believed to be an aggregation of individual GNP which were sparsely distributed on the surface due to its dispersion behaviour in solvents and aggregation during film formation. In contrast, bright areas are assumed to be the GNP with lesser number of layers. Bright areas have more well-defined shape and morphology of GNP compared to dark areas with very mild aggregation. This also agrees with the excellent stability results of GNP dispersion in NMP that represent the dispersion of thinner GNP compared to other solvents.

Good dispersion of GNP in NMP contribute to the well-distributed GNP on the surface covered with bright GNP islands in almost areas. These optical images were then used to measure the size of the GNP islands using imageJ and will be presented in the next section.

Figure 4.7 - Figure 4.9 show GNP distribution on substrates sonicated at different time from one to six hours using GNP/DMF, GNP/ethanol and GNP/NMP suspension respectively. Images on the right side of each figure represent the high magnification of each image on the left side. The results of GNP dispersion presented in Section 4.3 support the observation obtained from this test. Dark areas exist in most of the samples for GNP/DMF and GNP/ethanol which indicate the minor effect of sonication time on the GNPs distribution on substrates. For samples of GNP/NMP, other than 1-hour sonicated sample, the island size and distribution of GNP for GNP/NMP

samples are almost similar with no significant difference (Figure 4.9). These results will be further investigated in the section for the measurement of GNP size and percentage of coverage distribution using ImageJ.
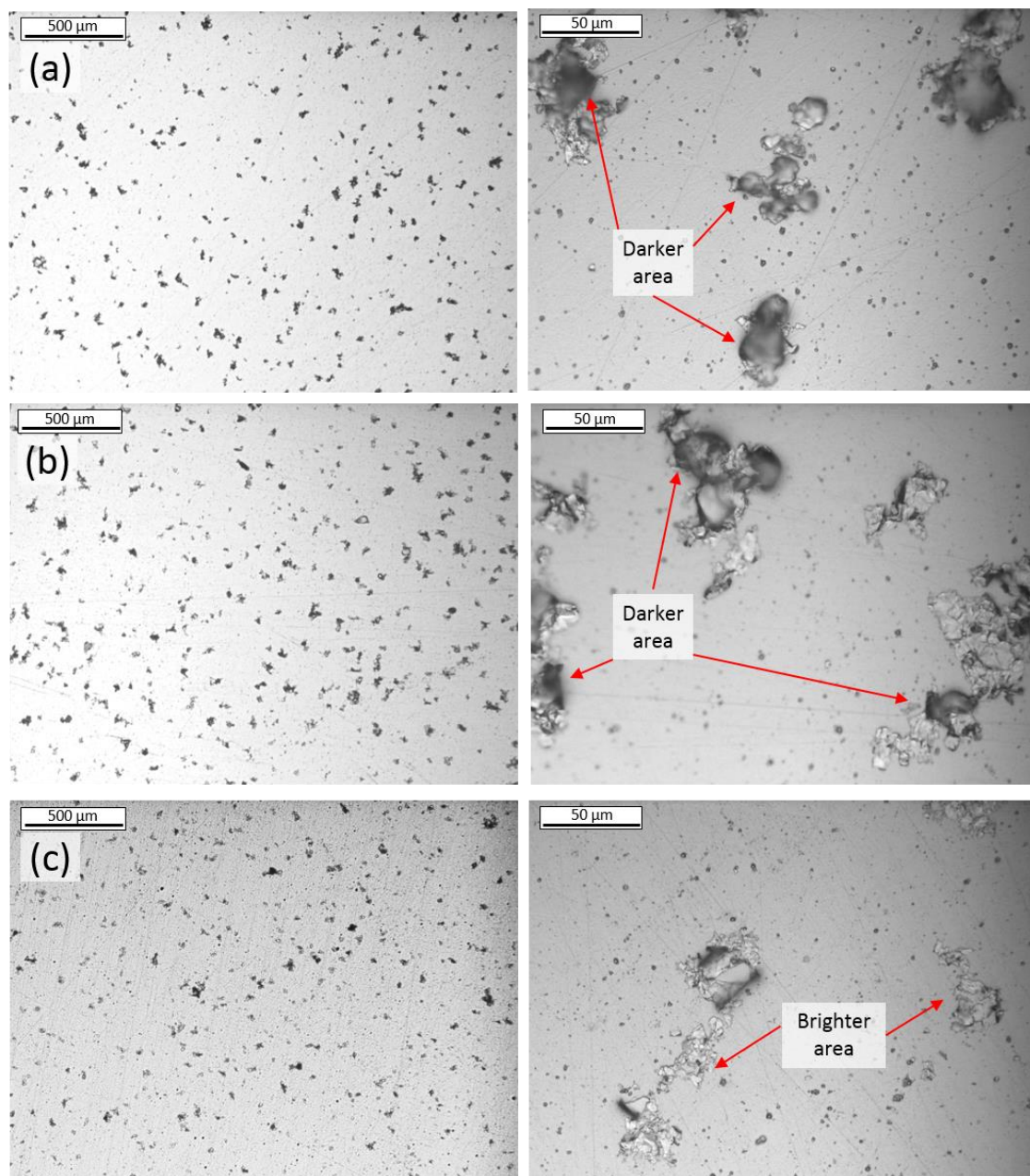
Figure 4.6 Optical micrographs of graphene coating of (a) GNP/ethanol, (b) GNP/DMF and (c) GNP/NMP (sonicated for six hours). Micrographs on the right side are the high magnification images of samples in (a), (b) and (c)
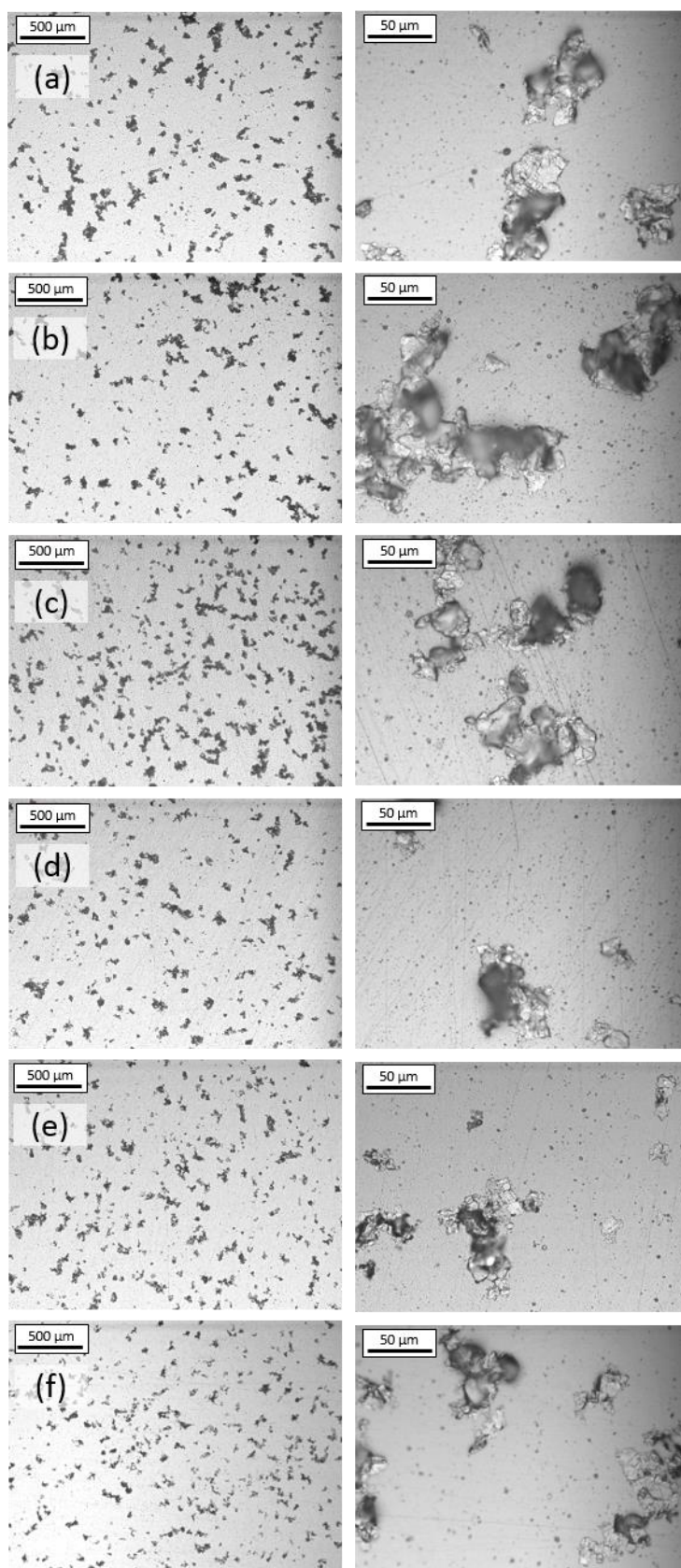
Figure 4.7 Optical micrograph of GNP coating using GNP/DMF as solvent at different sonication time of (a) 1 hour, (b) 2 hours, (c) 3 hours, (d) 4 hours, (e) 5 hours and (f) 6 hours. The corresponding high magnification of the optical micrographs are shown on the right side of each micrograph

92
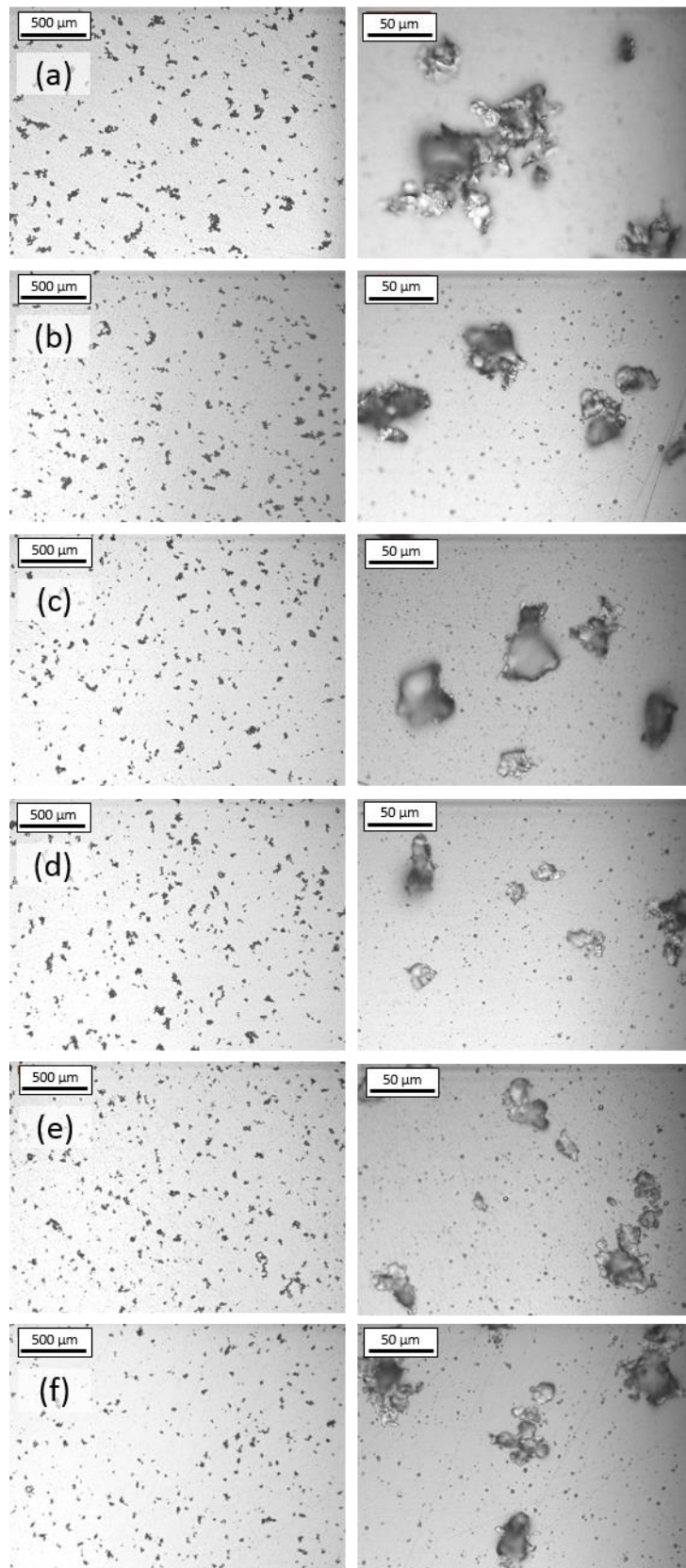
Figure 4.8 Optical micrograph of GNP coating using GNP/ethanol as solvent at different sonication time of solution of (a) 1 hour, (b) 2 hours, (c) 3 hours, (d) 4 hours, (e) 5 hours and (f) 6 hours. The corresponding high magnification of the optical micrographs is shown on the right side of each micrograph
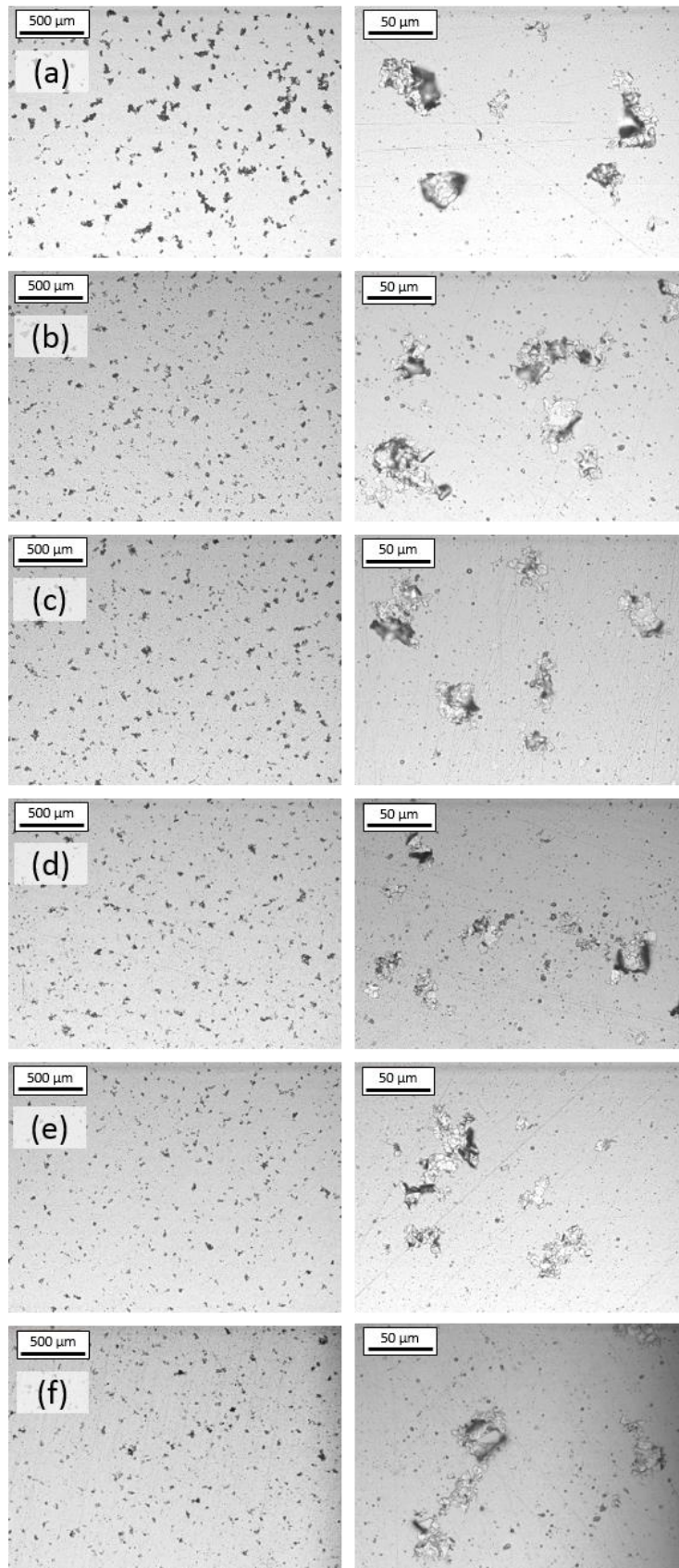
Figure 4.9 Optical micrograph of GNP coating using GNP/NMP as solvent at different sonication time of (a) 1 hour, (b) 2 hours, (c) 3 hours, (d) 4 hours, (e) 5 hours and (f) 6 hours. The corresponding high magnification of the optical micrographs is shown on the right side of each micrograph

4.4.2 Dispersion of graphene on substrates

All coverage area measurements in this work have been carried out using ImageJ. Figure 4.10 represents the typical images of GNP distribution captured with optical microscopy and its segmentation created using built-in analysis of particles in an ImageJ plugin. This segmentation is then used to measure the percentage of GNP coverage and island size.
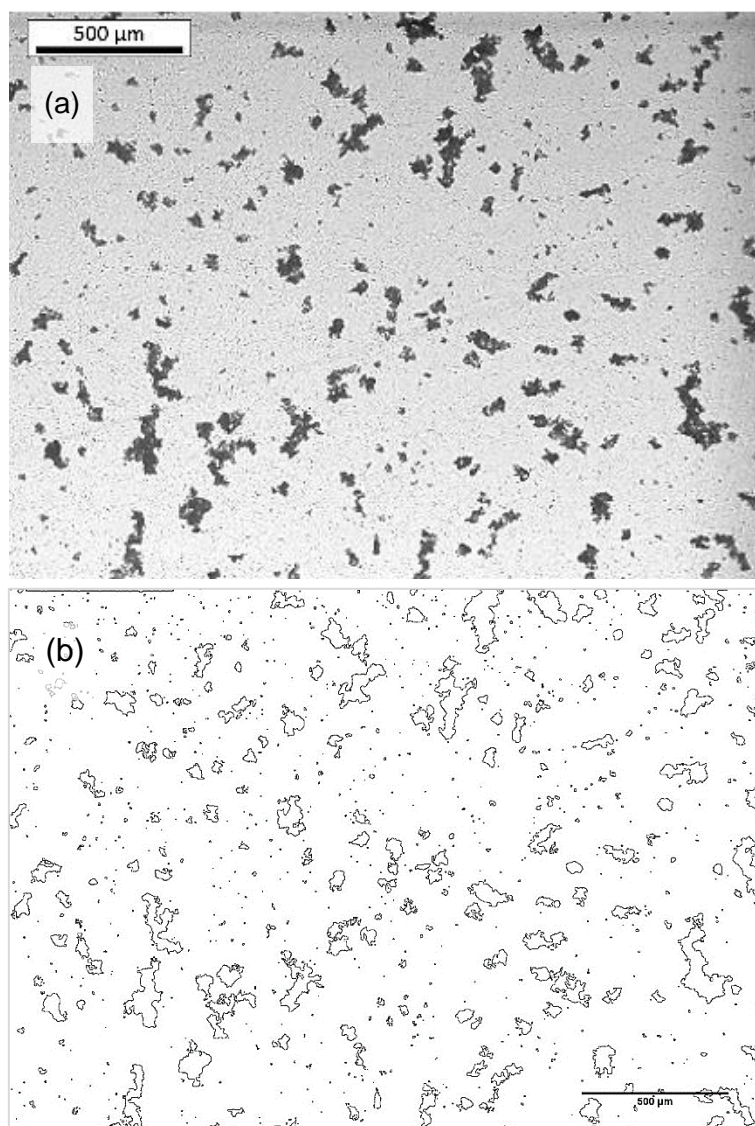
Figure 4.10 (a) Typical optical image of the GNP distribution on the substrate surface after spin coating deposition, (b) Corresponding segmentation after using built-in analyse particles ImageJ plugin

Coverage areas of GNP in three different solvents of DMF, ethanol and NMP at different sonication time are depicted in Figure 4.11. As expected from the optical micrograph results in Section 4.4.1, no significant change of GNP distribution over sonication time for samples of GNP/DMF and GNP/ethanol was observed. However, the coverage area of GNP on substrates reduced as the sonication time from one to three hours for samples of GNP/NMP before showing no significant change after three hours to six hours sonication time. Coverage area reduced one of the possible reason to this is because of smaller size and lesser big and dark GNP islands in GNP/NMP samples. ImageJ measurement might underestimate some smaller and bright areas due to the nature of the software wherein it detects the different brightnesses to represent measured areas.
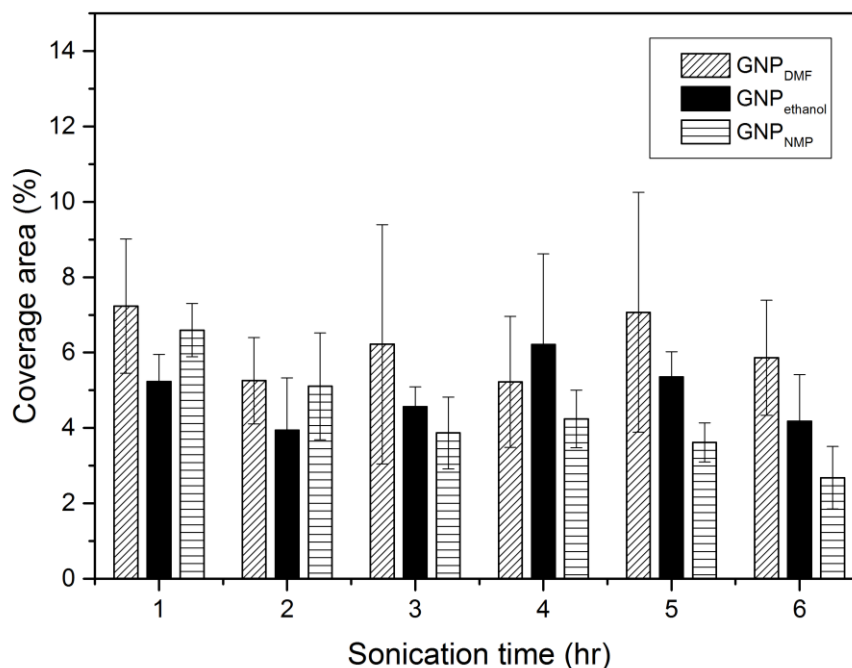
Figure 4.11 Coverage areas of GNP on substrates deposited using DMF, ethanol and NMP as solvent. Dotted lines are the linear correlation of GNP coverage area (%) with sonication time. Error bars represent standard deviation from the average values of five areas of measurements

To see a clear comparison of different types of solvent on GNP coverage area, samples deposited with GNP sonicated for six hours were used. The bar chart of coverage areas by the solvents of DMF, ethanol and NMP are shown in Figure 4.12. The coverage areas of GNP from DMF solvent show the highest

values of 5.9% but there is not much difference with ethanol at 5.2% and the lowest is with NMP of 3.9% coverage.
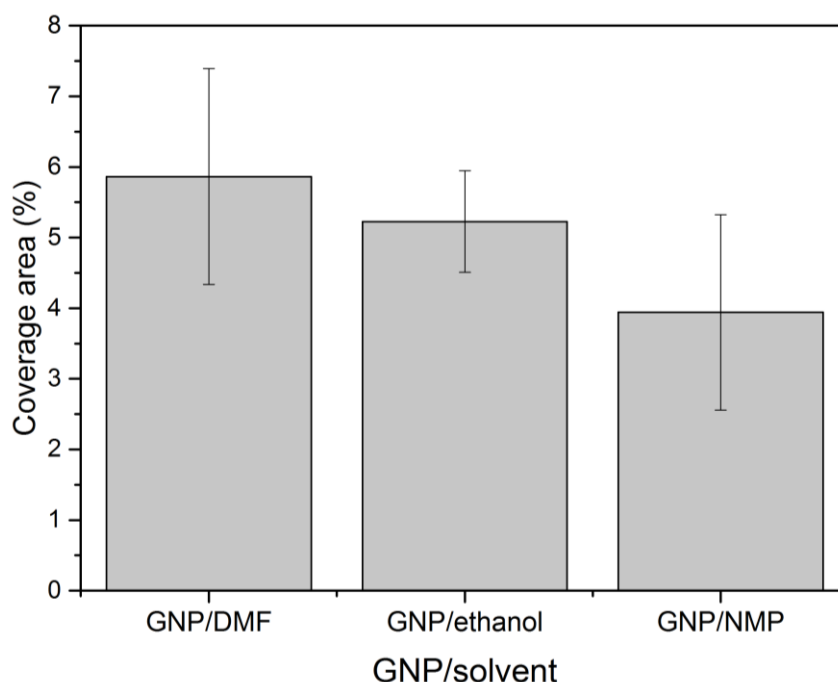
Figure 4.12 Comparison of GNP coverage area (%) by solvents of DMF, ethanol and NMP. Error bars represent standard deviation from the average values of five areas of measurements

Figure 4.13 shows the average size of GNP islands on GNP/DMF, GNP/ethanol and GNP/NMP samples at sonication times from one hour to six hours. The size of GNP islands created on the surface was also calculated using the same method of ImageJ described in the previous section. Observation through optical micrograph images showed that the size of GNP islands does not necessarily represent the size of single GNP. GNP islands are typically produced by several numbers of GNPs depending on the size of the island. Therefore, the measured size of GNP may indicate the dispersion behaviour of GNP in different solvents at different sonication time. GNP islands for sample GNP/ethanol appeared to be significantly reduced as the sonication time increased for more than five hours. As for GNP/NMP samples, other than the sample produced by GNP sonicated for one hour, no significant size reduction can be observed. In addition, the average size of GNP islands for GNP/DMF showed almost no change over sonication time.
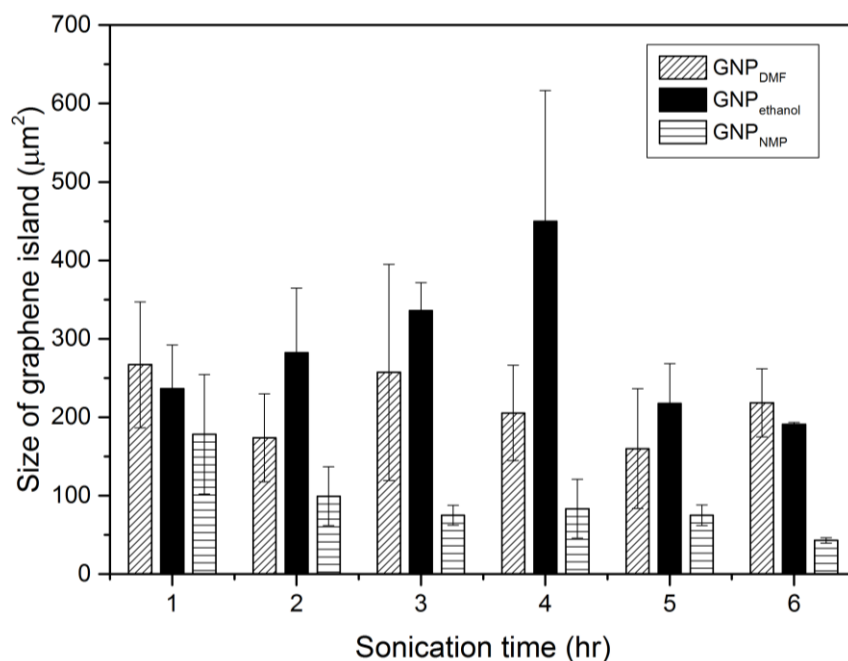
Figure 4.13 Size of GNP island on substrates deposited using DMF, ethanol and NMP as solvent. Dotted lines are the linear correlation of the size of GNP island (μm^2) with sonication time. Error bars represent standard deviation from the average values of five areas of measurements

4.4.3 Surface Roughness of graphene dispersion

Measurement of surface roughness of the spin-coated graphene was carried out using White Light Interferometry (WLI) to identify the effect of solvent type and sonication time. Images of topographical features of GNP/DMF, GNP/ethanol and GNP/NMP samples sonicated from one to six hours are in Appendix C. It is believed that the measured height from the surface topography does not represent the true thickness of GNP which corresponds to a number of layers. This could be seen clearly in the optical images presented in Figure 4.7 - Figure 4.9 where the platelets were randomly stacked and aggregated on the surface.

Measured surface roughness of samples GNP/DMF, GNP/ethanol and GNP/NMP deposited with GNP dispersion sonicated from one to six hours are presented in Figure 4.14. It can be seen that the sonication time between one to four hours does not strongly affect the surface roughness of GNP/ethanol samples. However, the surface roughness reduced significantly as the sonication time was increased to four and six hours. On the other hand, the

surface roughness of GNP/DMF and GNP/NMP reduced dramatically as the sonication hour was increased to two hours from one hour. The surface roughness of both types of samples was reduced to approximately 50% at sonication time of two hours. The surface roughness of sample GNP/DMF remained almost the same afterwards, while GNP/NMP decreased until it reached the lowest value at a sonication time of six hours.
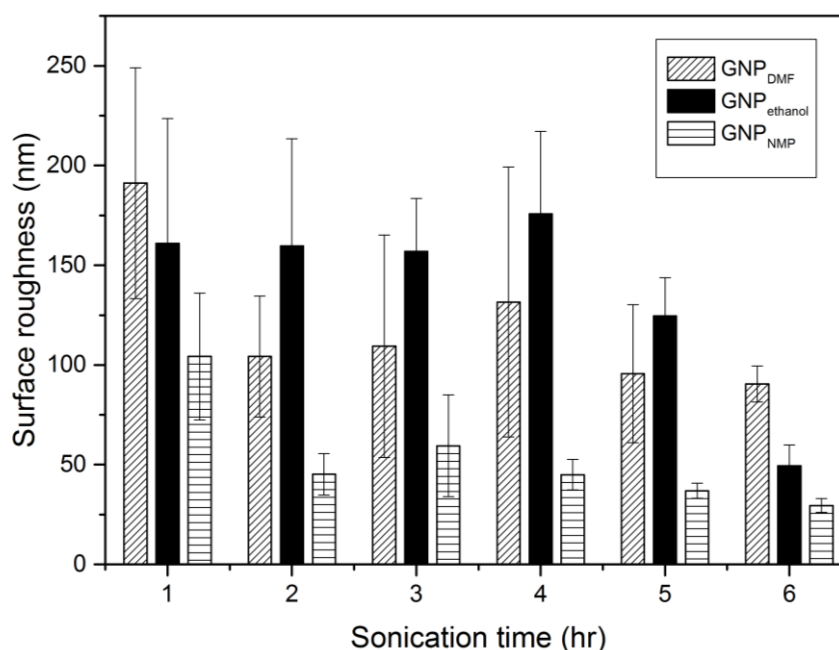
Figure 4.14 Surface roughness of substrates after GNP deposition

Figure 4.15 compares the surface roughness of samples deposited with GNP in ethanol, DMF and NMP. GNP dispersed for six hours was used to make this comparison. Surface roughness before deposition of GNP is 11 nm. The surface roughness of samples GNP/ethanol, GNP/DMF and GNP/NMP were measured to be 49 nm, 91 nm and 30 nm respectively. The sample of GNP/NMP has a relatively low surface roughness compared to GNP/ethanol and GNP/DMF. This outcome also supports the assumptions that have been made earlier, where dark areas correspond to areas with numbers of agglomerated GNP, while bright areas have a lesser number of GNP. More dark areas were observed on samples GNP/DMF, GNP/ethanol thus have higher surface roughness compared to GNP/NMP.

Despite having a good dispersibility in DMF compared to ethanol, GNP/DMF samples have the highest surface roughness, almost double the surface roughness of GNP/ethanol. High standard deviation of both samples corresponds to non-uniformity of GNP distribution over the substrates.
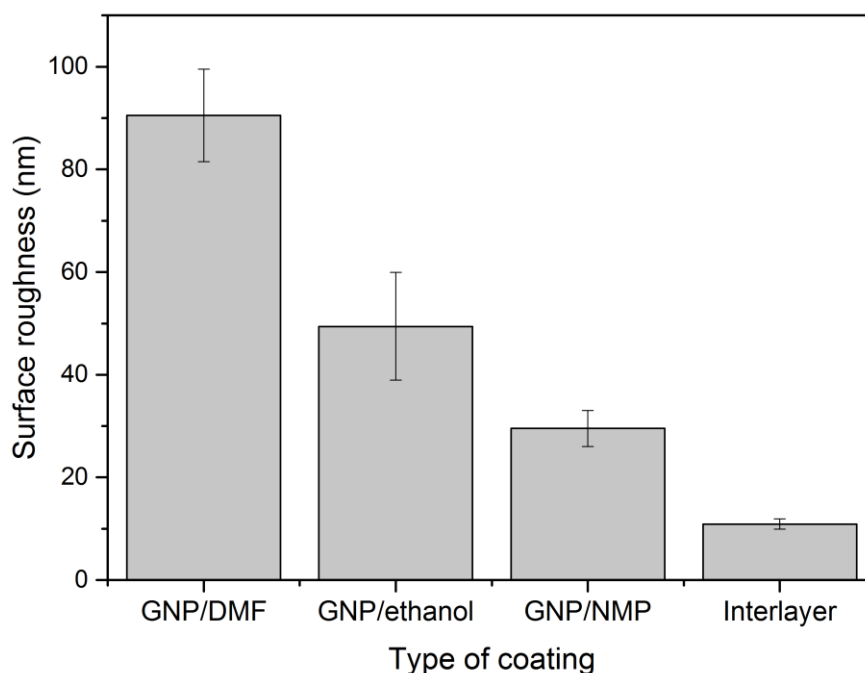
Figure 4.15 Surface roughness comparison of GNP/DMF, GNP/ethanol and GNP/NMP samples. All samples were sonicated for six hours.

To further assess the effect of sonication time on the characteristic of spin-coated GNP, GNP/NMP suspension sonicated for ten hours was prepared. Figure 4.16 is the optical micrograph of spin-coated GNP deposited using GNP/NMP sonicated for ten hours with the same conditions as used in the previous set of experiments. Seemingly, the size of GNPs was much smaller than the size recorded for GNP/NMP sonicated for six hours.
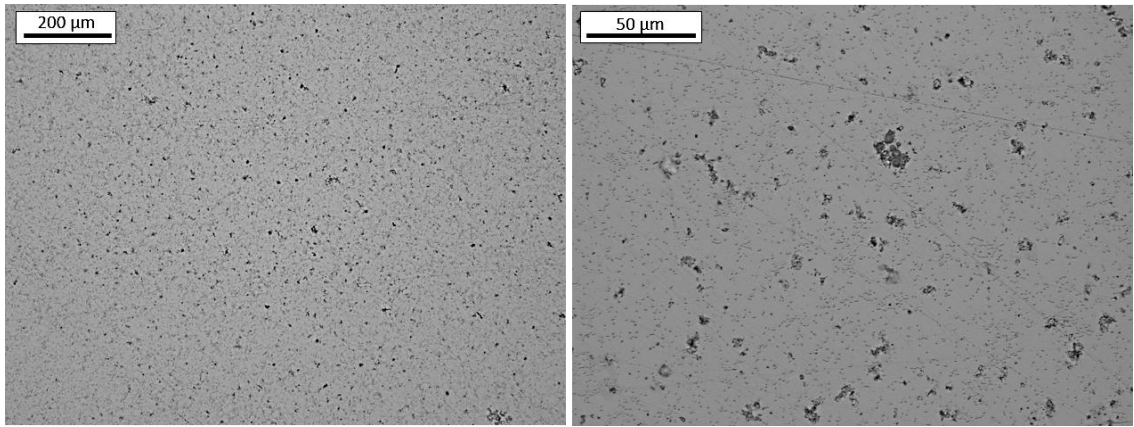
Figure 4.16 Optical images of one area of spin-coated GNP deposited using GNP/NMP sonicated for ten hours at a magnification of 10x (left) and 50x (right).

However, deposition of the suspension sonicated for ten hours was very poor, that spin-coated GNPs were not covering the whole area on the surface. Figure 4.17 shows some of the areas on the surface which were not covered by spin-coated GNP. Mean surface roughness was measured to be 12 ± 1 nm, which is almost similar to the surface roughness of interlayer. The comparison of the mean size of the GNP islands, the percentage of coverage and surface roughness is summarized and tabulated in Table 4.2.
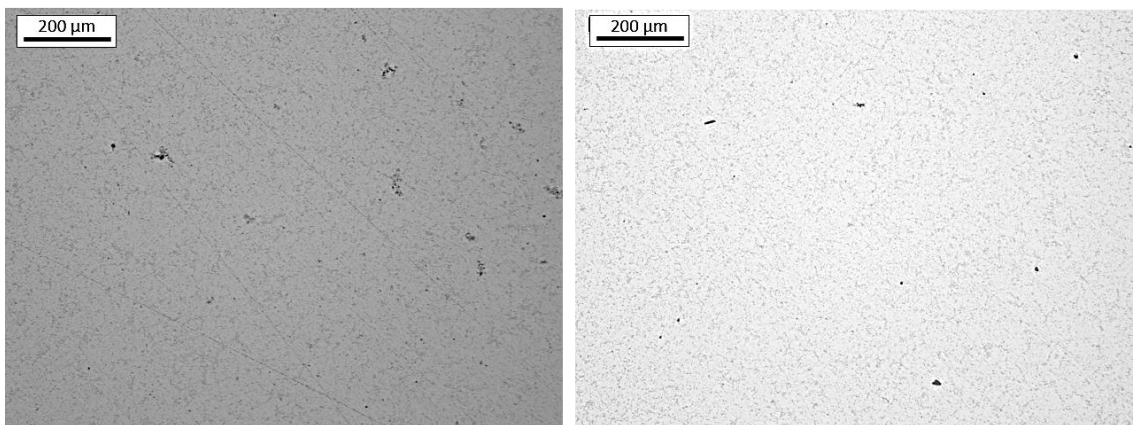
Figure 4.17 Optical micrographs of GNP/NMP sonicated for ten hours that has small amounts of GNP on the surface.

Table 4.2 Summary of the size, coverage area and surface roughness of spin-coated GNP/NMP as a function of time

Sonication time (hr)	Size of GNP island (μm^2)	Coverage area (%)	Surface roughness (nm)
1	179.24 ± 76.23	6.60 ± 0.71	104.3 ± 31.8
2	99.28 ± 37.39	5.11 ± 1.42	45.2 ± 10.4
3	74.96 ± 12.73	3.87 ± 0.95	59.4 ± 25.5
4	83.31 ± 37.45	4.24 ± 0.76	45.0 ± 7.7
5	75.05 ± 13.02	3.62 ± 0.52	37.0 ± 3.7
6	42.92 ± 3.41	2.68 ± 0.83	29.5 ± 3.5
10	Mean value cannot be measured due to poor coverage	Mean value cannot be measured due to poor coverage	12.6 ± 0.7

4.4.4 Raman analysis of spin-coated GNP

Raman analysis was conducted using a 488 nm laser in ambient conditions. The spectra was obtained using single spot analysis. Raman analysis was employed to investigate any changes in the chemical structure of GNP due to the usage of different type of solvent and sonication time. In this work, two regions were taken into consideration which is dark and bright areas as can be seen in Figure 4.6.

Figure 4.18 - Figure 4.20 shows typical Raman spectra obtained from samples deposited with GNP/DMF, GNP/ethanol and GNP/NMP respectively sonicated for one to six hours. Samples GNP/DMF, GNP/ethanol and GNP/NMP were composed of a mixture of both dark and bright areas. Therefore, Raman spectra of all samples was divided into two different areas which have dark and bright areas to observe the difference. Generally, all spectra show a noticeable G-peak (centred approximately at 1580 cm^{-1}), very small or almost unnoticeable D-peak (centred approximately at 1361 cm^{-1}), and a broad 2D-peak (centred approximately at 2740 cm^{-1}). These features are the three prominent Raman peaks of multi-layered graphene reported in many works [165, 166]. The G-peak position remains almost the same (~1580 cm^{-1}) in

Raman spectra, for all GNP dispersion types and sonication times. Low intensity and the subtle existence of D-peak in all samples indicate the absence of a disorder in sp^2-hybridized carbon system [167].There is a definite difference between the intensities of peaks in bright and dark areas for GNP in all solvents especially for sample GNP/DMF and GNP/ethanol.

Figure 4.21 plots the evolution of intensity ratios of 2D and G-peaks with sonication time for dark and bright area in all type of solvents. From the graph, it can be seen that almost no significant differences can be observed from all measured I_G/I_{2D} ratios. The measured I_G/I_{2D} ratios lie between 1.8 to 2.6 which is near to the value of five layers graphene reported elsewhere using 488 laser beam [166].
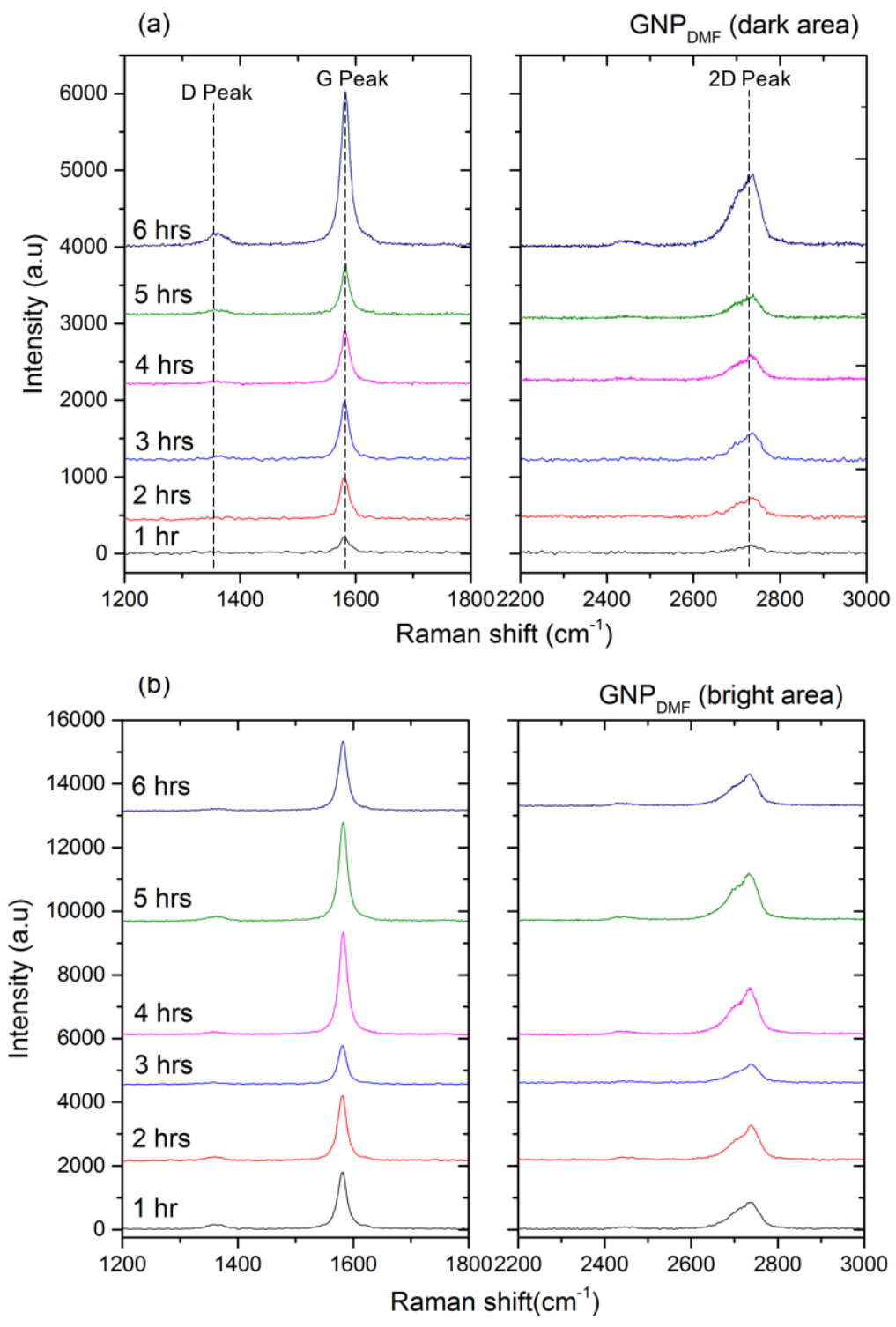
Figure 4.18 Raman spectra of GNP deposited with GNP suspension sonicated for one to six hours in DMF solvent. (a) dark area and (b) bright area
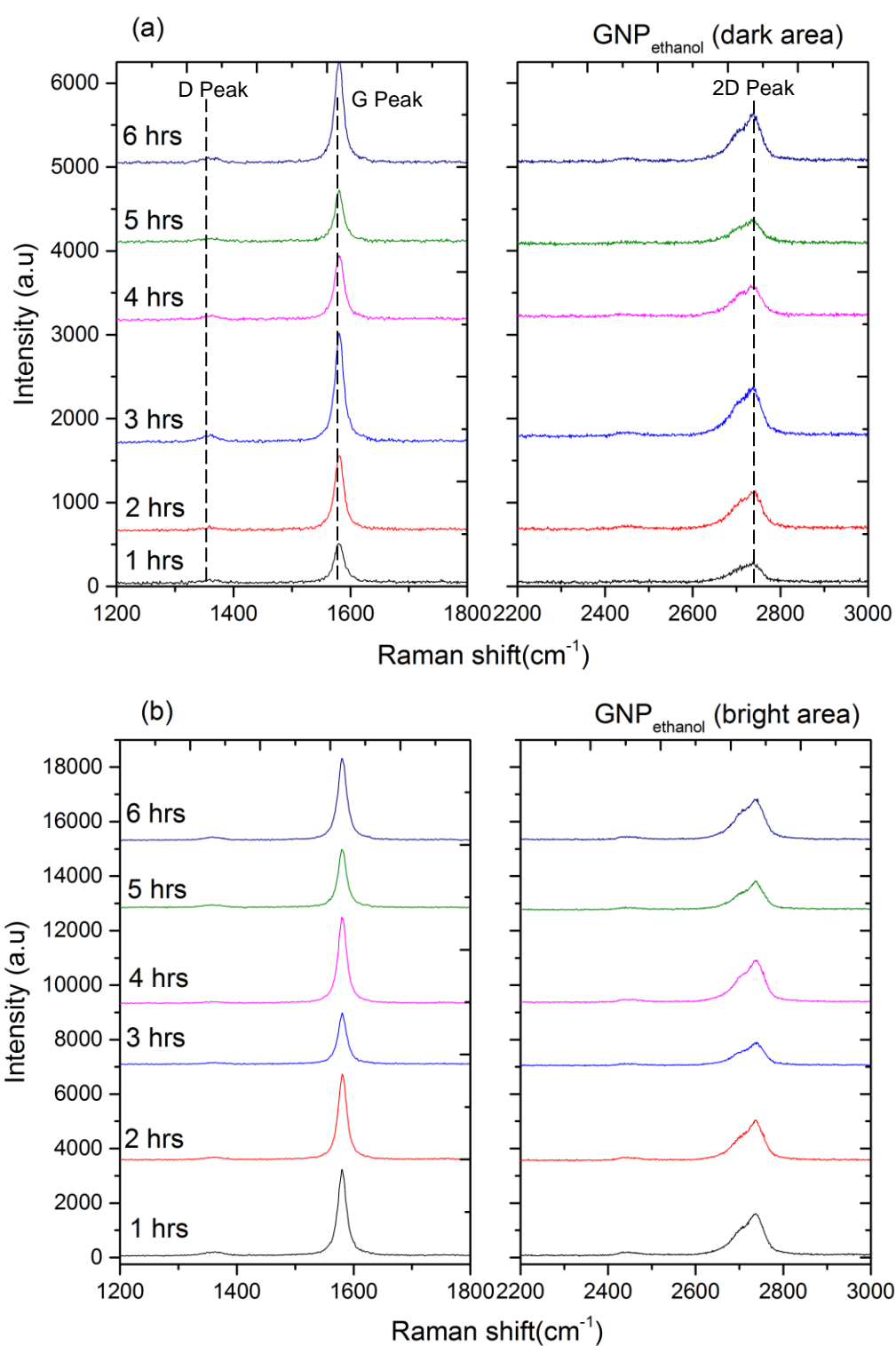
Figure 4.19 Raman spectra of GNP deposited with GNP suspension sonicated for one to six hours in ethanol solvent. (a) dark area and (b) bright area
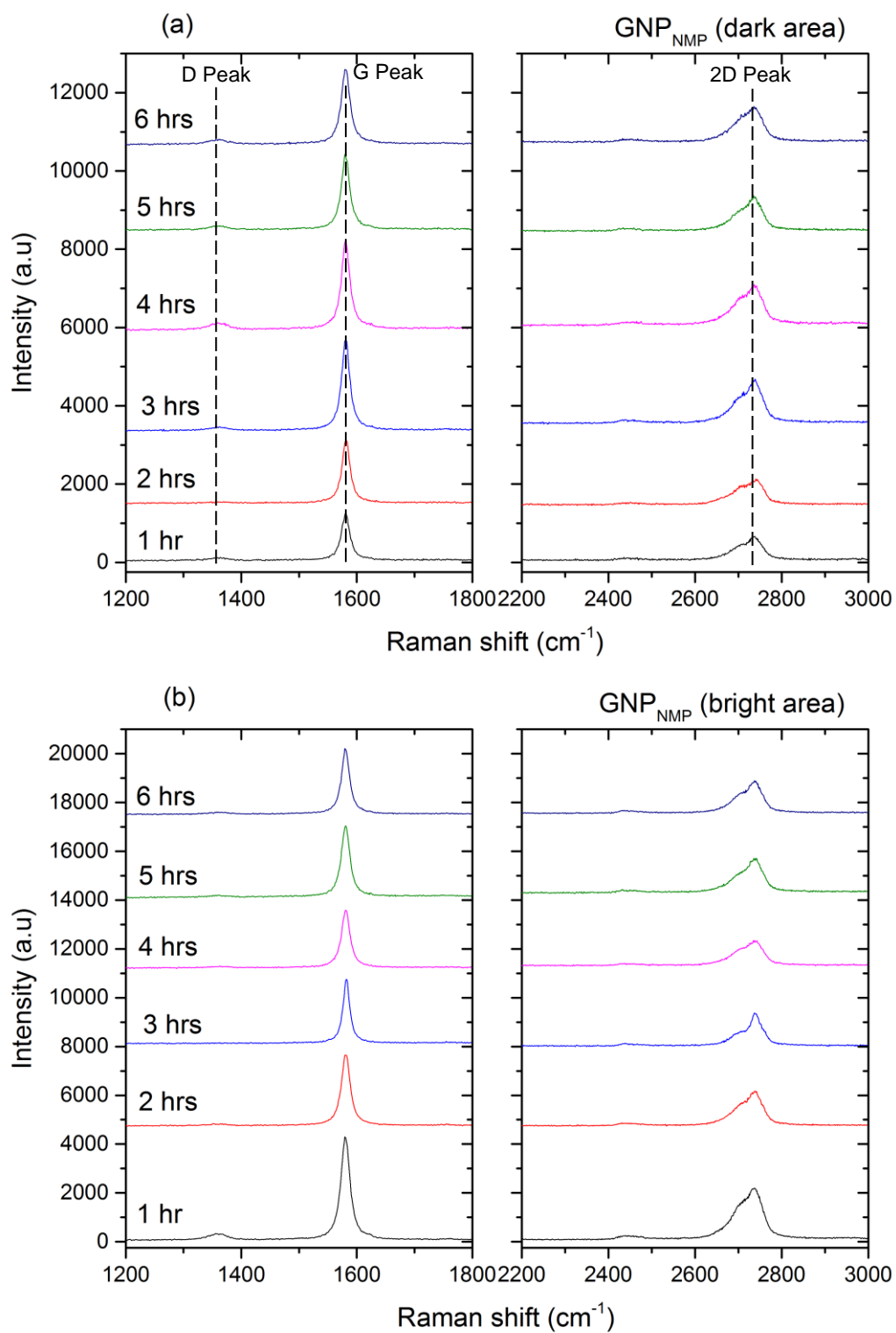
Figure 4.20 Raman spectra of GNP deposited with GNP suspension sonicated for one to six hours in NMP solvent. (a) dark area and (b) bright area
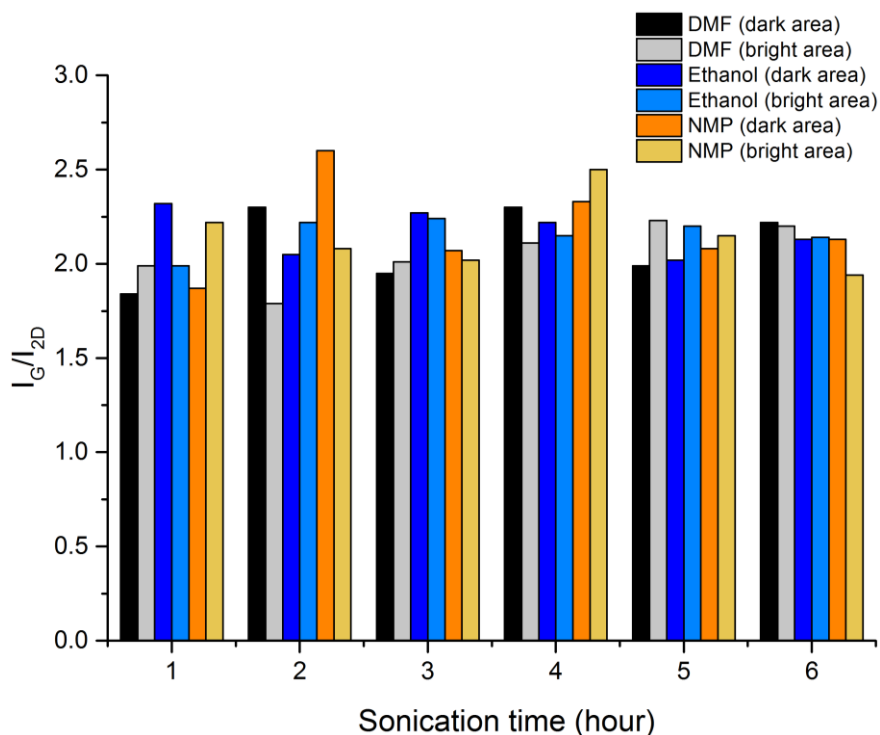
Figure 4.21 I_G/I_{2D} ratio of GNP suspensions in solvents of DMF, ethanol and NMP at both dark and bright areas

4.4.5 Summary of GNP deposition using a spin coating method

In this section, the stability of GNP suspensions was investigated as the function of solvent type and sonication time. The following summary can be obtained from the results:

i.   Sonication successfully suppresses the reaggregation of GNP during drying process on the substrate.

ii. GNP/NMP produced spin-coated-GNP with the lowest surface roughness and size of GNP islands compared to others.

iii. The stability of suspension contributes to the distribution of spin-coated GNP.

iv. There are almost no changes of I_D/I_G ratio over sonication time for the type of solvents. This indicates that sonication time does not influence the number of layers for GNP in all three solvents but does affect the size of GNP islands.

v.   Extending the sonication time to ten hours produced smaller sizes of GNP islands with inferior distribution all over the surface.

4.5   Optimisation of Spin Coating Process using Taguchi Method

4.5.1   Characterisation of graphene coating

In this work, optimisation of the spin coating process was carried out. NMP was used as a solvent for GNP suspension for the whole experiment. There are three factors that were studied to define the characteristics of spin-coated GNP. The three factors are spinning speed (A), spinning time (B) and volume of GNP suspension (C).

Micrographs of GNP distribution on substrates for all experiments 1 to 9 (Refer Table 4.3) are shown in Figure 4.22. Measurement of graphene distribution percentage was carried out using ImageJ software on two samples with each experimental condition. WLI was utilized for surface roughness measurement on each sample. GNP distribution in samples no. 1, 2 and 3 (Figure 4.22 (a, b and c)) was poor due to the low spinning speed of the spin coating that yielded substandard distribution of GNP. The spinning speed at 500 rpm may not be suitable for high viscosity solvents like NMP. The next section reveals the effect of spinning speed, time and amount of graphene on graphene distribution and surface roughness of coating using the Taguchi method of statistical analysis.
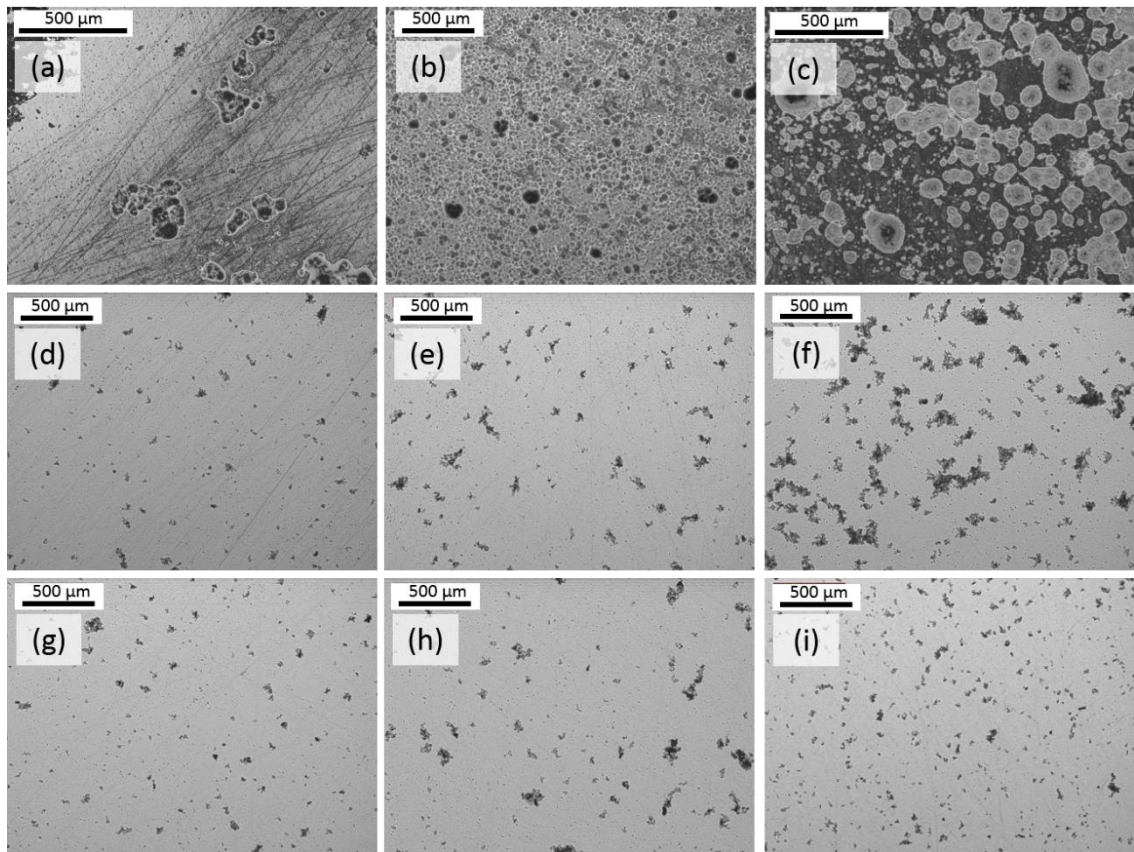
Figure 4.22 Optical images of spin-coated GNP on a substrate using different parameters as in Table 4.3.

4.5.2 Optimisation based on GNP distribution on the substrate

Five different images were captured by optical microscopy on one sample as in Figure 4.22. Graphene distribution with a quality metric of 'the bigger the better', was considered for computing the S/N ratio of graphene distribution. S/N ratio was calculated for each experiment using Eq. 3.2.

Mean values of the graphene distribution, standard deviation and the associated S/N ratios are presented in Table 4.3. A, B and C represent parameters of spinning speed, time and amount of GNP suspension as mentioned previously. Spinning speed, time and amount of GNP suspension of level 1, 2, 3 are 500, 1000 and 1500 rpm; 10, 20 and 30 seconds; and 0.25, 0.50 and 1.00 mL respectively. The first five columns show the process parameters for each experiment given by the Taguchi Design of Experiment matrix. The last three columns are the measured mean, standard deviation and S/N ratio from all the experiments. Details of experimental results and

calculation are shown in Appendix E1. No results were recorded for spinning speed of 500 rpm as the distributions were poor on all samples. The observation after spin coating showed that graphene clumped at certain areas and was not distributed over the whole surface of substrates.

Table 4.3 Taguchi Matrix, measured values of the graphene distribution and the corresponding S/N ratios

Exp No	Parameters and levels				Graphene distribution (%)		
	A	B	C		Mean	Std. Deviation	S/N ratio
1	1	1	1	$A_1B_1C_1$	NA	NA	NA
2	1	2	2	$A_1B_2C_2$	NA	NA	NA
3	1	3	3	$A_1B_3C_3$	NA	NA	NA
4	2	1	3	$A_2B_1C_3$	8.80	2.07	18.16
5	2	2	1	$A_2B_2C_1$	6.35	1.86	14.44
6	2	3	2	$A_2B_3C_2$	12.25	3.63	20.00
7	3	1	2	$A_3B_1C_2$	6.23	0.99	15.59
8	3	2	3	$A_3B_2C_3$	6.28	1.25	15.59
9	3	3	1	$A_3B_3C_1$	8.13	2.09	17.25
Mean					8.01		16.84

The mean S/N value for each level of 1, 2 and 3 within the parameters is shown in Table 4.4. Delta values were measured from the largest mean S/N subtracted from the lowest mean S/N of each parameter in the table. Ranks are based on the delta values; 1 is the highest delta and so on. The rank indicates the relative effect of each factor on the response. Raw data of S/N response for graphene distribution can be obtained in Appendix E1. S/N data obtained in Table 4.4 are plotted in Figure 4.23. It can be seen from both Table 4.4 and Figure 4.23 that spinning time has the most substantial effect on the graphene distribution, followed by the amount of solution and spinning speed. The optimal factor levels to achieve the highest graphene distribution are A_2, B_3 and

C_2 as can be seen by their larger S/N values in comparison to the other conditions.

Table 4.4 S/N responses for graphene distribution, optimal parameters and the rank of most influence factor.

Mean S/N ratio (dB)	Parameter		
	A	B	C
S/Ni_1	N/A	16.88	15.84
S/Ni_2	**17.53**	15.01	**17.79**
S/Ni_3	16.14	**18.62**	16.88
Optimal parameter	**A$_2$**	**B$_3$**	**C$_2$**
Delta	1.39	3.61	1.95
Rank	3	1	2
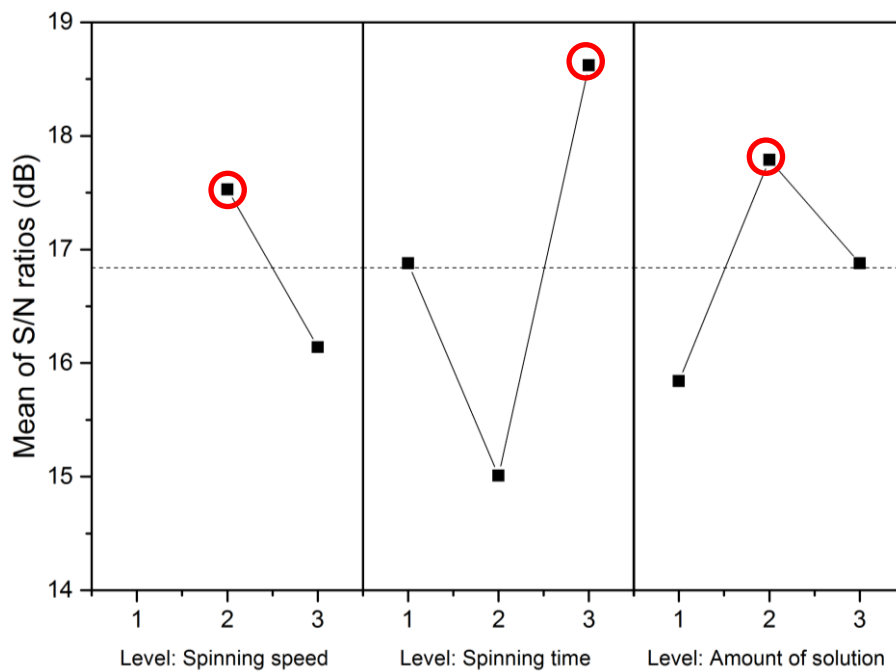
Figure 4.23 The means of the S/N ratios graphs on the effect of spin coating parameters on GNP distribution

Mean responses of GNP distribution for each parameter level, optimum parameter and the rank of most influential factors were tabulated in Table 4.5. The ranks are the same as has been measured by the response for S/N

(spinning time, spinning speed and amount of graphene). The mean values of graphene distribution are plotted in Figure 4.24. The optimal parameters for graphene distribution based on mean values are A_2, B_3 and C_2. This level of parameters agreed on the one obtained from the S/N response in Table 4.4 and Figure 4.23.

Spinning time was the most significant effect of all the factors. GNP distribution was slightly reduced when the time was raised to 20 seconds but increased drastically when the time was 30 seconds. With the exception of the spinning speed of 500 rpm, GNP distribution was decreased with spinning speed.

Acceleration of spinning speed improved the distribution of GNP of the surface but at the same time removed most of the GNP from the surface. Meanwhile, a spinning speed of 500 rpm might be too low to be used for high viscosity NMP solvent. Massive amounts of redundant GNP suspension was left on the surface after spin coating at 500 rpm. Due to slow evaporation of NMP, most of the GNP on the surface has ample time to agglomerate while leaving certain large areas without any suspension and creating clumps of GNP. This can be seen in Figure 4.22 (a-c). Therefore, measurement of the GNP distribution was not carried out on these samples.

Table 4.5 Mean responses for GNP distribution, optimal parameters and the rank of most influence factor.

Mean GNP distribution (%)	Parameter		
	A	B	C
Yi_1	N/A	7.51	7.24
Yi_2	9.13	6.31	9.24
Yi_3	6.88	10.19	7.54
Optimal parameter	**A2**	**B3**	**C2**
Delta	2.28	3.88	2.00
Rank	2	1	3
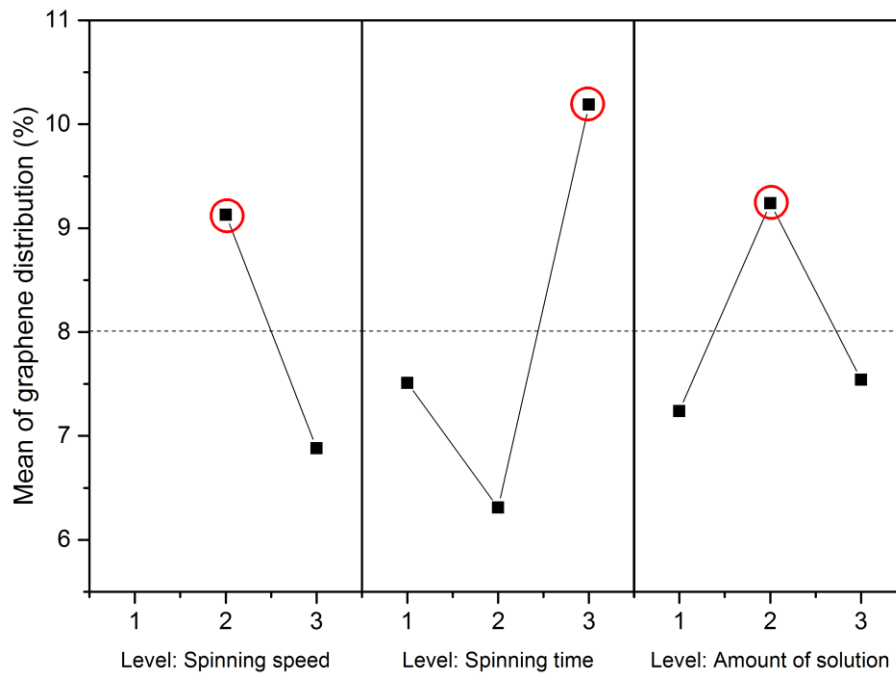
Figure 4.24 The means of the S/N ratios graphs on the effect of spin coating parameters on GNP distribution

4.5.3 Optimisation based on the surface roughness of spin-coated GNP

WLI was utilised to measure the surface roughness of spin-coated GNP. Graphene distribution with a quality metric of 'the smaller the better' was considered for computing the S/N ratio to minimize the surface roughness. The surface roughness measurement of all samples was carried out using White Light Interferometry (WLI). S/N ratio is defined by Eq. 3.1 in Chapter 3. Detail of experimental results including the S/N ratio for factor at each level is tabulated in Appendix G. Mean values of the graphene distribution, standard deviation and the associated S/N ratios are summarized in Table 4.6. S/N response to each level of a parameter for surface roughness is shown in Table 4.7.

Figure 4.25 shows the mean values of S/N ratios for each factor at levels from 1 to 3. Based on the graphs in Figure 4.25, the most influential factor of the experiment is spinning speed followed by the amount of solution and finally spinning time. This has also been calculated as delta in Table 4.7. Rank indicated in the table is the rank of most influential factor. The optimal factors to achieve the lowest surface roughness based on S/N ratios are A_2, B_1 and C_3

(A_2: 1000 rpm of spinning speed; B_1: 10 seconds of spinning time; C_3: 1.0 mL graphene solution). This experimental condition is the same as the condition in experiment no. 4 in Table 4.6. Raw data of S/N response for surface roughness can be obtained in Appendix E2.

Table 4.6 Measured values of the surface roughness and the corresponding S/N ratios

Exp No	Parameters and levels				Surface roughness (nm)		
	A	B	C		Mean	Std. Deviation	S/N ratio
1	1	1	1	$A_1B_1C_1$	105.1	68.2	-41.69
2	1	2	2	$A_1B_2C_2$	231.0	143.1	-48.44
3	1	3	3	$A_1B_3C_3$	40.9	20.3	-33.02
4	2	1	3	$A_2B_1C_3$	20.4	3.3	-26.26
5	2	2	1	$A_2B_2C_1$	23.1	4.2	-27.38
6	2	3	2	$A_2B_3C_2$	56.0	16.5	-35.25
7	3	1	2	$A_3B_1C_2$	26.1	9.9	-28.81
8	3	2	3	$A_3B_2C_3$	38.5	6.7	-31.81
9	3	3	1	$A_3B_3C_1$	50.7	13.6	-34.34
Mean							-34.11

Table 4.7 S/N responses for surface roughness, optimal parameters and the rank of most influence factor

Mean S/N ratio (dB)	Parameter		
	A	B	C
S/Ni_1	-41.05	**-32.25**	-34.47
S/Ni_2	**-29.63**	-35.88	-37.50
S/Ni_3	-31.66	-34.21	**-30.37**
Optimal parameter	**A_2**	**B_1**	**C_3**
Delta	11.42	3.63	7.13
Rank	1	3	2
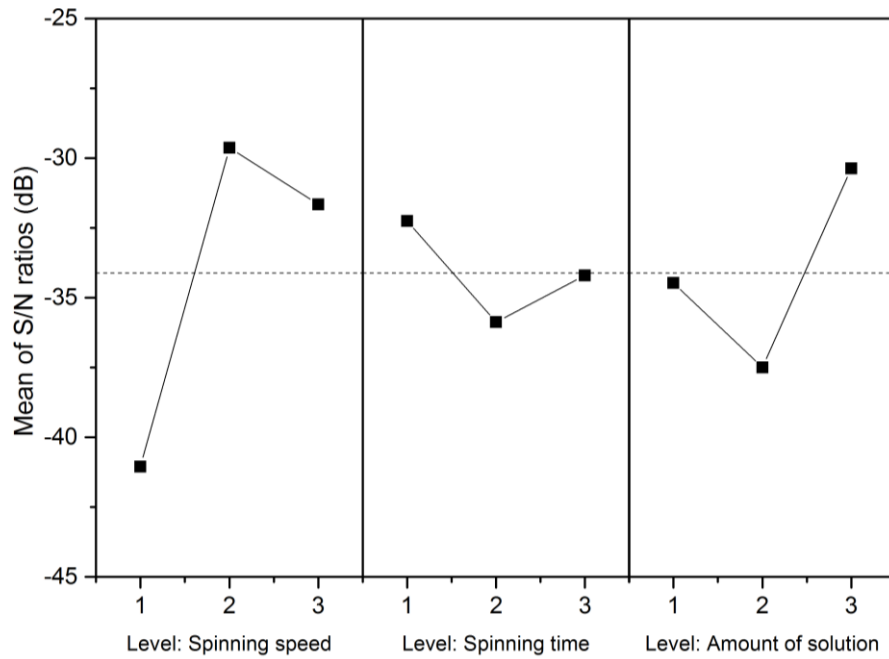
Figure 4.25 Main effects plot for S/N ratios (Surface roughness)

Table 4.8 presents calculated mean responses of each level of parameter for surface roughness. Surface roughness reduced significantly as the spinning speed was increased from 500 to 1000 rpm before slightly increasing at 1500 rpm. There is also the non-linear relationship between surface roughness and spinning time. Surface roughness increase as spinning time increases from 10 to 20 seconds and finally reduced when the duration was increased to 30 seconds.

Table 4.8 The mean responses for surface roughness, optimal parameters and the rank of the most influential factor

Mean Surface Roughness	Parameter		
	A	B	C
Yi_1	126	51	60
Yi_2	**33**	98	104
Yi_3	38	**49**	**33**
Optimal parameter	**A₂**	**B₃**	**C₃**
Delta	93	49	71
Rank	1	3	2
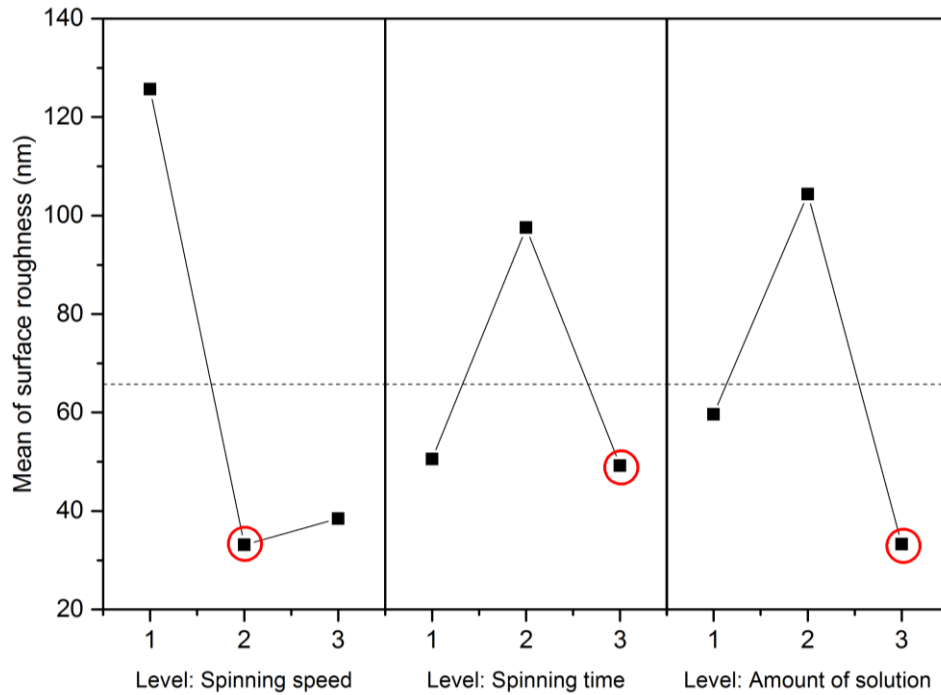
Figure 4.26 Main effects plot for mean values (Surface roughness)

Table 4.9 shows the experimental results of GNP distribution and surface roughness obtained from the optimum parametric combination of the highest GNP distribution of $A_2B_3C_2$ and the lowest surface roughness of $A_2B_1C_3$. The most influential factor for GNP distribution is spinning time while spinning speed is the factor that affects surface roughness most.

Table 4.9 Results of the optimum parametric combination based on Taguchi method

	Optimum GNP distribution	Optimum surface roughness
Combination	$A_2B_3C_2$	$A_2B_3C_3$
Most influence factor	Spinning time	Spinning speed

116

4.5.4 Summary of optimisation of spin coating process using Taguchi method

The process of optimisation was conducted and a Taguchi L_9 (3^3) orthogonal array was used to investigate the overall effects of spin coating parameters (spinning speed and time, and amount of graphene solution deposited on the substrate) on graphene distribution and surface roughness. The results of the work can be summarized as follows:

i. Spinning time is the factor that influences the GNP distribution (%) most while spinning speed is the dominant parameter that influences surface roughness.

ii. The method allowed understanding of the parameters that can be controlled in order to achieve a low surface roughness of spin-coated GNP.

iii. The highest GNP coverage percentage can be obtained by adopting a combination of $A_2B_3C_2$ (Spinning speed = 1000rpm; spinning duration = 30 minutes; and volume of graphene = 0.50 mL) and the lowest surface roughness by adopting $A_2B_3C_3$ (Spinning speed = 1000 rpm; spinning duration = 30 minutes; and colume of graphene = 1.0 mL).

Chapter 5

Results: Single-layer of DLC-GNP Nanocomposite Coating

5.1   Introduction

This chapter presents the experimental work carried out in the preparation of a single layer of DLC-GNP nanocomposite coating using a spin coating and PECVD methods. The pilot test of the work is presented followed by the effect of deposition time, post-treatment, and GNP concentration. Each section reports the physical, mechanical and tribological properties of the coating.

Section 5.2 introduces the aim of this section. The main part of this results chapter was divided into four sections as shown in Figure 5.1. Figure 5.1 summarises the topic, the test parameters and the findings of each section. The next section reports the pilot test carried out to study the recipe of the DLC film and its structure. Additionally, there was an initial study to investigate the DLC coating using previous recipe and deposition of DLC on the spin-coated GNP. Section 5.4 describes the effect of deposition time of DLC using PECVD, on the final products of the DLC-GNP nanocomposite coating. Section 5.5 considers post-treatment effects of spin-coated GNP on the characteristics of the DLC-GNP nanocomposite coating. Finally, Section 5.6 presents the effect of GNP concentration on the characteristics of the DLC-GNP coating. The last section summarises the outcomes obtained in this chapter.
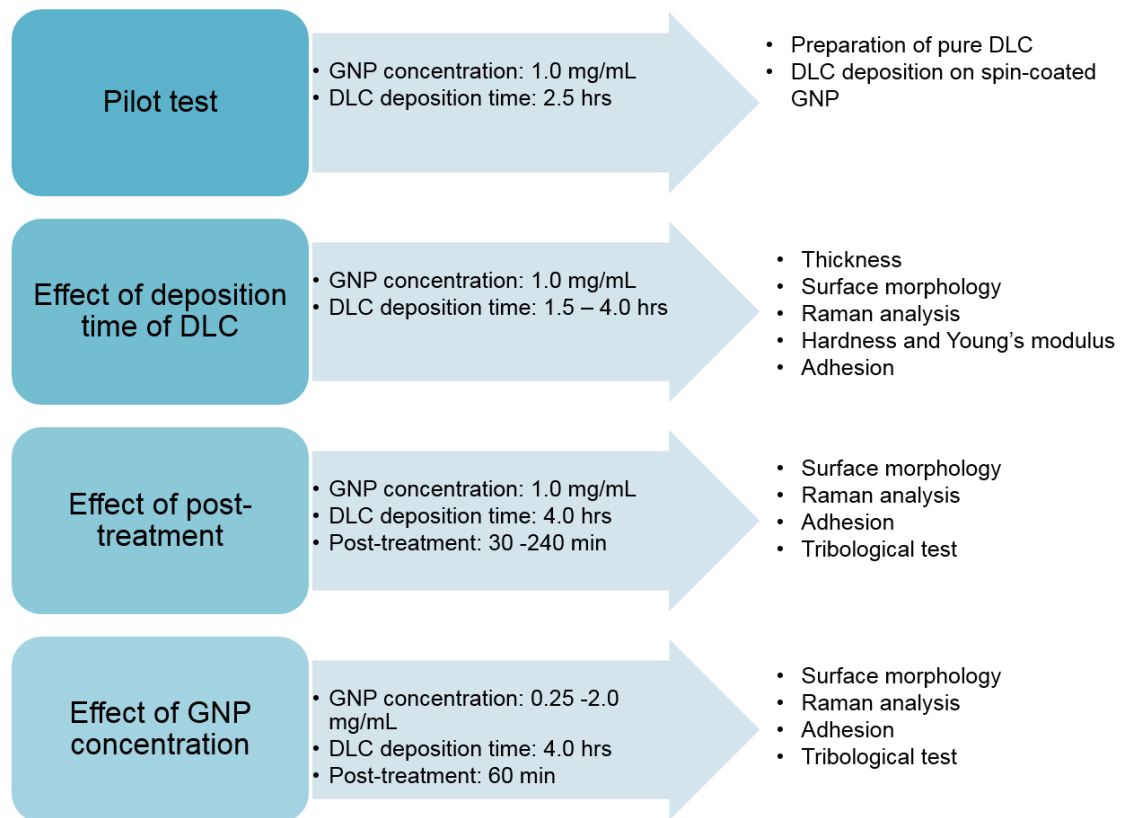
Figure 5.1 The experimental procedures in Chapter 5

5.2 Aim

The main aim of this chapter is to prepare and characterize single layer DLC-GNP nanocomposite coating. The objectives of this chapter are as follows:

i. To prepare single layer DLC-GNP nanocomposite coatings using spin coating methods for GNP and DLC deposition using PECVD.

ii. To investigate the effect of DLC deposition time on the nanocomposite coating (physical and mechanical properties).

iii. To study the influence of post-treatment of GNP in improving the physical and mechanical characteristics, as well as its tribological behaviour.

iv. To examine the effect of GNP concentration on its physical, mechanical and tribological properties.

5.3   Pilot Test

5.3.1   Preparation of pure DLC using PECVD

This section investigates the morphology and cross-section of pure DLC using one of the common recipes that have been produced previously using the PECVD Flexicoat 850 system (Hauzer Techno Coating, the Netherlands) in the Advanced Coating Design Laboratory in School of Mechanical Engineering, University of Leeds. The details of the deposition recipe for the coating deposition is shown in Table 5.1. The process involves step process of heating the chamber to a temperature of 200°C, target cleaning, plasma etching, followed by deposition of Cr, Cr/WC, W-C:H and DLC film layer.

Table 5.1 Recipe for DLC film deposition using PECVD

Step	Time (min)	Gas flow (sccm)		Bias (V)	Coil Current (A)	Cr Cathode (kW)	WC Cathode (kW)
		Ar	C_2H_2				
Heating 200°C	90	-	-	-	-	-	-
Target Clean	120	130	-	-500	1-4	1-6	1-3
Plasma etch	45	50	-	-200	-	-	-
Cr	40	130	-	-	4	3	-
Cr/WC	50	110	-		4	3-0.5	0.5-3
W-C:H	90	90	8-30		2	-	3
DLC	270	-	340	-740	4	-	-

The cross-section of the coating was investigated by SEM. Figure 5.2 depicts the cross-section of the interlayer and DLC film. The four layers in the coating that can be observed in the micrograph. Layers are labels as 1, 2, 3 and 4 from top to bottom. Layer number 2, 3 and 4 have columnar grain while the black layer at layer 1 shows a dense and featureless layer.

EDX scan mapping was carried out to identify the elemental composition of the coating is shown in Figure 5.3. Elements that exist in the cross section are C, Cr, W and Fe. Only C can be seen at the top most layer as it is the DLC layer.

Based on both mapping and line scans, elements of W, Cr/W and Cr are rich at each of layer 2, 3 and 4 respectively. The layer after layer 4 is the M2 HSS substrate which explains the existence of Fe elements in the analysis at that particular area. H also exist in the coating since the PECVD deposition used acetylene gas and therefore produces hydrogenated carbon in the DLC.
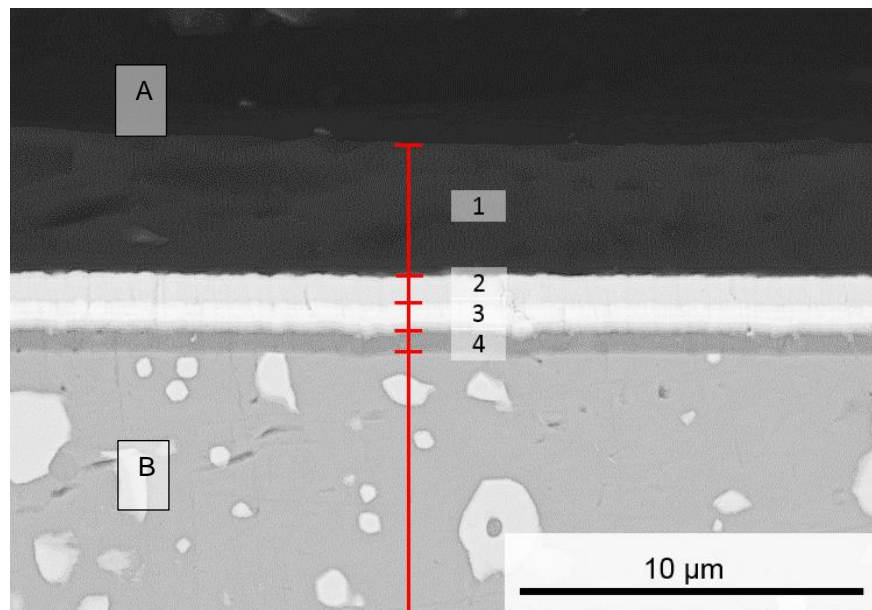
Figure 5.2 SEM micrograph of a cross-section of DLC coating

The thickness measured from SEM observation for all layers are listed in Table 5.2. The thickness of the adhesion layer of Cr-Cr/WC is measured to be about 2.31 µm, while DLC film thickness is approximately 4.10 µm. Regarding application, several works suggest that increase of DLC thickness may also improve the mechanical and tribological properties [168, 169]. This coating thickness can be considered as quite thick and not economical for a real application in industry. It is important to keep coating thickness low while maintaining its functional properties. Most of the reported works on DLC coating have a thickness of less than 2.0 µm [69, 168, 170-172].
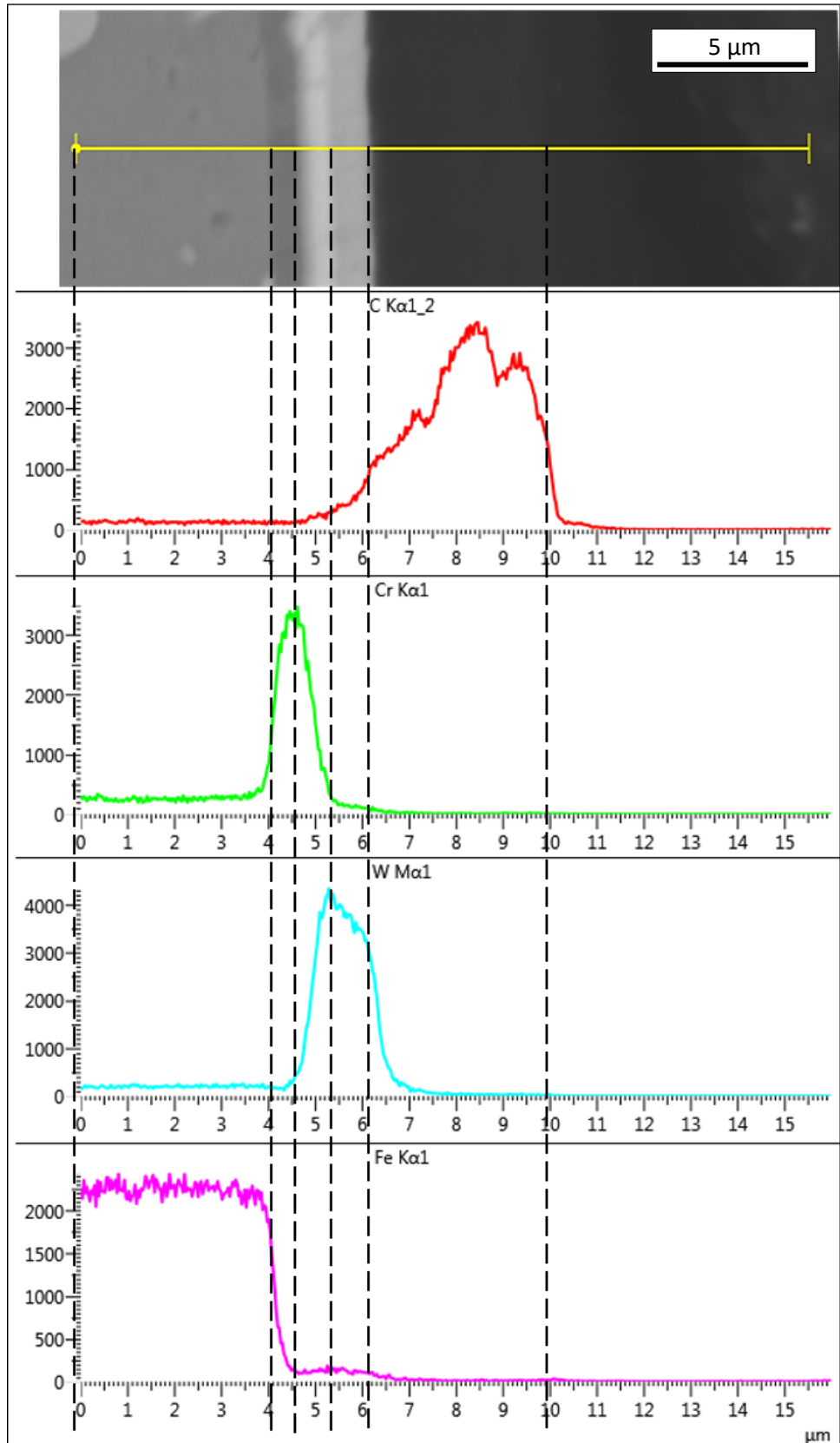
Figure 5.3 EDX scan mapping for the cross-section of DLC-graphene nanocomposite coating

Table 5.2 Measured thickness of each layer of DLC-GNP nanocomposite coating

Layer	Rich Element	Thickness (µm)
1	C	4.07 ± 0.15
2	W:C:H	0.84 ± 0.12
3	Cr/WC	0.80 ± 0.02
4	Cr	0.67 ± 0.05

Figure 5.4 shows the surface morphology of the DLC film. As can be seen, DLC film has nodular surface morphology which is also a typical morphology of hydrogenated DLC reported by many other works [173, 174].

LEMAS 5.0kV 16.0mm x10.0k SE(UL)   5.00µm
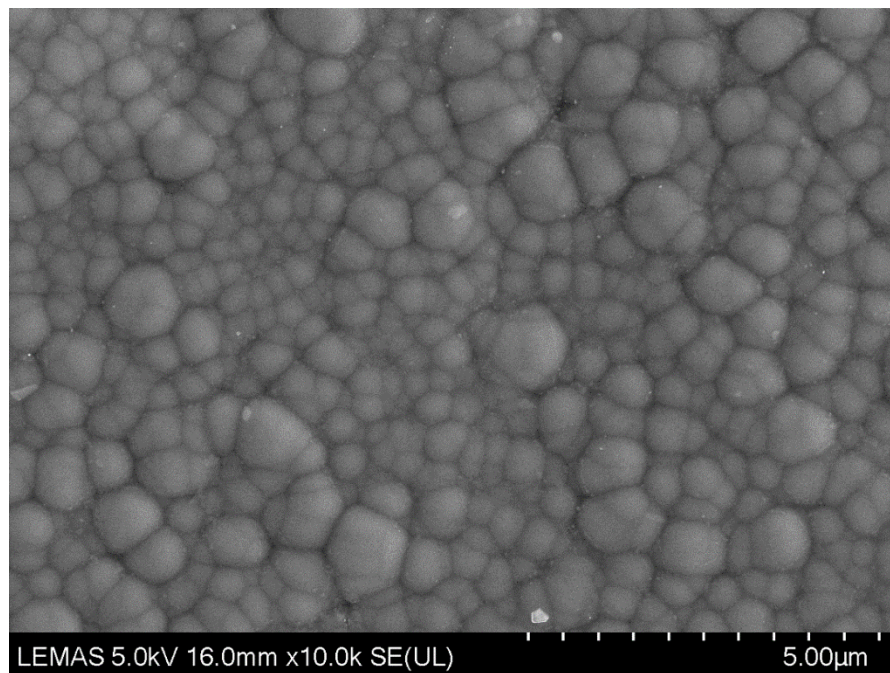
Figure 5.4 Surface morphology of DLC coating

5.3.2 DLC deposition on spin-coated GNP

5.3.2.1 Preparation of DLC deposition using PECVD

For this section, a different DLC recipe was used in an attempt to reduce the thickness of the interlayer and DLC film. Since the new design of DLC-GNP nanocomposite coating requires deposition of spin-coated GNP before DLC

film, the interlayer and DLC film need to be separated into two individual recipes. The recipe for the interlayer and DLC film is shown in Table 5.3. M2 HSS substrates were coated with interlayer prior to GNP deposition followed by DLC film deposition onto the spin-coated GNP. The recipe was the same used previously by Austin [69]. Austin has previously prepared amorphous hydrogenated DLC and silicon doped DLC using Hauzer Flexicoat 850 deposition system.

Table 5.3 Recipe for interlayer and DLC film deposition for the preparation of DLC-GNP using PECVD method

Layer	Step	Time (min)	Gas flow (sccm)		Bias (V)	Coil Current (A)	Cr Cathode (kW)	WC Cathode (kW)
			Ar	C_2H_2				
Interlayer	Heating	60	-	-	-	-	-	-
	Target cleaning	20	130	-	-500	1-4	1-6	1-3
	Plasma etch	45	50	-	-200	-	-	-
	Cr	25	130	-	-	4	3	-
	Cr/WC	30	110	-		4	3-0.5	0.5-3
	W-C:H	75	90	8-30		2	-	3
DLC film	Heating	90	-	-	-	-	-	-
	Plasma etch	30	50	-	-200	-	-	-
	DLC	150	-	270	-740	4	-	-

5.3.2.2 Coating characterisation

The surface morphology of spin-coated GNP and DLC-GNP was investigated using an optical microscope. Figure 5.5 shows the comparison between the surface morphology before and after DLC deposition. The existence of spin-coated GNP is still visible after DLC deposition as the black islands on the surface in Figure 5.5(b). The higher magnification of the micrographs can be observed in Figure 5.6 (a) and (b). The appearance of GNP islands after DLC deposition in Figure 5.6(b) seems to be looking more granular and spheroidal, while GNP islands before DLC deposition appear to be flakier (Figure 5.6(a)).

This may relate to the morphology of DLC in Figure 5.4 when globular DLC film grew on the spin-coated GNP.
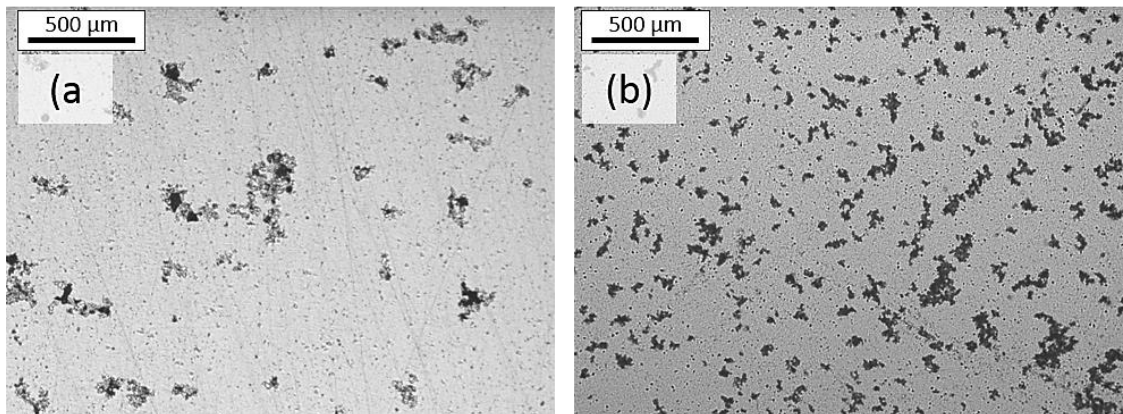
Figure 5.5 Surface morphology of (a) spin-coated GNP and (b) after DLC film deposition
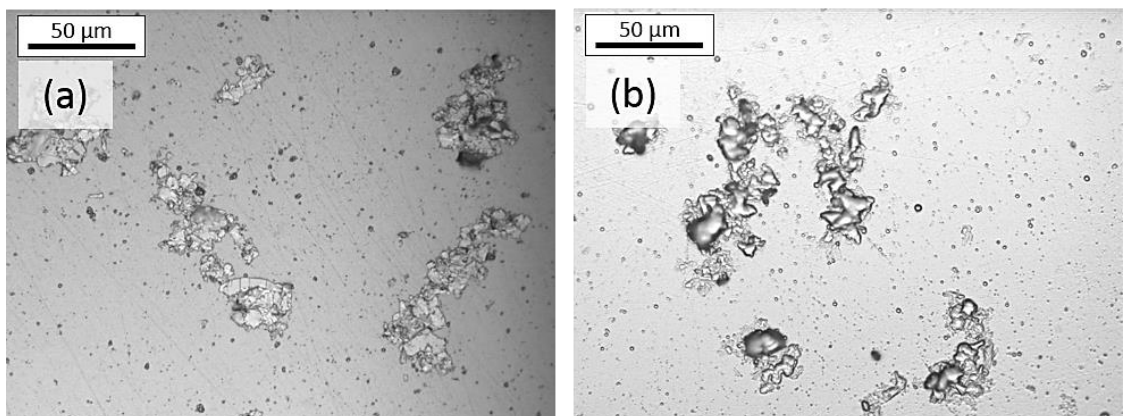
Figure 5.6 Surface morphology at higher magnification of (a) spin-coated GNP before DLC deposition and (b) after DLC deposition of the sample in Figure 5.5

The surface topography of spin-coated GNP and DLC-GNP nanocomposite coating was captured using WLI, and the surface roughness was analysed using Vision64 (control and analysis software for Bruker WLI) using Gaussian regression filter. Surface profile in Figure 5.7 reveals how the surface change from the interlayer, followed by deposition of GNP/NMP using spin coating method and after the deposition of DLC to produce DLC-GNP nanocomposite coating. The evolution of surface roughness can be noticeably seen after each of the deposition processes. The value of surface roughness of each surface was measured and presented in Figure 5.8. Surface roughness increased from around 30 nm to 89 nm after DLC deposition which is equivalent to more than

200% increase. It is therefore believed that the DLC film grew on the interlayer and encapsulate the GNP islands, thus creating a rougher surface.
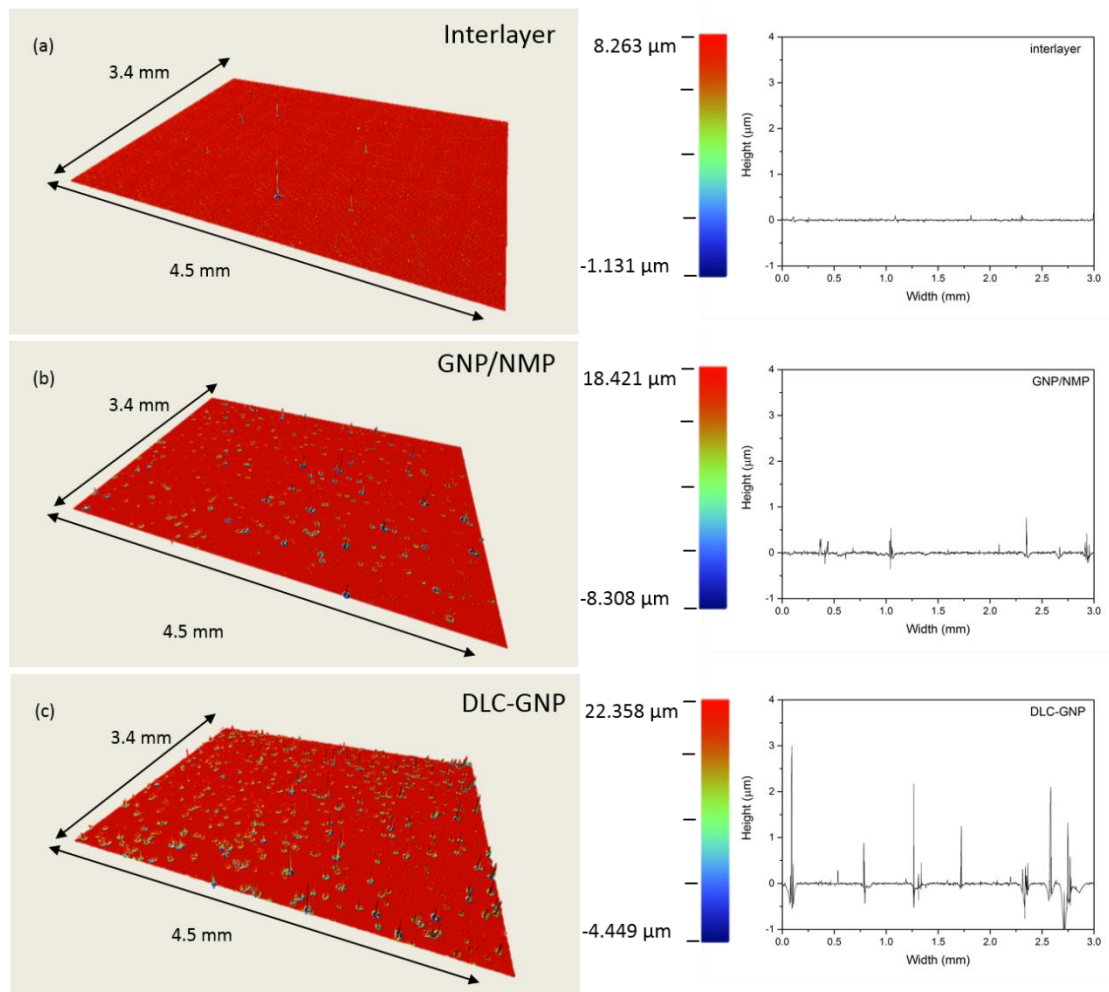
Figure 5.7 Surface topography and its corresponding surface profile of (a) interlayer, (b) before DLC deposition (spin-coated GNP/NMP) and (c) after DLC deposition (DLC-GNP)
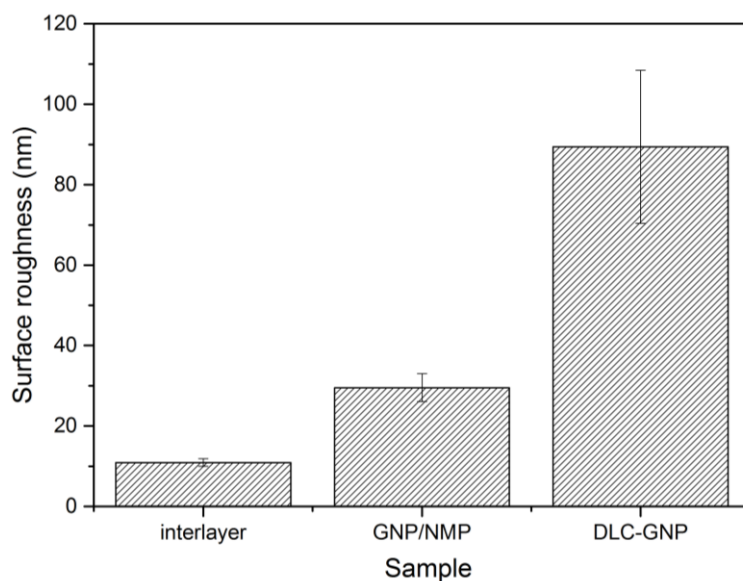
Figure 5.8 Surface roughness of interlayer, spin-coated GNP/NMP and DLC-GNP nanocomposite coating

5.3.2.3 Raman analysis

The Raman spectra of the coating were also investigated to study the chemical structure of the new DLC-GNP nanocomposite coating as compared to pure DLC coating. Comparison of Raman spectra of pure DLC, spin-coated GNP and DLC-GNP nanocomposite coating can be seen in Figure 5.9. The shape and position of the Raman spectra of DLC-GNP are similar to the pure DLC. No other peaks were observed beyond the scanned range. The position of D and G-peaks of GNP is in the same range as the pure DLC. In addition Full width half maximum (FWHD) of D and G-peaks of GNP is narrow compared to broad D and G-peaks of pure DLC. The D and G-peaks of GNP might be overlapping with pure DLC thus do not appear in the spectra.
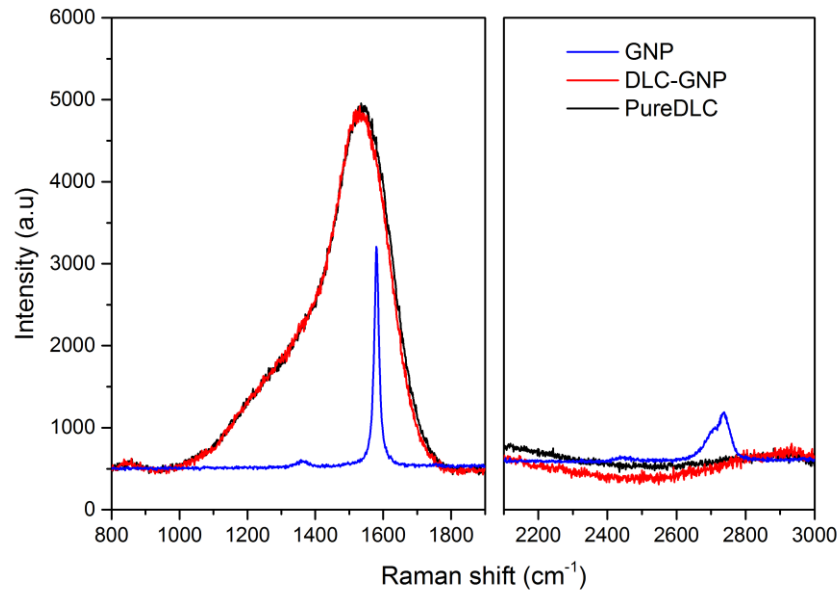
Figure 5.9 Comparison of Raman spectra of GNP, DLC-GNP nanocomposite and pure DLC coating

5.3.3 Summary of pilot test

Following are the summary of the results and outcomes obtained from the pilot test:

i.   DLC coating comprises of few layers of Cr-Cr/WC as interlayers and DLC film adhered atop.

ii.   DLC grew on the spin-coated GNP and the interlayer.

iii.   The surface roughness of DLC-GNP nanocomposite coating increases almost 200% compared to the surface roughness of spin-coated GNP.

iv.   The structure of DLC-GNP nanocomposite coating is similar to that of pure DLC coating.

5.4 Effect of Deposition Time of DLC on Characteristics of DLC-GNP Nanocomposite Coating

One of the most crucial features to be controlled to make a quality coating is surface roughness. From results in a pilot test in Section 5.3.2, the surface roughness of spin-coated GNP will influence the surface roughness of as-produced nanocomposite coating. Taking the results into consideration, a

128

combination of spin coating parameters that gives the lowest surface roughness was chosen. The combination of the spin coating process is $A_2B_3C_3$: spinning speed of 1000 rpm, spinning time of 30 seconds and GNP amount of 1.0 mL, is chosen as a parameter of spin coating in this section.

The deposition time of the DLC film coating has been varied from 1.5 to 4.0 hours. A deposition time of 1.5-2.5 hours is a standard deposition time used in previous work of Austin [69]. Deposition time was not further extended to maintain the thickness of the coating to be less than 2.0 µm. Pure DLC coatings deposited without any GNP were also prepared as a reference to the DLC-GNP nanocomposite coating. Pure DLC and DLC-GNP nanocomposite coating deposited with 1.5, 2.5 and 4.0 hours will be known as DLC1.5hr, DLC2.5hr, DLC4.0hr, DLC-GNP1.5hr, DLC-GNP2.5hr and DLC-GNP4.0hr onwards.

5.4.1 Thickness

Thickness was determined by step height method using WLI. The method of measurement using step height is explained in Chapter 3. Evolution of thickness over deposition time is plotted in Figure 5.10. Thickness increased from ~ 0.6 to 1.7 µm as deposition time increased for both pure DLC and DLC-GNP nanocomposite coating. The relationship between thickness and DLC deposition time is almost linear for DLC-GNP nanocomposite coating. No significant difference can be observed in any of the deposition time. This indicates that the existence of GNP on did not alter the deposition rate of DLC film on the surface.
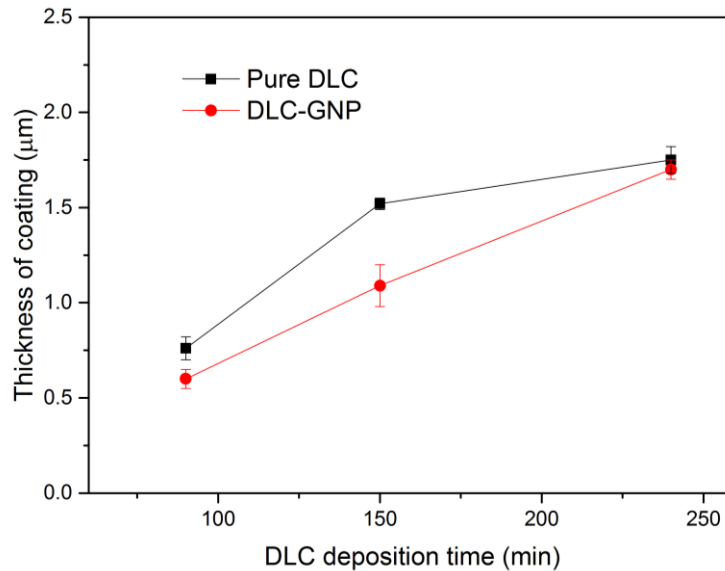
Figure 5.10 Thickness of coating as a function of DLC deposition time. The error bars in the graph indicate standard deviation for three measurements

5.4.2 Surface topography and surface roughness

Surface topography and surface profile of coatings were evaluated using WLI. The surface roughness values of all samples were then analysed using the Vision64 software and are shown in Figure 5.11. As can be seen, more peaks can be observed as the surface becomes rougher with DLC deposition time.

Figure 5.12 presents the measured surface roughness of pure DLC and DLC-GNP nanocomposite coating as a function of the deposition time. Although no significant change of thickness was found for deposition time 1.5 and 2.5 hours, surface roughness for both types of coating increased as deposition time increased. The surface roughness of pure DLC and DLC-GNP nanocomposite coating ranged between ~13 to18 nm and ~76 to 235 nm respectively. The highest surface roughness of pure DLC (DLC4) coating has an increment of approximately 38% compared to the surface roughness of DLC1.5. The increment of surface roughness from DLC-GNP1.5 to DLC-GNP2.5 and DLC-GNP2.5 to DLC-GNP4.0 is measured to be approximately 73% and 77% respectively. It is important to note that even at a higher thickness of 1.75 μm, the DLC film grown still has traces of the initial spin-coated GNP.
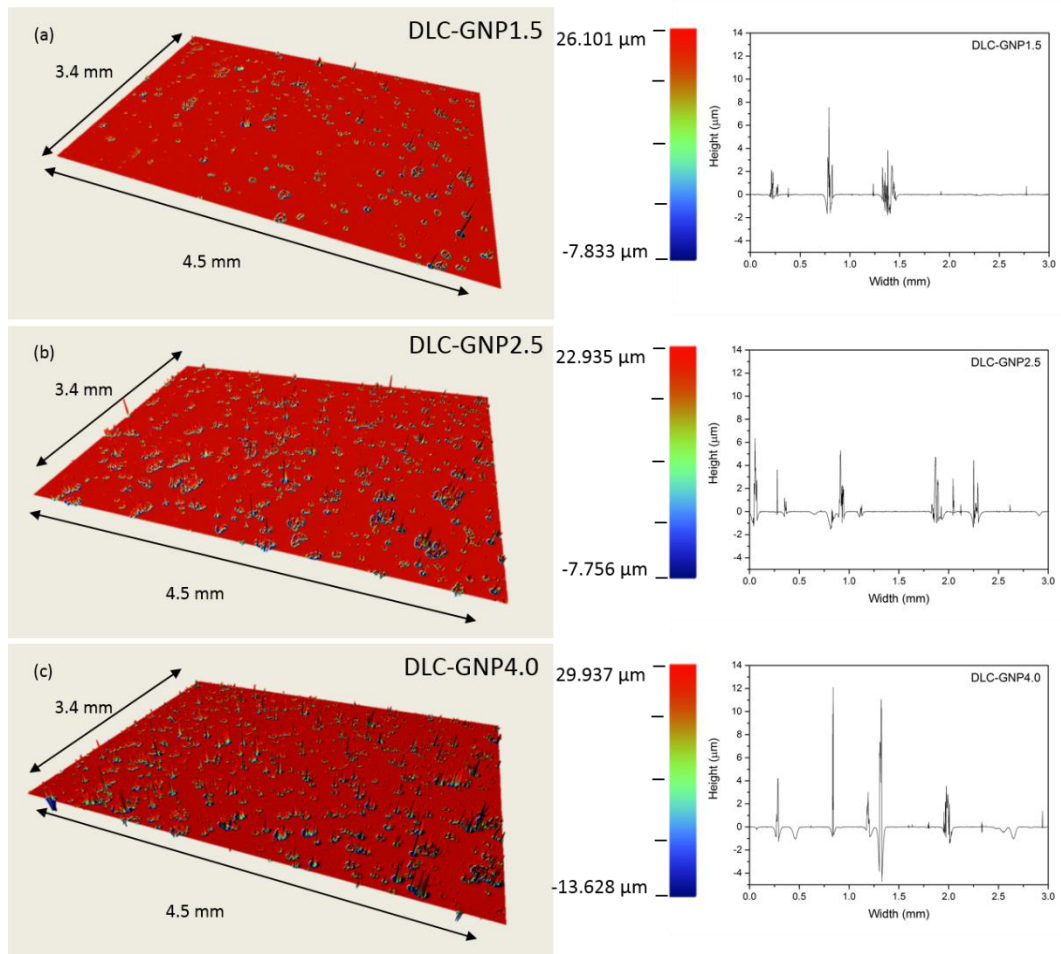
Figure 5.11 Surface topography and its corresponding surface profile of (a) DLC-GNP1.5, (b) DLC-GNP2.5 and (c) DLC-GNP4.0
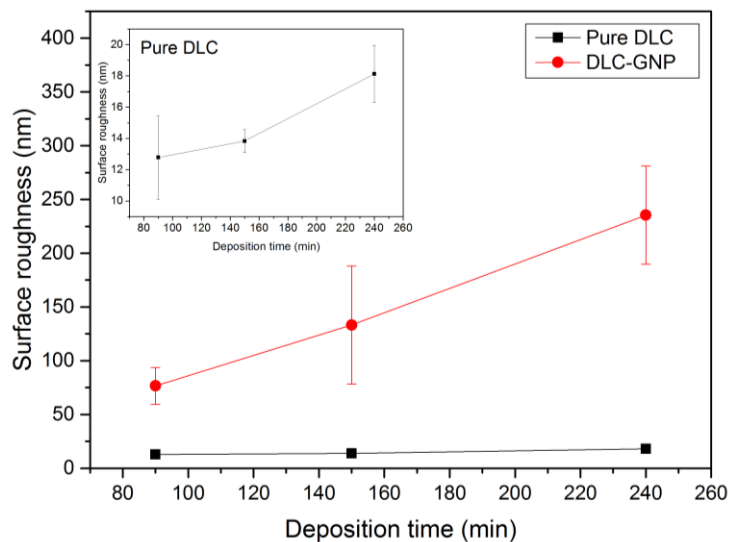
Figure 5.12 Surface roughness of pure DLC and DLC-GNP nanocomposite coating in a function of deposition time of DLC. Inset shows the details surface roughness of pure DLC. The error bars in the graph indicate standard deviation for ten measurements

131

5.4.3 Raman analysis of DLC-GNP nanocomposite coating

Raman spectroscopy was used to acquire information on bonding structure of DLC-GNP nanocomposite coating synthesised with different DLC deposition time. Figure 5.13 shows the comparison of Raman spectra of DLC-GNP and pure DLC deposited at (a) 1.5 hour, (b) 2.5 hour and (c) 4.0 hour. Each set of spectra include spectra of DLC-GNP nanocomposite coating in an area that no GNP was observed, a GNP-rich region and also pure DLC deposited with the same deposition time. All samples, in all measured areas, exhibit broad peaks which can be deconvoluted into two Gaussian peaks of D, and G. D-peak relates typically relates to disordered carbon bonding while G-peak relates to the graphitic carbon bonding [175]. G-peak varies between 1547 and 1553 cm^{-1}, while the shoulder of D-peaks at around ~1356 - 1428 cm^{-1}. These are the well-known signature peak positions for DLC films. The broad peak also confirms the amorphous structure of the film with a mix of sp^3 and sp^2 bonding [150, 176, 177].

The D-peak, G-peak and the integrated intensity ratio, I_D/I_G of the Gaussian line shape extracted from the Raman spectra in Figure 5.13 are summarized in Table 5.4. No peak appeared in a scanning range above 2000 cm^{-1} (Figure 5.14). This also indicates that no graphene peaks can be observed in any of the samples. The G-peak intensity slightly increased as the DLC deposition increased. Liu and Wang also reported an increase of G-peak intensity for DLC thickness between ~10 - 100 nm.
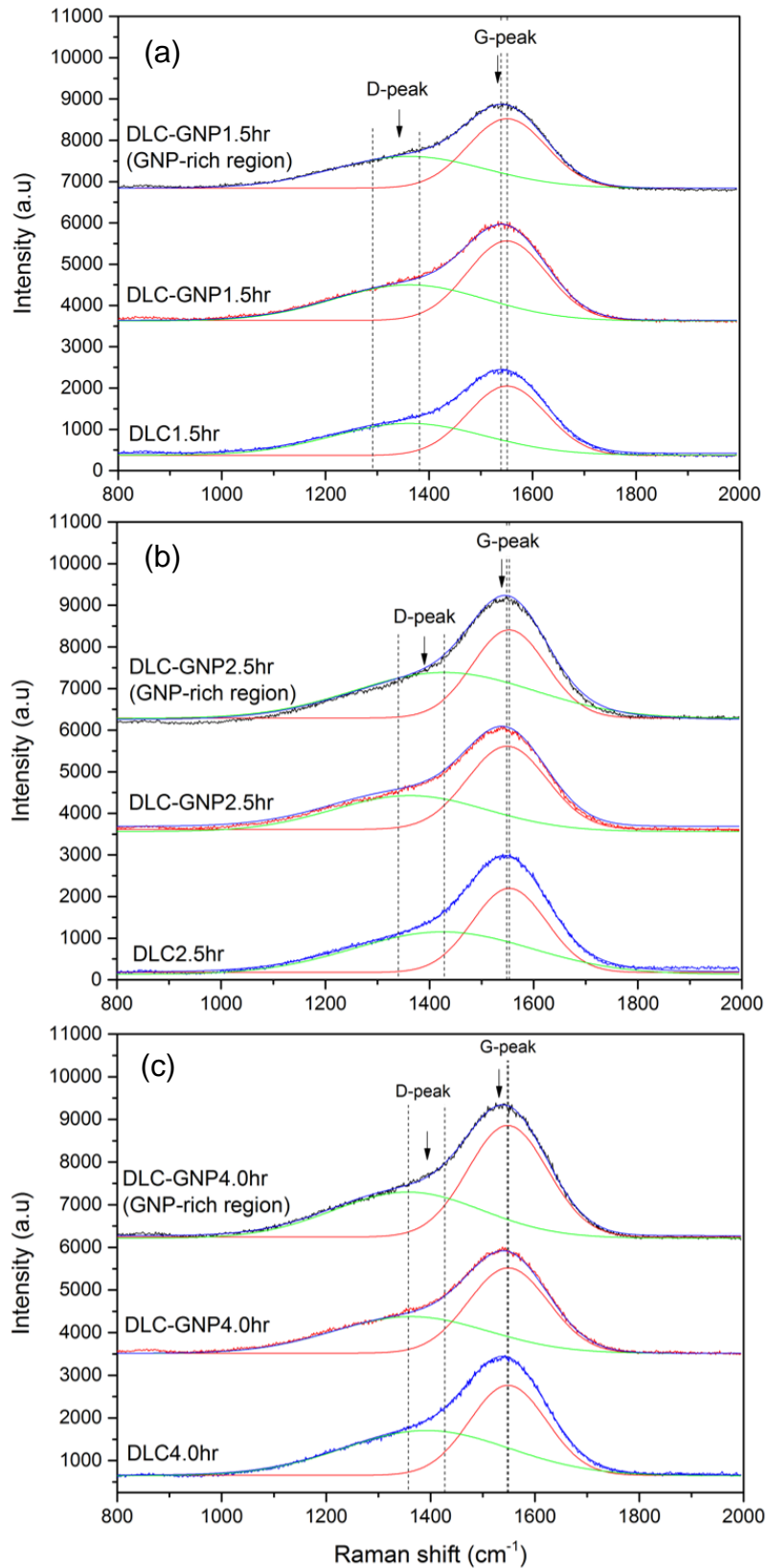
Figure 5.13 Representative Raman spectra of pure DLC and DLC-GNP nanocomposite coating deposited by (a) 1.5 hour, (b) 2.5 hour and (c) 4 hours of DLC film
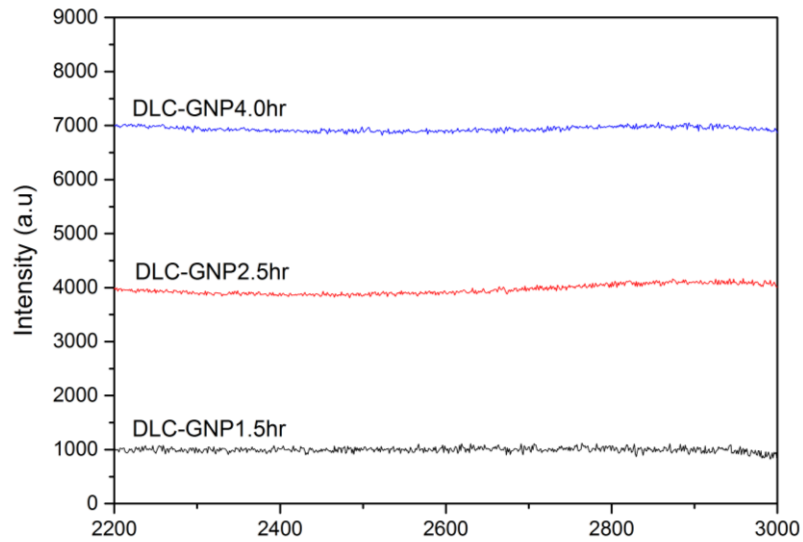
Figure 5.14 Raman spectra at scanning above 2000cm^{-1} of DLC-GNP1.5hr, DLC-GNP2.5hr, and DLC-GNP4.0hr

Table 5.4 Position and integrated intensity I_D/I_G of the main peaks in Raman spectra of pure DLC and DLC-GNP nanocomposite coating deposited at different deposition time

Sample	D-peak (position)	G-peak (position)	I_D/I_G
DLC1.5hr	1363-1372	1550-1551	0.46-0.47
DLC-GNP1.5hr	1292-1382	1539-1549	0.33-0.53
DLC2.5hr	1425	1553	0.36-0.37
DLC-GNP2.5hr	1341-1428	1548-1553	0.31-0.52
DLC4.0hr	1357-1366	1548-1549	0.41-0.43
DLC-GNP4.0hr	1363-1427	1547-1549	0.43-0.59

The relationship between coating thickness and I_D/I_G ratio and the range of I_D/I_G ratio of pure DLC and DLC-GNP is plotted in Figure 5.15. The range of I_D/I_G ratio for all DLC-GNP nanocomposite coatings is larger than pure DLC which may be due to high surface roughness. For pure DLC, the I_D/I_G ratio seems to reduce to smaller value from DLC deposition of 1.5 to 2.5 hours. It slightly increases for DLC4 but still lower than DLC1.5. For DLC-GNP however, the I_D/I_G ratio seems to shift to the higher range when the coating thickness was

increased. Similar results have also been obtained by Zavaleyez et al. for ta-C coating [178].
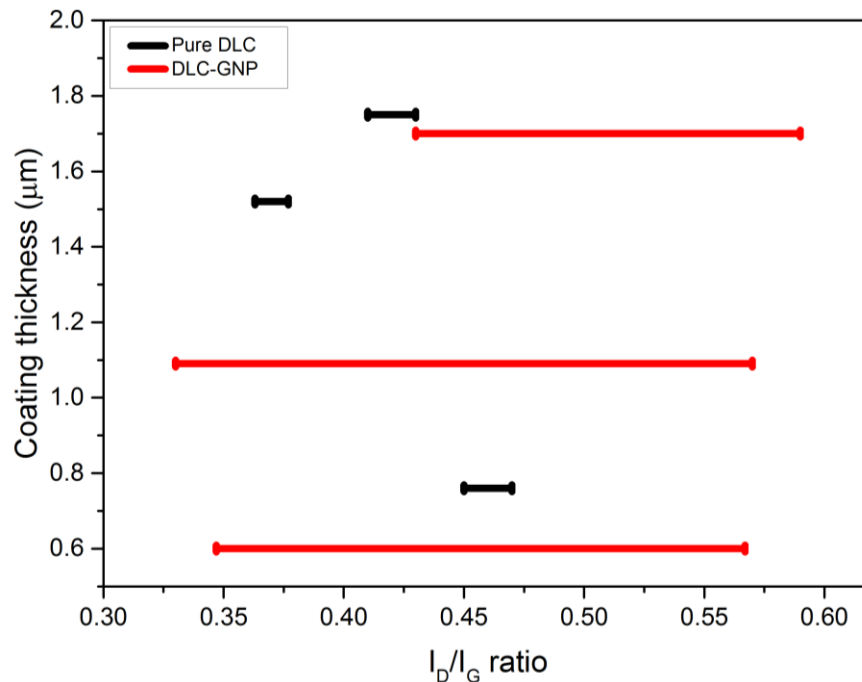
Figure 5.15 The range of I_D/I_G ratio for DLC-GNP with different coating thicknesses

5.4.4 Hardness and Elastic modulus

Nanoindentation was used to measure the nanohardness and reduced elastic modulus of all samples of pure DLC and DLC-GNP nanocomposite coating. 20 indentations were made on each sample and the mean values were calculated. Maximum load applied was 10mN. The indentation experiments were carried out in a depth control mode, so that the maximum depth penetration was less than 10% of the coating thickness.

The mean hardness and elastic modulus of an interlayer are measured to be 10.98 ± 2.75 GPa and 165.43 ± 24.51 GPa respectively. Figure 5.16 and Figure 5.17 demonstrate the load-depth curve of DLC4.0hr and DLC-GNP4.0hr respectively. The results obtained from DLC4.0hr show quite a consistent curve among all indentation. The average hardness and modulus were calculated to

be 25.19 ± 4.69 GPa and 211.23 ± 18.60 GPa respectively. This value is in good agreement in many works reported previously [44, 179].

As can be seen in Figure 5.17 the curve shape for sample DLC-GNP4.0hr varies widely. This might be due to the nature of the surface itself which has areas with and without GNP. Moreover, the surface roughness of this sample is quite high making it almost impossible to get the true value of the hardness and modulus. The curves represent the areas with and without GNP. Some of the curves that has been marked in the dotted oval look similar to pure DLC in Figure 5.16. The curves belong to the areas without GNP. The rest of the curves may signify the characteristics of areas with GNP. It can be said that the variation of curves in the sample were due to the nature of the coating itself which combined both characteristics of pure DLC and GNP.

The average hardness and modulus values were calculated to be 18.59 ± 10.61 GPa and 130.20 ± 78.25 GPa respectively. There was a reduction of 26% and 38% of hardness and modulus respectively, as compared to the pure DLC. Kinoshita et al. [40] also reported a reduction of elastic modulus and hardness with the increase of CNT in CNT/DLC composite coating. Very high standard deviation of both values implies a huge range of measured values for both its hardness and modulus. Table 5.5 presents the summary of measured hardness, elastic modulus and H/E ratio of the interlayer, pure DLC and DLC-GNP nanocomposite coatings. The H/E ratio of DLC-GNP nanocomposite was slightly higher than the pure DLC which might be an indication of a good tribological property of the nanocomposite. Measurement of hardness and modulus of DLC-GNP nanocomposite coating may not be able to provide a true value due to the non-homogenous condition of the surface. Due to this reason, it will not be carried out for the other samples in this work.
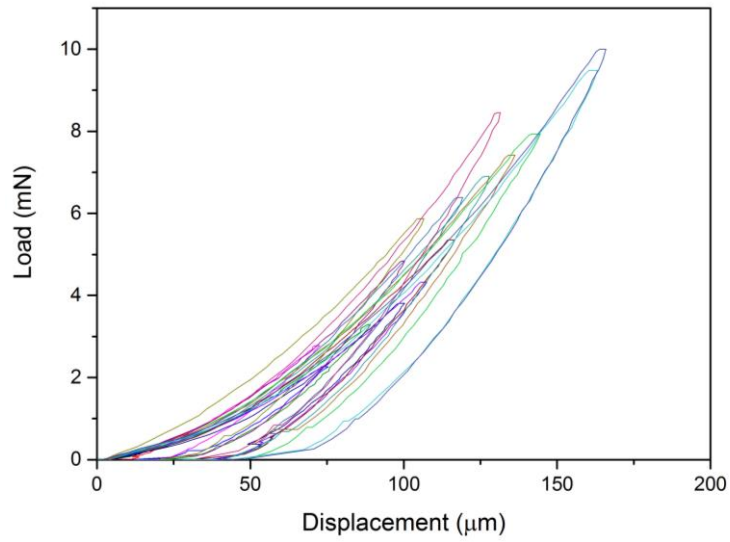
Figure 5.16 Load-depth curve of DLC4.0hr coating
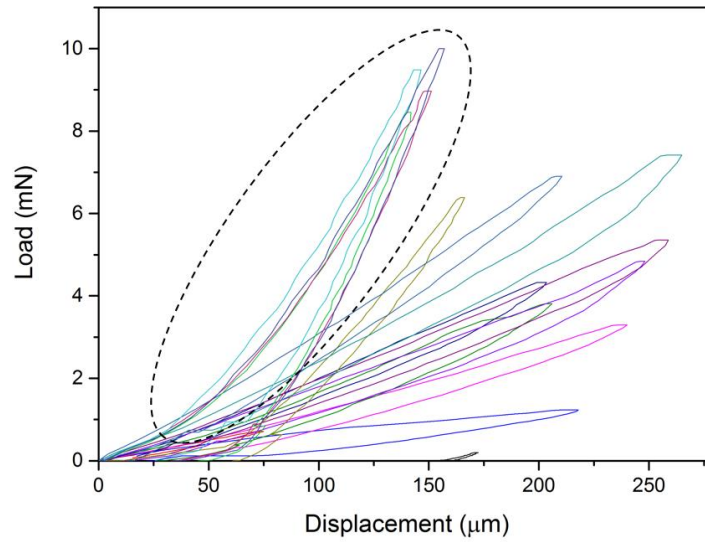
Figure 5.17 Load-depth curve of DLC-GNP4.0hr nanocomposite coating

Table 5.5 Hardness, elastic modulus and H/E ratio of the coatings

	Hardness, H (GPa)	Elastic Modulus, E (GPa)	H/E ratio
Interlayer	10.98 ± 2.75	165.43 ± 24.51	0.07
Pure DLC	25.19 ± 4.69	211.23 ± 18.60	0.12
DLC-GNP	18.59 ± 10.61	130.20 ± 78.25	0.14

5.4.5 Adhesion

Adhesion of DLC-GNP nanocomposite coatings was measured by using scratch test. The scratch test was performed by using Rockwell C diamond indenter (200 μm radius). The load was increased from 1 to 50 N. The cracking and delamination were qualitatively evaluated using an optical microscope. The test was carried out to examine the influence of DLC deposition time on adhesion strength of DLC-GNP nanocomposite coating.

Figure 5.18 represents the micrographs of scratch tracks for all pure DLC and DLC-GNP nanocomposite coatings. In this work, L_{C1} is regarded as the first initial adhesion failure marked by the red arrow in the figure. The scratch direction is from left to right. Generally, all DLC-GNP samples failed much earlier than pure DLC samples. The failure event that was observed in all samples was shell-shaped spallation. Interestingly, samples deposited with 1.5 hours DLC (DLC1.5 and DLC-GNP1.5) in Figure 5.18(a) and (b), appeared to have smaller shell-shaped spallation than other samples. The complete delamination of coating, which can be identified as the gross spallation at the bright area at the end of the scratch is seen in all samples except to sample DLC4. Complete coating delamination for sample DLC1.5 and DLC2.5 occurred much earlier than other samples.
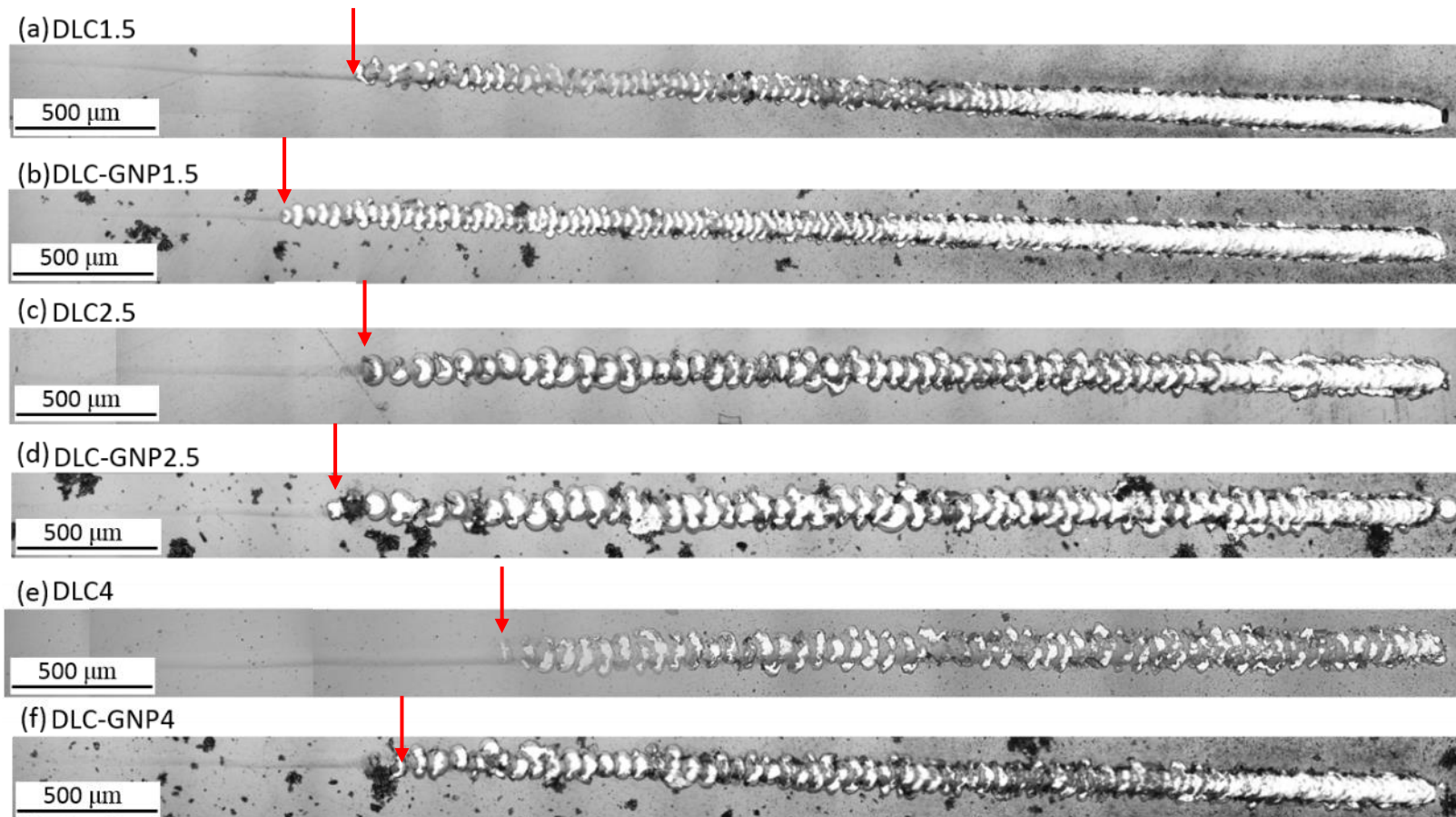
Figure 5.18 Optical micrographs of the scratch tracks showing the failure characteristics of (a) pure DLC1.5, (b)DLC-GNP1.5, (c)DLC2.5, (d)DLC-GNP2.5, (e)DLC4 and DLC-GNP4 nanocomposite coating. Scratch direction is from left to right

For pure DLC samples, critical load is slightly reduced when deposition time was increased to 150 minutes, before reaching the highest value when deposition time is 240 minutes, recorded to be 18.89 ± 2.68 N. As for composite samples, there is no significant difference of critical load between samples deposited for 90 and 150 minutes. The largest critical load value for DLC-GNP has also been achieved after four hours of deposition recorded as 10.40 ± 0.42 N. The value of critical load for pure DLC for all deposition times is much higher than the composite samples. The adhesion of DLC-GNP nanocomposite coating is reduced in the range of approximately 25-45% compared to pure DLC.
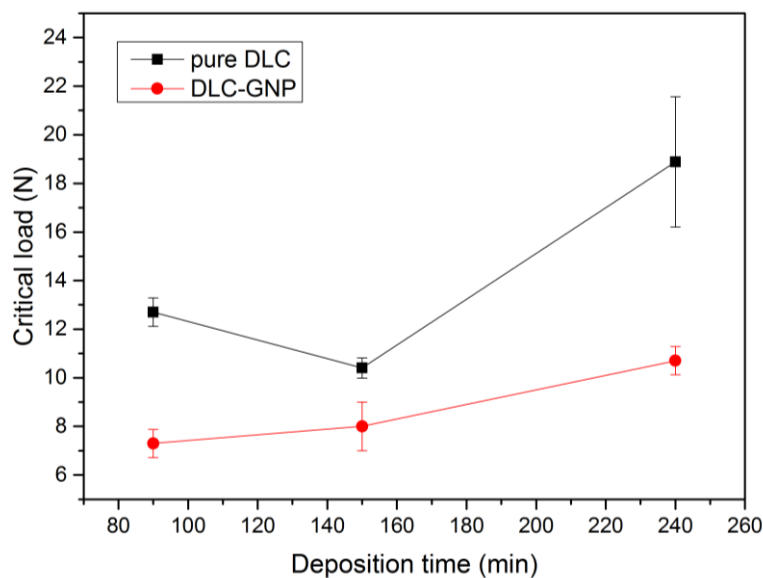
Figure 5.19 Critical load of pure DLC and DLC-GNP nanocomposite coating as a function of deposition time of DLC. The errors bars indicate standard deviation of six measurements

To investigate the role of coating thickness and surface roughness on the adhesion strength of coating, critical load as a function of coating thickness and surface roughness have been plotted in Figure 5.20 and Figure 5.21. Generally critical load value increases with coating thickness for both pure DLC and composite DLC coating. However, DLC-GNP4 has higher thickness compared to pure DLC of DLC1.5 and DLC2.5, it has weaker adhesion strength. The addition of GNP may deteriorate the adhesion strength of DLC-GNP composite

140

coating. Regarding the effect of surface roughness in Figure 5.21, although higher surface roughness of composite samples has lower values of critical load, there seems to be no clear relationship between surface roughness and critical load. Adhesion strength also increased with surface roughness in the case of DLC-GNP nanocomposite coatings.
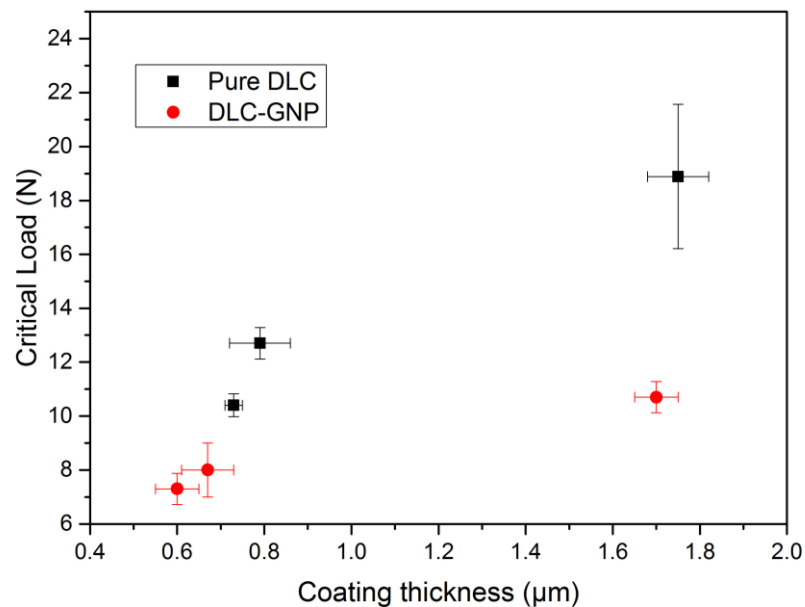
Figure 5.20 Critical load of pure DLC and DLC-GNP nanocomposite coating as a function of coating thickness
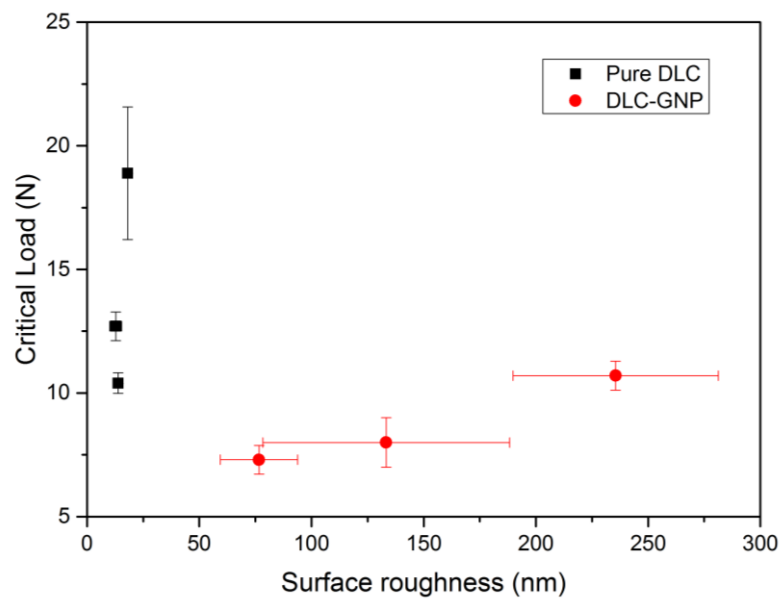
Figure 5.21 Critical load of pure DLC and DLC-GNP nanocomposite coating as a function of surface roughness

5.4.6 Summary of effect of deposition time of DLC on characteristics of DLC-GNP nanocomposite coatings

The results obtained in this section can be summarized as follows:

i. Addition of GNP using spin coating deteriorated the adhesion of the coating to the substrate.

ii. Coating thickness has a more dominant influence on adhesion of pure DLC coating than the surface roughness

iii. The increase of coating thickness increases the adhesion strength of both pure DLC and DLC-GNP nanocomposite coating.

iv. There is no direct correlation between adhesion strength and surface roughness of the coating

5.5 Effect of Post-treatment on Characteristics of DLC-GNP Nanocomposite Coating

Comparing the surface roughness of pure DLC and DLC-GNP nanocomposite coatings in Section 5.4 reveal how high surface roughness and robustness/adhesion of spin-coated GNP are the key factors that depreciate the adhesion of DCL-GNP nanocomposite coating. In order to overcome this problem, a set of experiment was designed as an approach towards reducing the surface roughness and at the same time improving the adhesion of spin-coated GNP. As a comparison pure DLC with the same deposition time was also prepared.

Figure 5.22 shows the process flow of the GNP post-treatment. The process of applying and pressing the spin-coated GNP with tape was utilized to reach better contact of the GNP on the interlayer and eliminating the gap between spin-coated GNP. Samples were then heated inside the oven at 200°C for the duration of 30 to 240 minutes. Figure 5.23 shows how Kapton tape was applied to spin-coated GNP on the substrate showing the photographs of before and after applying Teflon tape to the samples. The samples were then cleaned ultrasonically in acetone for 5 minutes. The whole process of post-treatment similar to several reported graphene transfer methods [180].
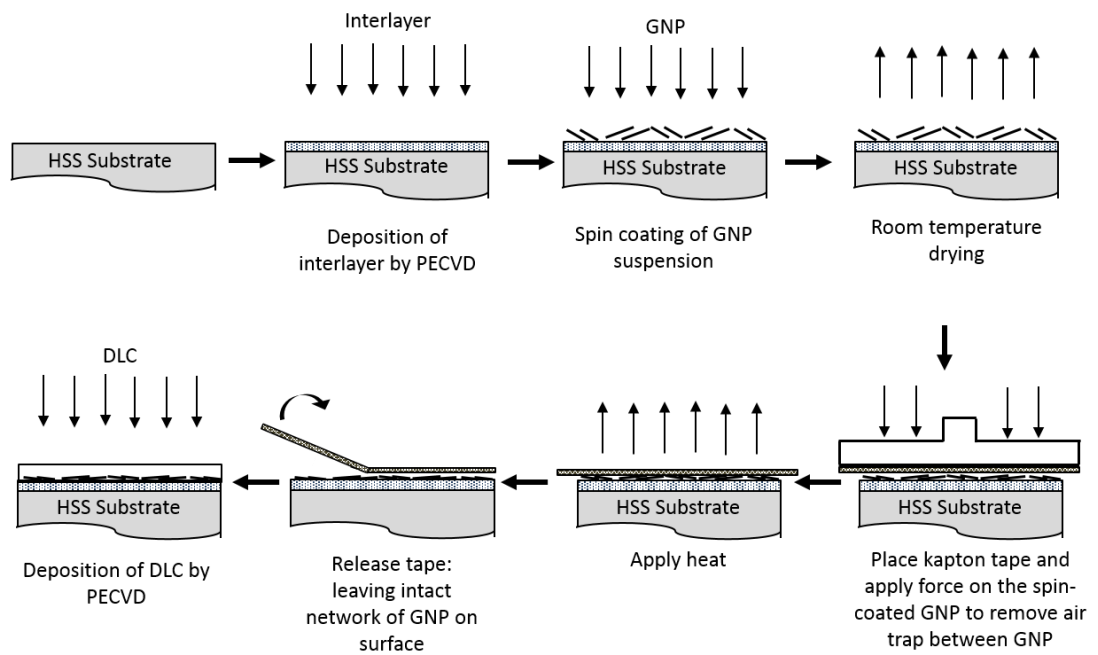
Figure 5.22 Schematic of the process flow of the GNP post-treatment

(a)   (b)
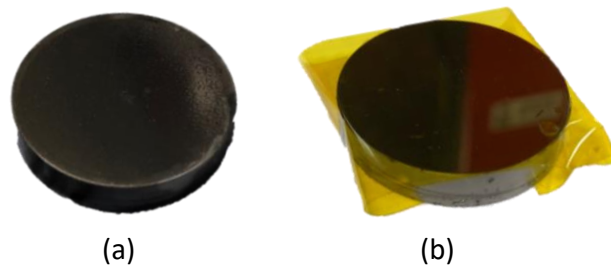
Figure 5.23 Photographs of M2 HSS substrate deposited with GNP (a) before and (b) after Kapton tape was applied to the sample. Diameter of the substrate is 30 mm

Many works reported the improved of coating adhesion after heat treatment. Applying and pressing with tape resembles the process of pressing which is commonly carried out in the production of the composites. A preliminary test was conducted where spin-coated GNP samples were covered with tape and released without any heating. Results showed that most GNPs stick to the tape and left almost no GNP on the surface (Refer Figure 5.24). The optical images of the sample after deposition and after ultrasonication cleaning is shown in Figure 5.24 (a) and (b) respectively. This is an early indication that GNP post-

143

treatment improve the adhesion of GNPs to the surface. Temperature 200°C was chosen to maintain the same temperature as the DLC deposition temperature in the PECVD as further work on the design of DLC-GNP nanocomposite coating will involve post-treatment of GNP on DLC.

In this section, GNP post-treated for 30, 60, 120 and 180 minutes, and its composite DLC-GNP will be denoted as GNP30, GNP60, GNP120, DLC-GNP30, DLC-GNP60, DLC-GNP120 and DLC-GNP180 respectively.
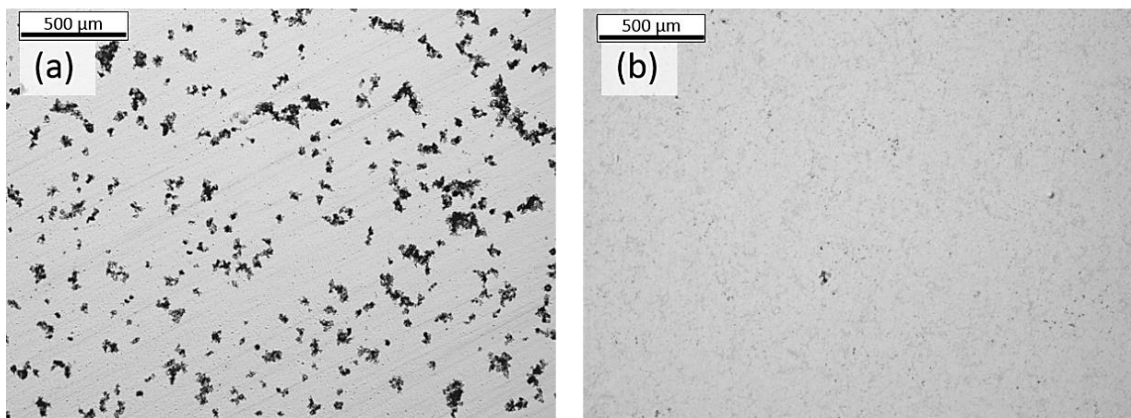
Figure 5.24   Spin-coated GNP without post-treatment (a) after deposition and (b) after surface cleaning using ultrasonication

5.5.1 Surface morphology and surface roughness of post-treated GNP

Morphology of post-treated GNPs was observed by optical microscopy. Size of GNPs was then measured using ImageJ. Figure 5.25 represents the optical micrographs of GNPs after the post-treatment from 30 to 180 minutes after cleaning process with ultrasonication. Micrographs on the right side of Figure 5.25 is the high magnification images of the one on the left side. The morphology of GNP does not show changes as compared to GNP before post-treatment captured in the previous section. It can be seen that the number of GNPs and the size of GNP islands on the surface seem to be increased as the heating time was increased. This might be the first indication that the adhesion of GNP increased with post-treatment time.
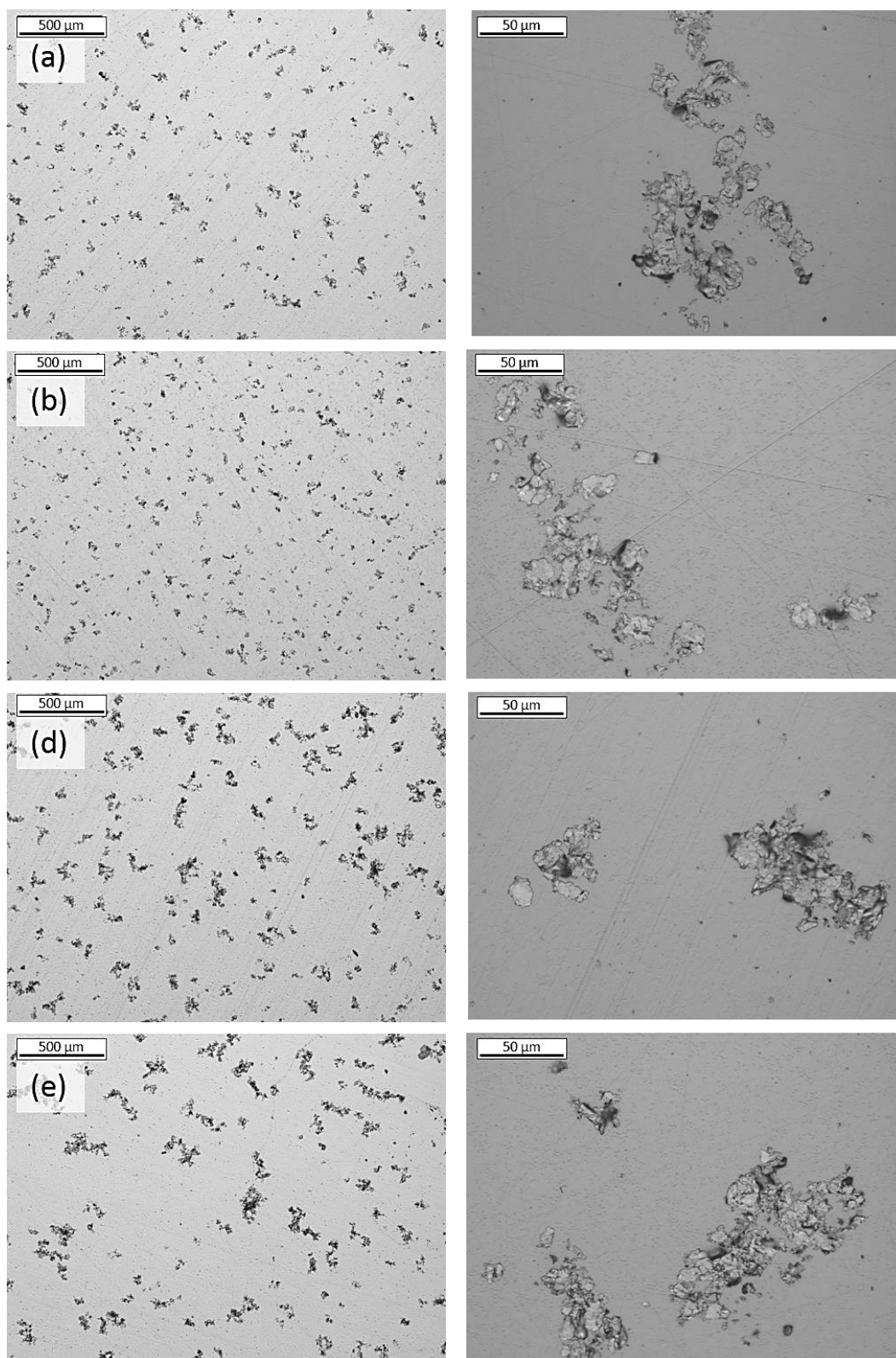
Figure 5.25 Representative optical micrographs of GNP post-treated after the cleaning process after post-treatment for (a) 30 minutes, (b) 60 minutes, (c) 120 minutes (d) 180 minutes and (f) 240 minutes respectively. The corresponding higher magnification of the optical micrographs is shown on the right side of each micrograph. (Continue)
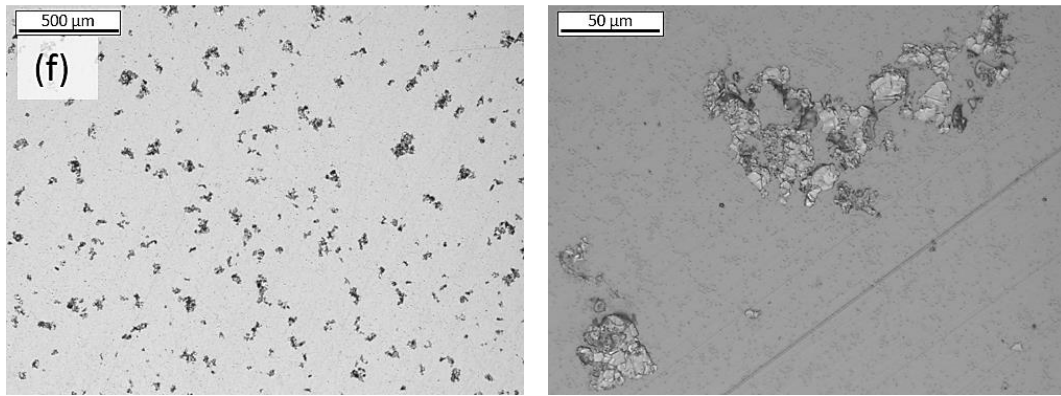
Figure 5.26 Representative optical micrographs of GNP post-treated after the cleaning process after post-treatment for (a) 30 minutes, (b) 60 minutes, (c) 120 minutes (d) 180 minutes and (f) 240 minutes respectively. The corresponding higher magnification of the optical micrographs is shown on the right side of each micrograph. (Continue)

Quantitative measurements on the post-treated GNP were also carried out to measure the GNP distribution and the size of the GNP islands. All micrographs were processed with ImageJ, and measurement also using ImageJ used the same technique used in Section 4.4.2 where morphological segmentation plugin was used to measure the percentage and size.

Figure 5.27 shows the GNP distribution (coverage area %) for pure DLC and DLC-GNP post-treated nanocomposite coating. Value at zero time heating indicates the value of GNP distribution without any post-treatment and cleaning as shown in Figure 5.24. Spin-coated GNP after deposition without any post-treatment and surface cleaning showed high coverage distribution of approximately 9.5% compared to other samples with post-treatment with a huge standard deviation. It demonstrates the highly inhomogeneous distribution of GNP on the surface without post-treatment. Heating time in the graph represents the heating time of spin-coated GNP. The graph shows an increasing trend of coverage area with a heating time of post-treatment process. The highest coverage area is when spin-coated GNPs were heated for 180 minutes where the GNP distribution is around 6.7%. GNP distribution is slightly reduced when the heating time of post-treatment was extended to 240 minutes. The decrease of GNP distribution on the surface after post-treatment demonstrates that 38-52% of the spin-coated GNP were removed from the

surface and the remaining GNPs have a good adhesion with the substrate surface and among GNP itself.
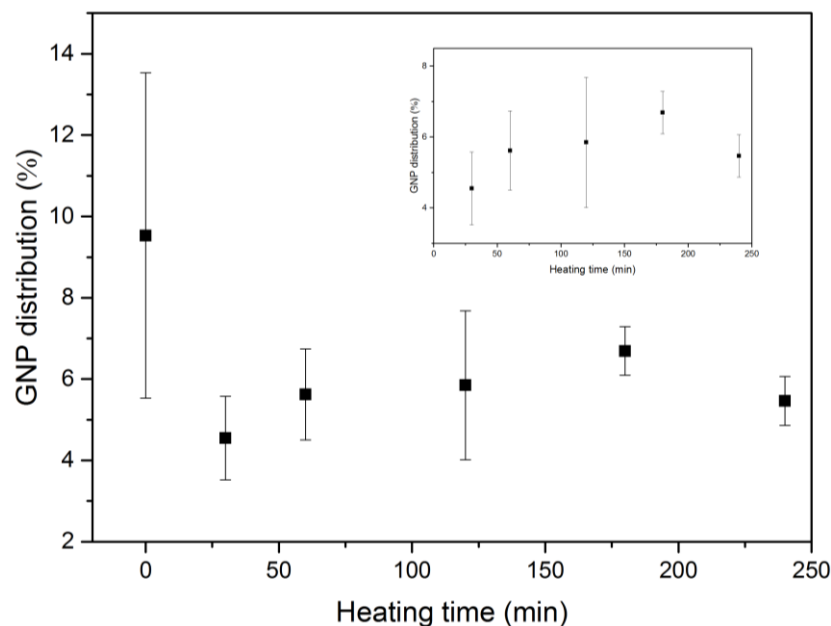
Figure 5.27 Distribution of spin-coated GNP island post-treated for 0, 30, 60, 120, 180 and 240 minutes after surface cleaning. The errors bars indicate the standard deviation of ten measurements.

Figure 5.28 shows the size of GNP islands measured after post-treatment and cleaning. As previously explained, zero time in this graph indicates samples without any post-treatment measured without cleaning process. The inset is the detailed graph of only post-treated samples from 30 to 240 minutes. The size of GNP islands reduced up to 65% compared to the sample without any post-treatment. No significant increase can be observed from 30 minutes to 60 minutes. However, the size of GNP islands shows significant size increase as heating time increased to 180 minutes. An increase of about 25% of size compared to sample GNPheat30. There was almost no change of size when GNP heating time extended to 240 minutes.

Figure 5.29 shows how surface roughness changed with GNP post-treatment time. Surface roughness reduced from around 29.5 nm to 19.5 nm as post-treatment of 30 minutes was applied. This demonstrates reduced of overlapping GNP thickness when it is pressed by the tape and heated. The

surface roughness rose gradually as the heating time increased to 120 minutes and remained almost the same value as the heating time increased to 180 and 240 minutes. The process of pressing and heating of GNP improved the adhesion of GNP to not only the substrate but also the adhesion between each GNP. Overlapping GNP remained together even after ultrasonication cleaning. These have increased the height of each GNP island thus increased the surface roughness.
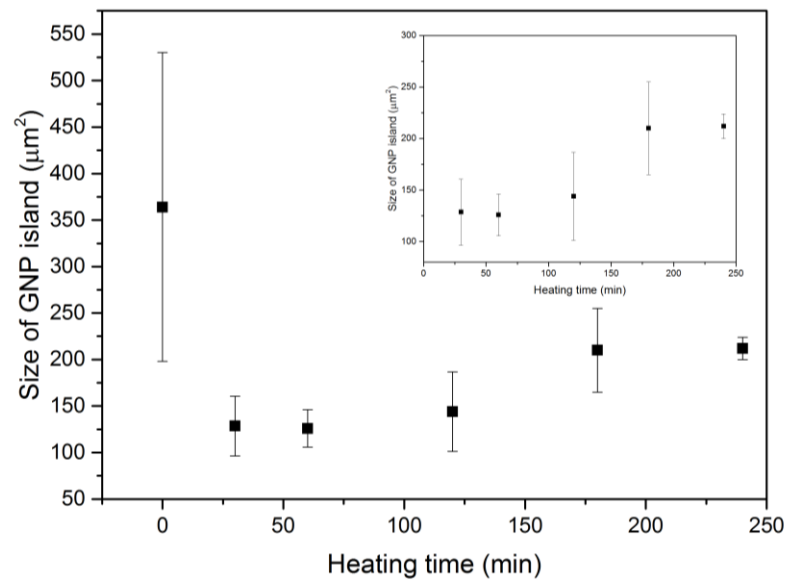
Figure 5.28 Size of spin-coated GNP island post-treated for 0, 30, 60, 120, 180 and 240 minutes after surface cleaning. The errors bars indicate the standard deviation of ten measurements
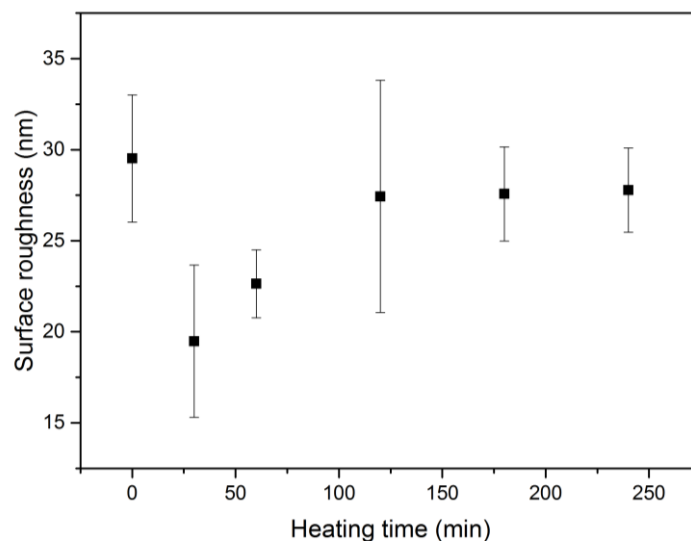
Figure 5.29 Surface roughness of GNP post-treated for 30, 60, 120, 180 and 240 minutes. The errors bars indicate the standard deviation of ten measurements.

5.5.2 Raman analysis of post-treated GNP

Raman spectra of post-treated GNP were also investigated to identify any structural changes of the GNP after post-treatment. Figure 5.30 represents the typical Raman spectra of spin-coated GNP with post-treatment from 30 to 240 minutes respectively. All spectra show high intensity of G- and 2D-peaks which can be deconvoluted into two Lorentz peaks of $2D_1$- and $2D_2$-peak as in Figure 5.31. Figure 5.31 is an example of 2D-peak deconvolution at 2741 and 2705 cm^{-1} for sample GNPheat240. The D-peak is either does not appear or only weakly appears in all samples. At this point, no obvious difference can be seen as compared to GNP without post-treatment.
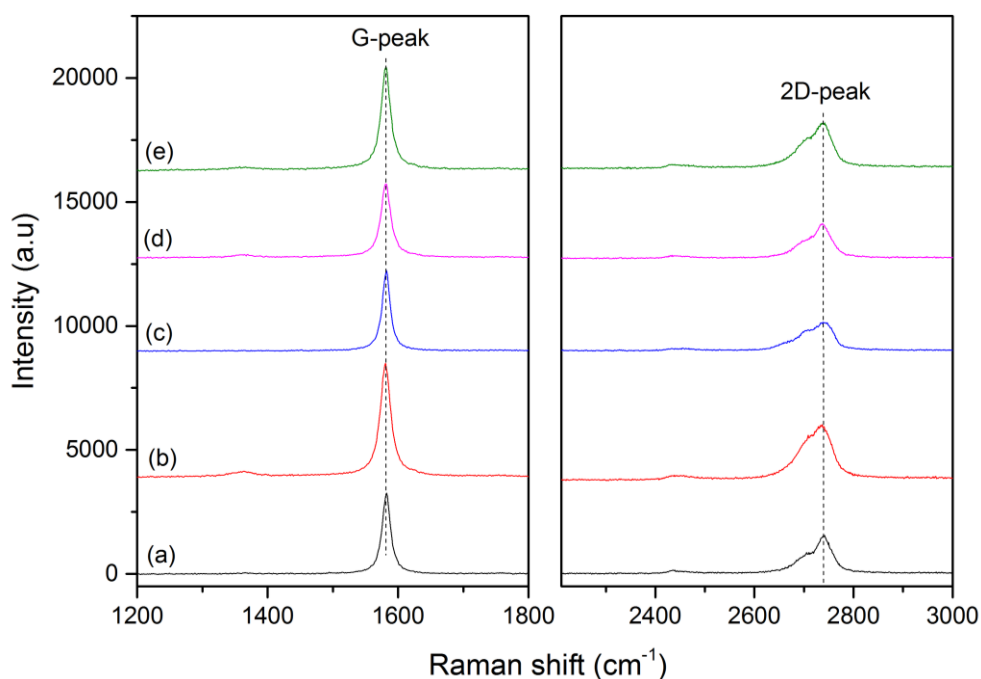
Figure 5.30 Representative Raman spectra of post-treated GNP for (a) 30, (b) 60, (c) 120 (d) 180 and (e) 240 minutes at temperature of 200°C
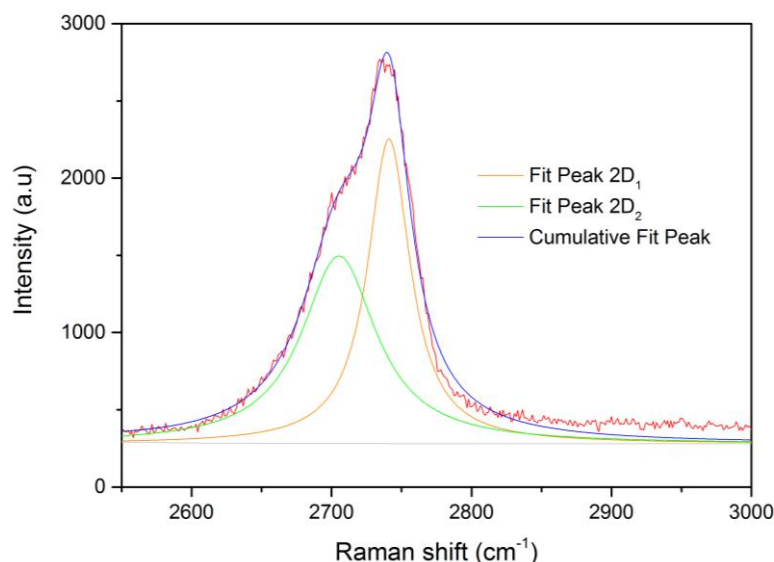
Figure 5.31 Fitted Raman spectra of spin-coated GNP after deconvolution of D and G-peaks

Table 5.6 summarised the G-peak, 2D-peak deconvolution of $2D_1$ and $2D_2$ and calculated I_G/I_{2D} ratio at three different spots on samples without post-treatment (GNPheat0) and samples post-treated for 30 to 240 minutes. The peak positions were obtained from three spectra of three different area on samples. All samples with and without post-treatment have a G-peak position at around ~ 1581 - 1582 cm^{-1}, $2D_1$-peak at ~2739 - 2743 cm^{-1} and $2D_2$-peak at around ~ 2700 - 2707 cm^{-1}. I_G/I_{2D} ratio lies between 1.97 and 3.50. However, no clear trend can be seen for the changes of I_G/I_{2D} value in all samples.

Table 5.6 Position and integrated intensity I_G/I_{2D} of the main peaks in Raman spectra of post-treated GNP samples

Sample	G-peak position (cm^{-1})	$2D_1$-peak position (cm^{-1})	$2D_2$-peak position (cm^{-1})	I_G/I_{2D} ratio
GNPheat0	1581	2739-2743	2702-2707	2.35-3.38
GNPheat30	1581-1582	2739-2741	2701-2705	2.27-2.49
GNPheat60	1581	2740-2741	2705-2706	2.55-2.77
GNPheat120	1581-1582	2740-2743	2705-2706	2.80-3.50
GNPheat180	1581	2738-2741	2700-2704	1.97-2.39
GNPheat240	1581	2740-2741	2704-2705	2.73-2.81

The intensity of G- and 2D-peak are plotted in Figure 5.32. The values were calculated from the average of three spectra from each sample. There is a major increase in the intensity of G-, $2D_1$- and $2D_2$-peaks for samples having post-treatment. The intensity for all mentioned peaks increases as 30 minutes post-treatment was applied to samples after remains almost constant as the duration of post-treatment increase. On increasing of GNP heating time to 240 minutes, the peak intensity of all peaks rose again especially the intensity of G-peak. The increase of G-peak intensity is many times describes as increases of graphene thickness as more carbon atoms are detected [181].
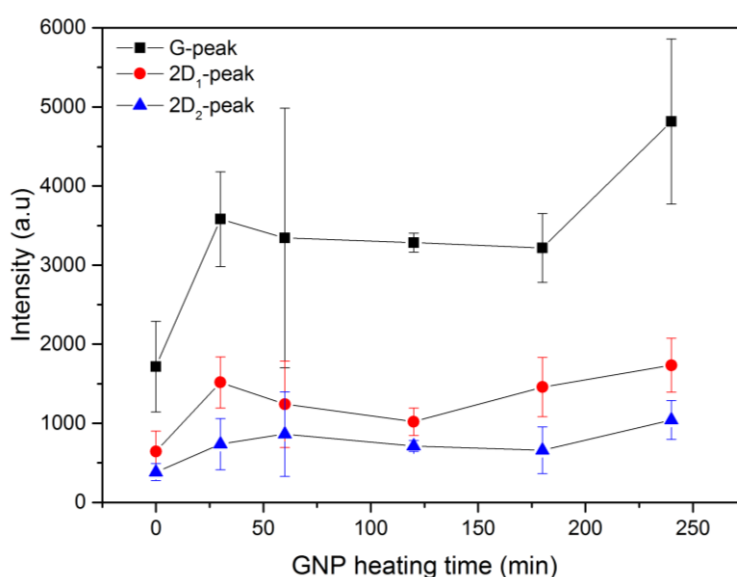
Figure 5.32 Intensity of G-, $2D_1$- and $2D_2$-peak of GNP by the function of GNP post-treatment time. Sample at heating time zero indicates sample without post-treatment. The errors bars indicate the standard deviation of three measurements

5.5.3 Surface morphology and surface roughness of DLC-GNP

Surface topography of DLC-GNP and pure DLC were characterised using WLI. The 3D images of the surface topography of sample DLC-GNPheat30, DLC-GNPheat60, DLC-GNPheat120, DLC-GNPheat180 and DLC-GNPheat240 and its corresponding surface profile are shown in Figure 5.33. The surface profile reveals rougher surface as post-treatment time was increased up to 120 minutes. The surface roughness appears to not change to a great degree as the time increased to 240 minutes.

151
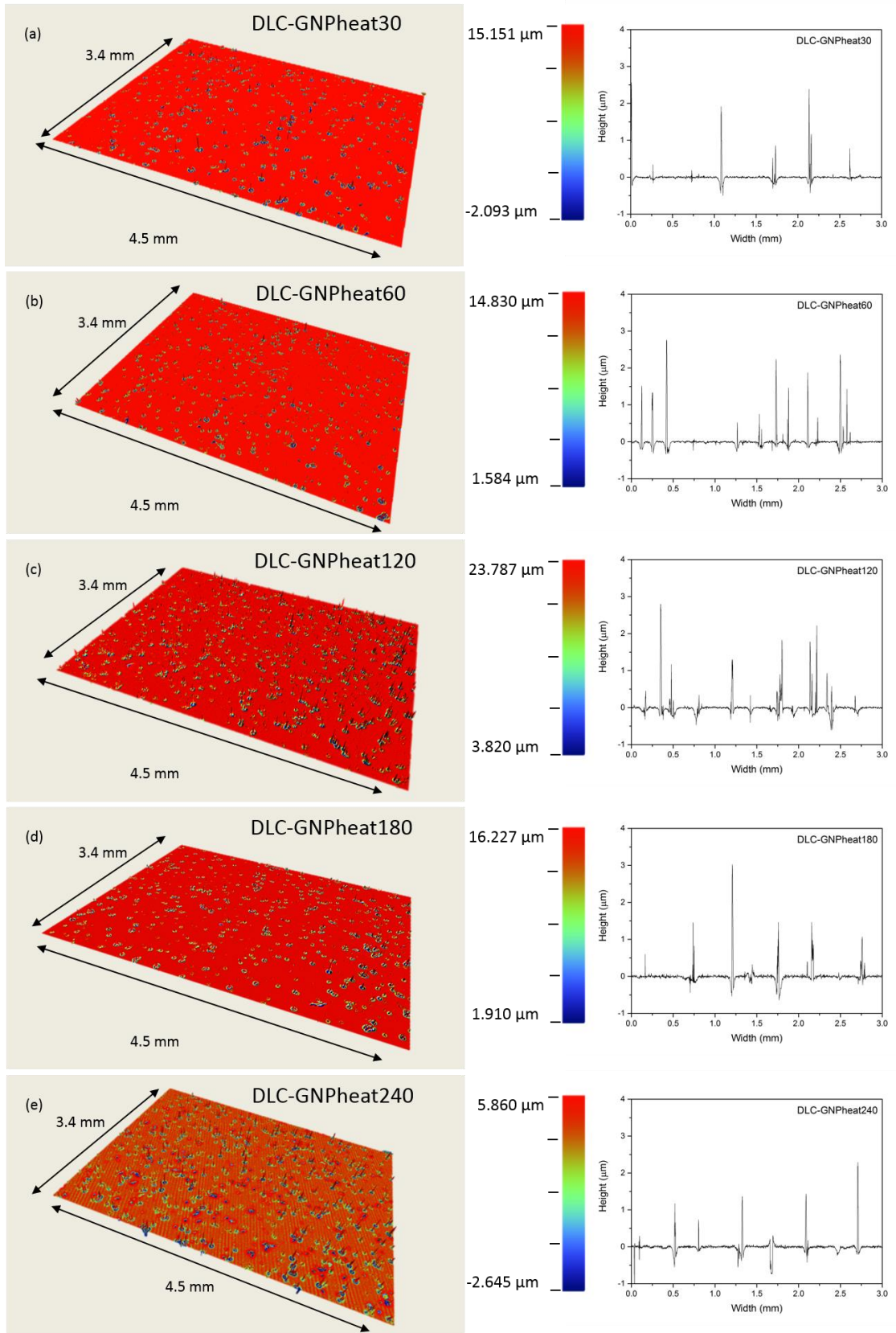
Figure 5.33 Surface topography and its corresponding surface profile of (a) DLC-GNPheat30, (b) DLC-GNPheat60, (c) DLC-GNPheat120 (d) DLC-GNPheat180 and (e) DLC-GNPheat240

152

The average of surface roughness was calculated and shown in Figure 5.34. As predicted earlier from the surface topography, the surface roughness of coating increased as the GNP heating time increased to 120 minutes before maintaining its level even when heating time was increased to 240 minutes. Sample DLC-GNPheat120 has the highest surface roughness while the lowest was sample DLC-GNPheat30. It is expected that as the surface roughness of spin-coated GNP in

Figure 5.29 also has a similar trend. Compared to the coating without post-treatment, even the highest surface roughness obtained in this work attained a reduction of more than 80%.
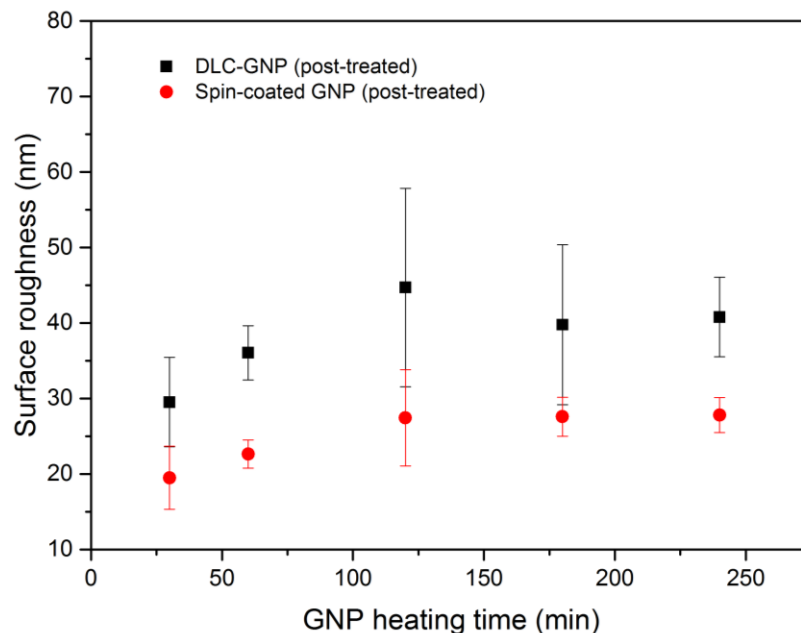
Figure 5.34 Surface roughness of DLC-GNP nanocomposite coating with GNP post-treated for 30, 60, 120, 180 and 240 minutes respectively. The error bars in the graph indicate standard deviation for ten measurements

Figure 5.35 shows the typical micrographs of DLC-GNP (Post-treatment) surface morphology. The surface of the coating has the typical nodular surface morphology of DLC with numbers of more massive nodular structure that are marked by the red arrows in Figure 5.35. As also observed before in Figure 5.6, this might be due to deposition of DLC film on spin-coated GNP. It is believed that all post-treated GNPs were covered by DLC during deposition.
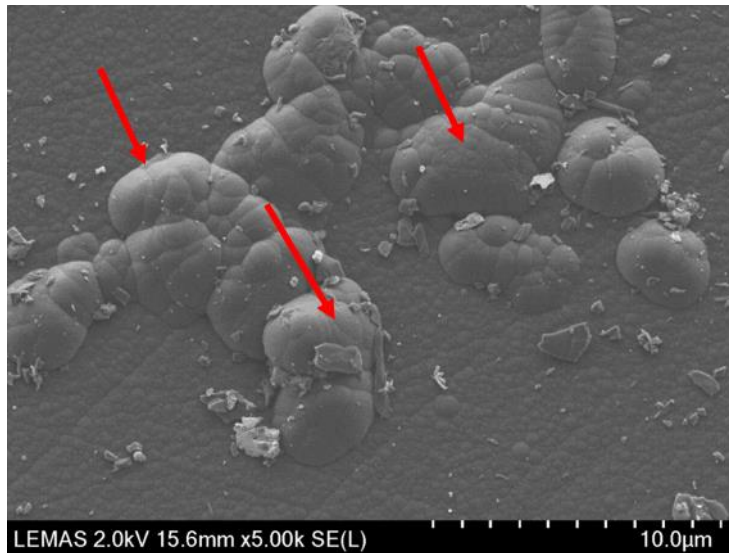
Figure 5.35 Typical micrograph of DLC-GNP post-treated GNP

The volume percentage (vol%) of GNP in the DLC-GNP nanocomposite was estimated by using the coverage percentage and surface roughness of spin-coated GNP obtained in Section 5.5.1. The change of GNP vol% as a function of post-treatment time is presented in Figure 5.36. Based on the thickness of a DLC coating deposited in four hours (1.7 μm), the content of GNP was calculated to be between 0.05 to 0.2 vol%, with the highest GNP content identified for DLC-GNPheat180 sample.
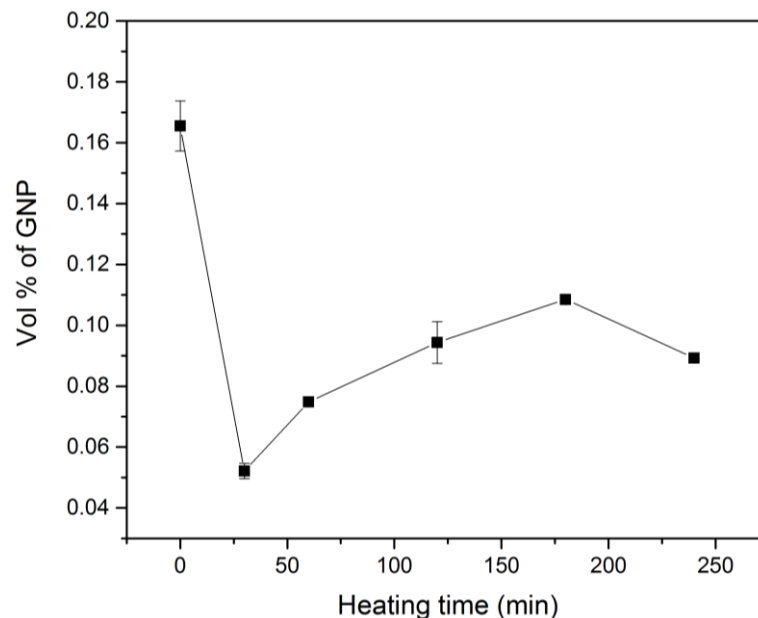
Figure 5.36 Volume percentage (vol%) of GNP in the DLC-GNP nanocomposite coating after 0, 30, 60 120, 180 and 240 minutes post-treatment. Heating time at 0 indicates coating without heat-treatment

5.5.4 Raman analysis of post-treated DLC-GNP

Raman spectroscopy was used to evaluate and compare the chemical bonding structure of DLC-GNP nanocomposite coating post-treated for 30 to 240 minutes. Measurements were collected from three different areas in each sample.

Figure 5.34 shows the typical Raman spectra of sample DLC-GNPheat30, DLC-GNPheat60, DLC-GNPheat120, DLC-GNPheat180 and DLC-GNPheat240. As shown in Figure 5.37, all Raman spectra obtained from post-treated samples have the same broad peaks that can be deconvoluted into two Gaussian peaks of D and G. No graphene peaks were observed in the range of spectra and at the higher range of scan. The summary of the D- and G-peaks position and the I_D/I_G ratios are tabulated in Table 5.7. D- and G-peaks of the samples are featured at around 1352 - 1359 cm^{-1} and 1544 - 1546 cm^{-1} respectively. The ratio of the peak intensity, I_D/I_G range between 0.27 - 0.59.
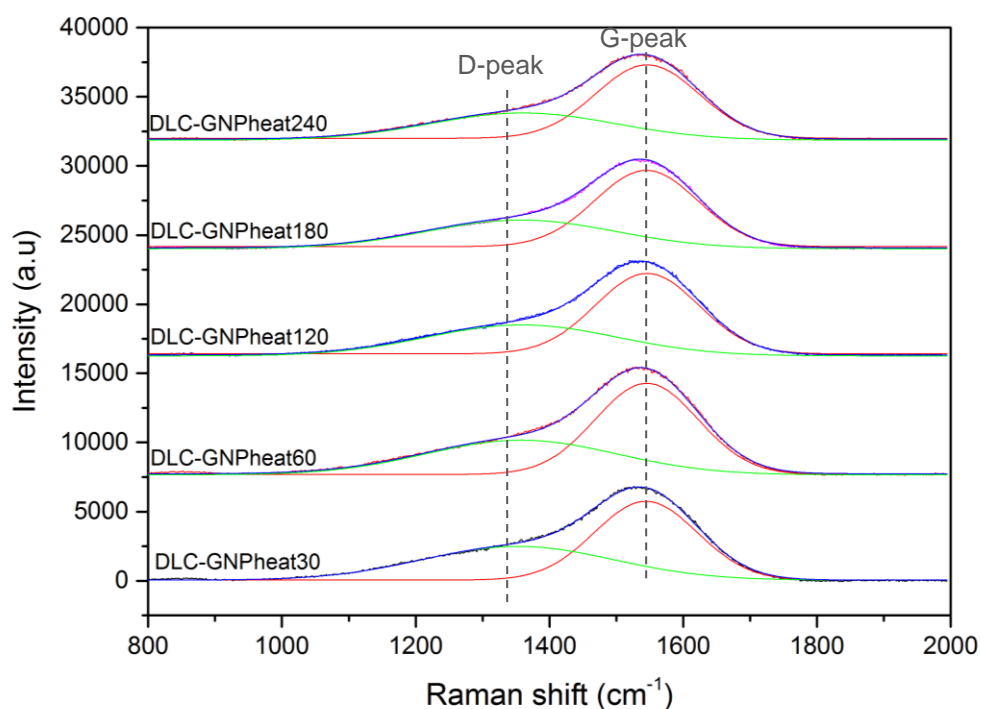
Figure 5.37 Representative Raman spectra of DLC-GNP nanocomposite coatings with post-treated GNP for 30, 60, 120 and 180 minutes respectively.

Table 5.7 Position and integrated intensity I_D/I_G of the main peaks in Raman spectra of post-treated DLC-GNP nanocomposite coating

Sample	D-peak position (cm^{-1})	G-peak position (cm^{-1})	I_D/I_G
DLC-GNPheat30	1357-1416	1545-1549	0.37-0.59
DLC-GNPheat60	1410-1418	1545-1546	0.35-0.58
DLC-GNPheat120	1409-1420	1545-1547	0.39-0.58
DLC-GNPheat180	1335-1417	1544-1547	0.33-0.55
DLC-GNPheat240	1331-1424	1544-1549	0.27-0.55

Figure 5.38 presents the range of I_D/I_G ratio for DLC-GNP with post-treatment between 30 to 240 minutes that have been obtained in Table 5.7. When the post-treatment is between 30 to 120 minutes, there is not much difference between the three samples of DLC-GNPheat30, DLC-GNPheat60 and DLC-GNPheat120. The I_D/I_G ratio shifts to a lower range as the post-treatment time was increased to 180 and 240 minutes.

It was predicted earlier in Section 5.4.3 that the big range of I_D/I_G value for DLC-GNP nanocomposite coatings might be due to the high surface roughness of the coatings. However, as can be seen in Figure 5.38, the I_D/I_G values recorded for the post-treated coatings are covering a wide range as obtained earlier in Section 5.4.3 although surface roughness was lower for most of the coatings. This indicates that the large range of I_D/I_G ratio of DLC-GNP nanocomposite coating is due to the characteristics of the coating itself.
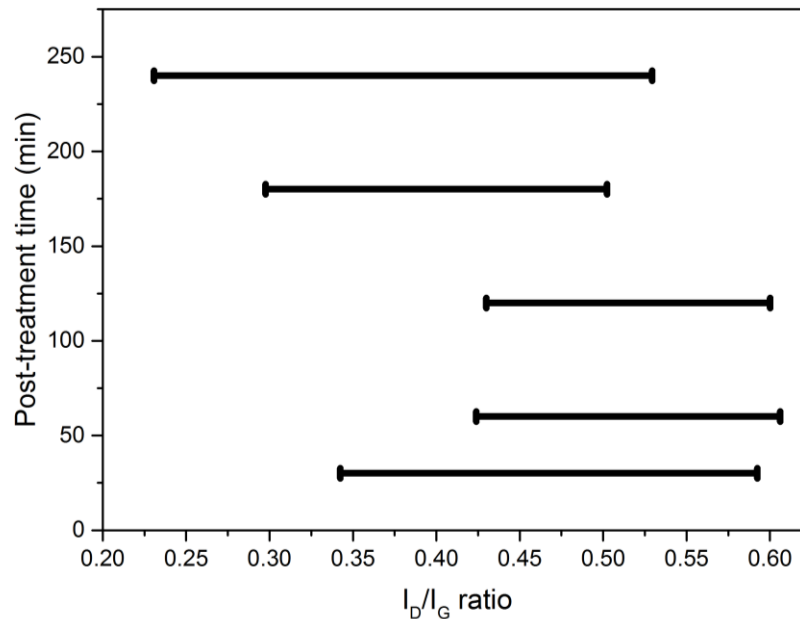
Figure 5.38 The range of I_D/I_G ratio for DLC-GNP prepared with different post-treatment time from 30 to 240 minutes

5.5.5 Adhesion

Scratch tests were conducted to investigate how adhesion strength changed with duration of post-treatment. Figure 5.39 shows the optical micrographs of the scratch tracks after the test and the L_{C1} position is marked as a red arrow in the figure. Pure DLC sample in Figure 5.39(a) is also listed as a reference. Scratch direction is from left to right of the track. Other than pure DLC coating, it is hard to justify through the visual comparison which coating failed first as the failure locations (L_{C1}) are quite near to each other. Adhesion failure of all samples showed a shell-shaped spallation, but smaller in size compared to scratch tracks observed for samples without post-treatment in Section 5.4. Gross spallation could obviously be seen in the scratch track on sample DLC-GNPheat30, DLC-GNPheat60 and DLC-GNPheat120 in Figure 5.39(a-c).

Figure 5.40 summarises the measured critical load, Lc_1 for sample DLC-GNPheat30, DLC-GNPheat60, DLC-GNPheat120, DLC-GNPheat180 and DLC-GNPheat240. Standard deviation is measured from three critical load values. The critical load of pure DLC deposited with the same hour was also measured as a comparison. The critical load of all DLC-GNP post-treated samples was in the range of 14 - 15 N, comparatively lower than pure DLC

which was measured to be around 18.89 N. However, the values obtained by all DLC-GNP coatings that went through post-treatment are much higher than the values recorded by samples without GNP post-treatment in Section 5.4. Adhesion improvement of approximately 36% is achieved with post-treatment process.
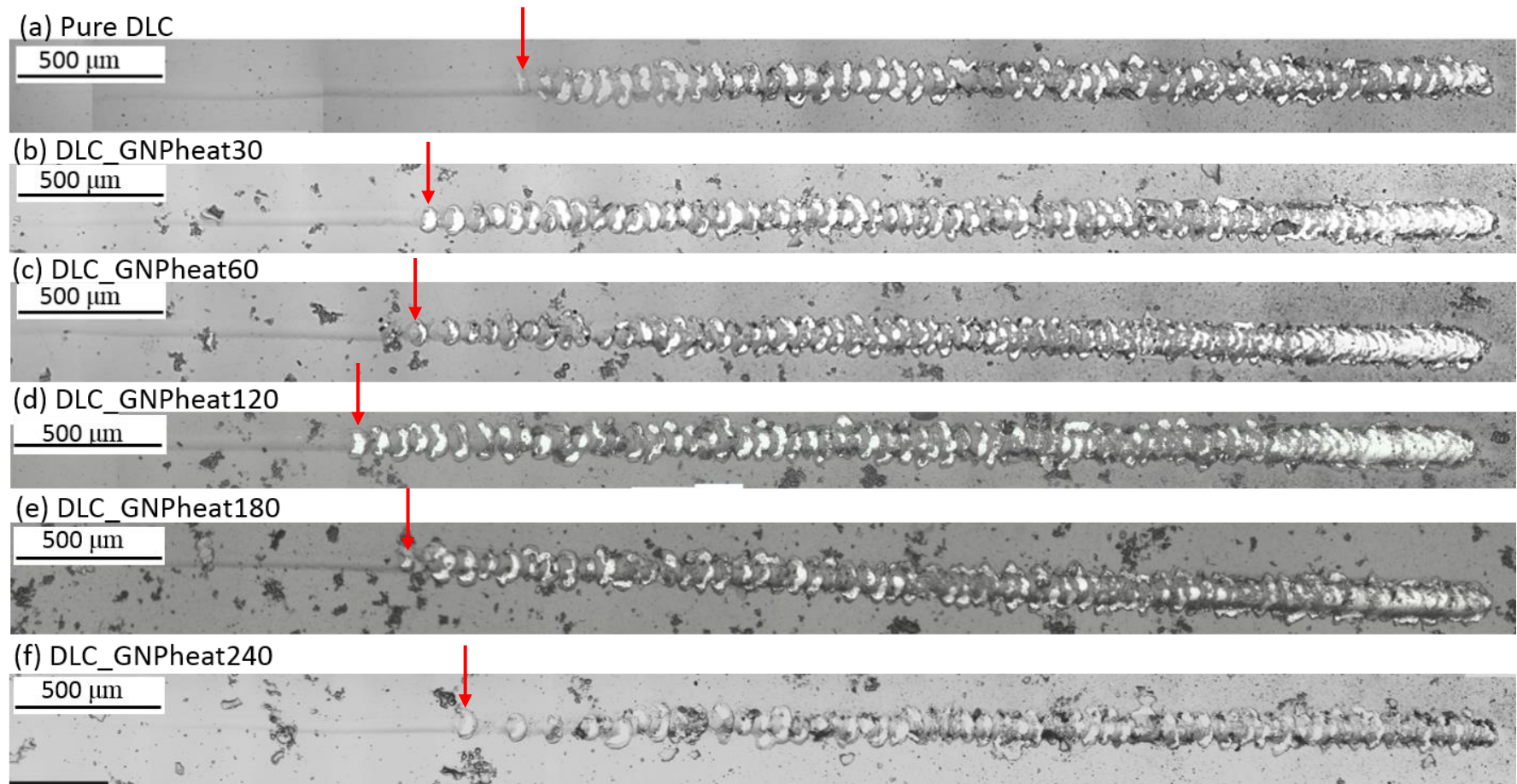
Figure 5.39 Optical micrographs of the scratch tracks for (a) Pure DLC, (b) DLC-GNPheat30, (c) DLC-GNPheat60, (d) DLC-GNPheat120, (e) DLC-GNPheat180 and (f) DLC-GNPheat240
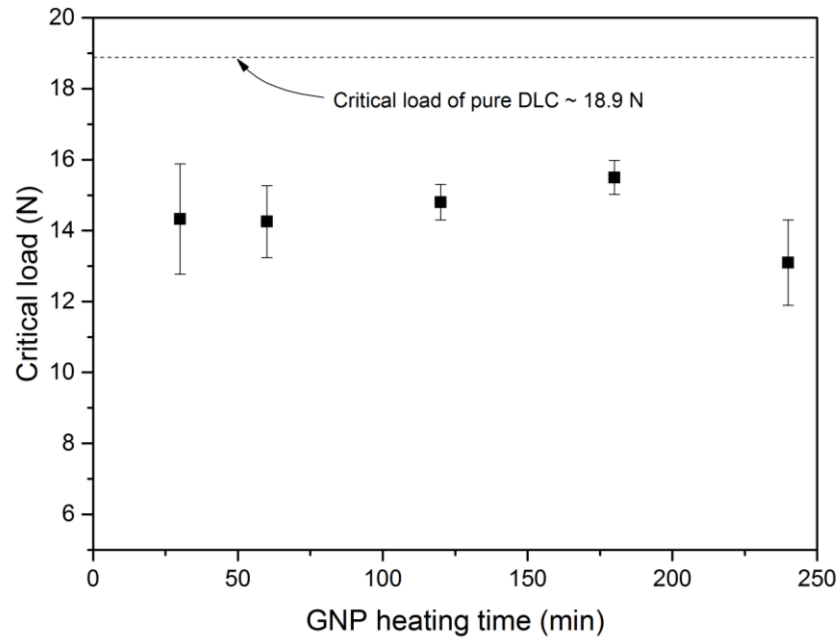
Figure 5.40 Critical load of DLC-GNP samples of post-treated GNP from 30 to 240 minutes. The errors bars indicate the standard deviation of six measurements.

Figure 5.41 shows the cross-section of scratch depth at L_{C1} and the end of the scratch track. The depth at L_{C1} for all samples is almost at the same level. The width of scratch all samples is almost similar. Pure DLC and DLC-GNPheat180 having narrower widths compared to the other samples. Pure DLC also has the shallowest depth at the end of the scratch track compare to the others. The result indicates that pure DLC may have higher hardness compared to all other coatings in this study which is in accord with the hardness measurement of pure DLC and DLC-GNP.
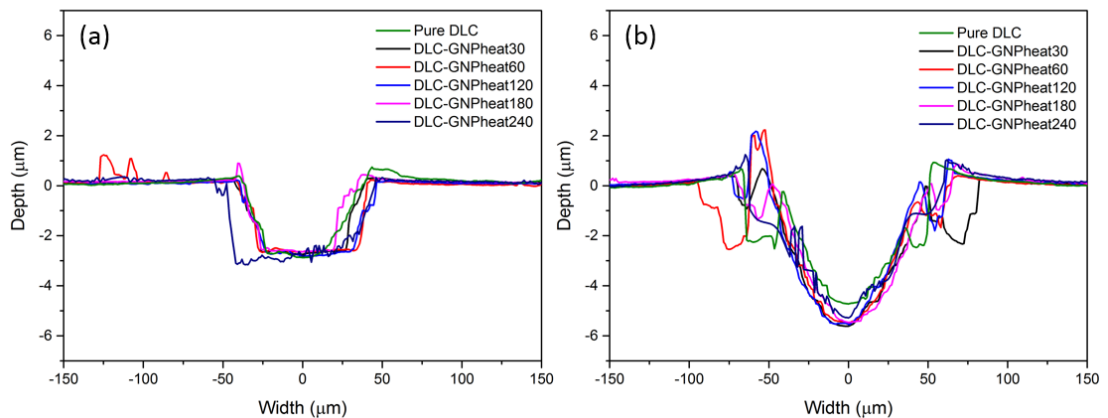
Figure 5.41 Scratch depth at (a) L_{C1} and (b) end of scratch for DLC-GNP post-treated coatings

5.5.6 Tribological tests

The tribological test was carried out using pin-on-reciprocating-plate tribometer in group III base oil to investigate the tribological behaviour of the coating after different durations of post-treatment. The details of the experimental conditions are described in Section 3.8. Each test was repeated for three times to ensure reliability and repeatability of the results.

Due to interesting tribological characteristics of sample DLC-GNPheat180, the extended sliding test was carried out to obtain the steady state coefficient of friction (CoF). In addition, the durability of the coating over extended sliding test up to 24 hours was also investigated.

5.5.6.1 Friction evaluation

Figure 5.42 represents the typical coefficient of friction (CoF) evolution of all four DLC-GNP treated for 30-240 minutes in base oil in three hours. Pure DLC was also tested as a comparison. As can be seen from the graph, it can be suggested that there are two stages of CoF progression. The first stage is a running-in stage which occurred in all samples at the beginning of the test. It is evident that the evolution of running-in stage for all DLC-GNP coatings was different from pure DLC. The next stage is when CoF begins to stabilise before reaching its steady-state condition. In the results, all samples except sample DLC-GNPheat180 and DLC-GNPheat240 showed an increase in CoF after the running-in stage. Both samples also have the shortest running-in stage compared to the others. Sample DLC-GNPheat180 did not reach its steady state during 3-hour test.

Example of repeatability of CoF trend for sample DLC-GNPheat180 is shown in Figure 5.43. The standard deviation was measured to be less than 10% for almost all test for all samples.
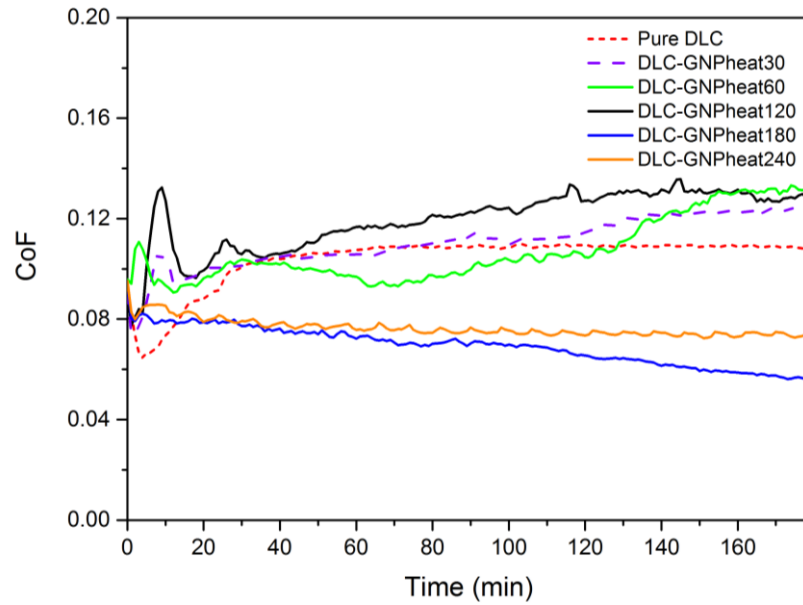
Figure 5.42 Representative CoF evolution of pure DLC and DLC-GNP (post-treated) samples as a function of sliding time in base oil for three hours on pin-on-reciprocating plate tribometer.
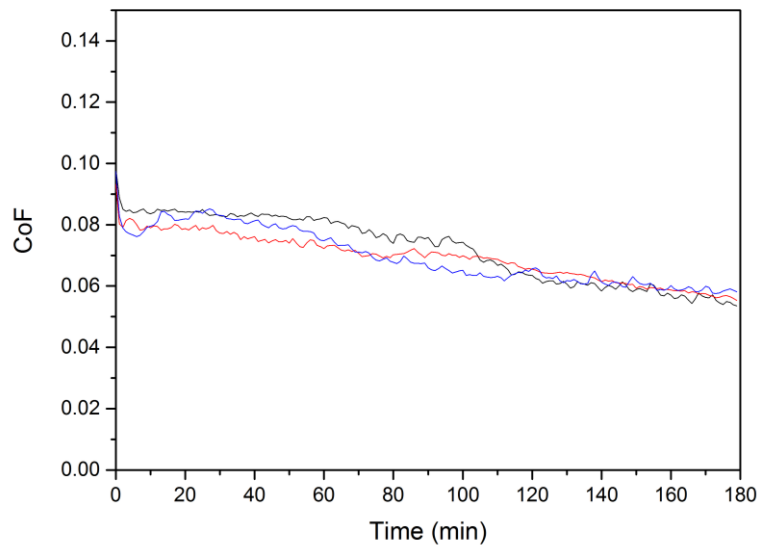
Figure 5.43 Example of repeatability of sample DLC-GNPheat180

The average CoF of all coatings as a function of post-treatment time is shown in Figure 5.44. The average CoF was measured in the last two hours of the test. The values of friction vary between 0.11 and 0.13 for all samples except for sample DLC-GNPheat180 and DLC-GNPheat240 which have the CoF of ~0.06 and 0.08. The average CoF for pure DLC was recorded to be approximately ~0.11.
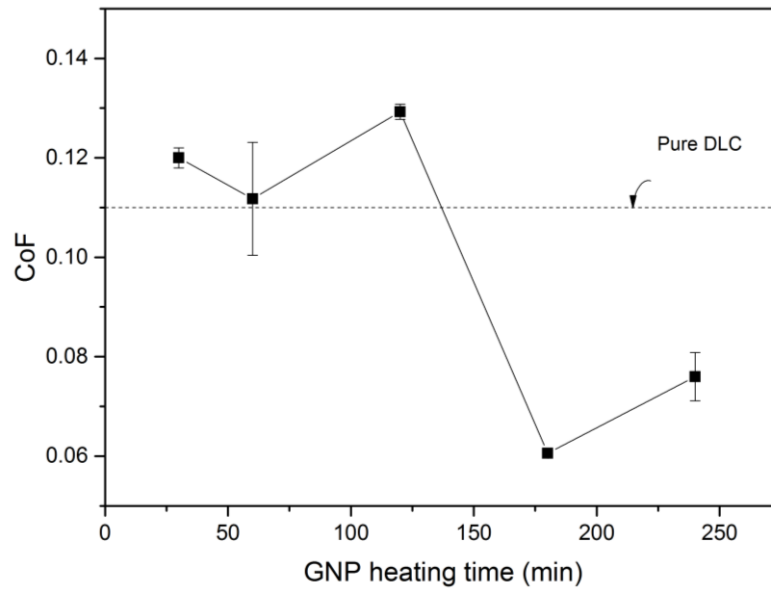
Figure 5.44 Average coefficient of friction for DLC-GNP (post-treated) coatings measured in the last two hours of the test. The errors bars indicate the standard deviation of three measurements

Figure 5.45 represents the relationship between values of coefficient of friction and surface roughness of coating surface before tribological tests were conducted. The graph shows that friction of DLC-GNP nanocomposite coating appeared to be independent of the surface roughness of coating.
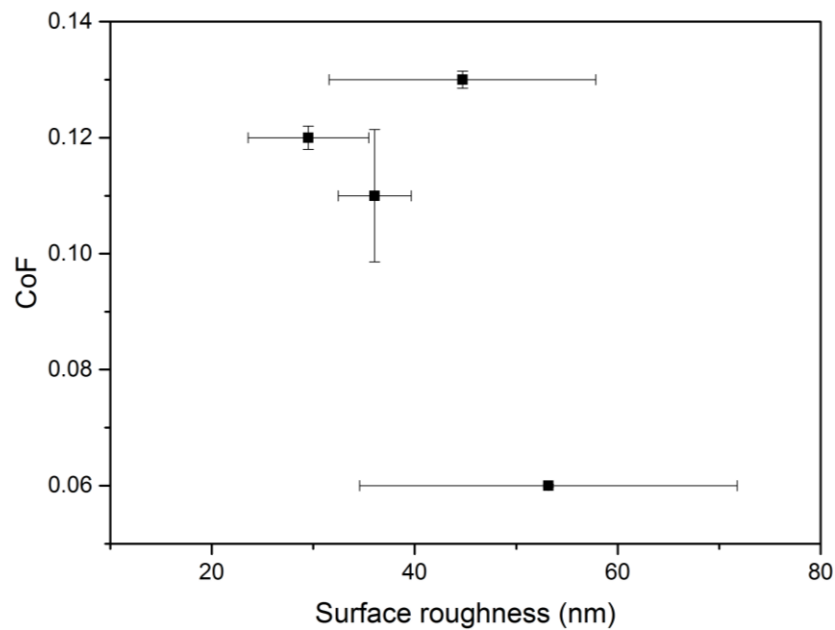
Figure 5.45 Relationship between CoF and DLC-GNP (Post-treated) surface roughness

163

5.5.6.2 Observation of wear track of coating and wear scar of the counterpart

In order to understand the tribological behaviour of coatings' wear, the wear scar depth, cross-sectional areas were investigated by optical microscopy and WLI. Figure 5.46 shows the optical micrographs of the worn track of all samples including pure DLC after 3-hour tests in base oil. As shown in the micrographs, the pure DLC coating remained intact without appreciable wear. The wear track width is measured to be approximately 1.1 mm. Samples DLC-GNPheat30, GNPheat60 and DLC-GNPheat120 were deeply abraded, and the machining marks were obvious. The wear tracks width range between 2.7 - 3.0 mm. Both sample DLC-GNPheat180 and DLC-GNPheat240 exhibit irregular delamination leaving columnar wear structure. Specific areas in the wear track remain intact adhered to the substrate.

Figure 5.47 show surface topographies of the wear tracks and the corresponding cross-section profile of the wear tracks. The lines and dot lines in the depth profile indicate the barrier of the substrate, interlayer, and DLC-GNP film layer. The wear on pure DLC coating in Figure 5.47(a) is very mild that the wear track is hardly distinguishable. DLC-GNPheat30, DLC-GNPheat60, and DLC-GNPheat120 have the most extensive wear. The wear depth reached the M2 HSS substrate having removed both DLC-GNP and interlayer completely. As mentioned earlier, samples DLC-GNPheat180 and DLC-GNP240 (Figure 5.47(e) and (f)) have completely different shape of wear topography. The wear tracks have a columnar structure. Delamination only occurred to reach the interlayer film for sample DLC-GNPheat180. For sample DLC-GNPheat240 where there were more delaminated areas than DLC-GNPheat180, delamination areas reached up to the substrate.
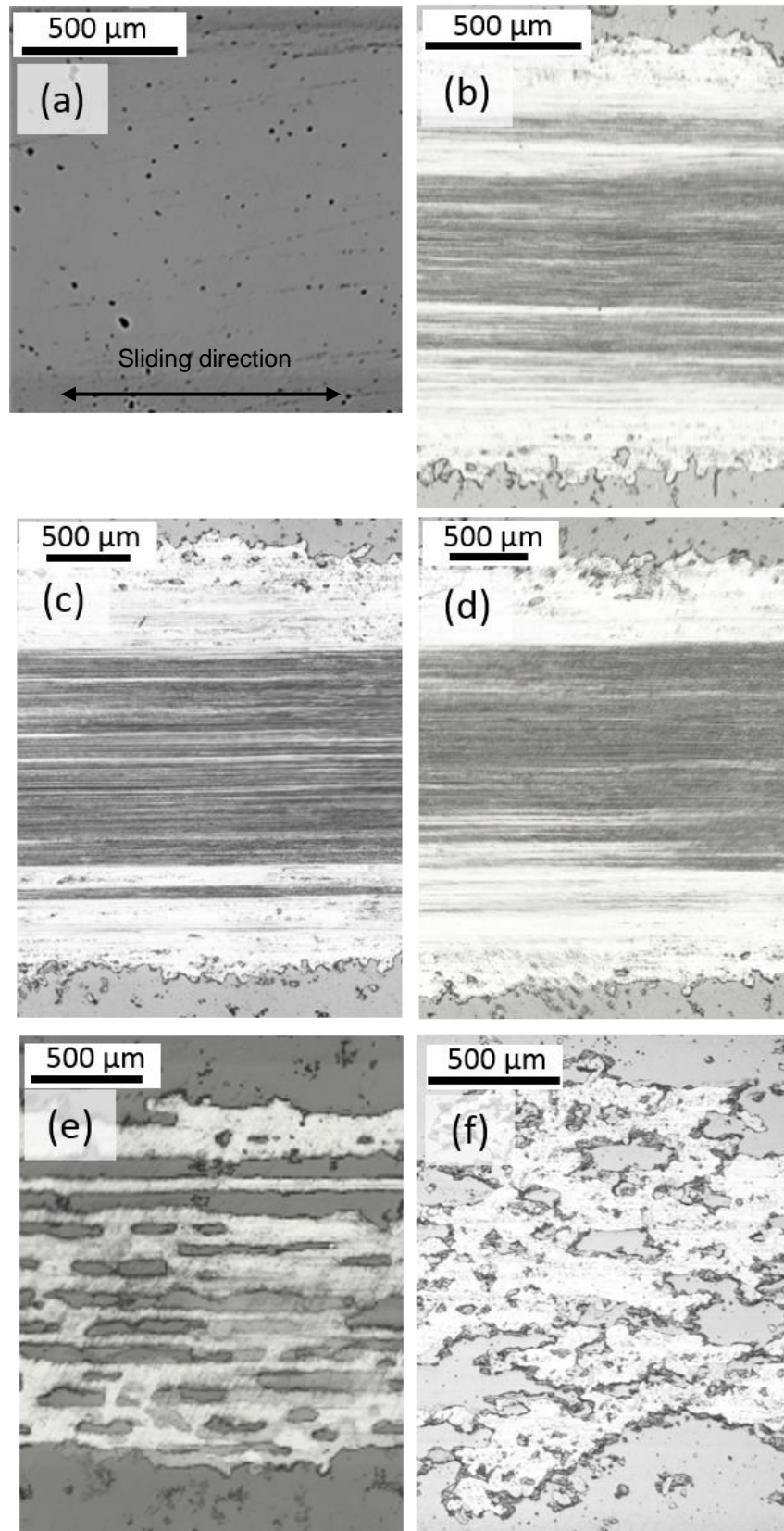
Figure 5.46 Wear images of (a) pure DLC, (b) DLC-GNPheat30, (c) DLC-GNPheat60, (d) DLC-GNPheat120, (e) DLC-GNPheat180 and (f) DLC-GNPheat240 after 3-hour of test in base oil

165
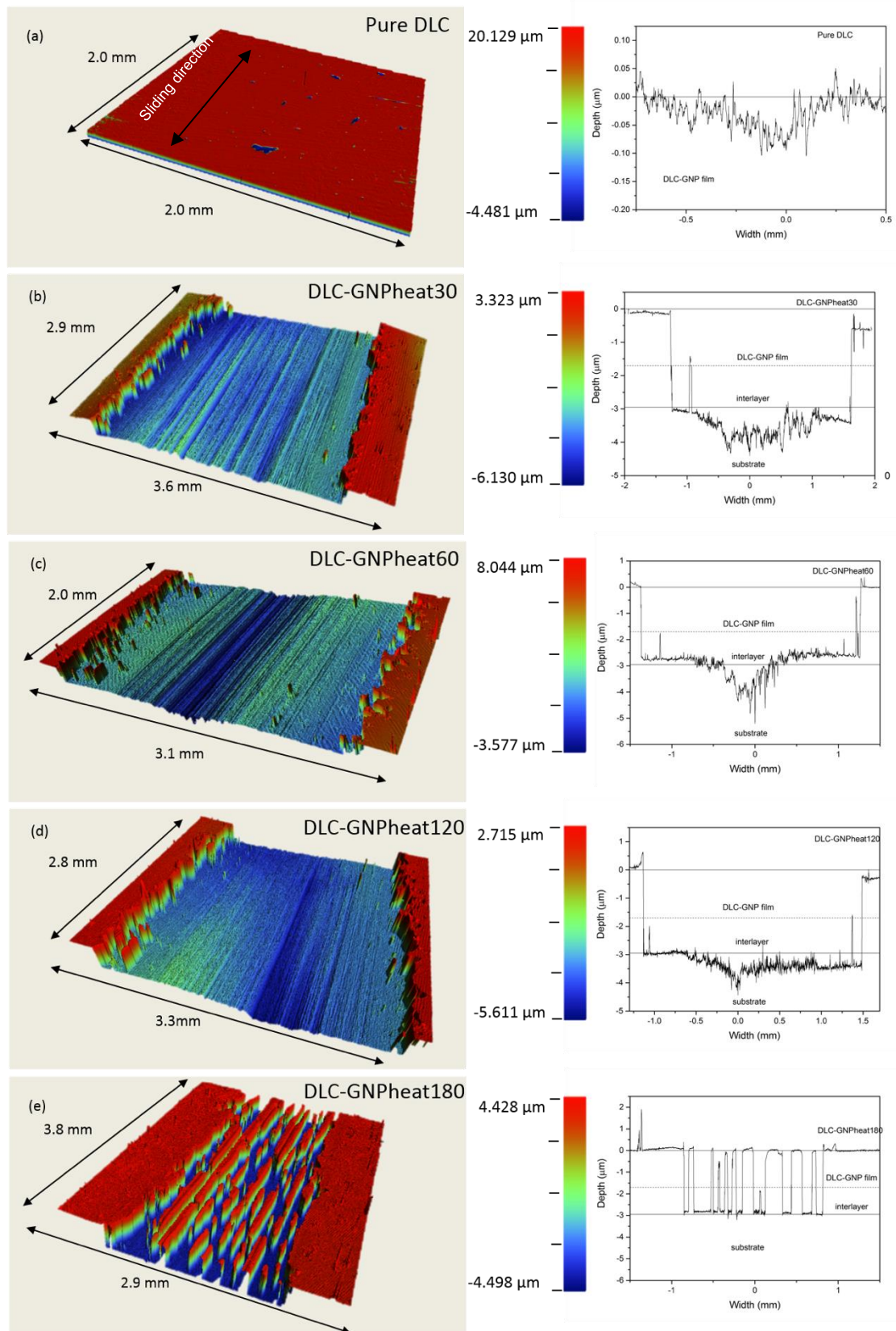
Figure 5.47 Surface topography and cross-section profiles of wear tracks for (a) Pure DLC, (b) DLC-GNPheat30, (c) DLC-GNPheat60, (d) DLC-GNPheat120, (e) DLC-GNPheat180 and (f) DLC-GNPheat240 respectively after three hours of tribotest in base oil. (Continue)
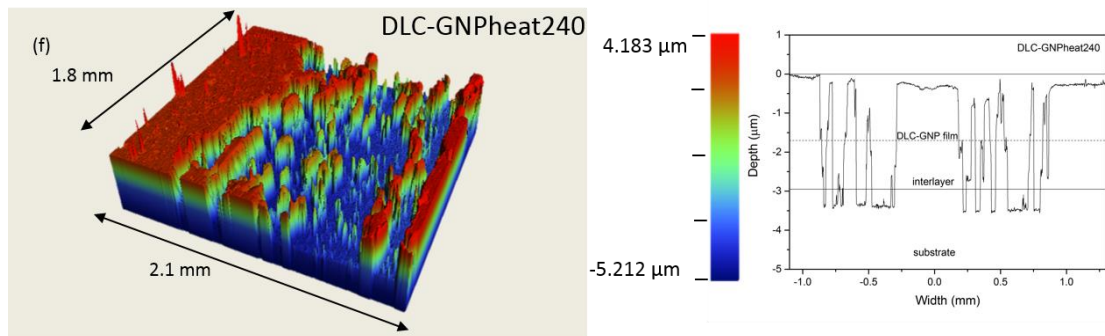
Figure 5.48 Surface topography and cross-section profiles of wear tracks for (a) Pure DLC, (b) DLC-GNPheat30, (c) DLC-GNPheat60, (d) DLC-GNPheat120 and (e) DLC-GNPheat180 and (f) DLC-GNPheat240 respectively after three hours of tribotest in base oil. (Continue)

The wear scars of the counterparts are shown in Figure 5.49 (a- f). The width of wear tracks for samples post-treated for 30 to 120 minutes have almost the same size of approximately 3.0 mm. Sample DLC-GNPheat180 has the smallest size of scar of about 2.0 mm. It should be noted that the estimation of diameter was made based on the largest side of wear scar. It is observed that dark transfer layers are present in the wear scars of all counterparts.

Figure 5.50 shows the topography of wear scar with the corresponding cross-section profile for cast iron counterpart of pure DLC and DLC-GNP post-treated samples. As can be seen earlier in the micrographs the surface of wear scar for counterpart DLC-GNPheat30, DLC-GNPheat60 and DLC-GNPheat120 are very rough and also larger than counterpart DLC-GNPheat180 and DLC-GNPheat240.
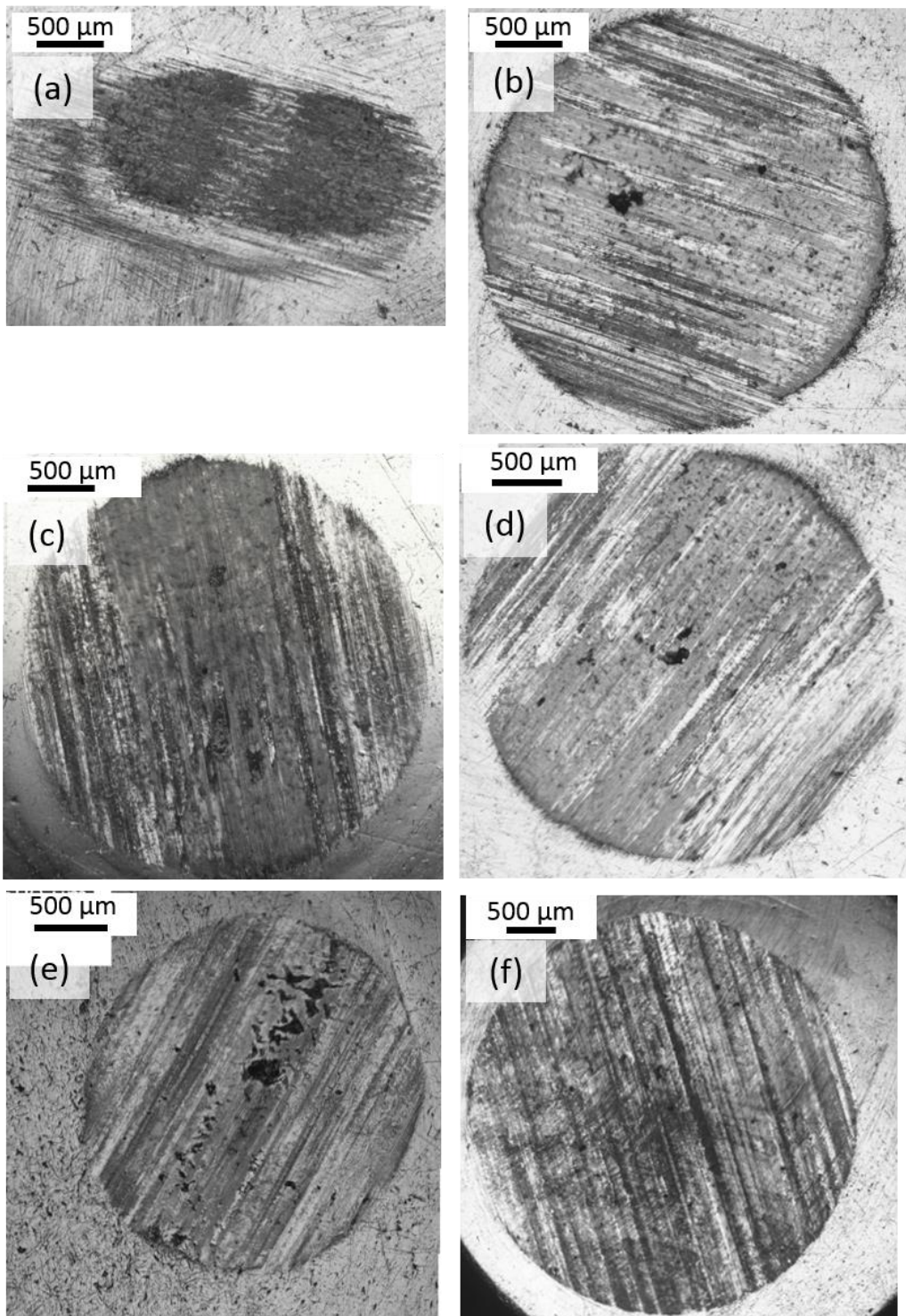
Figure 5.49 Optical images of counterpart wear scar of (a) Pure DLC, (b) DLC-GNPheat30, (c) DLC-GNPheat60, (d) DLC-GNPheat120, (e) DLC-GNPheat180 and (f) DLC-GNPheat240 after three hours of test in base oil
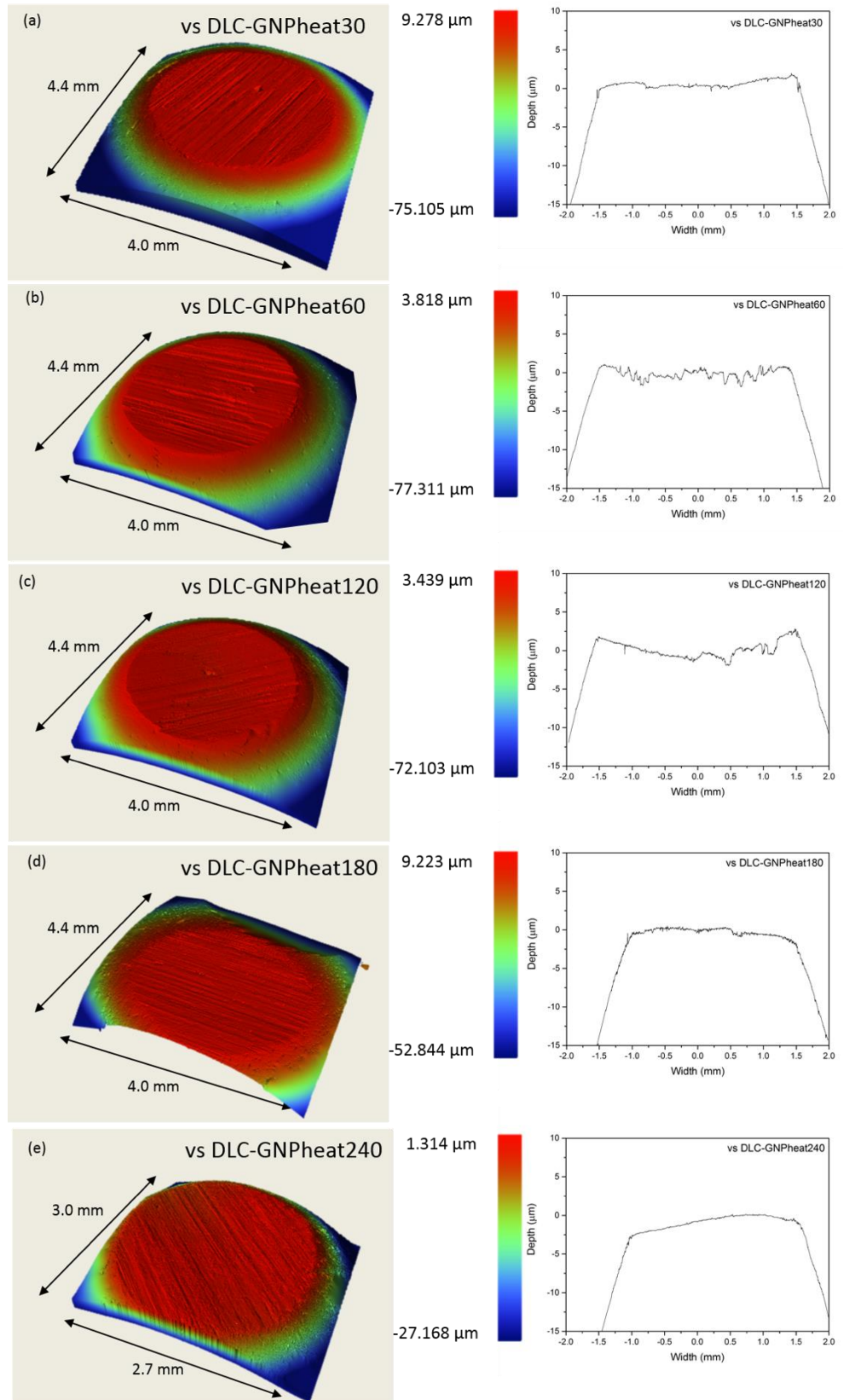
Figure 5.50 Surface topography and the corresponding cross-section profiles of the counterpart wear scar for (a) Pure DLC, (b) DLC-GNPheat30, (c) DLC-GNPheat60, (d) DLC-GNPheat120 and (e) DLC-GNPheat180

5.5.6.3 Analysis of wear rate of DLC-GNP (GNP post-treated)

The WLI and optical microscopy were employed to analyse the wear of all coatings. Due to the irregular shape of some of the wear tracks obtained in this work, wear volume of all wear tracks was measured using volume measurement tools in Vision64 software. The wear rate for the wear tracks of the coatings was calculated using Archard's equation as in Eq 3.2. Wear depth was also recorded as a reference.

The wear rate and the wear depth of DLC-GNP post-treated samples as a function of GNP heating time is shown Figure 5.51. There is almost no difference in wear rate and wear depth for samples DLC-GNPheat30, DLC-GNPheat60 and DLC-GNPheat120, which is in the range of ~6.6 – 7.1 x 10^{-7} mm^3/Nm. Wear rate of sample DLC-GNPheat180 and DLC-GNPheat240 is reduced to more than half that of other samples. The wear depth is consistent with the measured of wear rate. The wear rate of pure DLC is recorded to be ~ 0.13 x10^{-7} mm^3/Nm.
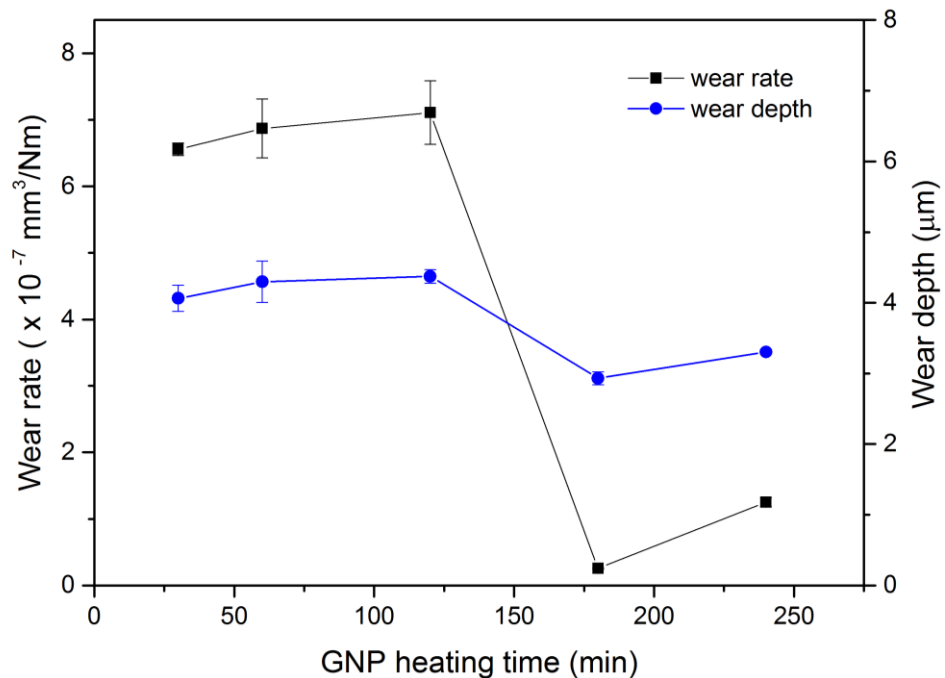
Figure 5.51 Wear rate for DLC-GNP post-treated samples after tribological test in base oil for three hours

Figure 5.47 represents the comparison of CoF and the corresponding wear rate of coating for pure DLC and DLC-GNP post-treated samples. Despite having almost the same CoF to pure DLC, samples DLC-GNPheat30, DLC-GNPheat60 and GNPheat120 exhibit higher wear rate. The CoF of post-treated DLC-GNP is consistent with the wear rate. Sample DLC-GNPheat180 exhibits the lowest CoF and wear rate of all.
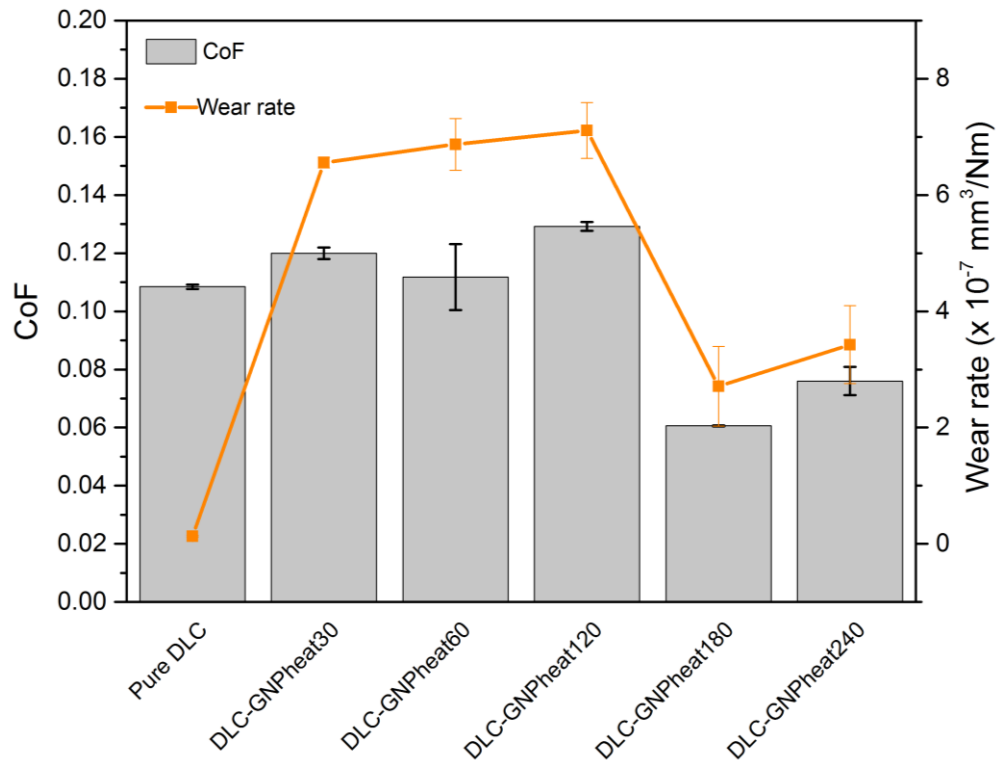
Figure 5.52 Comparison of CoF and wear rate of GNP post-treated samples of DLC-GNPheat30, DLC-GNPheat60, DLC-GNPheat120, DLC-GNPheat180, DLC-GNPheat240 and pure DLC as a comparison.

5.5.6.4 Analysis of the wear rate of the counterpart of DLC-GNP (GNP post-treated)

Wear volume of all counterparts was measured using WLI and calculated using Eq 3.5 and 3.6. The wear rate was calculated using Eq. 3.7. The wear rate for the cast iron counterparts for 3-hour tests in base oil is plotted in Figure 5.53. As a comparison, the wear rate of pure DLC counterpart is recorded to be 1.58 x 10^{-2} mm^3/Nm. A significant reduction of wear rate of counterpart was observed when samples were heated more than 180 minutes.
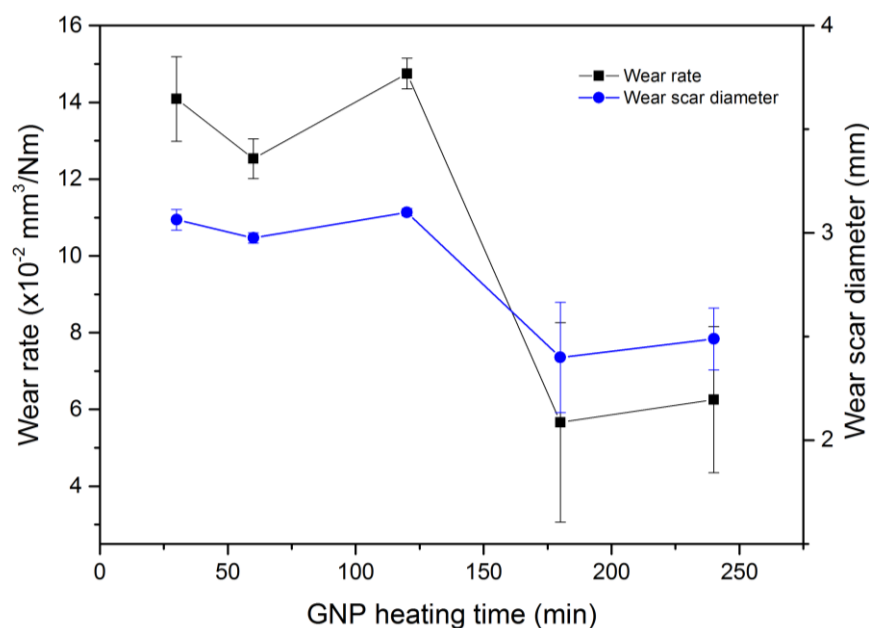
Figure 5.53 Wear rate of cast iron counterpart pins as a function of GNP heating time after sliding against DLC-GNP(Post-treated) coating for three hours test in base oil

5.5.6.5   Raman analysis of wear

Raman analyses of the wear tracks and scars were carried out to evaluate the structure present for better understanding and interpretation of its tribological behaviour. The spectra measurement was performed at several areas within the wear track as well as the counterpart wear scar. All samples and counterparts have undergone copious cleaning with heptane with ultrasonic bath. The results of this section will contribute to understanding the wear mechanism of DLC-GNP post-treatment process was carried out on samples.

Figure 5.54 presents the Raman spectra obtained inside the wear track after three hours of the testing in base oil. The spectra were deconvoluted using Gaussian and Lorentz functions. D- and G-peaks are the most prominent peaks that can be observed in all Raman spectra. The wear track of pure DLC exhibits similar spectra to that of pure DLC in both wear areas. The other wear tracks of samples were either a mixture of DLC and disordered graphitic structure or both display disordered graphitic structure. The D- and G-peaks in DLC-GNPheat30 and DLC-GNPheat60 have the lowest intensity of all. Another peak that sometimes appears in the measurement at around ~670 cm^{-1} may belong to Fe-oxide.

172
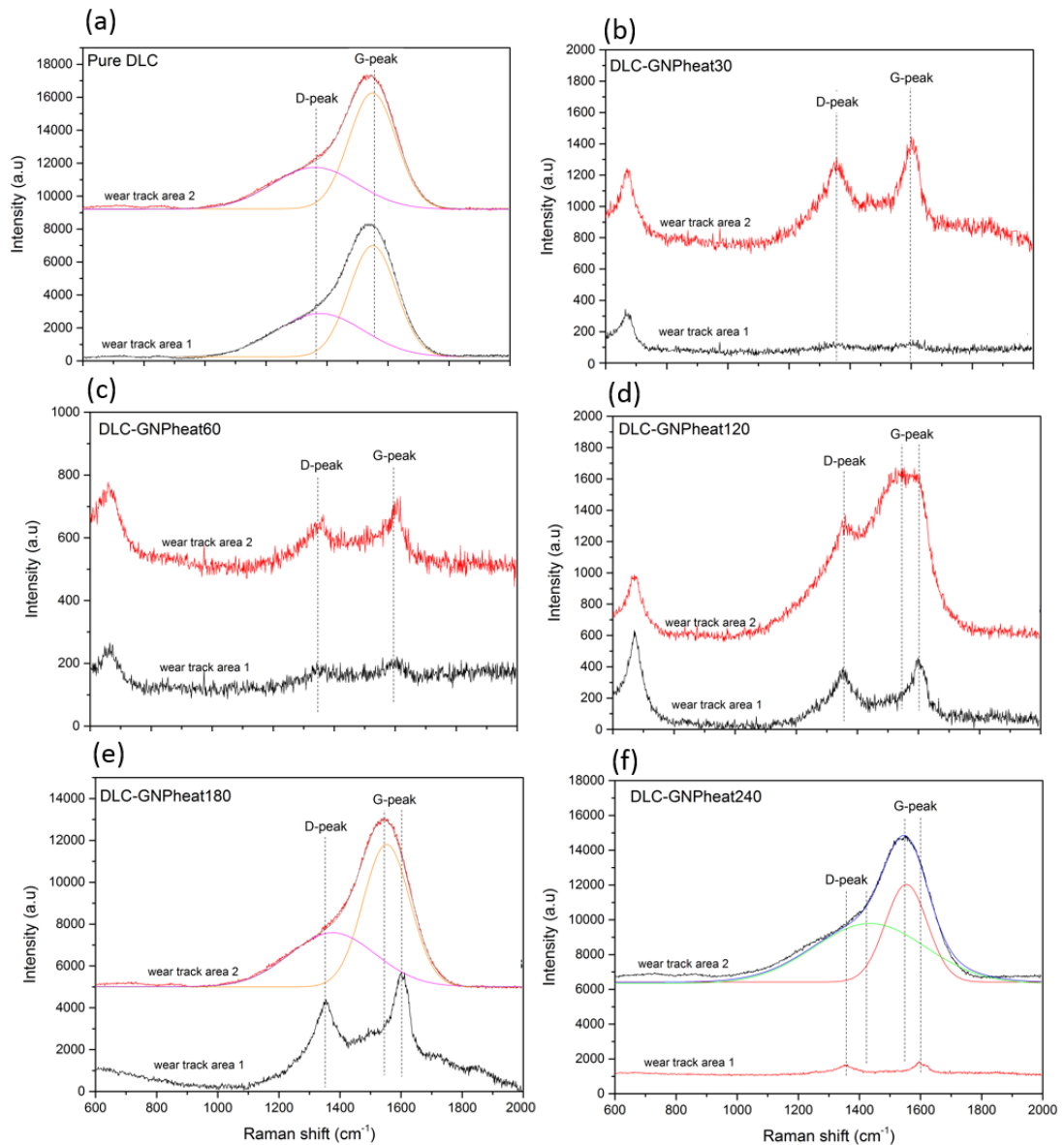
Figure 5.54 Raman spectra collected within the wear track of (a) pure DLC and DLC-GNP (GNP Post-treated) of (b) DLC-GNPheat30, (c) DLC-GNPheat60, (d) DLC-GNPheat120, (e) DLC-GNPheat180 and (f) DLC-GNPheat240

As summary of the position of the characteristic peaks (D, G and Fe-oxide) and the I_D/I_G ratio is summarized in Table 5.8. Except for the wear track of pure DLC and an area on wear track of DLC-GNPheat180, all other samples show an increase of I_D/I_G ratio. The increase of I_D/I_G implies the increase of carbon-carbon disorder contributing to a reduction of CoF due to the irregularity of the bonds [182]. It can also be observed that the G-peak shifted to the higher wave number when the I_D/I_G ratio increased. The peak of Fe-oxide appeared in the

173

three post-treated samples of DLC-GNPheat30, DLC-GNPheat60 and DLC-GNPheat120.

Table 5.8 Position and integrated intensity I_D/I_G of the main peaks in Raman spectra within the wear tracks of pure DLC and DLC-GNP (post-treatment)

Sample	Area	G-peak position (cm^{-1})	D-peak position (cm^{-1})	Fe-oxide position (cm^{-1})	I_D/I_G
Pure DLC	Wear track area 1	1550	1377	-	0.39
	Wear track area 2	1549	1360	-	0.36
DLC-GNPheat30	Wear track area 1	1603	1357	668	0.94
	Wear track area 2	1597	1359	671	0.76
DLC-GNPheat60	Wear track area 1	1595	1355		0.67
	Wear track area 2	1595	1355	661	NA
DLC-GNPheat120	Wear track area 1	1598	1355	670	0.77
	Wear track area 2	1555	1373	670	0.56
DLC-GNPheat180	Wear track area 1	1594	1356	-	0.76
	Wear track area 2	1553	1376	-	0.38
DLC-GNPheat240	Wear track area 1	1554	1435	-	0.62
	Wear track area 2	1598	1355	-	0.76

Figure 5.55 shows the I_D/I_G ratio on the wear tracks as a function of GNP heating time. The shaded area represents the range of I_D/I_G ratio of as-prepared coatings before sliding. The horizontal lines represent the I_D/I_G on the wear track of pure DLC. As can be seen, most of the value of I_D/I_G are outside and higher than the range of the as-prepared coating. Only two areas in the wear track of sample DLC-GNPheat120 and DLC-GNPheat180 have similar I_D/I_G as the as-prepared coating. The results demonstrate that graphitisation occurred on all coatings after 3-hour sliding wear. However, graphitisation does not arise in all areas in wear track of sample DLC-GNPheat120 and DLC-GNPheat180. The value of I_D/I_G appears to decrease as the heat-treatment is increased from 30 to 120 minutes before remaining almost the same.
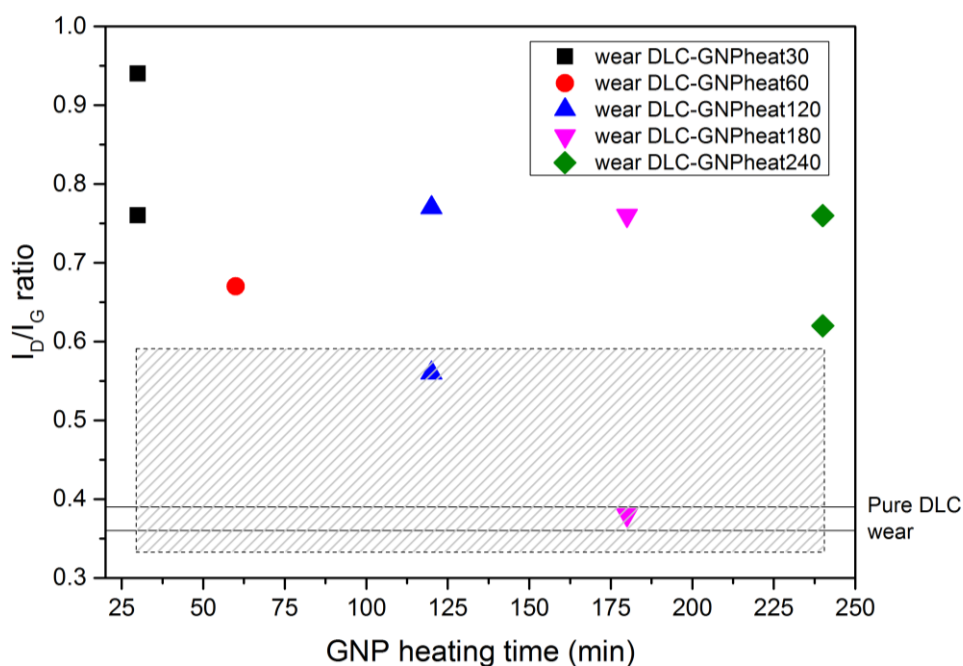
Figure 5.55 I_D/I_G ratio of wear track as a function of GNP heating time of post-treatment

The Raman spectra of the wear scar on counterparts are displayed in Figure 5.56. The spectra for a clean counterpart of cast iron also is presented in Figure 5.57 as a reference. Most of the spectra of wear scars display a very similar spectrum to that of highly disordered graphite [183]. Some show a broad D- and G-peaks similar to that of amorphous carbon. A peak at around ~680 cm^{-1} also appears in some of the spectra, which may belong to Fe-oxides.

Table 5.9 summarises the main peaks positions and the I_D/I_G ratios of all the wear scars on the counterparts. The spectra exhibit D and G-peak with wave number oscillating at 1350 - 1411 cm^{-1} and 1567 - 1600 cm^{-1} respectively. The I_D/I_G ratio is between a huge range from 0.47 to 1.06. There is evidence of film transfer from DLC-GNP composite to the counterpart. Fe-oxide peak is found on all coatings except DLC-GNPC0.25 and is believed to come from the substrate as the delamination reached to substrate level.
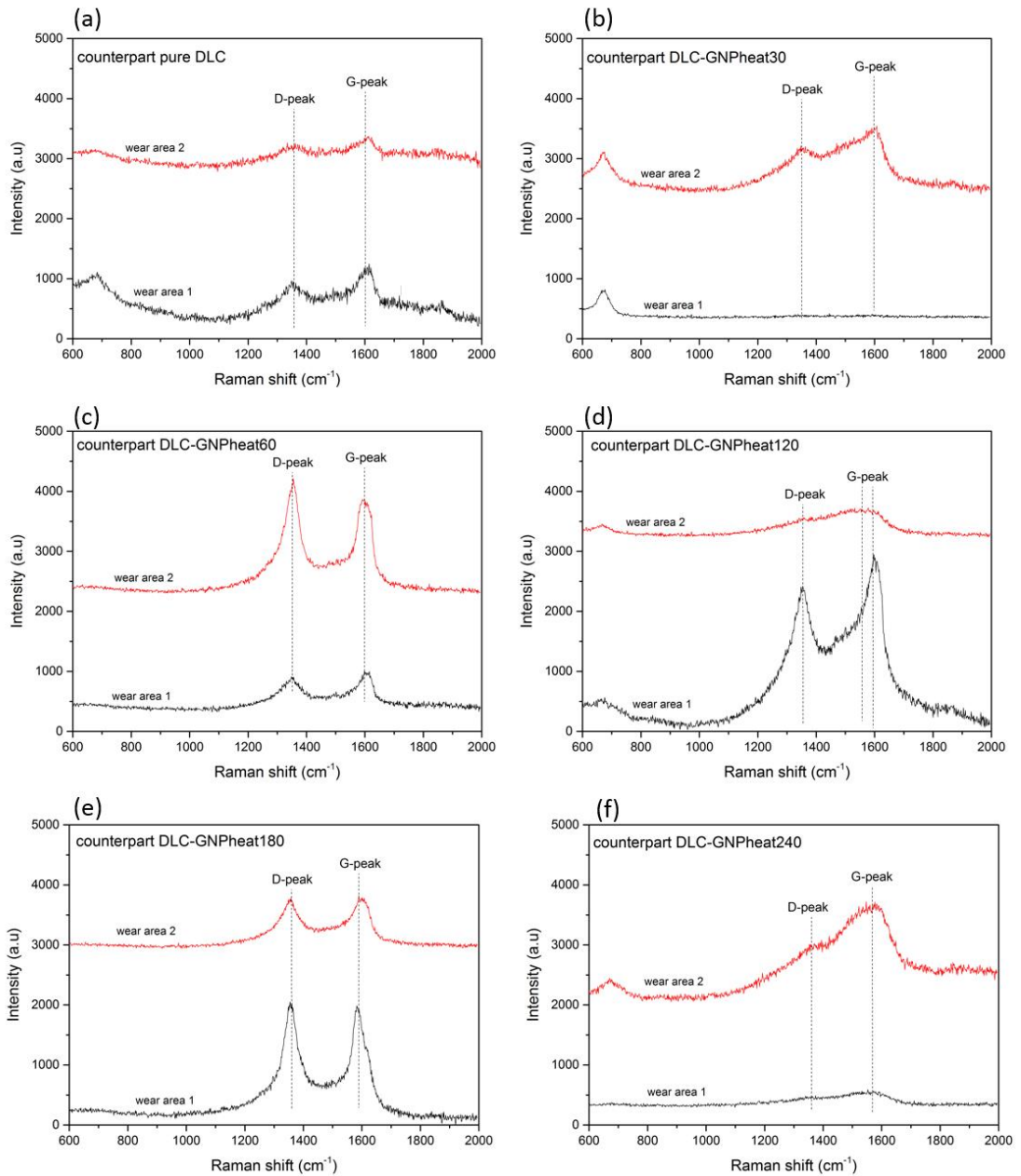
Figure 5.56 Raman spectra collected within the wear scar of counterpart (a) pure DLC, (b) DLC-GNPheat30, (c) DLC-GNPheat60, (d) DLC-GNP120, (e) DLC-GNPheat180 and (f) DLC-GNPheat240
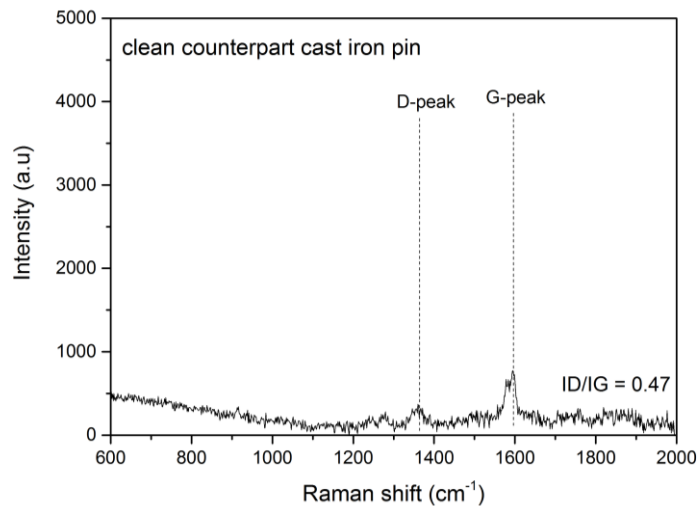
Figure 5.57 Raman spectra of clean cast iron pin counterpart

Table 5.9 Position and integrated intensity I_D/I_G of the main peaks in the Raman spectra within the wear scars of pure DLC and DLC-GNP (post-treatment) counterparts

Counterpart	Area	D-peak position (cm^{-1})	G-peak position (cm^{-1})	Fe-oxide position (cm^{-1})	I_D/I_G
Pure DLC	Wear area 1	1359	1600	684	0.59
	Wear area 2	1357	1600	-	0.69
DLC-GNPheat30	Wear area 1	-	-	671	-
	Wear area 2	1376	1574	671	0.61
DLC-GNPheat60	Wear area 1	1349	1598	-	0.82
	Wear area 2	1350	1595	-	1.06
DLC-GNPheat120	Wear area 1	1357	1586	668	0.77
	Wear area 2	1402	1567	668	0.75
DLC-GNPheat180	Wear area 1	1353	1598	-	0.92
	Wear area 2	1357	1598	-	0.96
DLC-GNPheat240	Wear area 1	1408	1567		0.81
	Wear area 2	1411	1567	672	0.78
Clean Cast iron counterpart		1361	1597	-	0.47

5.5.6.6 Extended test for DLC-GNPheat180 nanocomposite coatings

In addition to the 3-hour test in base oil, an extended time test was also conducted on the sample DLC-GNPheat180 to investigate the steady-state

friction of the coating and to study its durability. Test conditions were kept the same as sliding times were extended to 6, 12 and 24 hours.

Figure 5.58 shows the evolution of average CoF for sample DLC-GNPheat180 in base oil from 3 to 24-hour test. The average CoF was calculated from the final two hours of each test. The CoF appears to be reduced to ~ 0.05 after 6-hour of test before increasing to ~ 0.07 and remained almost the same. The increased of CoF after 6-hour test may be due to the increased of wear after 6-hour test that generated more wear debris thus increased the mechanical vibration in the sliding system.
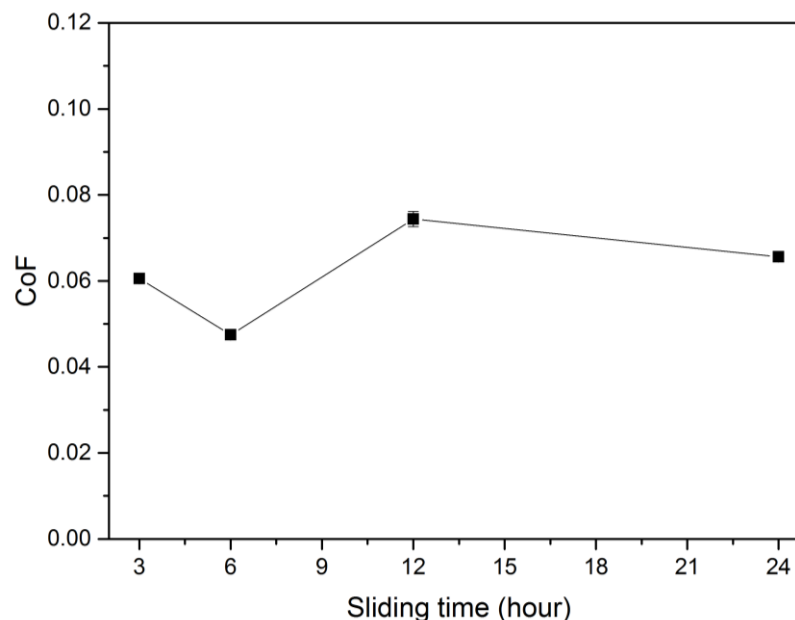
Figure 5.58 The CoF of DLC-GNPheat180 as a function of sliding time in base oil for six hours with pin-on-reciprocating plate tribometer.

Durability test of the coating was conducted for 6, 12 and 24 hours. Figure 5.59 presents the surface topographies of the wear tracks after 6, 12 and 24-hour test. It is interesting to see that the columnar structure remained almost unchanged even after 24-hour of sliding test although the CoF increased after 12-hour of testing. The depth of the wear also is more or less the same as earlier wear tracks of DLC-GNPheat180 after 3-hour test which is around ~ 3.0 μm. Figure 5.60 summarises the measured wear rate and depth of the wear track after 6, 12 and 24 hours of sliding test. Only slight increases of wear

depth can be observed after 6-hour tests before remaining almost equivalent even after 24 hours. A rise of wear rate can be seen after 6-hour tests and the rate reduced as the time progressed. This indicates that there is only low levels of wear occurring after 6-hour of testing.
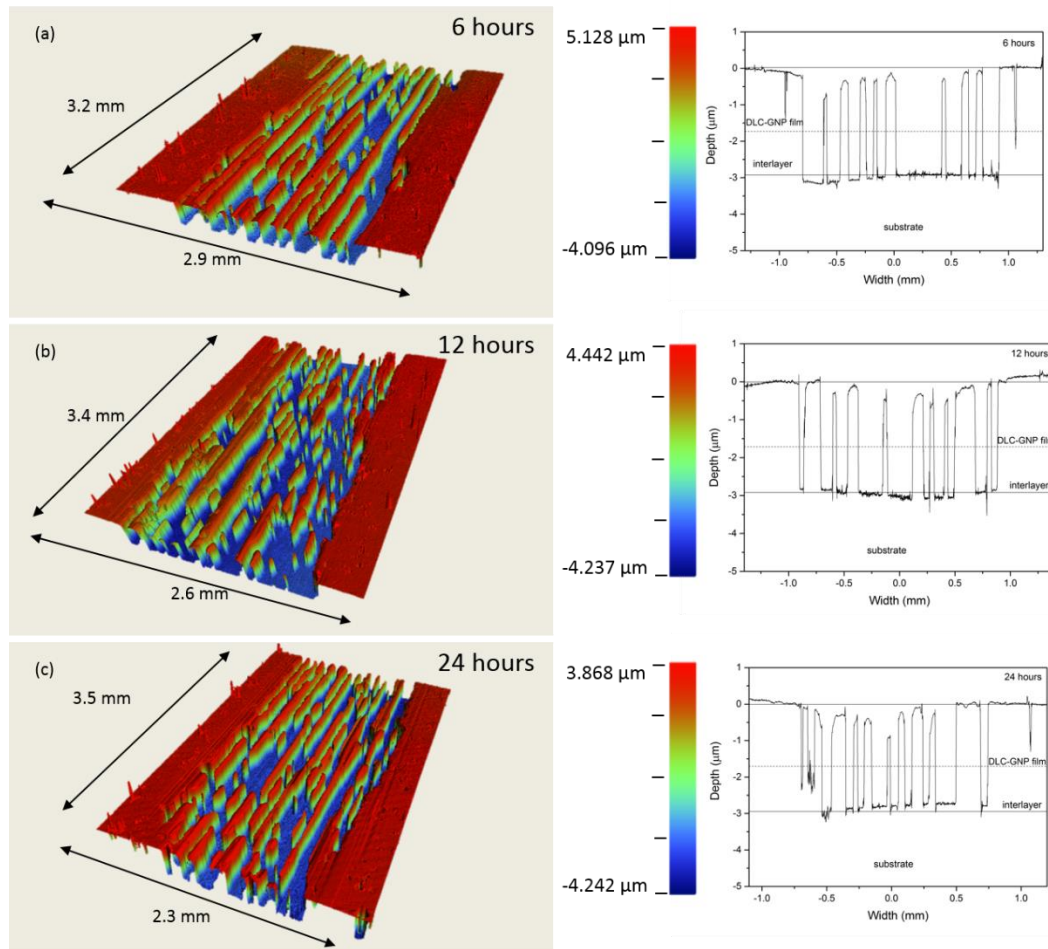
Figure 5.59 Surface topography and cross-section profiles of the wear tracks for DLC-GNPheat180 after sliding test of (a) 6 hours, (b) 12 hours and (c) 24 hours
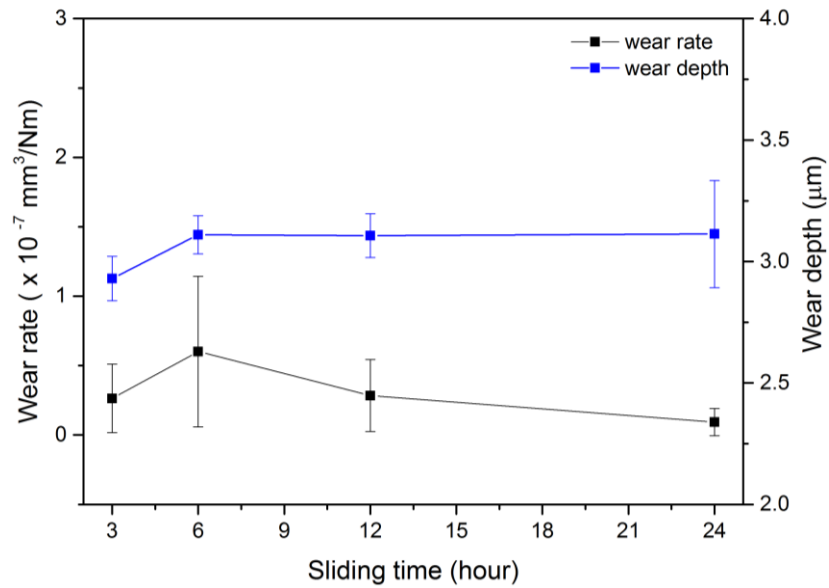
Figure 5.60 Wear rate and depth for DLC-GNPheat180 as a function of sliding time from 3 to 24 hours

5.5.7 Summary of effect of post-treatment

Based on the results obtained of post-treatment between 30 and 240 minutes, the following is the summary of this section:

i. Post-treatment does improve adhesion of GNP to the substrate as well as adhesion of GNP to GNP layers.

ii. The DLC-GNP prepared with post-treatment process has smoother and flatter morphology compared to DLC-GNP without post-treatment.

iii. Critical load of DLC-GNP nanocomposite coating increased as the post-treatment duration was increased, but slightly decreased when post-treatment time was increased to 240 minutes.

iv. Sample DLC-GNPheat180 recorded the lowest average CoF of 0.06 and better wear rate compared to samples without post-treatment.

v. A tribolayer from a mixture of reordered C-C structure and FeO appeared in almost all wear tracks on the coating and wear scars on the counterpart.

5.6 Effect of GNP Concentration on the Characteristics of DLC-GNP Nanocomposite Coating

On the study of the effect of GNP concentration, GNPs were spin-coated on substrate using the same parameter as used in Section 5.5 where the spinning speed, spinning time, amount of GNP used were 1000 rpm, 30 seconds, 1.0 mL respectively. All samples have been through a post-treatment process with the heating time fixed at one hour. One hour has been selected as the test was carried out before the final results of Section 5.5 has been obtained. Concentration of GNP used were 0.25, 0.50, 1.0 and 2.0 mg/mL. The range of concentration was chosen as it is the most commonly reported concentration of GNP in solvent [135, 140, 184, 185]. The DLC-GNP nanocomposite coatings prepared in this section are abbreviated as DLC-GNPC0.25, DLC-GNPC0.50, DLC-GNPC1.0 and DLC-GNPC2.0 for coating deposited with GNP concentration of 0.25, 0.50, 1.0 and 2.0 mg/mL respectively The parameters used for each spin-coated GNP and DLC-GNPP composite samples are summarized in Table 5.10.

Table 5.10 Experimental parameters for preparation of GNP and DLC-GNP with different GNP concentration samples

Sample	GNP concentration (mg/mL)	Spinning speed (rpm)	Spinning time (sec)	GNP amount (mL)	Post-treatment heating duration (min)	DLC deposition time (hour)
GNPC0.25	0.25					
GNPC0.50	0.50	1000	30	1	60	-
GNPC1.0	1.0					
GNPC2.0	2.0					
DLC-GNPC0.25	0.25					
DLC-GNPC0.50	0.50	1000	30	1	60	4
DLC-GNPC1.0	1.0					
DLC-GNP2.0	2.0					

5.6.1 Surface morphology and surface roughness of spin-coated GNP

Spin-coated GNPs were observed under the optical microscope to investigate the effect of GNP concentration on the distribution and size of GNP islands. Figure 5.61 represent the typical optical micrographs of spin-coated GNP at different concentrations of 0.25, 0.5, 1.o and 2.0 mg/mL of GNP. Micrographs on the right side are the higher magnification images of spin-coated GNP. It can be seen that the distribution of GNP on surface increased as the concentration of GNP increased. This is expected as the number of GNP is greater as we increase the concentration of GNP. It can also be observed that the size of GNP islands is increased with GNP concentration. Sample GNPC1.0 has the most evenly dispersed spin-coated GNP of all. The distance between each GNP is becoming closer as the concentration increased thus promoted high surface area GNP to attach to each other due to Van der Waals forces.
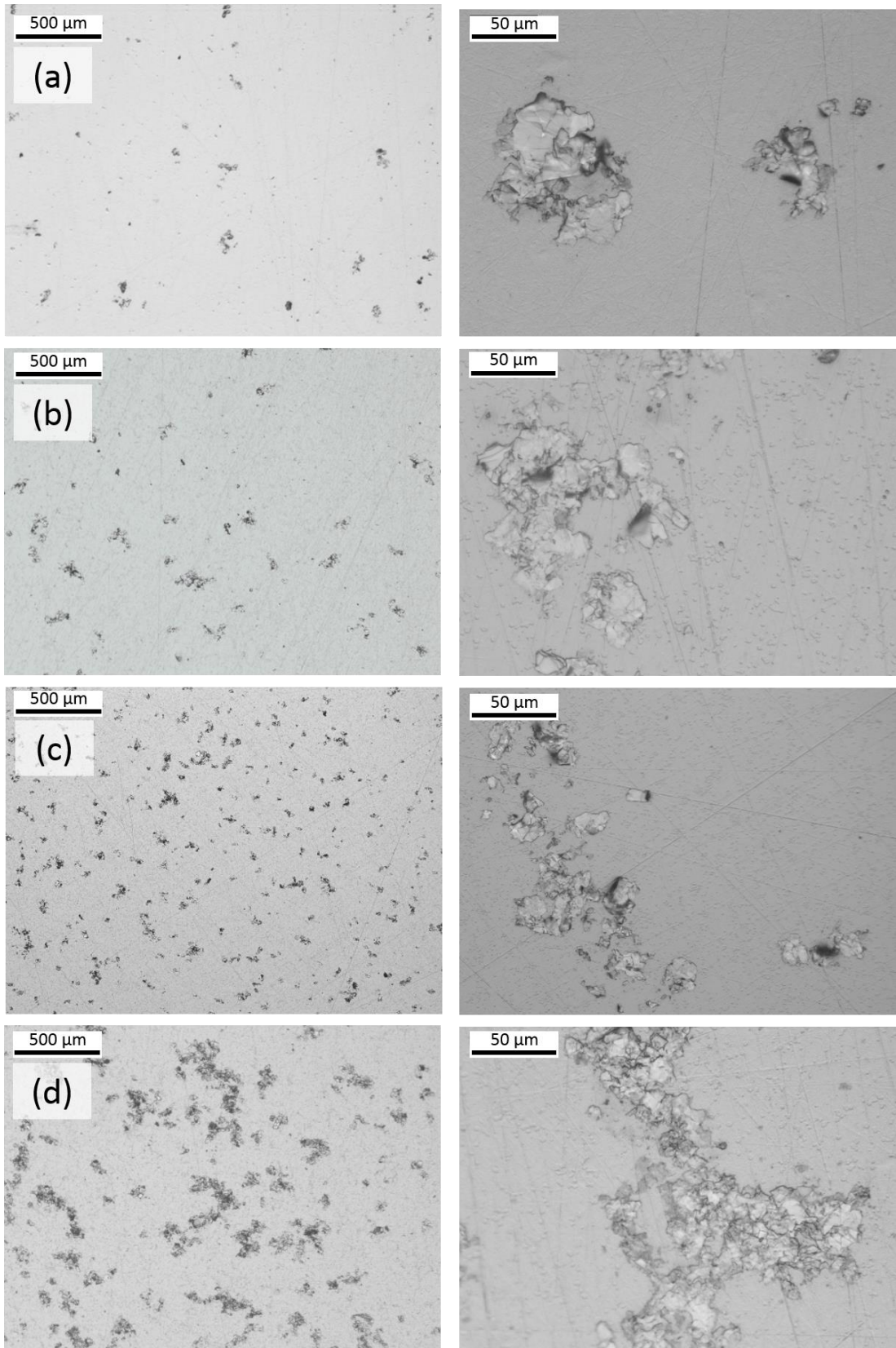
Figure 5.61 Optical micrographs of spin-coated GNP at different concentration of (a) 0.25 mg/mL, (b) 0.50 mg/mL, (c) 1.0 mg/mL and (d) 2.0 mg/mL. The corresponding high magnification of the optical micrographs is shown on the right side of each micrograph

A distribution versus concentration plot of spin-coated GNP on surface measured by ImageJ is shown in Figure 5.62. The percentage of GNP distribution increased almost linearly with GNP concentration. The highest GNP distribution was achieved with sample DLC-GNPC2.0 measured as 8.53 ± 2.5 %.
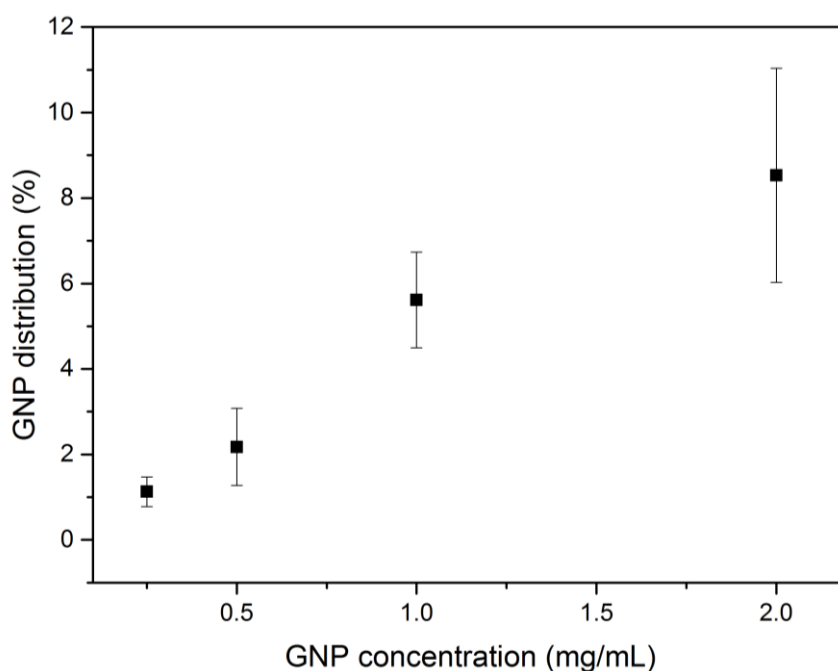
Figure 5.62 Coverage distribution of spin-coated GNP as a function of GNP concentration. The errors bars indicate the standard deviation of ten measurements.

The size of GNP island is measured and plotted in Figure 5.63. As expected, the size of GNP island increased with GNP concentration. Although the mean size is almost the same for sample GNPC1.0 and GNPC2.0, GNPC2.0 has a larger standard deviation. This demonstrates a wide range of sizes of GNP islands on the surface which also indicates the uneven distribution of GNP on the surface.

184
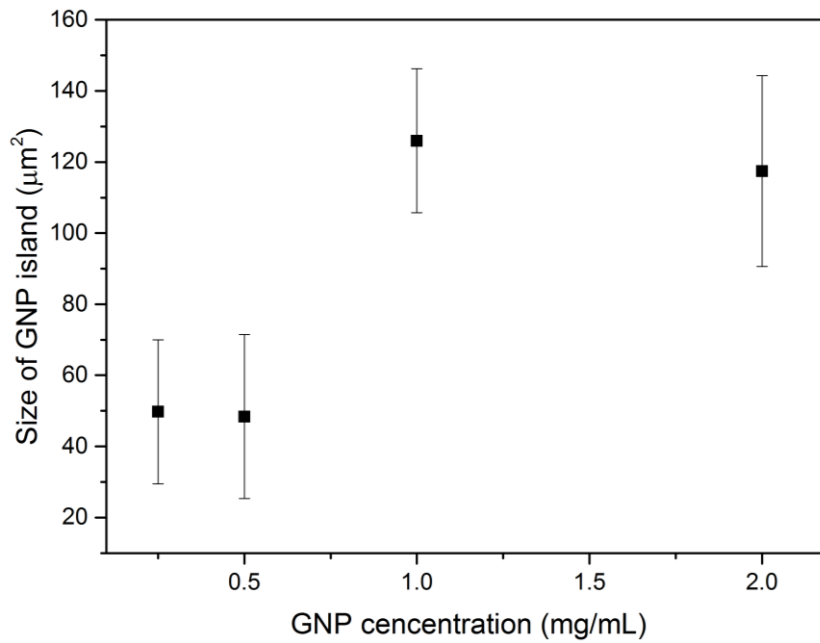
Figure 5.63 Size of spin-coated GNP island by a function of GNP concentration

The surface roughness of spin-coated GNP was measured using WLI and plotted in Figure 5.64. Surface roughness increased with GNP concentration. The highest surface roughness was achieved at 26 nm when the concentration of GNP was at 2.0 mg/mL with also the highest standard deviation. This result agreed with what has been predicted previously in Figure 5.61.
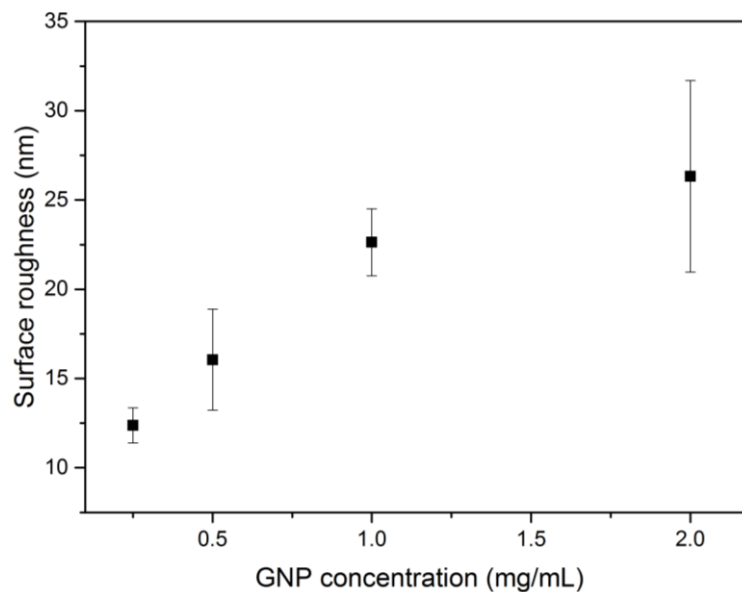
Figure 5.64 Surface roughness of GNP spin-coating in the function of GNP concentration

5.6.2 Raman analysis of spin-coated GNP

Raman spectra of spin-coated GNP was analysed to investigate the effect of GNP concentration on their chemical structure. Figure 5.65 represents the typical Raman spectra of spin-coated GNP at different concentrations. It is evident that all samples have the typical appearance of G- and 2D-peaks with almost unnoticeable D-peak. No obvious change between the Raman spectra can be observed.
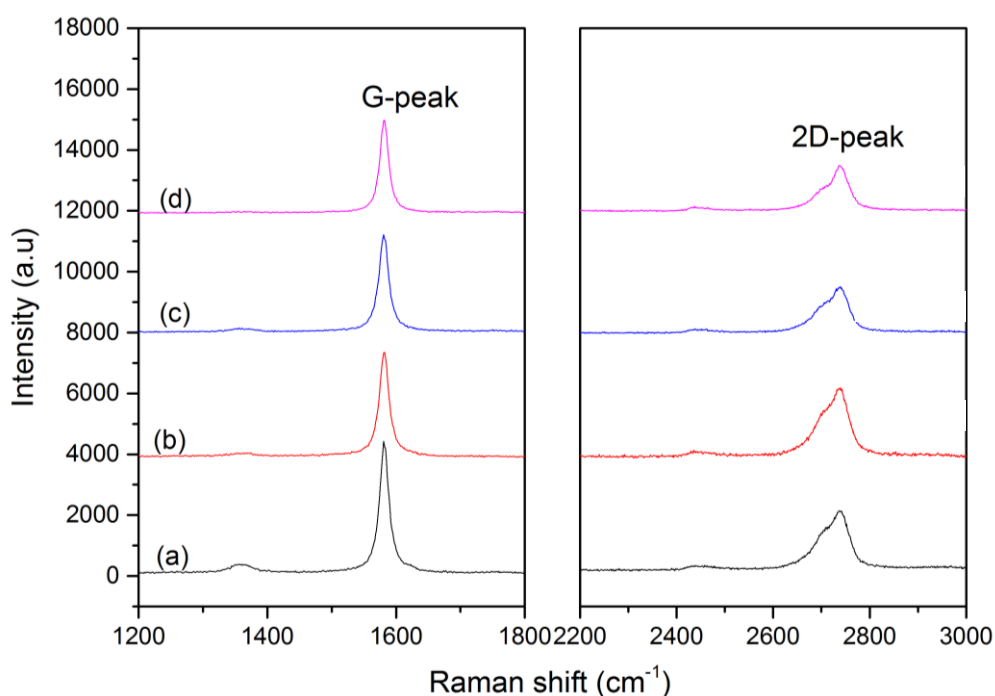
Figure 5.65 Representative Raman spectra of spin-coated GNP at concentration of (a) 0.25, (b) 0.50, (c) 1.0 and (d) 2.0 mg/mL respectively

The G-peak, 2D-peak and I_G/I_{2D} ratio obtained from three different spots in samples is summarized in Table 5.11. The G-peak position is almost similar in all samples in that it varies between 1581 - 1582 cm^{-1}. There is also no noticeable difference of 2D-peak point in any of the samples. The 2D-peak was deconvoluted to 2D$_1$- and 2D$_2$-peaks as has been shown earlier in Figure 5.31. The I_G/I_{2D} values were recorded in the range of values of 2.26 - 3.05.

The position of G-, 2D$_1$-, and 2D$_2$-peaks were then plotted in Figure 5.66. There seem to be no apparent changes of the peaks intensity regardless of GNP

concentration. The results confirmed no changes of GNP structure when the concentration was reduced or increased.

Table 5.11 Position and integrated intensity I_G/I_{2D} of the main peaks in Raman spectra of spin-coated GNP at different concentration

Sample	G-peak position (cm^{-1})	2D$_1$-peak position (cm^{-1})	2D$_2$-peak position (cm^{-1})	I_G/I_{2D} ratio
GNPC0.25	1581-1582	2741-2742	2706-2710	2.75-3.05
GNPC0.5	1581-1582	2739-2743	2703-2718	2.64-2.96
GNPC1.0	1581	2740-2741	2703-2704	2.44-2.76
GNPC2.0	1581-1582	2740-2741	2701-2709	2.26-3.11
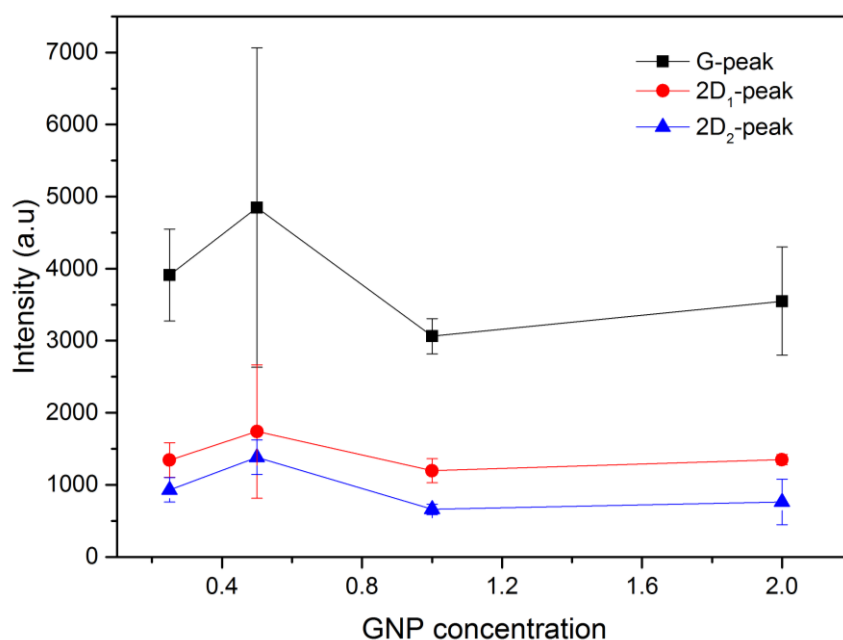
Figure 5.66 Intensity of G-, 2D$_1$- and 2D$_2$-peak of GNP as a function of GNP concentration.

5.6.3 Surface Morphology and surface roughness of DLC-GNP

Surface morphology and surface roughness of all samples were investigated by means of optical microscopy and WLI. Figure 5.67 shows the optical micrographs of DLC-GNP nanocomposite coating produced with different concentration of GNP at 0.25, 0.5, 1.0 and 2.0 mg/mL respectively. Micrograph

on the right represents images at higher magnification. As can be seen, the number of black areas which represent the GNP islands increases with the GNP concentration increase from 0.25 to 2.0 mg/mL.

The surface roughness of DLC-GNP nanocomposite coating was measured using WLI to compare the changes of surface roughness before and after DLC deposition. Figure 5.68 shows surface topography images of DLC-GNP at different GNP concentration. Generally, as GNP concentration increase, the number of peaks also rise. The results reflected the observation in Figure 5.67.

The measured surface roughness of DLC-GNP samples with different GNP concentration is plotted in the graph in Figure 5.69. The surface roughness of spin-coated GNP at different concentration was also plotted in the same graph. The increase of surface roughness of DLC-GNP is in the range of approximately ~60 - 129% compared to pre-DLC deposition of spin-coated GNP. Sample DLC-GNPC2.0 which was deposited with GNP concentration of 2.0 mg/mL showed the highest surface roughness at 60.2 nm relatively higher than another sample. The sample also has a high standard deviation which indicates non-homogenous roughness over the surface.
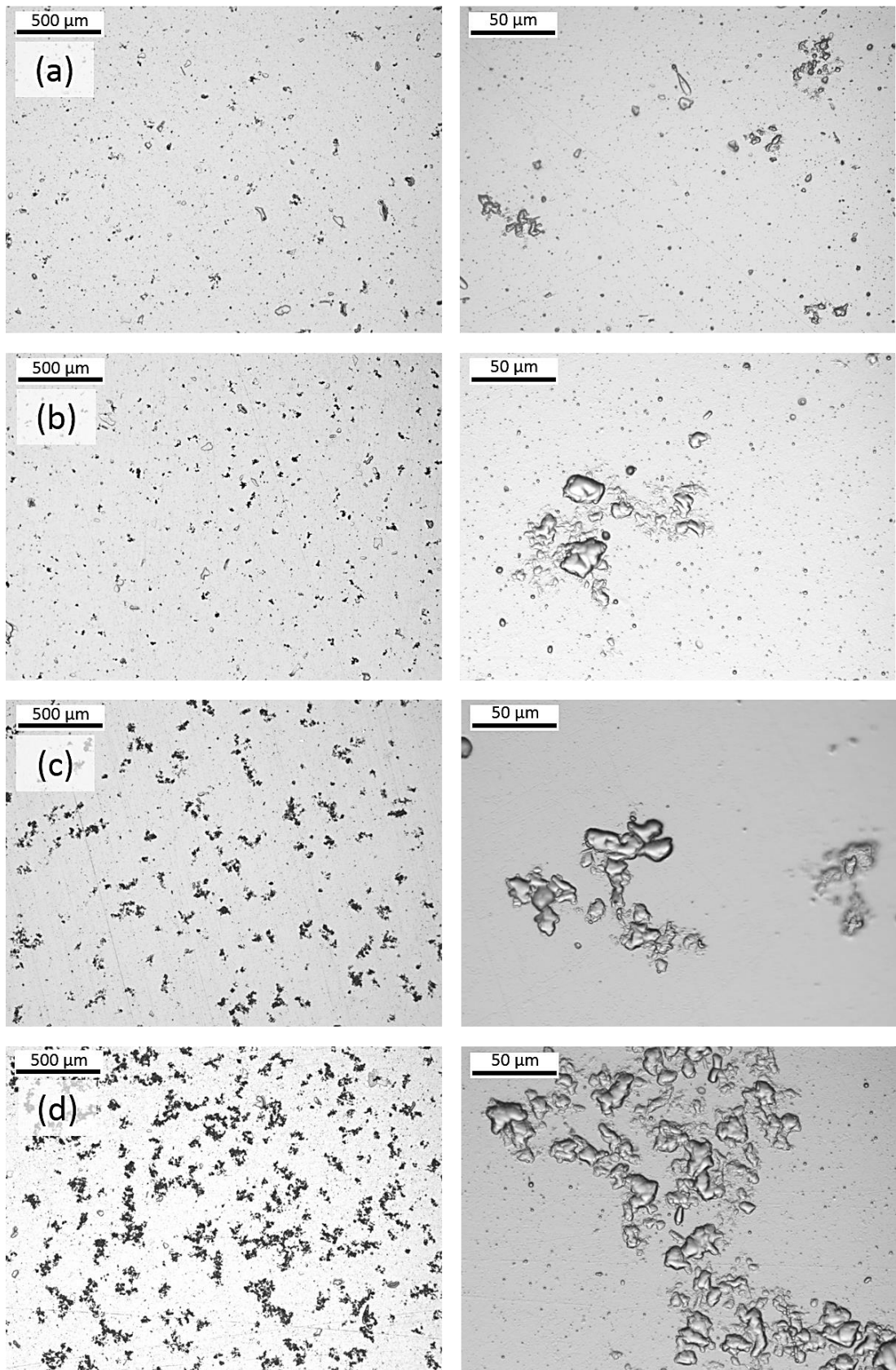
Figure 5.67 Representative optical micrographs of DLC-GNP nanocomposite coating at GNP concentration of (a) 0.25, (b) 0.50, (c) 1.0 and (d) 2.0 mg/mL respectively. The corresponding high magnification of the optical micrographs is shown on the right side of each micrograph
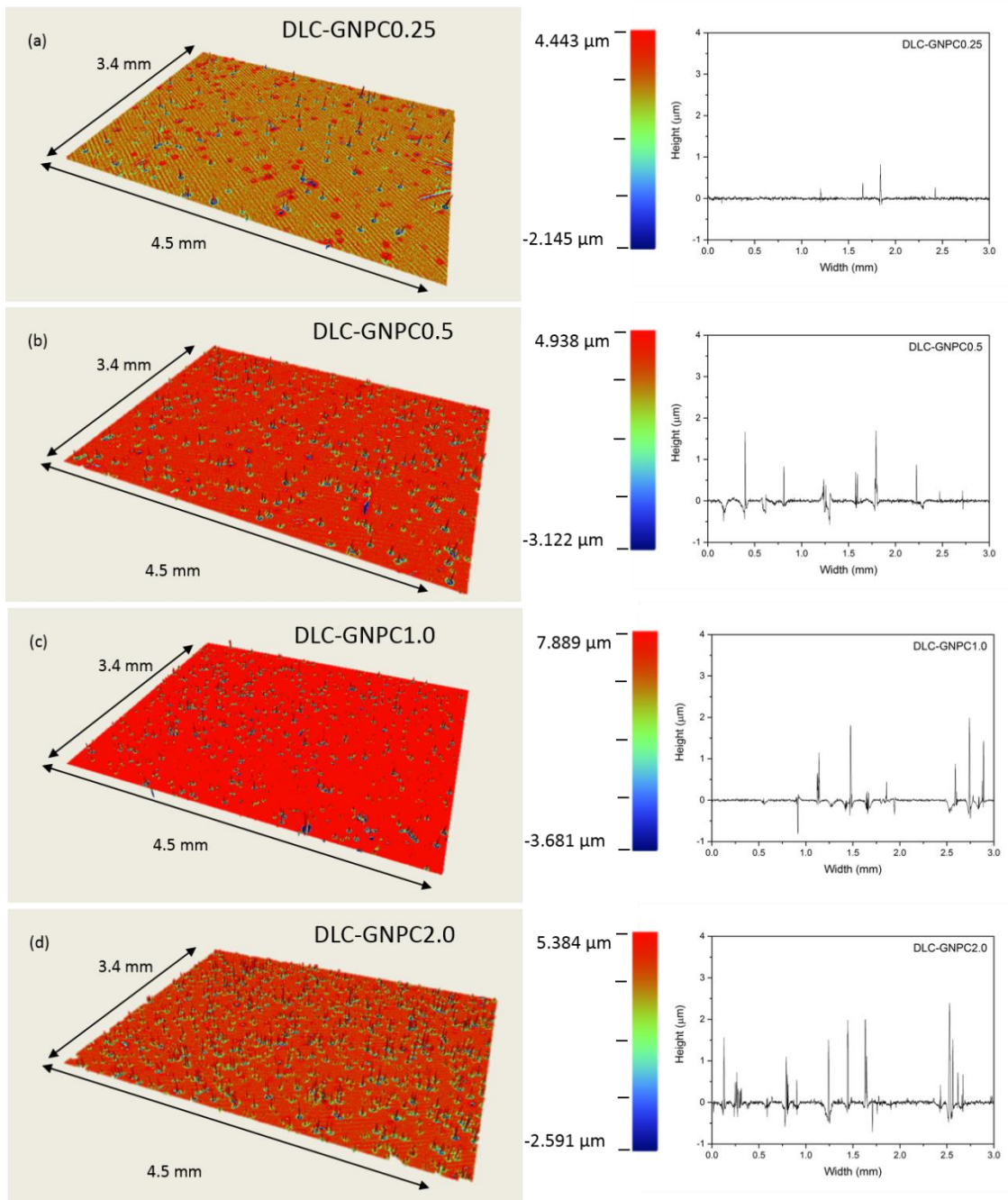
Figure 5.68 Surface topography its corresponding surface profile of (a) DLC-GNPC0.25, (b) DLC-GNPC0.5, (c) DLC-GNPC1.0 and (d) DLC-GNPC2.0
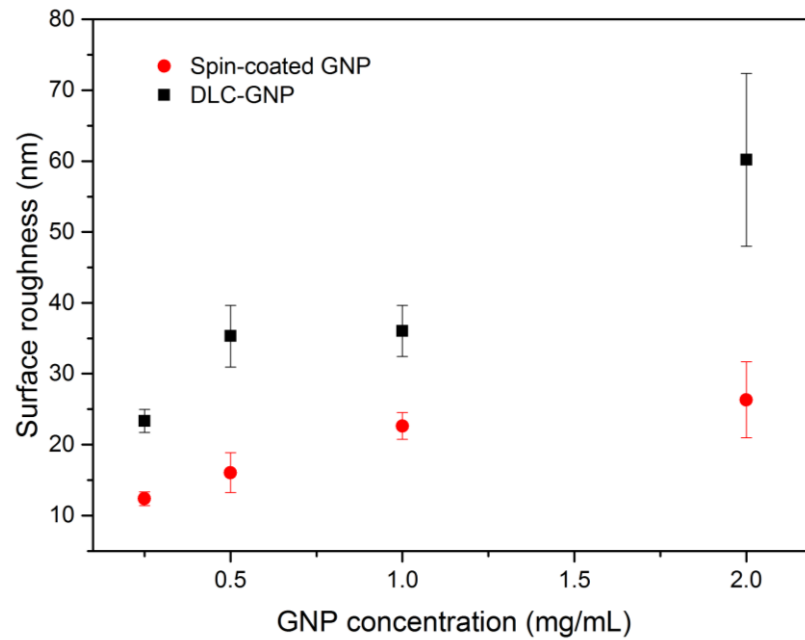
Figure 5.69 Comparison of surface roughness of spin-coated GNP and DLC-GNP nanocomposite coating as a function of GNP concentration. The error bars in the graph indicate standard deviation for ten measurements

The volume GNP concentration (vol%) in DLC-GNP nanocomposite at different mg/mL GNP concentration is shown in Figure 5.70. Vol% of GNP increased from ~ 0.08 to ~0.13 when GNP concentration was increased from 0.25 to 2.0 mg/mL.
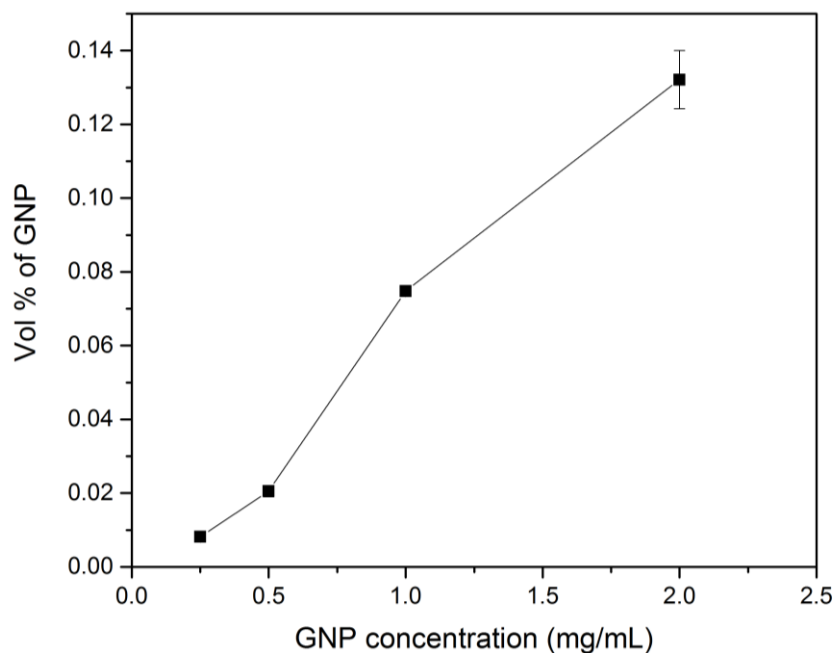
Figure 5.70 Volume percentage (vol%) of GNP in the DLC-GNP
nanocomposite coating as a function of GNP concentration

5.6.4 Raman Analysis of DLC-GNP nanocomposite coating

Raman analysis was carried out to measure any changes in the chemical structure of DLC-GNP composite deposited with different concentrations of GNP. Figure 5.71 shows the typical Raman spectra of sample DLC-GNPC0.25, DLC-GNPC0.5, DLC-GNPC1.0 and DLC-GNPC2.0. The spectra are deconvoluteable into two Gaussian peaks of D and G. All DLC-GNP coatings have a broad single G-peak with a shoulder that belongs to D-peak. No other peak can be observed in the spectra.

The D and G-peak positions and the ratio of I_D/I_G of all spectra in Figure 5.71 are tabulated in Table 5.12. The position and I_D/I_G ratio were considered based on three different spots on samples. As can be seen in the table, all samples have a different range of D and G-peak positions. I_D/I_G ratio also varies in a certain range for the different type of sample. The range of I_D/I_G values for all samples were plotted in Figure 5.72. With the exception of sample DLC-GNPC2.0, the I_D/I_G ratio seems to be shifted to a higher range value as GNP concentration increased. The increase of I_D/I_G ratio usually demonstrates an increase of sp^2 structure [186]. The high concentration and uneven orientation of GNP in sample DLC-GNPC2.0 must be the reason contributing to its irregular trend compared to other samples.

192
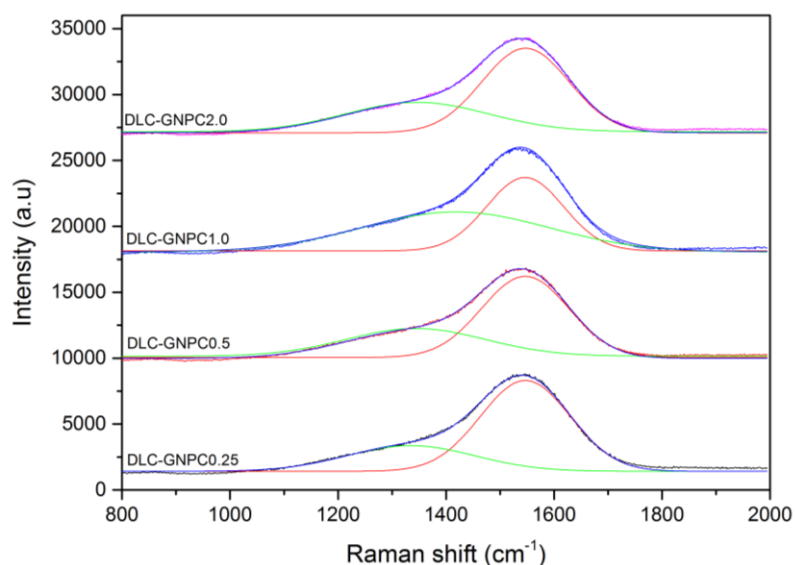
Figure 5.71 Representative Raman spectra of DLC-GNP nanocomposite coatings with different GNP concentration of 0.25, 0.5, 1.0 and 2.0 mg/mL respectively

Table 5.12 Position and integrated intensity I_D/I_G of the main peaks in Raman spectra of samples DLC-GNP with different GNP concentration

Sample	D-peak position (cm⁻¹)	G-peak position (cm⁻¹)	I_D/I_G
DLC-GNPC0.25	1335-1341	1547-1549	0.28-0.30
DLC-GNPC0.5	1320-1425	1544-1550	0.29-0.53
DLC-GNPC1.0	1410-1418	1545-1546	0.55-0.58
DLC-GNPC2.0	1318-1426	1544-1550	0.28-0.54
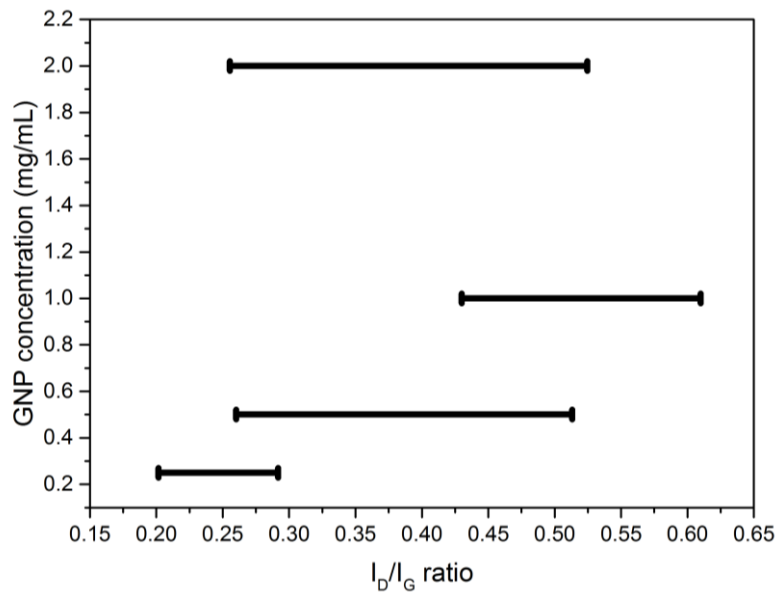
Figure 5.72 The range of I_D/I_G ratio for DLC-GNP with different GNP concentration of 0.25, 0.5, 1.0 and 2.0 mg/mL

5.6.5 Adhesion

The scratch test was performed to understand the effect of GNP concentration on the adhesion strength of DLC-GNP nanocomposite coating. Micrographs of scratch tracks captured using optical microscopy are shown in Figure 5.73. The position of adhesion failure (L_{C1}) is shown by the red arrow in the figure. Sample DLC-GNPC0.25 in Figure 5.73(a) exhibit its initial failure, L_{C1} slightly later than sample DLC-GNPC0.5 and DLC-GNPC1.0, but almost the same with DLC-GNPC2.0. As can be seen, all adhesion failure featured shell-shaped spallation. No complete removal of coating can be observed in any of the samples.

The mean value of a critical load of DLC-GNP nanocomposite coating with different GNP concentration is presented in Figure 5.74. The critical load was first reduced from 16.6 N to 13.4 N as the GNP concentration increased from 0.25 mg/mL to 0.5 mg/mL. It was increased once again with increasing GNP concentration; the highest value of 15.8 N was reached at GNP concentration 2.0mg/mL.

Figure 5.75 represents the scratch depth profile at the point where coating failure happened (L_{C1}) and maximum depth at the end of the scratch. Scratch

width of sample DLC-GNPC0.25 at point L_{C1} is the smallest although the scratch depth is almost the same for all samples. Regarding the maximum depth of scratch, it can be seen in Figure 5.75(b) that sample DLC-GNPC0.25 has the shallowest depth than all.

(a) DLC-GNPC0.25
500 μm
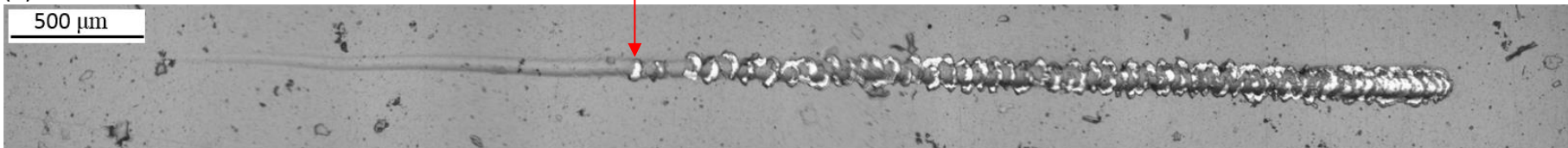
(b) DLC-GNPC0.5
500 μm
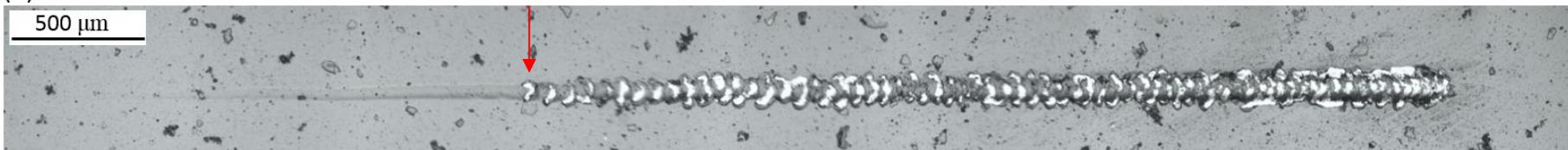
(c) DLC-GNPC1.0
500 μm
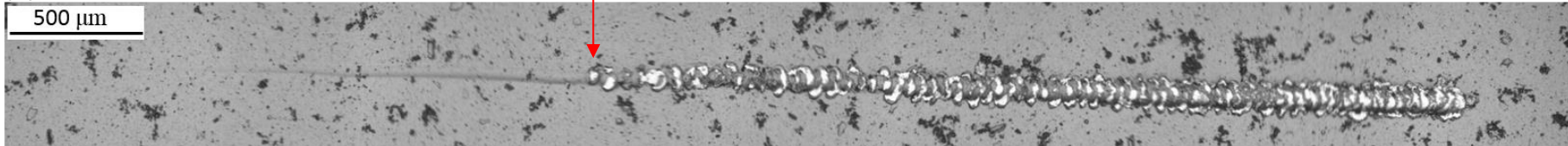
(d) DLC-GNPC2.0
500 μm

Figure 5.73 Optical micrographs of the scratch tracks for (a) DLC-GNPC0.25, (b) DLC-GNPC0.5, (c) DLC-GNPC1.0 and (d) DLC-GNPC2.0 nanocomposite coatings
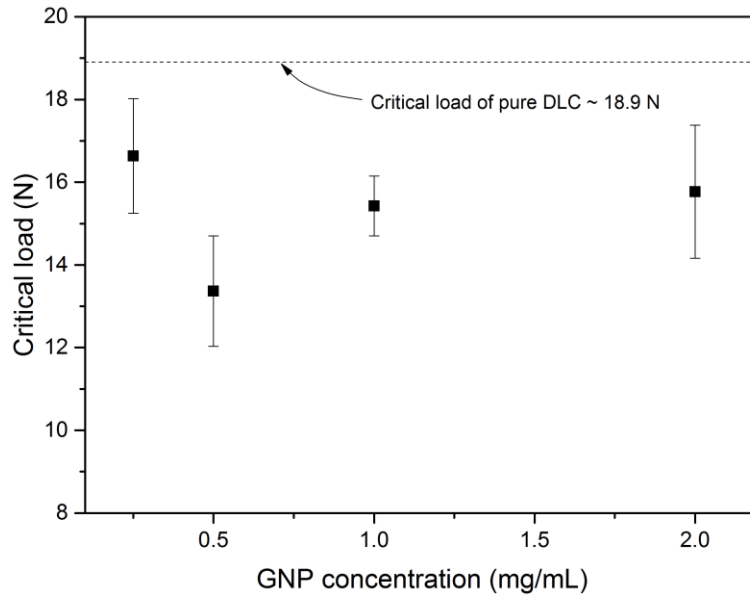
Figure 5.74 Critical load of DLC-GNP nanocomposite coating as a function of GNP concentration. The errors bars indicate the standard deviation of six measurements
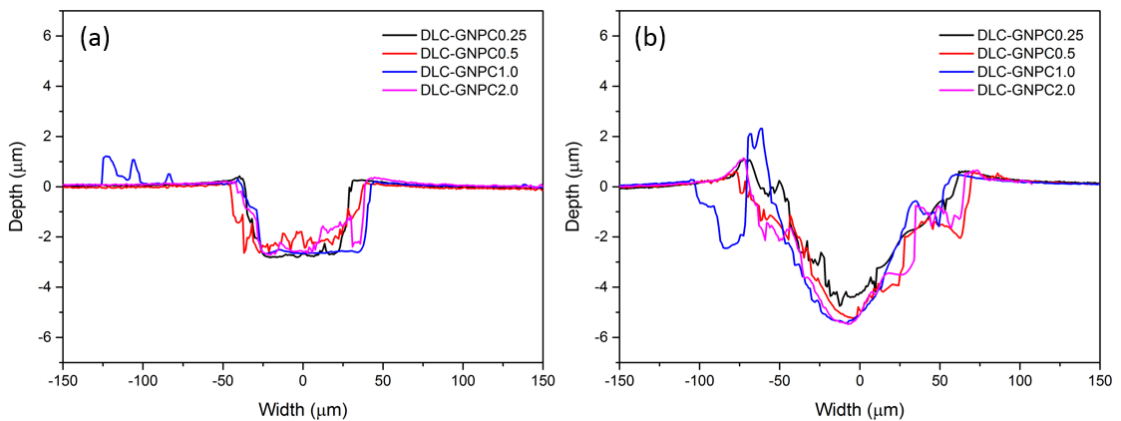
Figure 5.75 Scratch depth at (a) L_{C1} and (b) end of scratch for DLC-GNP at different GNP concentration of 0.25, 0.5, 1.0 and 2.0 mg/mL

5.6.6 Tribological Tests

The tribological tests were conducted to investigate the effect of GNP concentration on the friction and wear of DLC-GNP nanocomposite coating. All tests are repeated three times to ensure repeatability and reliability. Reported frictional change over time represents one example of the evolution of each sample. Method of measurement is explained in Section 5.5.6 and Chapter 3.

197

5.6.6.1   Friction evaluation

The CoF evolution of DLC-GNP nanocomposite coating at different GNP concentrations tested in base oil for three hours is shown in Figure 5.76. Coating of DLC-GNPC0.5 and DLC-GNPC1.0 have almost the same progression, with DLC-GNP2.0 having slightly lower CoF compared to DLC-GNPC0.5 and DLC-GNPC1.0. Contrarily, sample DLC-GNPC0.25 has a comparatively lower CoF although started almost the same progression after the running-in period. All samples have similar running-in periods which is about 40 minutes. Only sample DLC-GNPC2.0 seems to reach its steady-state before the end of the three hours of the test.
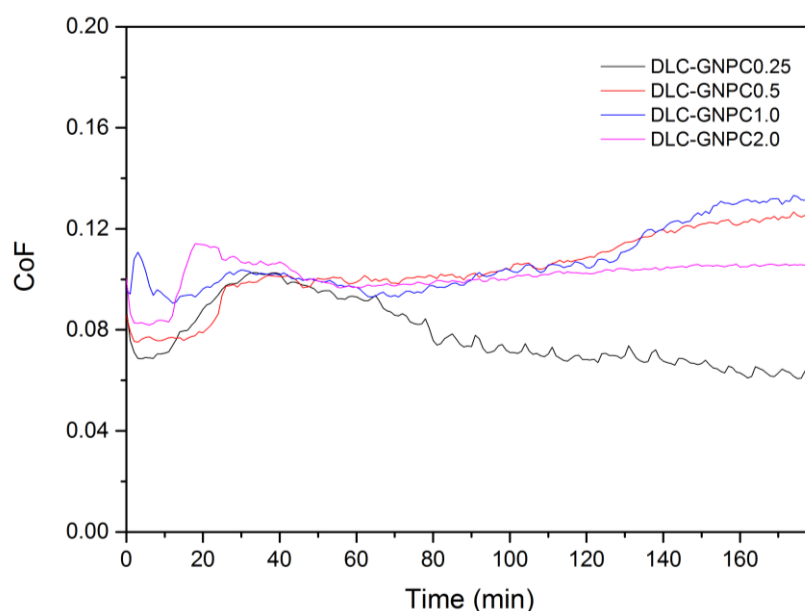
Figure 5.76 Representative CoF evolution of DLC-GNP coatings with different GNP concentration from 0.25 to 2.0 mg/mL, as a function of sliding time in base oil for three hours on pin-on-reciprocating plate tribometer.

The average CoF was calculated from the last two hours of the test, and the values are plotted in Figure 5.77. The dotted line in the graph represents the average CoF of pure DLC as reference measured in section 5.5. It can be seen that sample DLC-GNPC0.25 has the lowest at CoF of 0.08 ± 0.01, while the highest CoF was achieved at 0.12 by sample DLC-GNPC0.5.
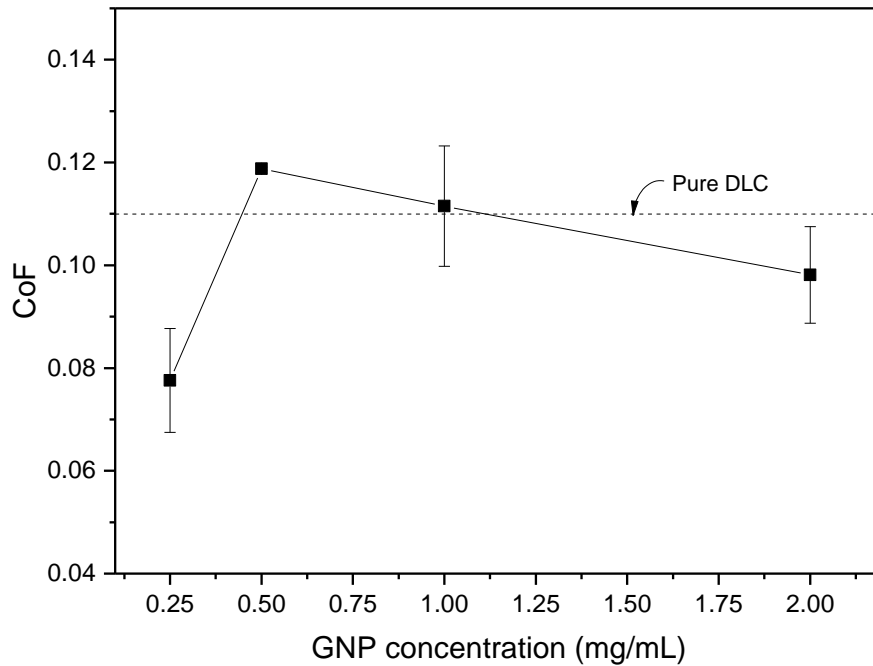
Figure 5.77 Average CoF for DLC-GNP coatings measured in the last two hours of the test by a function of GNP concentration. The error bars in the graph indicate standard deviation for three measurements

5.6.6.2 Observation of the coating wear track and wear scar of counterpart

In order to further investigate the effect of GNP concentration on the tribological behaviour of the nanocomposite coating, wear scar depth, cross-sectional areas were studied by means of optical microscope and WLI. Figure 5.78 shows the optical micrographs of the wear tracks for sample DLC-GNPC0.25, DLC-GNPC5.0, DLC-GNPC1.0 and DLC-GNPC2.0 respectively. As can be seen the appearance of wear for sample DLC-GNPC0.5, DLC-GNPC1.0 and DLC-GNPC2.0 are very severe. These samples have almost the same width of wear track of approximately 3.0 mm. Machining mark is also very obvious in the wear tracks (Figure 5.78(b)-(d)). On the other hand, wear track of sample DLC-GNPC0.25 has most of the coating remained intact with "spot-wear" at certain areas marked with the red arrow in the figure. The width of the wear track is measured to be approximately 1.2 mm.
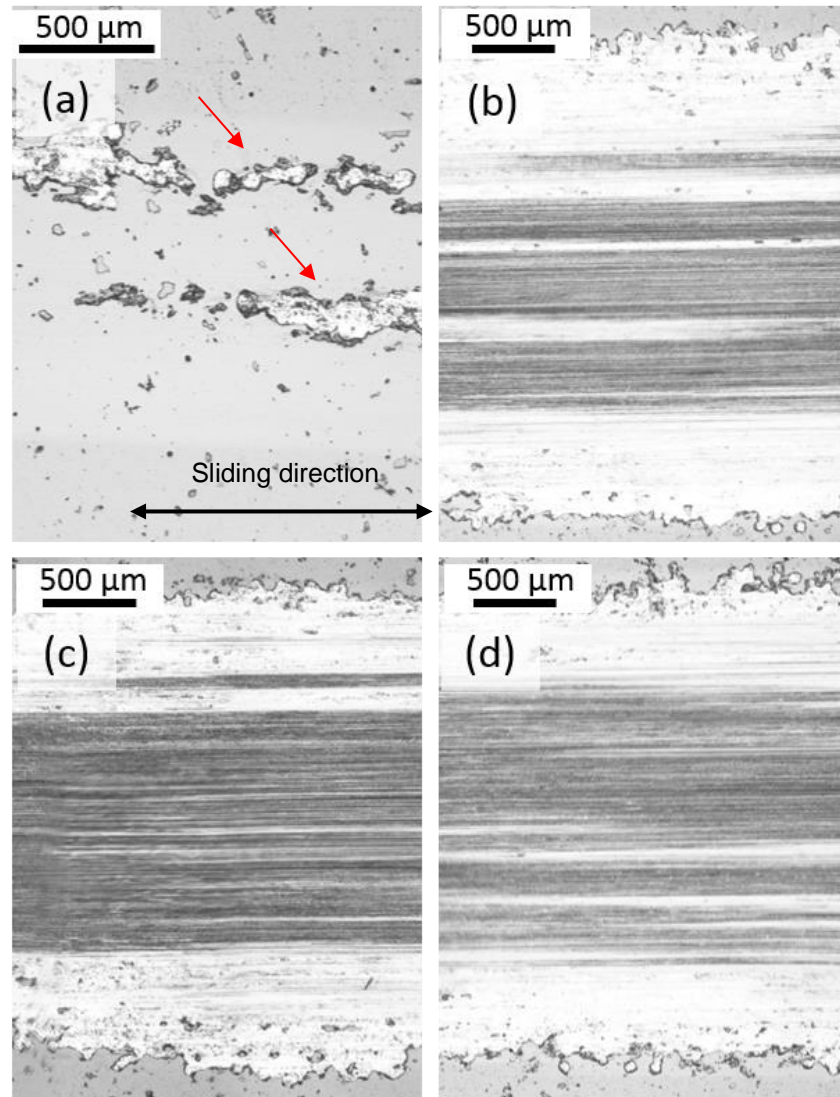
Figure 5.78 Optical micrographs of wear track of sample (a) DLC-GNPC0.25, (b) DLC-GNPC0.5, (c) DLC-GNPC1.0 and (d) DLC-GNPC2.0

The surface topography of the wear tracks is shown in Figure 5.79. The wear tracks that can be seen in Figure 5.78(a) are narrow and deep delamination of coating created dimples on the coating surface (Figure 5.79(a)). Complete delamination of the coating can be observed in sample DLC-GNPC0.5, DLC-GNPC1.0 and DLC-GNPC2.0 in Figure 5.79(b-d). Wear tracks of sample DLC-GNPC0.5 and DLC-GNPC1.0 have the deepest wear track depth of all. Based on the shape of the wear track cross-section, the wear severity of coating from the most severe can be listed as follows: DLC-GNPC0.5 > DLC-GNPC1.0 > DLC-GNPC2.0 > DLC-GNPC0.25.
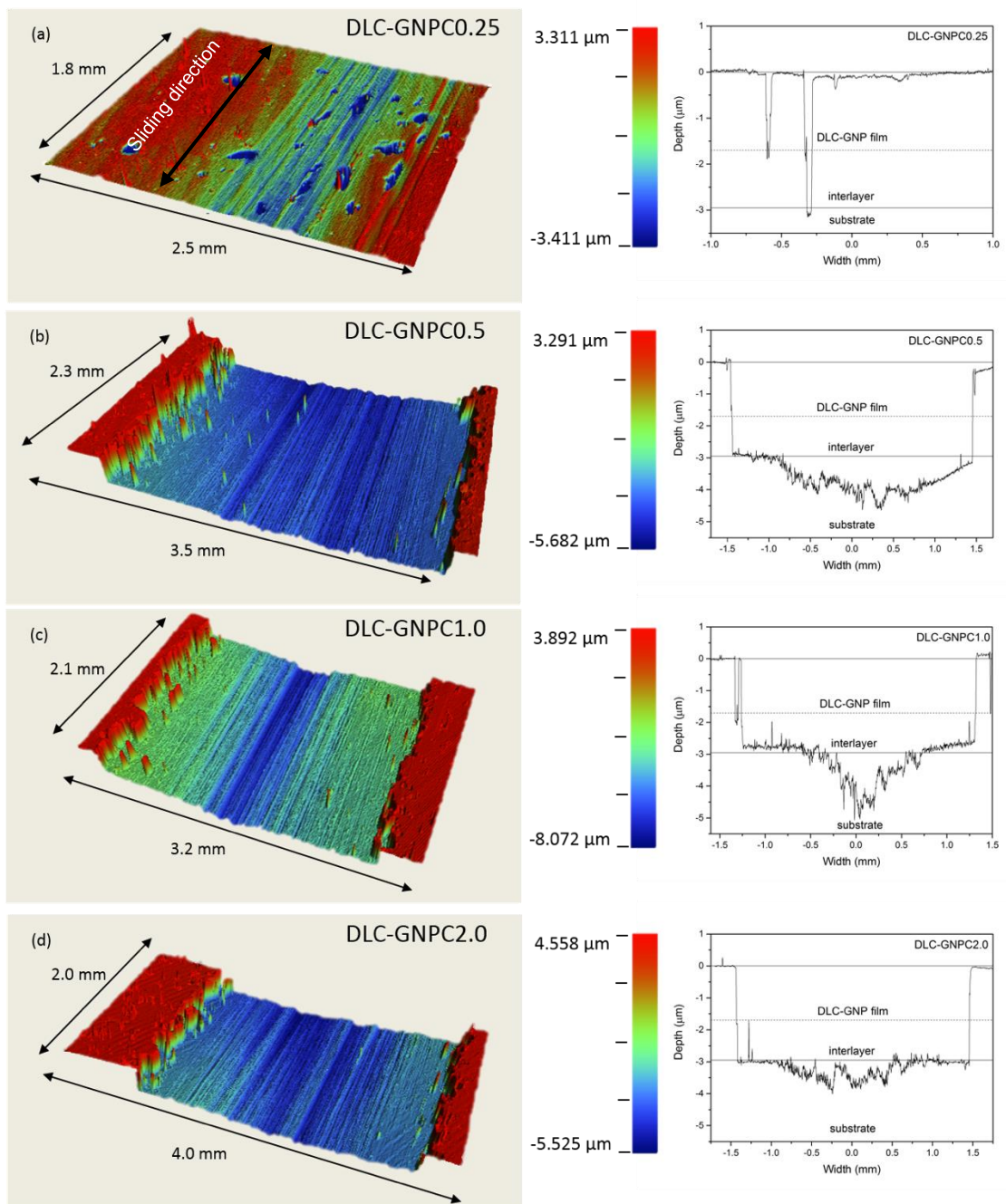
Figure 5.79 Surface topography and corresponding cross-section profiles of wear tracks for (a) DLC-GNPC0.25, (b) DLC-GNPC0.5, (c) DLC-GNPC1.0 and (d) DLC-GNPC2.0 respectively after three hours of tribotest in base oil.

Figure 5.80 shows the representative optical micrographs of the wear scar of the counterparts for DLC-GNP coatings at different GNP concentrations. Relatively large wear scar diameters with severe scuffing can be observed on counterpart pins of samples DLC-GNPC0.5, DLC-GNPC1.0 and DLC-GNPC2.0

in Figure 5.80 (b-d). The counterpart of DLC-GNPC0.25 exhibits the smallest scar diameter size among all counterparts with very fine scratching marks. The dark areas in the wear scars indicate the existence of transfer layer.
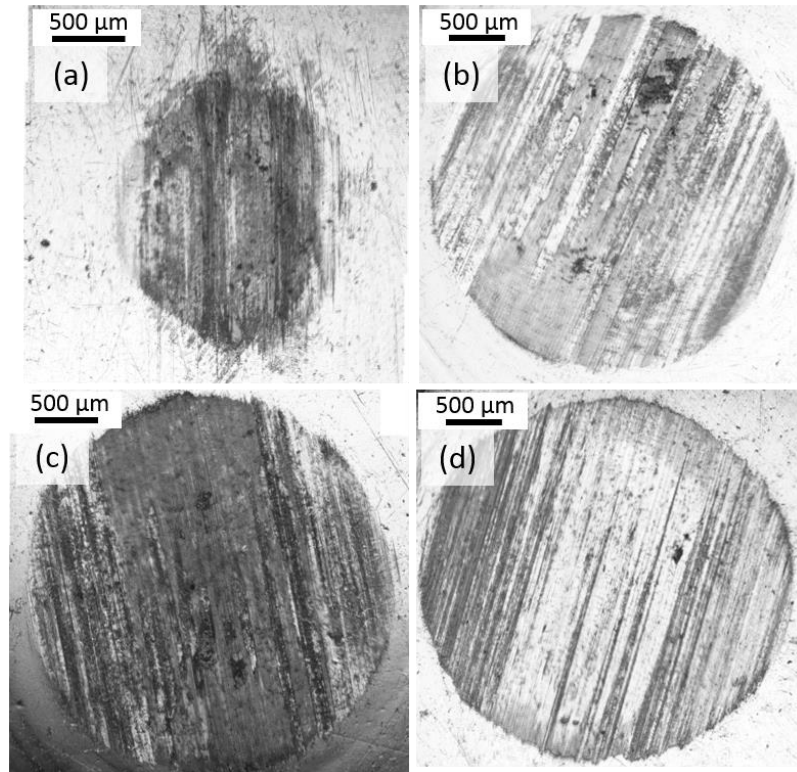
Figure 5.80 Optical micrographs of wear scar of counterpart for (a) DLC-GNPC0.25, (b) DLC-GNPC0.5, (c) DLC-GNPC1.0 and (d) DLC-GNPC2.0 nanocomposite coatings

The surface topography of the wear scar of counterpart pins is presented in Figure 5.81. Deep scratches and grooves on the wear surface are observed on the counterpart of DLC-GNPC1.0 and DLC-GNPC2.0. On the one hand, counterpart DLC-GNPC0.5 and DLC-GNPC0.25 have a smoother surface.
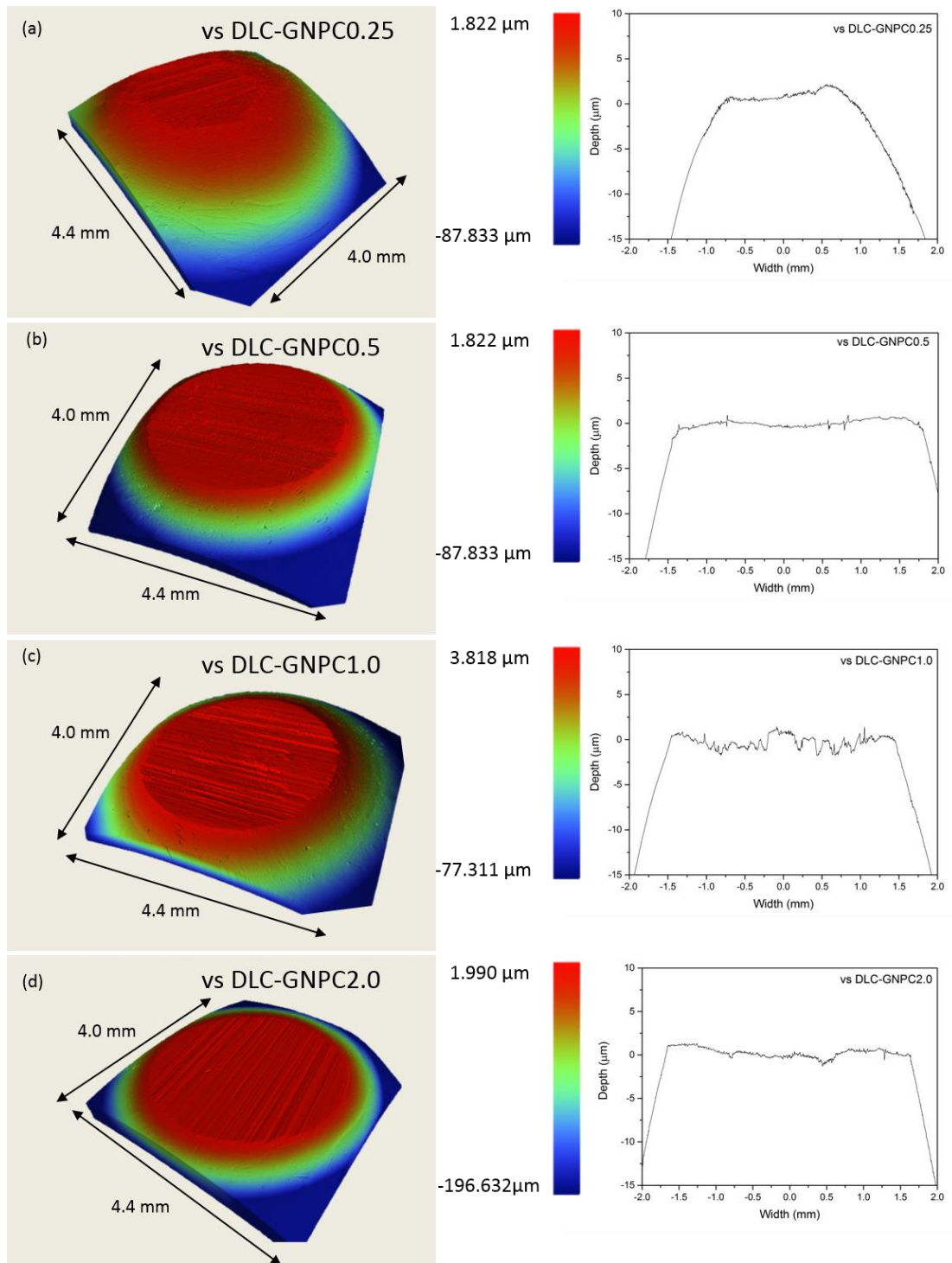
Figure 5.81 Surface topography and cross-section profiles of the counterpart wear scar for (a) DLC-GNPC0.25, (b) DLC-GNPC0.5, (c) DLC-GNPC1.0 and (d) DLC-GNPC2.0

5.6.6.3   Analysis of the wear rate of DLC-GNP

WLI and optical microscopy was employed to analyse the wear of all coatings. From the results obtained in section 5.6.6.2, the wear rate of the coatings was calculated using Archard's equation as in Eq 3.7. The wear rate and the wear depth of DLC-GNP post-treated samples are plotted in Figure 5.82. Coating DLC-GNP0.25 demonstrates lowest wear rate, while DLC-GNPC0.5 is the highest. The wear rate was then reduced as the GNP concentration was increased to 1.0 and 2.0mg/mL.
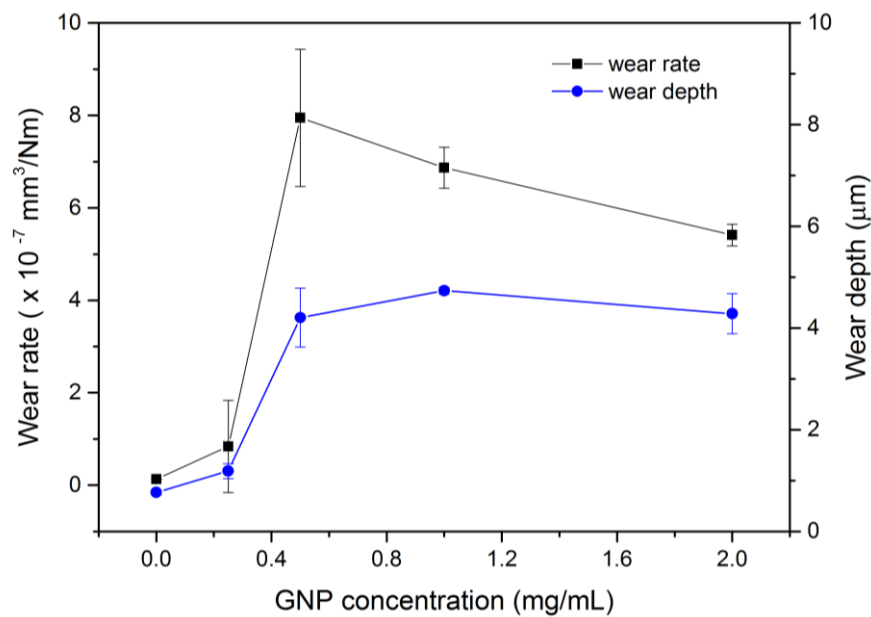
Figure 5.82 Wear rate and depth of wear track of DLC-GNP nanocomposite coating at a concentration from 0.25 to 2.0 mg/mL. The error bars in the graph indicate standard deviation for three measurements

Figure 5.83 summarises the values of average CoF and the wear rate for DLC-GNP nanocomposite coatings with concentration from 0.25 to 2.0 mg/mL. It can be seen that the change of the wear rate is in accordance to the change of average CoF of the coatings. DLC-GNPC0.25 coating recorded the lowest CoF and wear rate of all.
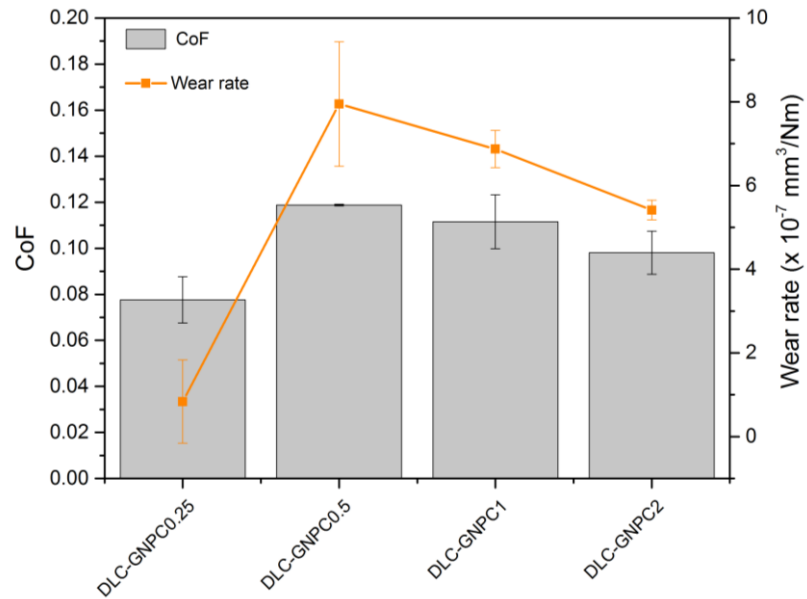
Figure 5.83 The CoF and wear rate of DLC-GNP nanocomposite coating at different GNP concentrations

5.6.6.4 Analysis of wear rate of the counterpart of DLC-GNP

Wear volume of all counterparts was measured using WLI and calculated using Eq 3.2 and 3.3. The wear rate was calculated using Eq. 3.4 and the results of which can be seen in Figure 5.84. The wear scar diameter is also plotted on the same graph as a reference. The lowest wear rate is observed from counterpart DLC-GNPC0.25 (GNP concentration 0.25 mg/mL) at 1.58×10^{-2} mm^3/Nm. The wear rate increased rapidly for counterpart of DLC-GNP0.5 before remaining almost the same in the range of $14 - 17 \times 10^{-2}$ mm^3/Nm. The wear scar diameter at the three GNP concentration of 0.5, 1.0 and 2.0 mg/mL are almost the same size.
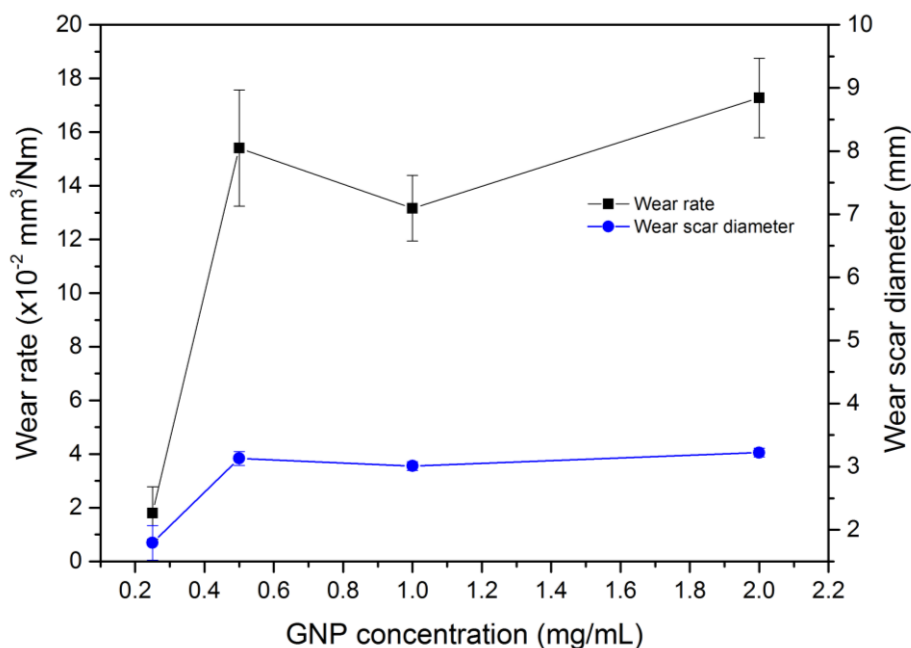
Figure 5.84 Wear rate of cast iron counterpart pins as a function of GNP concentration after sliding against DLC-GNP with different GNP concentration coating for three hours test in the base oil. The error bars in the graph indicate standard deviation for three measurements

5.6.6.5 Raman analysis of the wear

Raman spectra of the wear tracks and wear scars was analysed to investigate the wear mechanism of DLC-GNP coating when GNP concentration was changed. Figure 5.85 presents the Raman spectra collected from two different areas of the wear track region after 3-hour test in the base oil. For wear track of sample DLC-GNPC0.25, after deconvolution of the spectra, dominant and distinct D and G-peaks are observed at around 1422 and 1549 cm^{-1} respectively. The I_D/I_G ratio is almost the same as the ratio of the as-prepared coating. All other spectra show main carbon D and G-peak of graphitised carbon structure with some spectra also having Fe-oxide.

The analysis of the D- and G-peaks position, and the I_D/I_G ratio for the spectra are summarized in Table 5.13. Most of the measured I_D/I_G ratio of the wear tracks is higher than the as-prepared coating in the range between 0.81 – 0.91. High I_D/I_G ratio is commonly related to coating graphitic nature. Fe peak found on all coatings except DLC-GNPC0.25 is believed to come from the substrate as the delamination reached the substrate level.
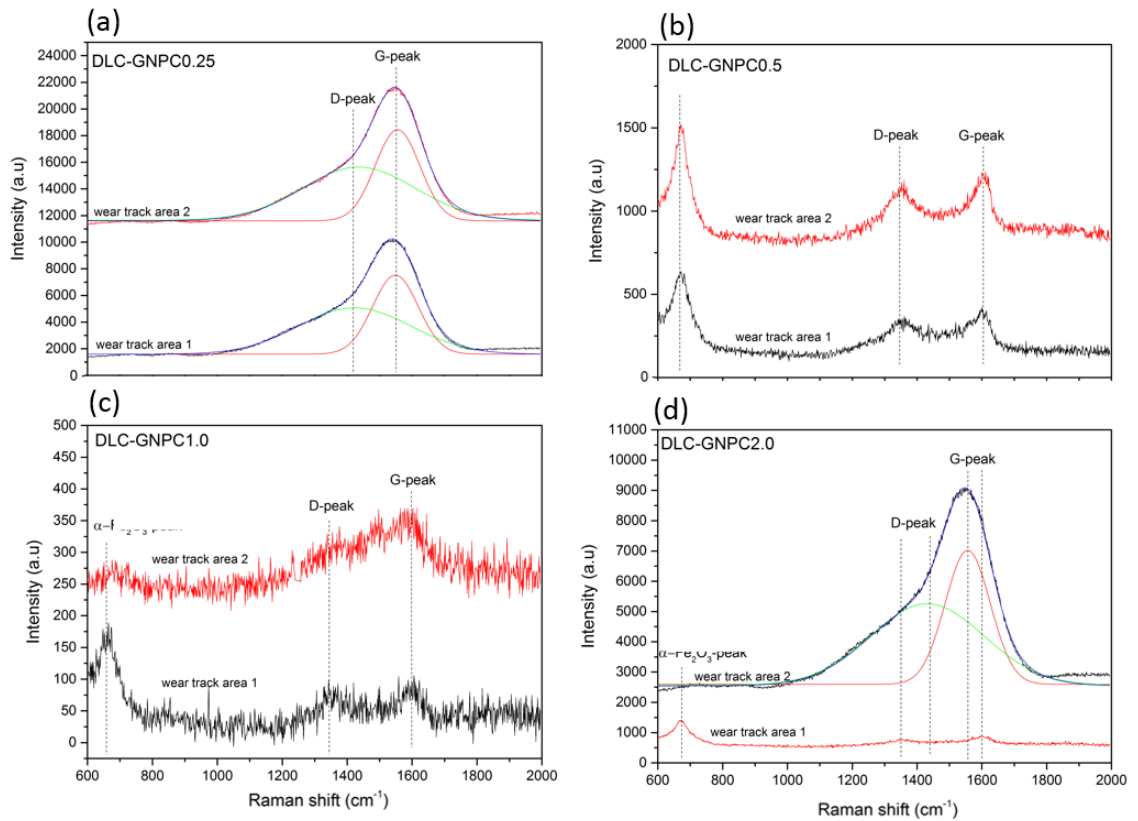
Figure 5.85 Raman spectra collected within the wear track of (a) DLC-GNPC0.25, (b) DLC-GNPC0.5, (c) DLC-GNPC1.0 and (d) DLC-GNPC2.0

The I_D/I_G on wear tracks of sample DLC-GNPC0.25, DLC-GNPC0.5, DLC-GNPC1.0 and DLC-GNPC2.0 are plotted in Figure 5.86. The shaded area represents the range of I_D/I_G value for all samples before the test. Most of the I_D/I_G values of the wear tracks are outside the region which demonstrated the change of coating after sliding wear. The wear track of DLC-GNPC0.25, which has the lowest wear rate has the less change of I_D/I_G compared to the as-prepared I_D/I_G ratio. High I_D/I_G value commonly represent the occurrences of graphitisation of coating. The results will be discussed further in Chapter 7.

Table 5.13 Position and integrated intensity I_D/I_G of the main peaks in Raman spectra of within the wear tracks of samples DLC-GNP with different concentration

Sample	Area	D-peak position (cm⁻¹)	G-peak position (cm⁻¹)	Fe-oxide position (cm⁻¹)	I_D/I_G
DLC-GNPC0.25	Wear track area 1	1422	1549	-	0.58
	Wear track area 2	1423	1549	-	0.59
DLC-GNPC0.5	Wear track area 1	1363	1589	662	0.83
	Wear track area 2	1361	1587	664	0.81
DLC-GNPC1.0	Wear track area 1	1358	1591	647	0.91
	Wear track area 2	1324	1542	684	0.24
DLC-GNPC2.0	Wear track area 1	1360	1592	667	0.68
	Wear track area 2	1431	1556	-	0.61
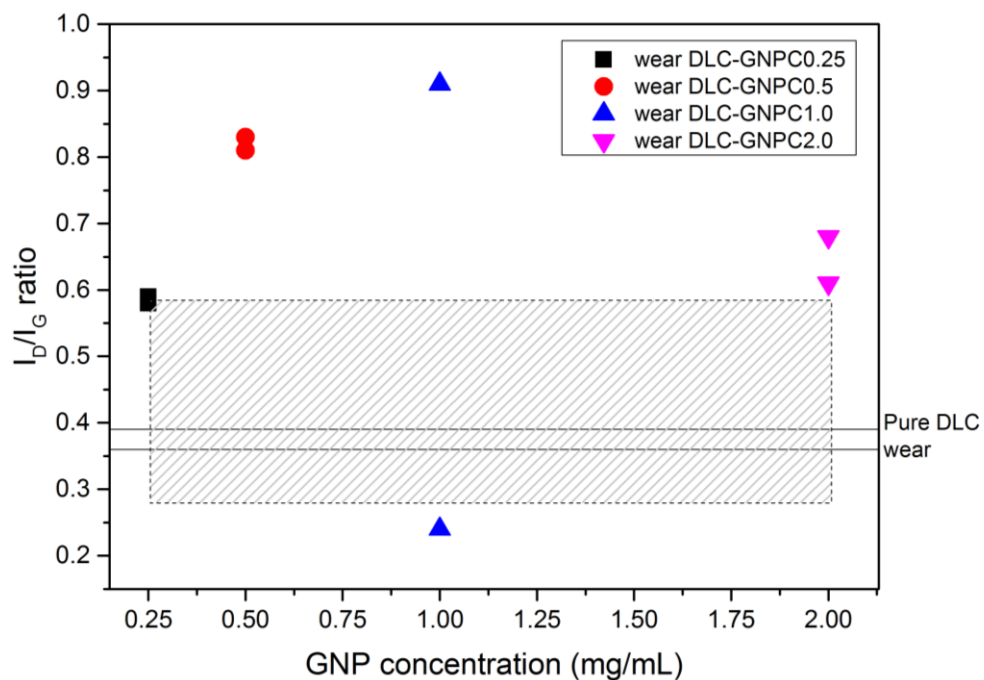
Figure 5.86 I_D/I_G ratio of wear track by a function of GNP concentration

The Raman spectra on wear scar of multilayer DLC-GNP at different GNP concentrations is shown in Figure 5.87. All spectra show intense peaks at D and G with Fe-oxide that appears in some of the spectra. The peak position and measured I_D/I_G ratio are summarised in Table 5.14. The position of D- and

G-peaks are within the range of 1344 - 1375 cm^{-1} and 1553 - 1600 cm^{-1} respectively. The highest I_D/I_G ratio recorded is 1.06 and the lowest is 0.37.
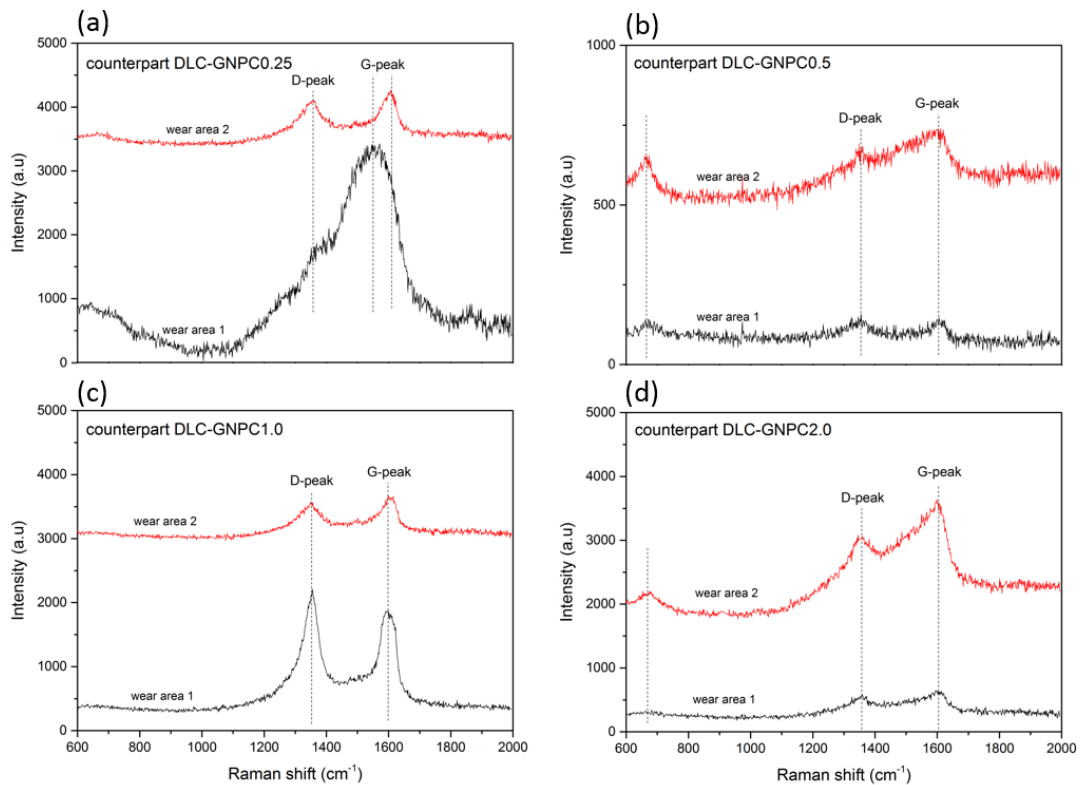
Figure 5.87 Raman spectra collected within the wear scar of counterpart (a) DLC-GNPC0.25, (b) DLC-GNPC0.5, (c) DLC-GNPC1.0 and (d) DLC-GNPC2.0

Table 5.14 Position and integrated intensity I_D/I_G of the main peaks in Raman spectra within the wear scar on the counterpart of DLC-GNP with different concentrations

Sample	Area	D-peak position (cm^{-1})	G-peak position (cm^{-1})	Fe-oxide position (cm^{-1})	I_D/I_G
DLC-GNPC0.25	Wear area 1	1375	1553	-	0.37
	Wear area 2	1352	1598	634	0.41
DLC-GNPC0.5	Wear area 1	1348	1600	660	0.93
	Wear area 2	1344	1560	658	0.35
DLC-GNPC1.0	Wear area 1	1350	1595	-	1.06
	Wear area 2	1349	1598	-	0.82
DLC-GNPC2.0	Wear area 1	1355	1580	-	0.75
	Wear area 2	1351	1569	664	0.56

5.6.7 Summary of effect of GNP concentration

The following summary can be drawn from the results presented herein.

i. Surface roughness increased as GNP concentration was increased

ii. The ranking of adhesion of coating is as follows; (highest) DLC-GNPC0.25 > DLC-GNPC2.0 > DLC-GNPC1.0 > DLC-GNPC0.5 (lowest).

iii. DLC-GNP composite coating with GNP concentration of 0.25 mg/mL demonstrates the lowest friction and wear rate, whereas the highest is when the GNP concentration is 1.0 mg/mL.

iv. The lowest wear rate of coating is recorded from sample DLC-GNPC0.25 while the highest is for the sample with GNP concentration of 1.0 mg/mL.

v. Graphitisation of coating occurred on all samples after sliding test.

vi. Transfer layer exists on all counterparts.

Chapter 6

Results: Deposition of Multilayer DLC-GNP Nanocomposite Coating

6.1   Introduction

Multilayer coatings have garnered much attention due to their advantages over single-layer coatings. Multilayer DLC coatings have been reported to overcome the high residual stresses of thick single layer DLC thus producing coatings with higher adhesion strength, better frictional and wear resistance. In this work, double-layer DLC-GNP nanocomposite coatings were prepared.

This chapter presents the experimental work on preparation of double-layer DLC-GNP nanocomposite coatings using a spin coating and PECVD methods. The procedure of deposition of GNP and DLC is the same as been described in Chapter 5 of single-layer DLC-GNP nanocomposite coating with post-treatment process.

The structure of the experimental results of this chapter is shown in Figure 6.1. Figure 6.1 summarises the topic, test parameters and the findings of each section. Section 6.1 describes introduction and the objectives of the experimental work. The aims are defined in Section 6.2. Section 6.3 reports the physical and mechanical properties of the coating. Section 6.4 explains the tribological properties of the coatings.
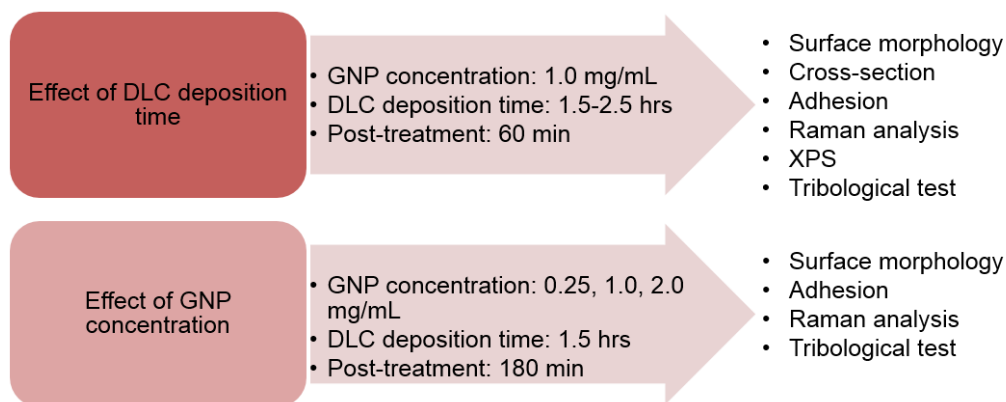
Figure 6.1 The experimental procedures in Chapter 6

6.2 Aims

This chapter aims to produce and characterise multilayer DLC-GNP nanocomposite coatings. The main objectives of this chapter are as follows:

i. To prepare multilayer DLC-GNP nanocomposite coatings.

ii. To investigate the effect of DLC deposition time on the properties of multilayer DLC-GNP nanocomposite coatings.

iii. To study the effect of GNP concentration on the properties of multilayer DLC-GNP nanocomposite coatings.

6.3 Effect of DLC Deposition Time

In this work, GNPs were spin-coated on a substrate using the same parameters as used in Section 5.5, where spinning speed, spinning time, amount of GNP used were 1000 rpm, 30 seconds and 1.0 mL respectively. After the first deposition of DLC using PECVD, the process of GNP spin coating was repeated followed by another layer of DLC deposition. All samples have been through post-treatment process with the heating hour fixed at one hour. Concentration of GNP was fixed at 1.0 mg/mL. In order to control the thickness of the whole coating to be less than 2.0 μm, DLC deposition time of 1.5 and 2.5 hours were selected for the study. The spinning condition were the same as described previously. The flow of the preparation of multilayer DLC-GNP nanocomposite coating is shown in Figure 6.2. The parameters used for each sample are summarized in Table 6.1. DLC-GNP multilayer samples for this

section are abbreviated as DLC-GNPML1.5 and DLC-GNPML2.5 for different DLC deposition time of 1.5 and 2.5 hours respectively.
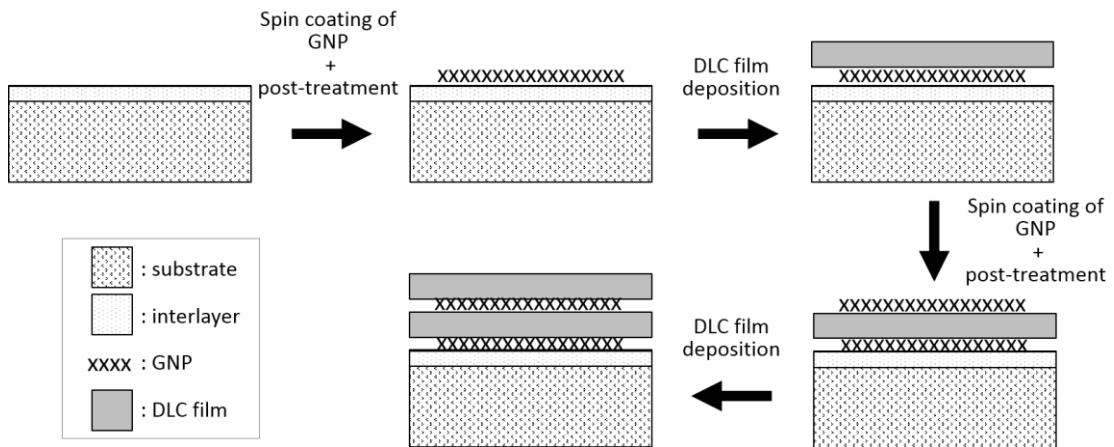
Figure 6.2 Process flow of the preparation of multilayer DLC-GNP nanocomposite coating

Table 6.1 Experimental parameters for preparation of multilayer DLC-GNP with different DLC deposition

Sample	GNP concentration	Spinning speed	Spinning time	GNP amount	treatment heating duration	DLC deposition time
	(mg/mL)	(rpm)	(sec)	(mL)	(min)	(hour)
DLC-GNPML1.5						1.5
	1.0	1000	30	1	60	
DLC-GNPML2.5						2.5

6.3.1 Cross-sectional and thickness of the coating

To investigate the thickness and cross-section view of the coatings, FIB-SEM was employed. Several areas with and without GNP were selected on each sample. Figure 6.3 shows the cross-section of sample DLC-GNPML1.5 and DLC-GNMPML2.5. It should be noted that all micrographs are at a different magnifications. Figure 6.3(a) is the cross-section at one area of sample DLC-GNPML1.5 without the appearance of GNP. The black film at the topmost layer

is the DLC film. It is hard to differentiate the first and second layer of DLC film. The border is marked with a yellow dotted line underneath DLC layer 2 in Figure 6.3(a). No GNP can be observed in film coating in Figure 6.3(a) and the thickness of the DLC thickness is measured to be about 1.54 μm comprised of 0.77 μm thickness of each layer of DLC. Figure 6.3(b) shows the same coating of DLC-GNPML1.5 but with the massive amount of GNP below the second layer of the coating. The GNPs were observed in curling shape thereby creating voids in the nanocomposite. From the image, it is clear that DLC film is deposited and grew on spin-coated GNP. The rough surface of DLC-GNP coating originated from the arrangement of spin-coated GNP.

Sample DLC-GNPML2.5 has larger coating thickness due to its longer DLC deposition time of 1.5 hours. As can be seen in Figure 6.3(c) and (d), the coating has a similar structure with DLC-GNPML1.5 described previously, where there are a few areas without GNP and there are areas with GNP. The GNP in Figure 6.3(c) is underneath the first layer DLC film, while the GNP in Figure 6.3(d) was deposited above the first layer below the second layer of DLC film. The DLC film appeared to be deposited on wrinkled GNP and shadowed the shape of the GNP beneath it. The shape of the GNP is almost similar to the model illustrated by Cranford et al. in their study of self-fold of multilayer graphene sheet [187].
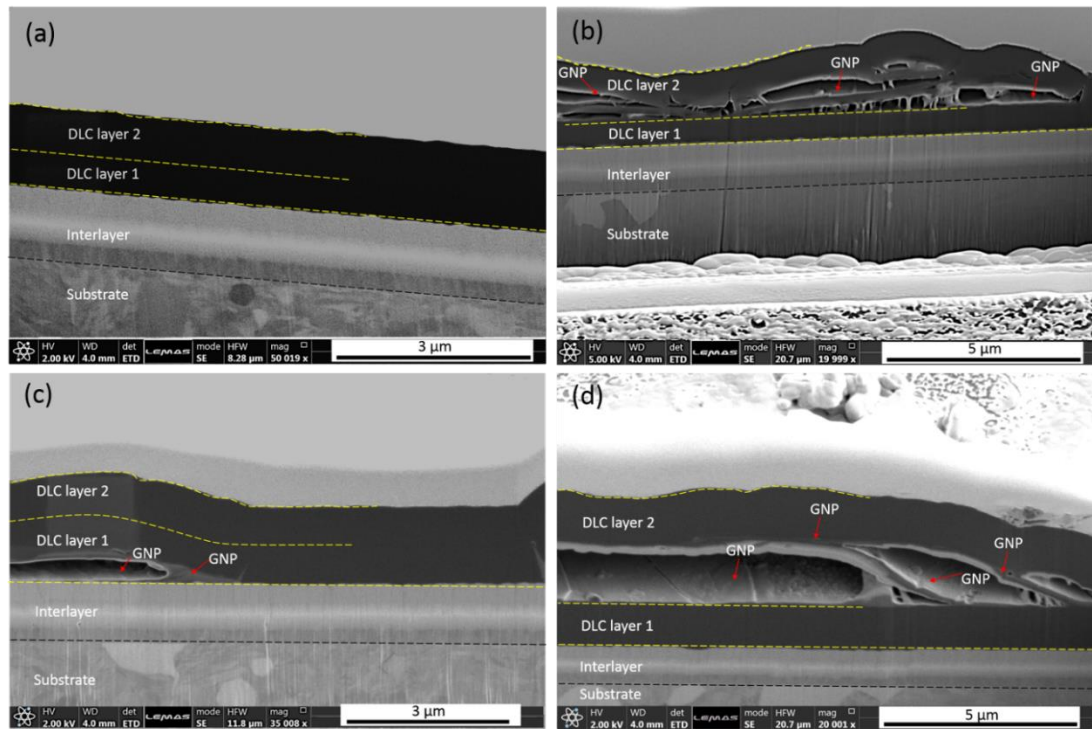
Figure 6.3 Cross-section of sample (a and b) DLC-GNPML1.5 and (c and d) DLC-GNPML2.5

The thickness of coating estimated from the thickness of single-layer DLC-GNP (measured in Section 5.4) and from the measurement of the cross-section is presented in Table 6.2. The actual thickness of the coatings measured from the cross-section in Figure 6.3 is larger than the thickness of DLC film estimated from the single layer deposition in Chapter 5. This may be due to the double deposition of spin-coated GNP that enhanced waviness of the surface hence increased the thickness.

Table 6.2 Thickness of multilayer DLC-GNP nanocomposite coating deposited with different DLC deposition time

Sample	DLC deposition time (hour)	Estimated thickness of DLC-GNP (μm)	Thickness from SEM measurement (μm)
DLC-GNPML1.5	1.5	1.20	2.05 ± 0.53
DLC-GNPML2.5	2.5	2.18	3.11 ± 0.60

6.3.2 Surface morphology and surface roughness of multilayer DLC-GNP

The surface morphology of all coatings was examined using the optical microscope and is displayed in Figure 6.4. No noticeable difference can be observed in the micrographs. Both samples showed similar morphology with single-layer DLC-GNP presented before in Chapter 5. However, it is apparent that more black islands (GNP islands) covered by DLC can be observed when compared to single-layer DLC-GNP that has been produced with the same concentration of GNP. Theoretically, with the same concentration, the amount of GNP in the composite should be double that the single DLC-GNP.
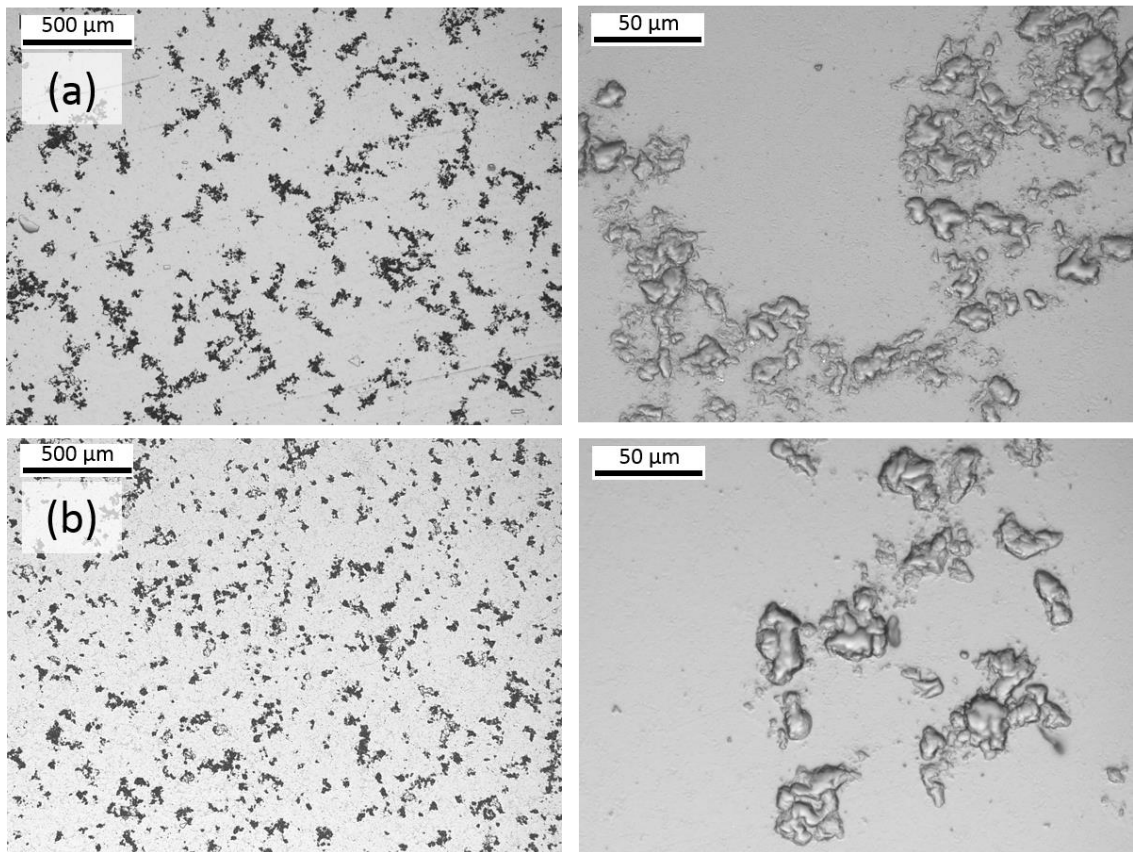
Figure 6.4 Representative optical micrographs of (a) DLC-GNPML1.5 and (b) DLC-GNPML2.5. The corresponding higher magnification of the optical micrographs is shown on the right side of each micrograph

The surface topography of sample DLC-GNPML1.5 and DLC-GNPML2.5 are shown in Figure 6.5 respectively. As can be seen, sample DLC-GNPML2.5

appears rougher than sample DLC-GNPML1.5. The same results have also been obtained earlier for single-layer DLC-GNP when longer deposition times of DLC produced higher surface roughness.
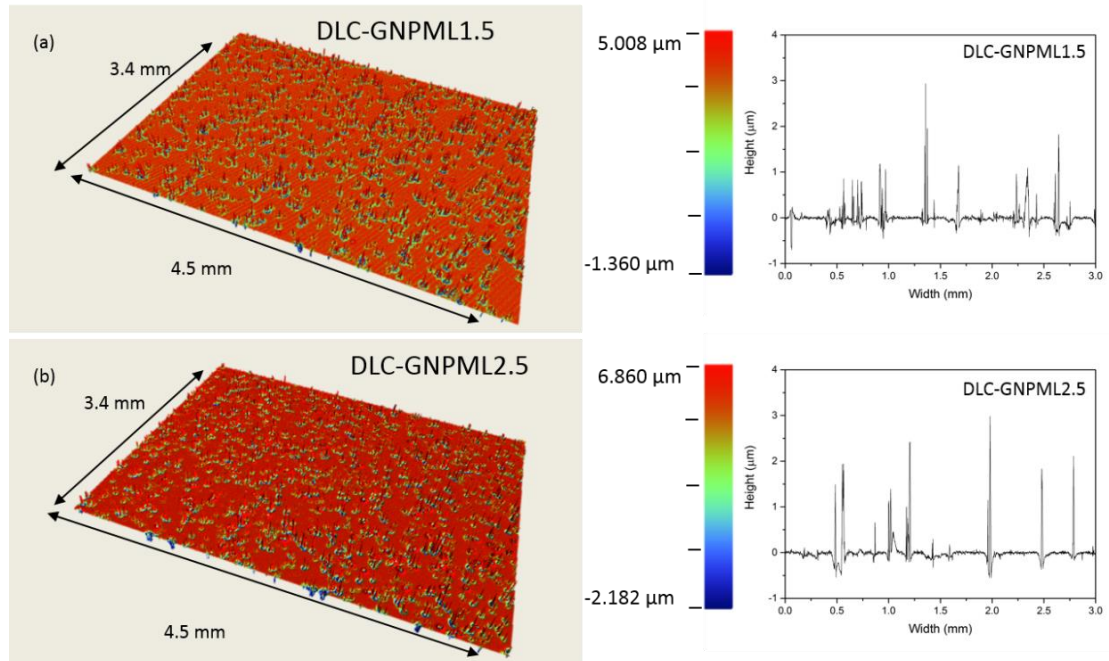
Figure 6.5 Surface topography and the corresponding surface profile of multilayer (a) DLC-GNPML1.5 and (b) DLC-GNPML2.5

The results for surface roughness as a function of DLC deposition time are depicted in Figure 6.6. From the graph, it can be seen that surface roughness was reduced almost half when DLC deposition time was 2.5 hours. The results agree with what has been observed in Figure 6.5. The surface roughness of multilayer DLC-GNPML2.5 increased around 61% compared to DLC-GNPML1.5. The increment is lower than increment recorded for single-layer DLC-GNP1.5 before which is 73%.
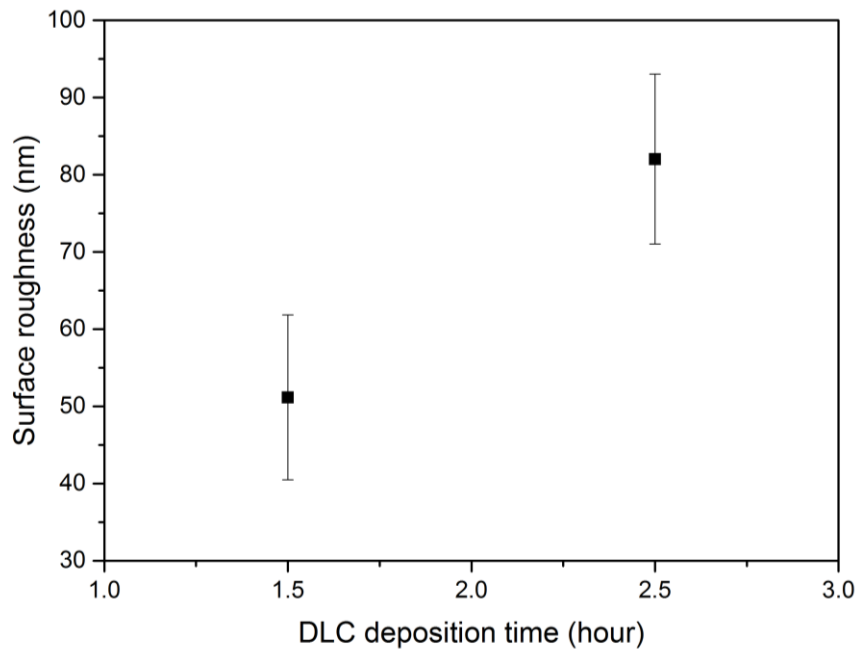
Figure 6.6 The surface roughness of multilayer DLC-GNP nanocomposite coating by the function of deposition time of DLC. The error bars in the graph indicate standard deviation for ten measurements

The volumetric concentration of GNP for multilayer DLC-GNPML1.5 and DLC-GNPML2.5 was estimated to be approximately 0.17 and 0.10 vol% respectively. The values were calculated based on the vol% obtained in Section 5.5.1 and DLC thickness in Section 5.4.1. The values also were measured assuming that the GNP amount is double of that in the single-layer DLC-GNP nanocomposite coatings. The GNP vol% for multilayer coatings is generally slightly higher than single-layer DLC-GNP due to lower thickness of both layers of DLC and higher amount of GNP in the nanocomposite.

6.3.3 Adhesion

The scratch test was performed with the same method explained previously in Chapter 3 and 5. Figure 6.7 shows optical micrographs of scratch tracks of DLC-GNP multilayer nanocomposite coating with different DLC deposition time of 1.5 and 2.5 hours. The position of L_{C1} in each scratch track is marked as a black arrow. As can be seen in the figure, coating failure of sample DLC-GNPML2.5 occurred much earlier than DLC-GNPML1.5. Areas A, B, C and D

in Figure 6.7 represents the area at coating failure (L_{C1}) and end of the scratch track for sample DLC-GNPML1.5 and DLC-GNPML2.5 respectively.

Higher magnification of areas A, B, C and D are shown in Figure 6.8. As can be seen in Figure 6.8 (a) and (c), both scratches start with tensile cracking before having wedge spallation. This is a common coating failure that was also seen with the single layer DLC-GNP nanocomposite coating in Chapter 5. The major difference between the two coatings is the gross spallation that occurred towards the end of the scratch track in Figure 6.8(d) which is sample DLC-GNPML2.5. While for sample DLC-GNPML1.5 (Figure 6.8(b)), no gross spallation can be observed.

The recorded critical load is plotted in Figure 6.9. Critical load of sample DLC-GNPML1.5 has higher critical load at 20.26 N compare to DLC-GNPML2.5. The adhesion strength of DLC-GNPML1.5 increased to almost double that of DLC-GNPML2.5. DLC-GNPML1.5 has much higher critical load than the single-layer DLC-GNP.
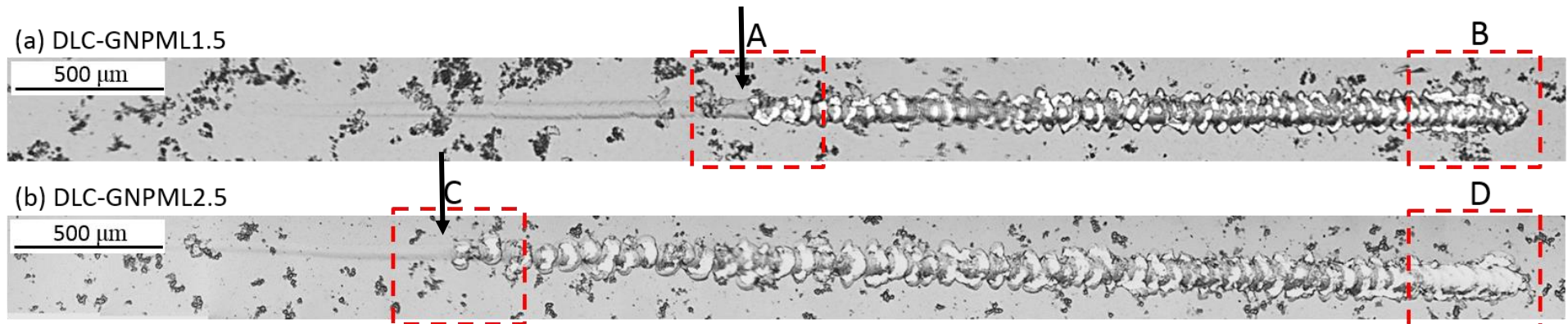
Figure 6.7 Optical micrographs of the scratch tracks showing the failure characteristics of (a) DLC-GNPML1.5 and (b)DLC-GNPML2.5 nanocomposite coating. Scratch direction is from left to right
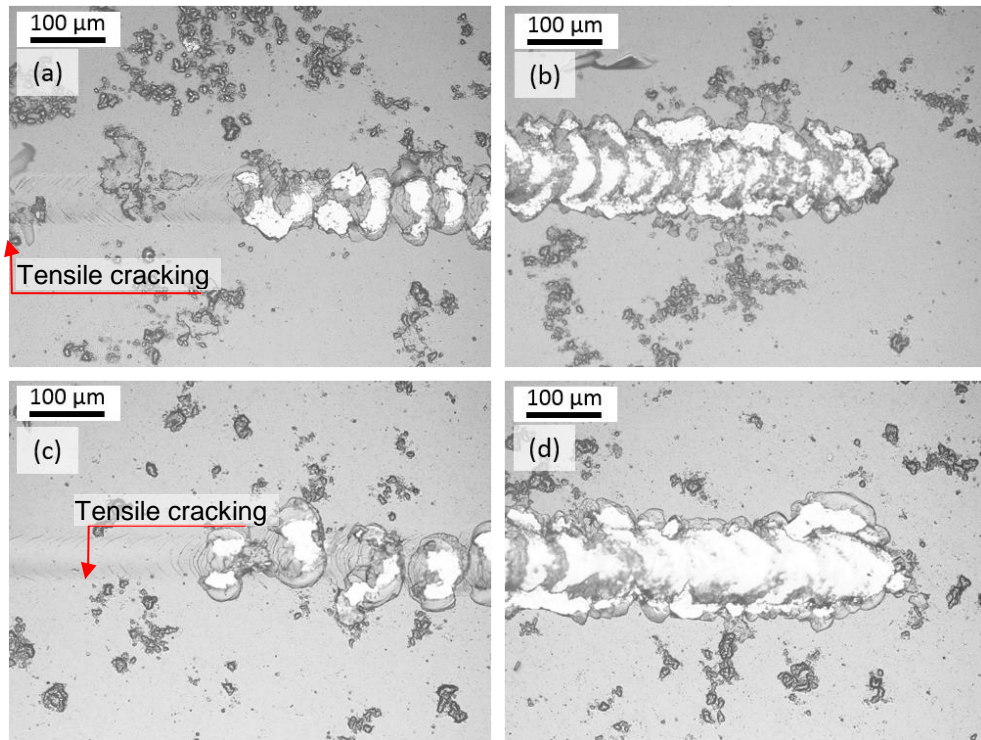
Figure 6.8 Higher magnification of optical micrographs at (a) area A, (b) area B, (c) area C and (d) area D labelled in Figure 6.7
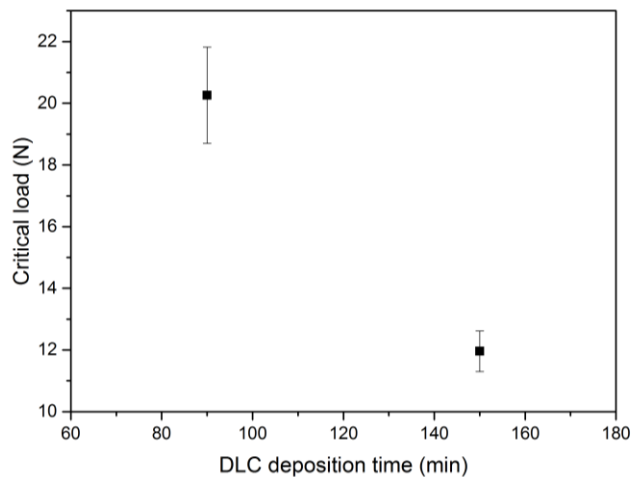
Figure 6.9 Critical load of multilayer DLC-GNP nanocomposite coating as a function of deposition time of DLC. The errors bars indicate the standard deviation of six measurements.

The scratch depth at L_{C1} and the maximum depth at the end of scratch were also analysed using WLI. The scratch depth at both positions of sample DLC-GNPML1.5 and DLC-GNPML2.5 are shown in Figure 6.10. The cross-section profile displays that DLC-GNPML2.5 had only slightly deeper penetration depth

and a wider scratch when the coating failure occurred. The same condition was also observed at the end of the scratch where maximum depth of scratch was achieved. Sample DLC-GNPML1.5 has shallower maximum depth at around 4.5 µm. This indicates that the surface of DLC-GNPML2.5 can be penetrated deeper.
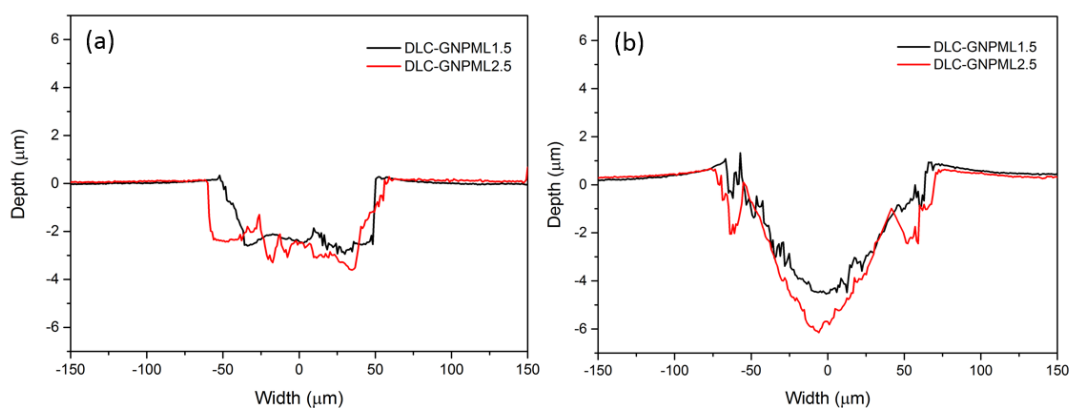
Figure 6.10 Scratch depth at (a) L_{C1} and (b) end of scratch for multilayer DLC-GNP nanocomposite coating

6.3.4 Raman analysis

Raman spectra of the multilayer DLC-GNP nanocomposite coating was analysed to investigate the chemical structure of multilayer DLC-GNP deposited with different DLC deposition times. Figure 6.11 exhibit the typical Raman spectra of multilayer DLC-GNPML1.5 and DLC-GNPML2.5 nanocomposite coating respectively. The Raman spectra were deconvoluted to D and G-peaks using Gaussian line shapes. Summary of the D and G-peaks position; and the measured I_D/I_G ratio based on the different areas of coating were tabulated in Table 6.3. D and G-peak for both samples lie in the same range recorded as the single layer DLC-GNP in Chapter 5. The range of I_D/I_G ratio for both samples is shown in Figure 6.12. Sample DLC-GNPML1.5 has a slightly higher range of I_D/I_G ratio, but no significant difference can be seen.
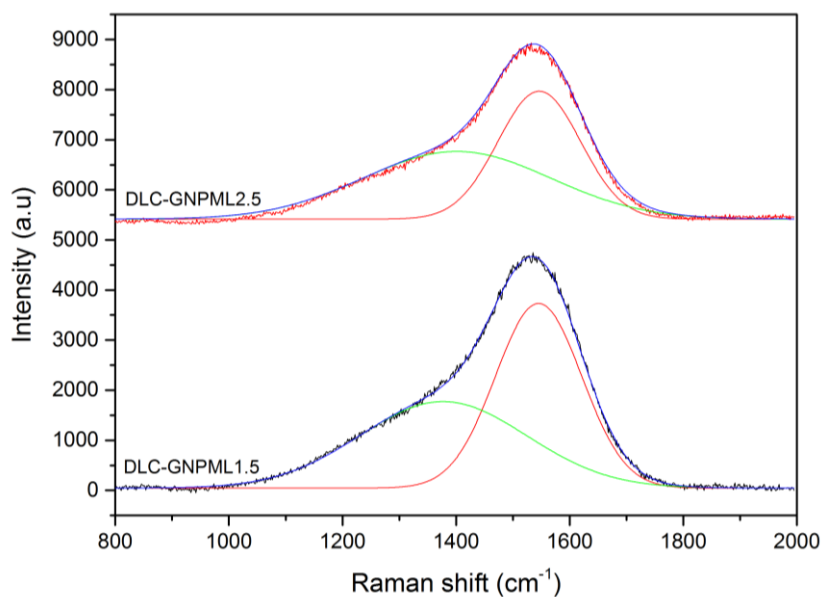
Figure 6.11 Representative Raman spectra of multilayer DLC-GNP with different DLC deposition time of 1.5 and 2.5 hour

Table 6.3 Position and integrated intensity I_D/I_G of the main peaks in Raman spectra of multilayer DLC-GNP nanocomposite coatings

Sample	D-peak position (cm^{-1})	G-peak position (cm^{-1})	I_D/I_G
DLC-GNPML1.5	1377-1411	1545-1552	0.47-0.58
DLC-GNPML2.5	1369-1413	1544-1549	0.44-0.57
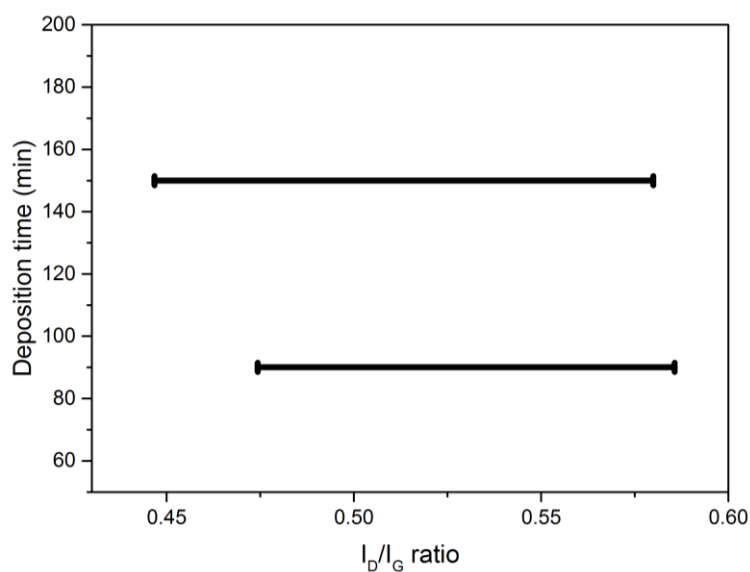
Figure 6.12 The range of I_D/I_G ratio for DLC-GNP with different coating thickness

223

6.3.5   XPS analysis of DLC-GNP nanocomposite coating

XPS analysis was carried out on DLC-GNP nanocomposite coating to derive the quantitative evaluation of sp^2 and sp^3 bond content in the nanocomposite coating. Sample DLC-GNPML1.5 was selected as it has the strongest adhesion strength of all tested samples (see Section 6.3.3). As a comparison, XPS analysis was also conducted on pure DLC coating. After the subtraction of Shirley background, the peak corresponding to sp^2 and sp^3 and C-O were fitted with symmetric Gaussian-Lorentzian sum function.

The XPS C1s and O1s scan spectra of pure DLC and as deposited DLC-GNPML1.5 are shown in Figure 6.13 (a) and Figure 6.14 (a and c) respectively. The existence of O1s peak is negligible due to a weak intensity compared to the intensity of C1s peak. The O1s peak may results from surface contamination cause by air exposure [188, 186, 200]. This kind of contamination is commonly observed in surface analysis including XPS. C1s peak is the major characteristic for both pure DLC and DLC-GNPML1.5 coatings.

As it has been mentioned earlier, since GNP does not cover the entire samples's surface, there are two distinct areas in DLC-GNPML1.5 coating: (i) area with GNP + DLC, and (ii) area with DLC only. The two spectra of those areas are shown in Figure 6.14. Figure 6.13 (b) and Figure 6.14 (b) shows the deconvolution results of XPS C1s line by using curve-fitting with Gaussian and Lorentz function. The spectrum was deconvoluted into three peaks which are assigned to the C-O, sp^3 and sp^2 bonds respectively. The sp^2 and sp^3 ratios of the coatings were determined from the area of the curves-fitted for XPS C1s spectrum.
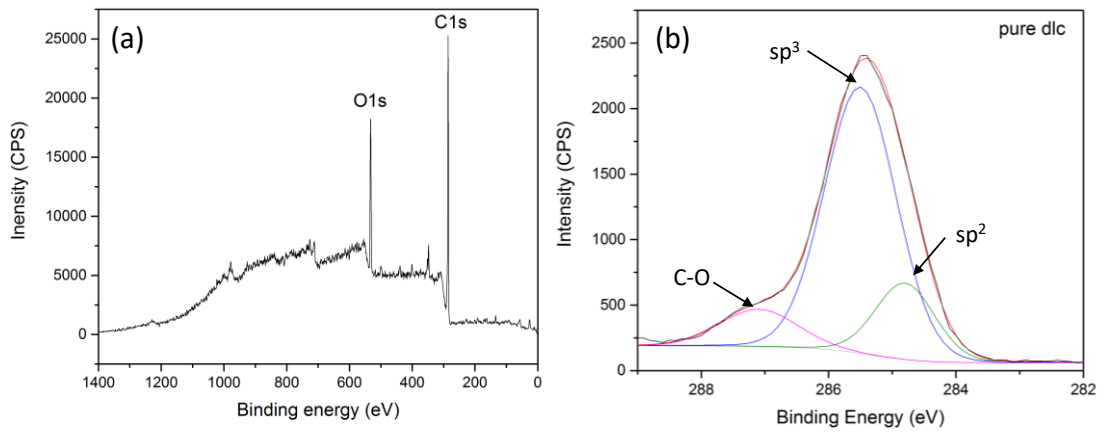
Figure 6.13 (a) XPS survey spectrum and (b) deconvolution of C1s peak for pure DLC coating
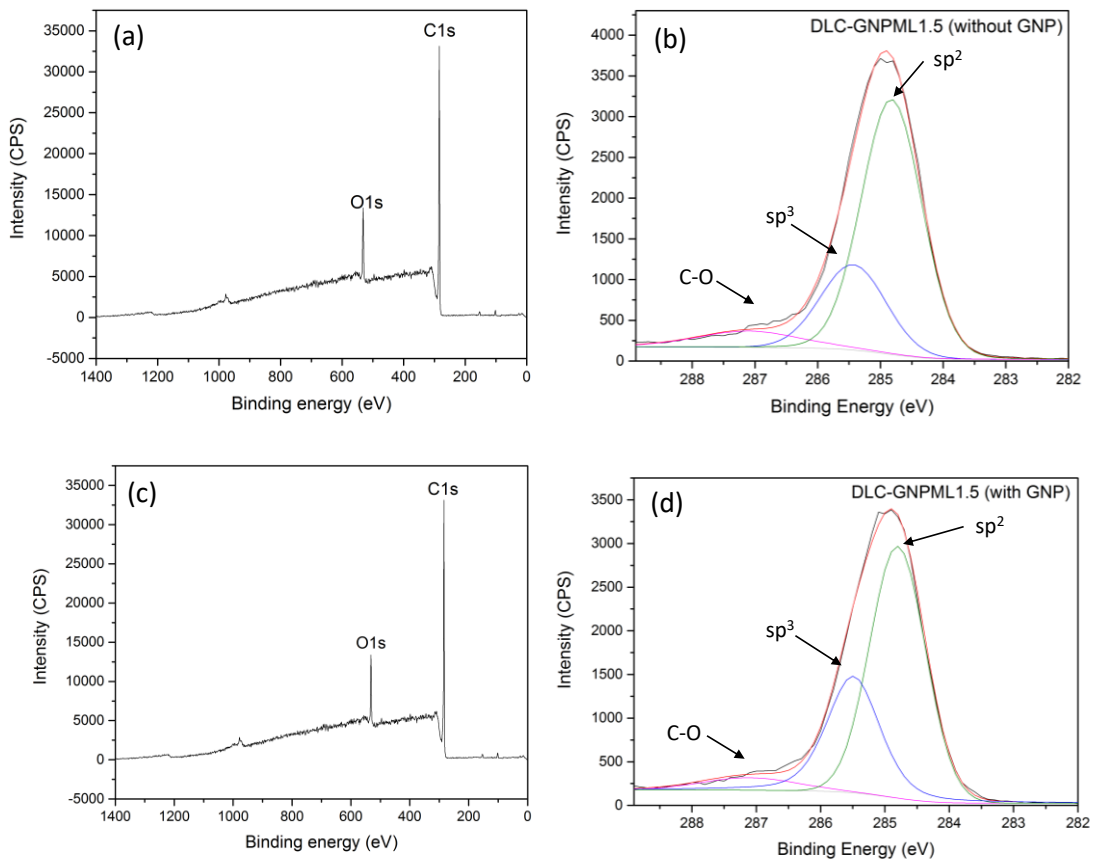
Figure 6.14 (a and c) XPS survey spectrum, and (b and d) deconvolution of C1s peak for multilayer DLC-GNPML1.5 nanocomposite coating at the area with and without GNP respectively

Table 6.4 summarises the measured binding energy, peak contribution of sp^2, sp^3 and C-O configuration, and sp^2/sp^3 ratio for pure DLC and multilayer DLC-GNPML1.5 nanocomposite coatings. As can be seen, sp^2 content increased significantly when GNPs were added into the multilayer DLC-GNP coating. This attributed to rich sp^2 content at the outer layer of the coating.

Table 6.4 Results of XPS analysis on pure DLC and DLC-GNPML1.5

Sample	Binding energy (eV)			Peak contribution (%)			sp^2/sp^3 ratio
	sp^2	sp^3	C-O	sp^2	sp^3	C-O	
Pure DLC	284.9	285.6	287.2	16.0	74.0	10.0	0.2
DLC-GNPML1.5 (Area DLC+GNP)	284.8	285.5	287.1	62.6	32.1	5.2	2.0
DLC-GNPML1.5 (Area DLC)	284.8	285.4	287.1	67.4	24.3	8.3	2.8

6.3.6 Tribological properties of multilayer DLC-GNP nanocomposite coating

The tribological test was conducted with the same condition described previously in Chapter 3 and 5. The test was carried out to investigate the effect of DLC deposition time on the tribological behaviour of multilayer DLC-GNP nanocomposite coating. All tests are repeated three times to ensure repeatability and accuracy.

6.3.6.1 Friction evaluation

Figure 6.15 presents the CoF by a function of time for multilayer DLC-GNP nanocomposite coating with different DLC deposition time. In general, the CoF value for multilayer DLC-GNPML1.5 and DLC-GNPML2.5 varies in the range of 0.08 - 0.10 and 0.08 – 0.12 respectively. Sample DLC-GNPML2.5 is still not in steady state condition within three hours of the start of the test. CoF increased steadily with time. It is predicted that the value may rise with further time increase. In contrast, for sample DLC-GNPML1.5, the steady-state condition

was achieved after reaching a peak at about 90 minutes of the test. The CoF remained almost the same after 90 minutes. The running-in period for sample DLC-GNPML1.5 is shorter than DLC-GNPML2.5 as can be seen in Figure 6.15.
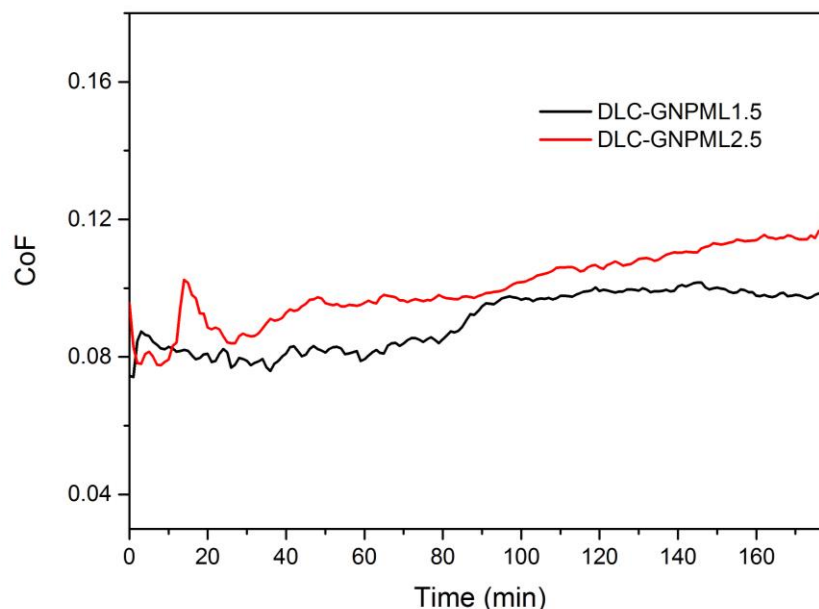
Figure 6.15 Representative of CoF by a function of time for sample
DLC-GNPML1.5 and DLC-GNPML2.5 tested for three hours in base oil

The average CoF calculated at the last two hours of the test is plotted in Figure 6.16. The lowest average CoF is recorded from sample DLC-GNPML1.5 with a value of approximately 0.10. Although the average CoF value for sample DLC-GNPML2.5 does not differ much from DLC-GNPML1.5, the value was calculated from unsteady-state values that change with time as shown in Figure 6.15.
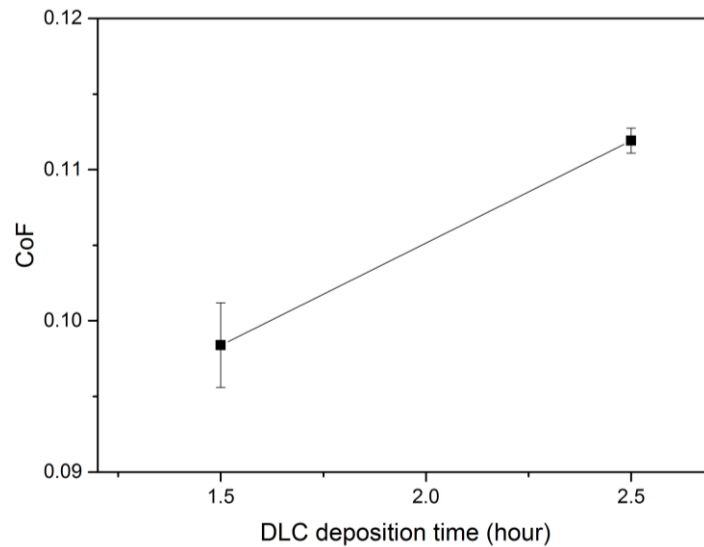
Figure 6.16 Average CoF for multilayer DLC-GNP coatings measured in the last two hours of the test by a function of DLC deposition time. The error bars in the graph indicate standard deviation for three measurements

6.3.6.2 Observation of wear track of coating and wear scar of the counterpart

An optical microscope was employed to observe the morphology of wear track of coating and wear scar of the counterpart. The morphology of wear tracks is displayed in Figure 6.17. The wear track appearance of sample DLC-GNPML2.5 is more severe than DLC-GNPML1.5 with slightly a wider wear track. This may associate to a longer running-in period of sample DLC-GNPML2.5 as seen earlier in Figure 6.15. Worn machining mark is more severe for sample DLC-GNPML2.5 compared to DLC-GNPML1.5. Adhered coating materials can still be seen in some areas in sample DLC-GNPML1.5. Both may be classed as severely worn which involved delamination of the coating. Adhesive wear may be the dominant mechanism considering the severe wear of both samples.
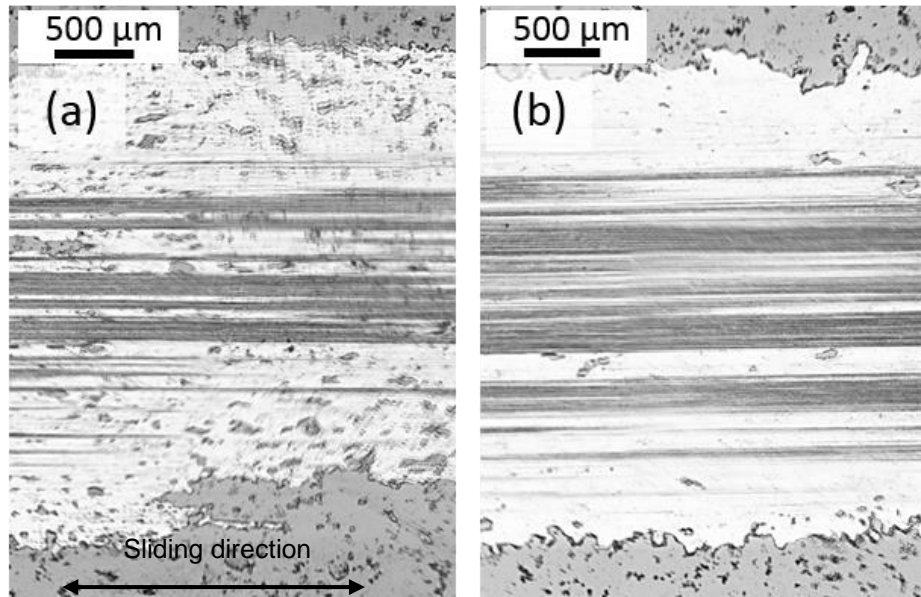
Figure 6.17 Optical micrographs of wear track of sample (a) DLC-GNPML1.5 and (b) DLC-GNPML2.5 after three hours of test in base oil

Figure 6.18 shows the topography of the wear scar for samples DLC-GNPML1.5 and DLC-GNPML2.5. Cross-section profile demonstrated complete delamination of DLC-GNPML1.5 to the interlayer but did not reach the substrate. As seen earlier in Figure 6.17(a), adhered coating materials exist in some areas in the wear track of DLC-GNPML1.5. This is similar to the columnar structure that has been observed for sample DLC-GNPheat180 and DLC-GNPheat240 in Section 5.4.6, but with more severe wear. Coating of DLC-GNPML2.5 was deeply abraded to the substrate leaving a large wear track width of approximately 3.3 mm which also can be observed in Figure 6.17(b).
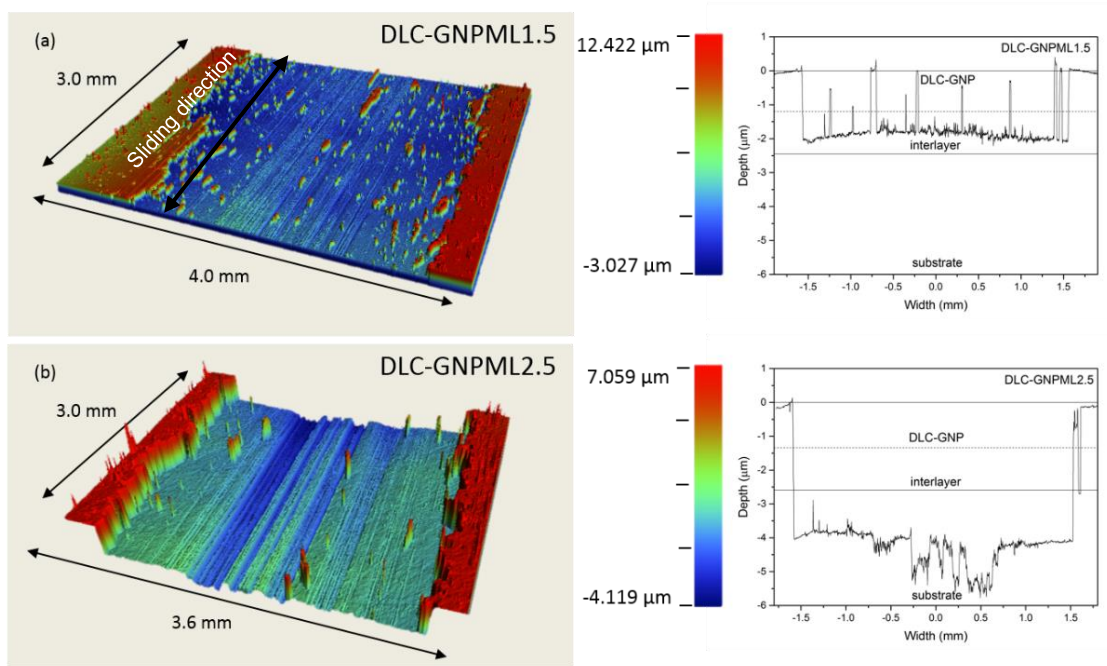
Figure 6.18 Surface topography and the corresponding cross-section profiles of wear tracks for (a) DLC-GNPML1.5 and (b) DLC-GNPML2.5 respectively after three hours of tribotest in base oil

The optical micrographs of counterpart for samples DLC-GNPMLC1.5 and DLC-GNPML2.5 are shown in Figure 6.19. The wear scars exhibit clear abrasion wear scars after the three hours test in base oil with a massive size of the diameter of approximately 3.70 and 3.80 mm respectively. The wear scar of counterpart DLC-GNPML2.5 is rougher and displays deeper machining marks as compared to the counterpart of DLC-GNPML1.5.

The surface topography and cross-section profile of the wear scar in Figure 6.20 clearly shows the wear severity on the counterpart of DLC-GNPML2.5. The wear scar of counterpart DLC-GNPML2.5 is very rough with deep scratches. Meanwhile, the wear scar on counterpart DLC-GNPML1.5 in Figure 6.20(a) is not as rough or severe as the wear scar on counterpart DLC-GNPML2.5.
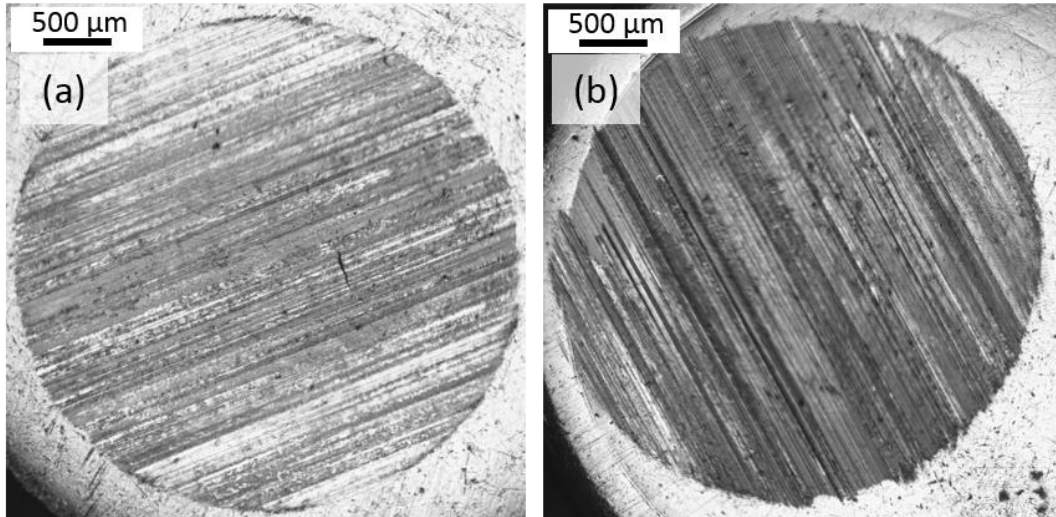
Figure 6.19 Optical micrographs of wear scar of counterpart for (a) DLC-GNPML1.5 and (b) DLC-GNPML2.5 after three hours of test in base oil
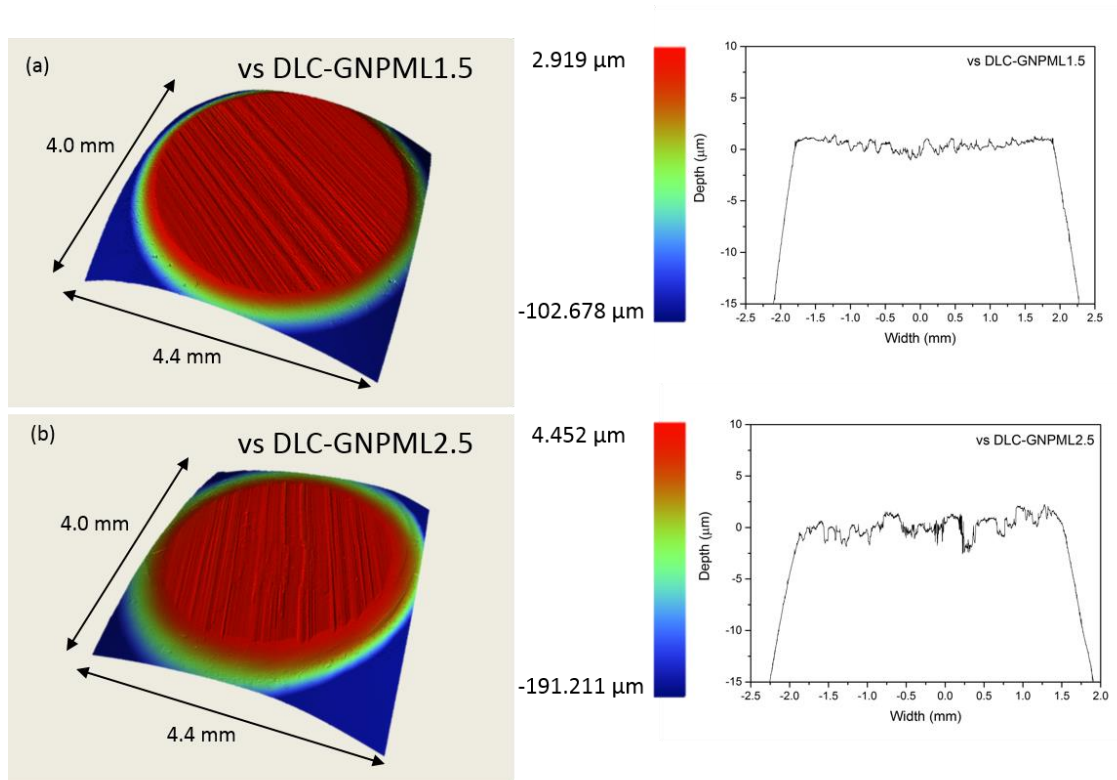
Figure 6.20 Surface topography and the corresponding cross-section profiles of the counterpart wear scar for (a) DLC-GNPML1.5 and (b) DLC-GNPML2.5

6.3.6.3 Analysis of wear rate of DLC-GNPML

The wear rate of all samples was measured using the same method mentioned in Section 3.8.3. Figure 6.21 presents the wear rate and depth of multilayer DLC-GNP deposited with 1.5 and 2.5 hours. The wear rate increased with coatings of greater deposition time. This is in accordance with the experimental results from surface morphology and topography of the wear track. The wear depth value is also consistent with the calculated of wear rate.

The correlation between CoF and the wear rate is plotted in Figure 6.22. Both CoF and wear rate shows an increase in DLC deposition time. It is evident from the results that higher wear of DLC-GNPML2.5 is related to higher CoF of the coating.
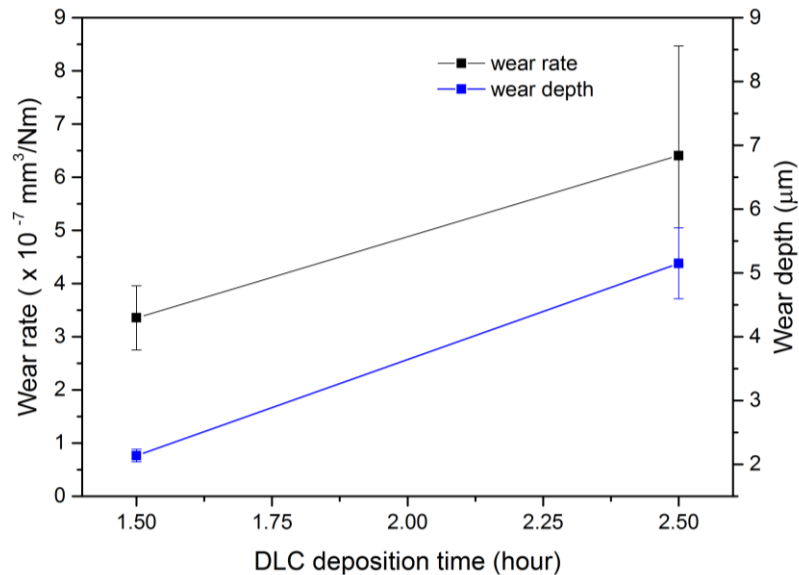
Figure 6.21 Wear rate and depth of wear track of multilayer DLC-GNP nanocomposite coatings at DLC deposition time of 1.5 and 2.5 hours. The error bars in the graph indicate standard deviation for three measurements
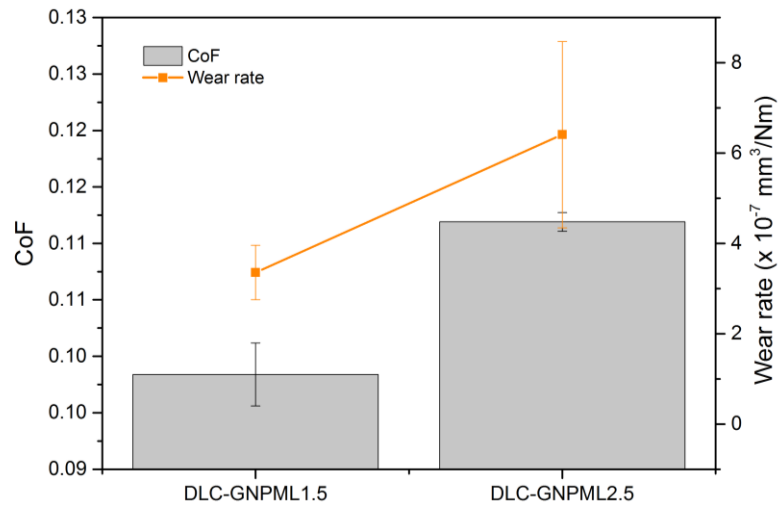
Figure 6.22 The CoF and the wear rate of multilayer DLC-GNP nanocomposite coating at different DLC deposition time of 1.5 and 2.5 hours

6.3.6.4 Analysis of wear rate of the counterpart of DLC-GNPML

The wear rate and wear scar diameter of sample DLC-GNPML1.5 and DLC-GNPML2.5 are presented in Figure 6.23. As can be seen in the graph, there is only marginal difference in the wear rate of both samples. However, sample DLC-GNPML2.5 has a huge standard deviation which is more than double compared to DLC-GNPML1.5.
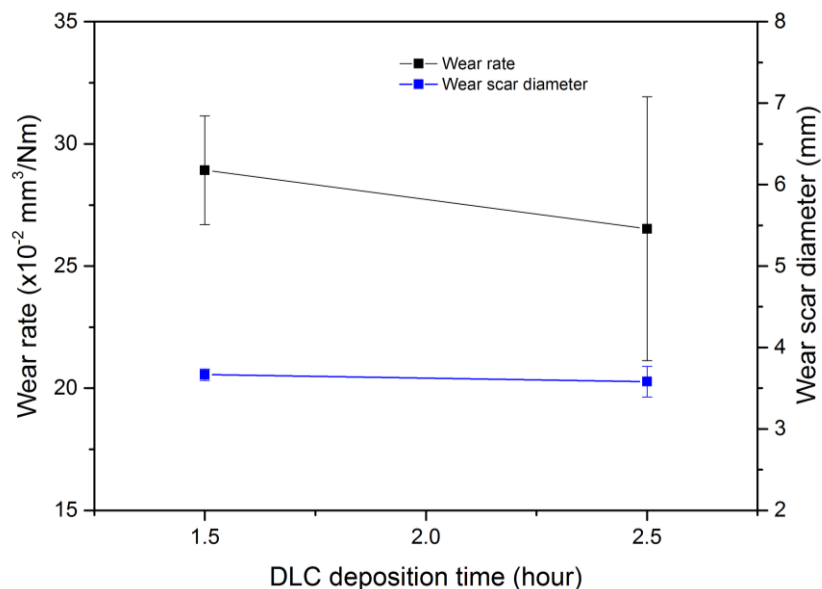
Figure 6.23 Wear rate of the counterpart as a function of DLC deposition time

6.3.6.5 Raman analysis of wear

Raman analysis was carried out on the wear tracks after 3-hour of the test in base oil and shown in Figure 6.24 for interpretation of the wear mechanism. One of the wear track area of DLC-GNPML1.5 in Figure 6.8(a) exhibits similar spectrum to that of DLC-GNP nanocomposite coating. The spectrum of the other wear area has peaks which can be associated with the disordered carbon spectrum. Both spectra on the wear tracks for sample DLC-GNPML2.5 in Figure 6.24(b) are comparable to the disordered carbon spectrum mentioned before in the wear of DLC-GNPML1.5. A peak at around ~680 cm^{-1} that has also been seen before in other wear tracks, belong to Fe-oxide can also be observed in some of the spectra. It can also be observed that the intensity of all peaks for wear of DLC-GNPML2.5 is noticeably lower than the wear in DLC-GNPML1.5. The position and I_D/I_G ratio of the peaks in the Raman spectra is summarized in Table 6.5. The D-peak position lies between 1351 and 1404 cm^{-1}, whereas the G-peak position is found in the range of 1555 - 1640 cm^{-1}. The I_D/I_G ratio varies between 0.52 and 0.89. Compare to the I_D/I_G ratio of as-prepared coating, the I_D/I_G value in some of the wear areas are high. An increase of I_D/I_G ratio indicates an increase of carbon-carbon bonds disorder in coating [182].
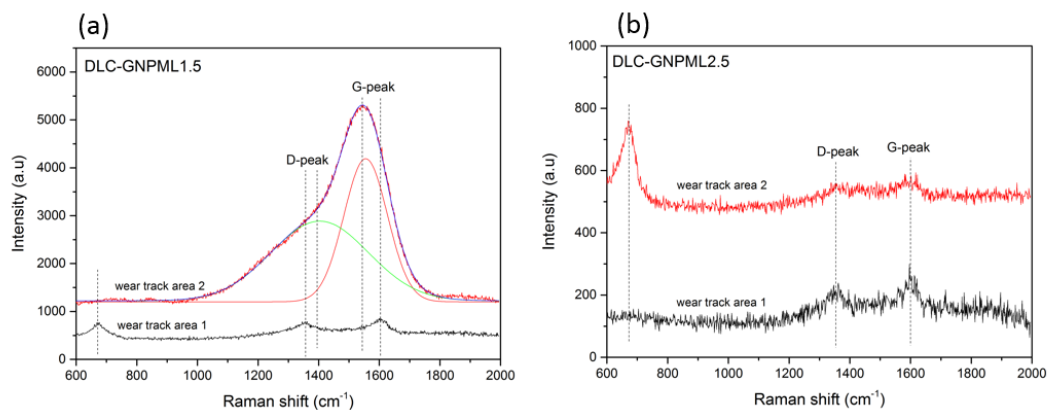
Figure 6.24 Raman spectra collected within the wear track of (a) DLC-GNPML1.5 and (b) DLC-GNPML2.5

Table 6.5 Position and integrated intensity I_D/I_G of the main peaks in Raman spectra of the wear tracks

Sample	Area	D-peak position (cm^{-1})	G-peak position (cm^{-1})	Fe-oxide position (cm^{-1})	I_D/I_G
DLC-GNPML1.5	Wear track area 1	1404	1555	-	0.56
	Wear track area 2	1351	1594	671	0.89
DLC-GNPML2.5	Wear track area 1	1352	1594	-	0.86
	Wear track area 2	1371	1640	664	0.52

Figure 6.25 presents the I_D/I_G ratio of the wear tracks as a function of DLC deposition time. The shaded area is the range of I_D/I_G ratio of multilayer DLC-GNP coating before wear test. As can be seen, there are two regions exist on the wear tracks. One is the region which almost remained unchanged compared to ratio before the test. The other region has a higher I_D/I_G ratio that be attributed to graphitisation of the coatings [176, 188, 189].
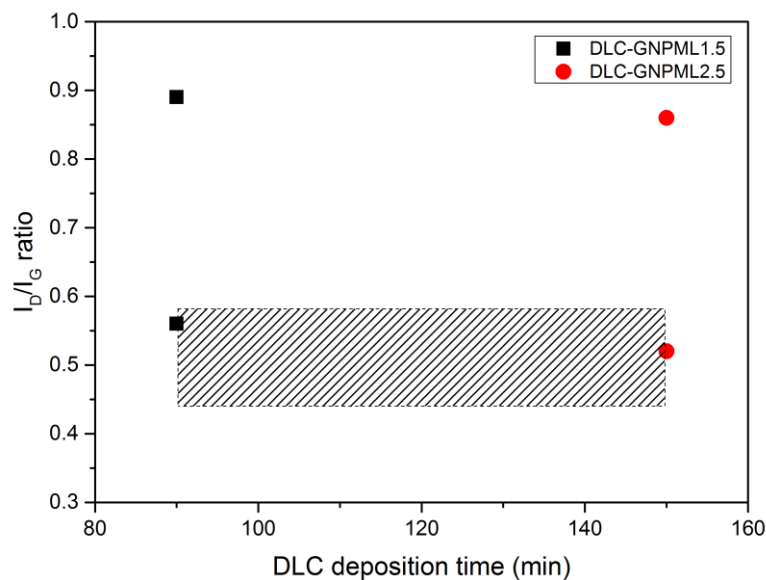
Figure 6.25 I_D/I_G ratio of wear track as a function of DLC deposition time for multilayer DLC-GNP with DLC deposition time of 90 and 150 minutes

Raman analysis of the wear scar of both multilayer DLC-GNP nanocomposite coatings is shown in Figure 6.26. The Raman spectra reveals peaks of D and G of disordered carbon. A similar peak to as-prepared DLC-GNP also can be observed in one spectrum in Figure 6.26(b). The position and the measured I_D/I_G were summarized in Table 6.6. The D and G-peak in the spectra were located at between 1345 - 1352 cm^{-1} and 1556 - 1594 cm^{-1} respectively. The I_D/I_G ratio of wear scar on DLC-GNPML1.5 is higher at both wear areas as compared to the wear scar on DLC-GNPML2.5.
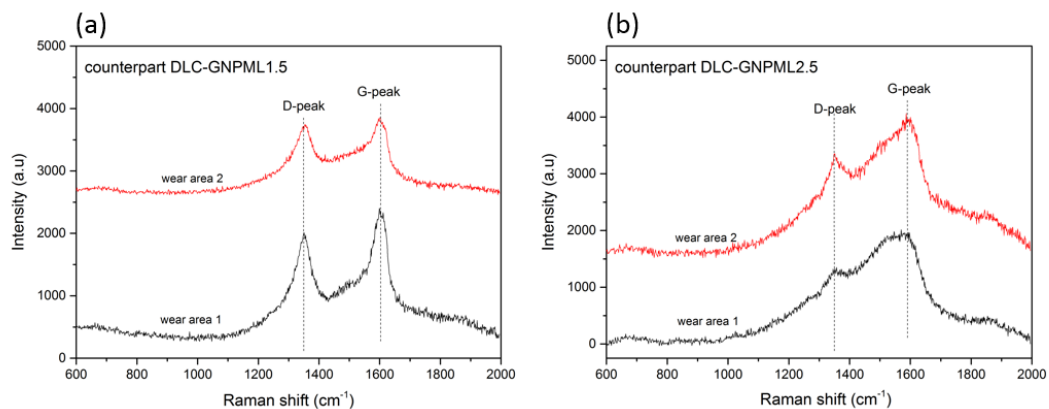
Figure 6.26 Raman spectra collected within the wear scar of counterpart (a) DLC-GNPML1.5 and (b) DLC-GNPML2.5

Table 6.6 Position and integrated intensity I_D/I_G of the main peaks in Raman spectra of the wear scars

Sample	Area	D-peak position (cm^{-1})	G-peak position (cm^{-1})	I_D/I_G
DLC-GNPML1.5	Wear area 1	1349	1594	0.81
	Wear area 2	1352	1586	0.88
DLC-GNPML2.5	Wear area 1	1352	1556	0.47
	Wear area 2	1345	1564	0.45

6.3.7 Summary of effect of DLC deposition time

The following summary can be drawn from the results obtained:

i.   The thickness of multi-layer DLC-GNP nanocomposite coating is much higher than estimated thickness due to the arrangement of spin-coated GNP in each layer.

ii.   The adhesion strength of DLC-GNP nanocomposite coating prepared with DLC deposition of 1.5 hours is double than the coating with longer DLC deposition of 1.5 hours.

iii.   The I_D/I_G ratio of both multilayer DLC-GNP deposited with different thickness is about the same.

iv.   The sample prepared with DLC deposition of 1.5 hours has better CoF of 0.1 and wear rate compare the other sample.

v.   Raman spectra analysis suggest that graphitisation occurred in some area of the coating and left some area unchanged after the sliding test.

6.4   Effect of GNP Concentration

In this section, the effect of GNP concentration on the physical, mechanical and tribological properties of multilayer DLC-GNP nanocomposite coating was investigated. Taking into consideration the results obtained in Section 1.3 on the effect of DLC deposition time, a DLC deposition time of 1.5 hours was selected for this work. The GNP heating time for the post-treatment process was set to 180 minutes, considering the optimum conditions that have been obtained in Section 5.5. Three concentration of GNP was chosen which are 0.25, 1.0 and 2.0 mg/mL. Process condition for spin coating remained the same as previous test. The deposition steps are the same as been described in Section 6.3. The conditions of sample preparation are summarised in Table 6.7. Samples in this section are abbreviated as DLC-GNPMLC0.25, DLC-GNPMLC1.0 and DLC-GNPMLC2.0 for GNP concentrated of 0.25, 1.0 and 2.0 mg/mL respectively.

Table 6.7 Experimental parameters for preparation of multilayer DLC-GNP with different GNP concentration

Sample	GNP concentration (mg/mL)	Spinning speed (rpm)	Spinning time (sec)	GNP amount (mL)	Post-treatment heating duration (min)	DLC deposition time (hour)
DLC-GNPMLC0.25	0.25					
DLC-GNPMLC1.0	1.0	1000	30	1	180	1.5
DLC-GNPMLC2.0	2.0					

6.4.1 Surface morphology and surface roughness of multilayer DLC-GNP

Surface morphology of multilayer DLC-GNP prepared with different GNP concentration were investigated using an optical microscope. Figure 6.27 displays the optical micrographs of DLC-GNPMLC0.25, DLC-GNPML1.0 and DLC-GNPML2.0 respectively. The number of black areas which represent the GNP islands increased as the GNP concentration increased. The results are similar to that obtained with single layer DLC-GNP with different concentrations of GNP.

Figure 6.28 shows the surface topography and the corresponding surface profile of multilayer DLC-GNP samples with different GNP concentration of 0.25, 1.0 and 2.0 mg/mL. As can be seen from the figure, the surface becomes rougher as the concentration of GNP was increased. This is due to the amount of spin-coated GNP on the surface. Higher concentrations deposit more GNP on the surface, thereby making the surface rougher. The same phenomena also have been observed before in Section 5.6.

The surface roughness was measured and displays in Figure 6.29. The plot of surface roughness as a function of GNP concentration shows that the surface roughness increases almost linearly with GNP concentration. The surface

roughness of coating range between ~ 23 -104 nm. The surface roughness of multilayer DLC-GNP increased more than 90% and up to almost 300% compared to the surface roughness obtained in Section 5.6.
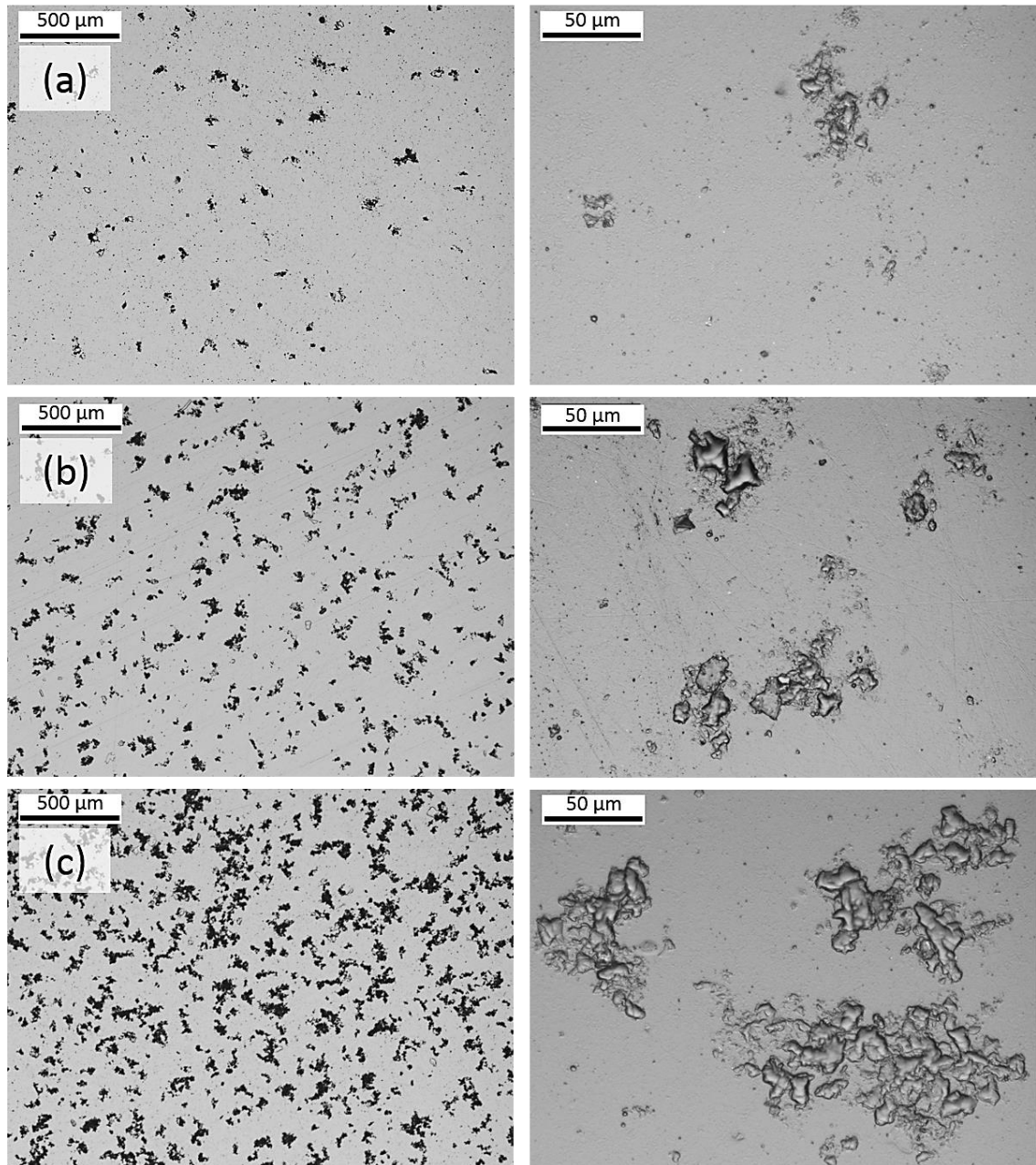
Figure 6.27 Optical micrographs of (a) DLC-GNPMLC0.25, (b) DLC-GNPMLC1.0 and (c) DLC-GNPMLC2.0. The corresponding higher magnification of the optical micrographs is shown on the right side of each micrograph
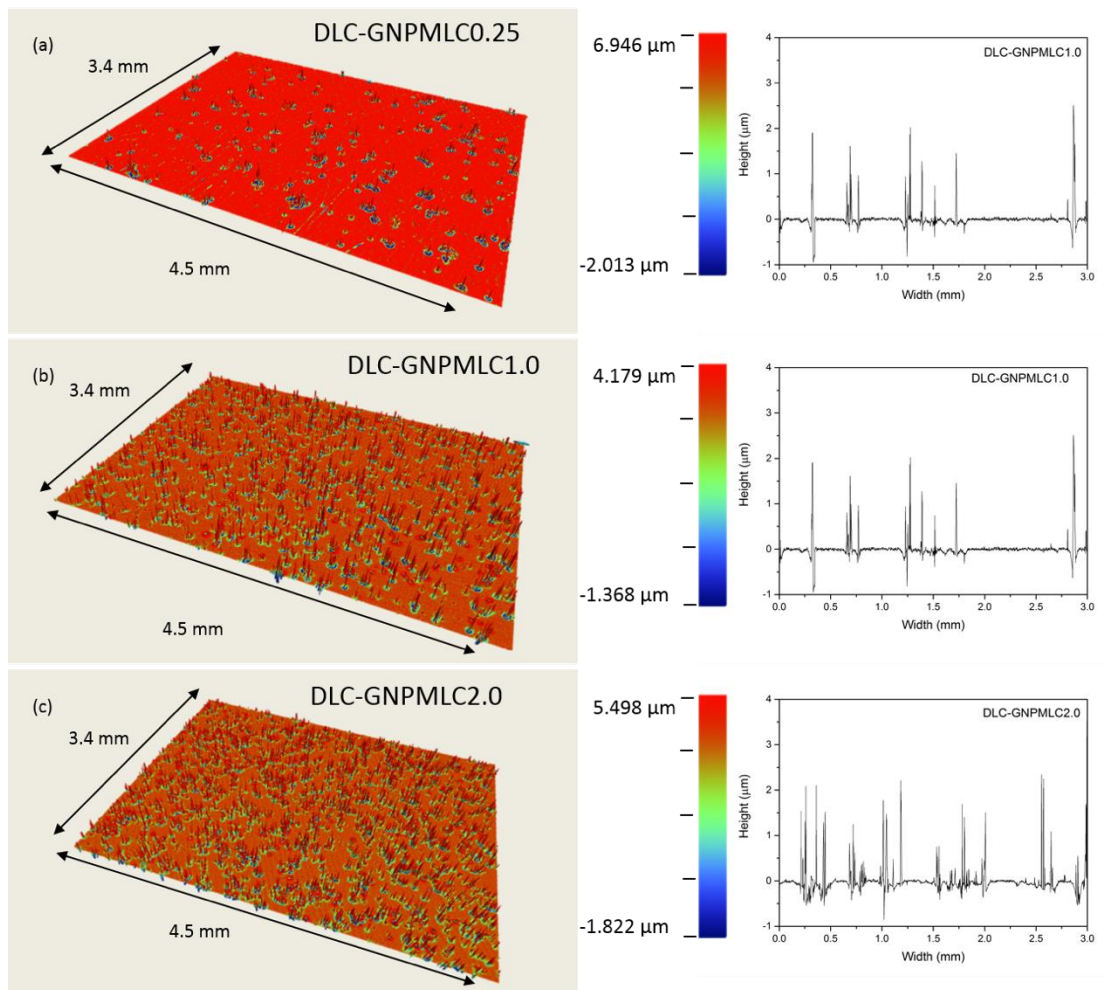
Figure 6.28 Surface topography and its corresponding surface profile of (a) DLC-GNPMLC0.25, (b) DLC-GNPML1.0 and (c) DLC-GNPMLC2.0
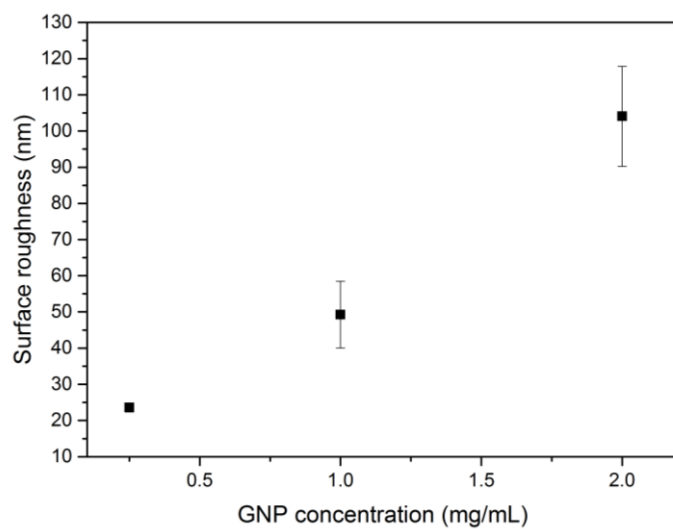
Figure 6.29 Surface roughness of multilayer DLC-GNP nanocomposite coating by a function of GNP concentration. The error bars in the graph indicate standard deviation for ten measurements

The GNP vol% in the multilayer DLC-GNP coatings at GNP concentration of 0.25, 1.0 and 2.0 mg/mL was calculated to be approximately 0.03, 0.25 and 0.44% respectively. The measurement was made considering the results obtained in Section 5.5.1 and 5.6.1. The vol% of GNP almost doubled when the concentration was increased to 2.0 mg/mL and reduced nearly by 90% when the concentration was reduced to 0.25 mg/mL.

6.4.2 Adhesion

Critical load of coated samples has been measured using scratch tests with the same method described previously. The critical load was measured to study the effect of GNP concentration on the adhesion strength of multilayer DLC-GNP nanocomposite coating. Figure 6.30 shows the optical micrographs of scratch tracks for multilayer DLC-GNP nanocomposite coating prepared with different GNP concentration of 0.25, 1.0 and 2.0 mg/mL. The scratch direction was from left to right direction. The point of initial coating failure, L_{C1} is marked as a black arrow in each track. All the coatings exhibit scratch track with peculiar serrated patterns above L_{C1}. In general, no gross spallation that involves complete delamination of coating took place in any of the scratch tracks in Figure 6.30. This can be seen clearly in high magnification view of areas marked as A, B, C and D in Figure 6.31. The scratch tracks in Figure 6.31(a, c and e) display the failure mode of tensile cracking before initial failure at L_{C1} as can be seen in Figure 6.30.

Figure 6.32 shows the critical load over GNP concentration. The critical load increase as the GNP concentration in DLC-GNP composite increase. The highest critical load is recorded from sample DLC-GNPMLC2.0 of approximately 31.2 N. Overall value of critical load recorded for all samples in this section is higher than any other samples prepared before.

The comparison of the penetration depth profile at L_{C1} and at maximum depth at the end of the scratch track for multilayer DLC-GNP with different GNP concentration is shown in Figure 6.33. All samples have almost the same depth penetration at LC1 at around 2.6 µm. The maximum depth of the scratch track of the sample lies between ~4.0 - 4.7 µm with sample DLC-GNPMLC0.25 having slightly lower depth compare to others.

241
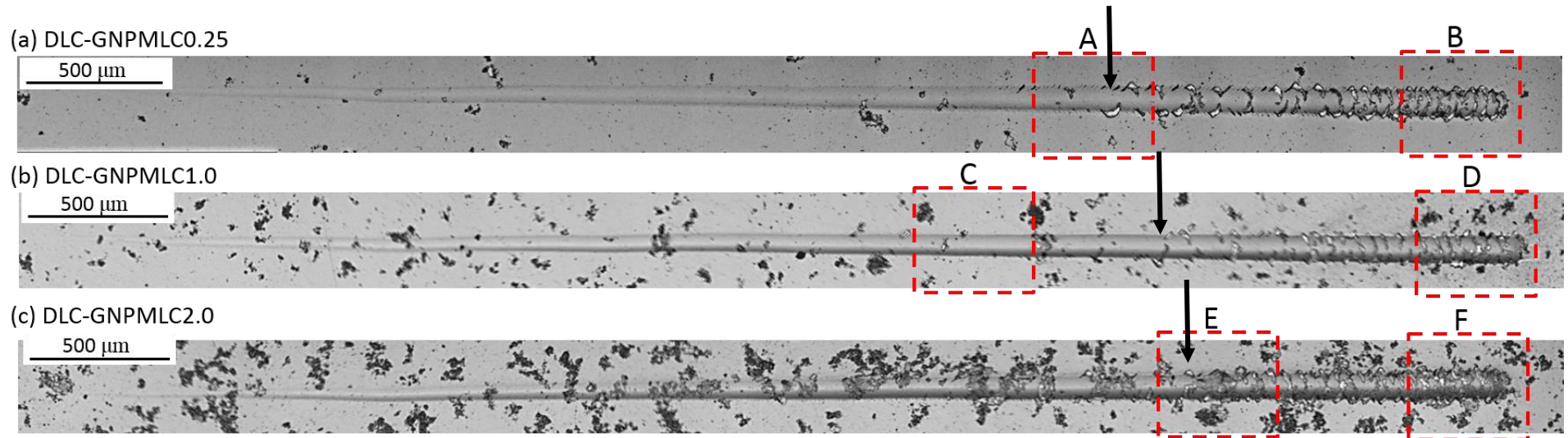
Figure 6.30 Scratch track for (a) DLC-GNPMLC0.25, (b) DLC-GNPMLC1.0 and (c) DLC-GNPMLC2.0 respectively
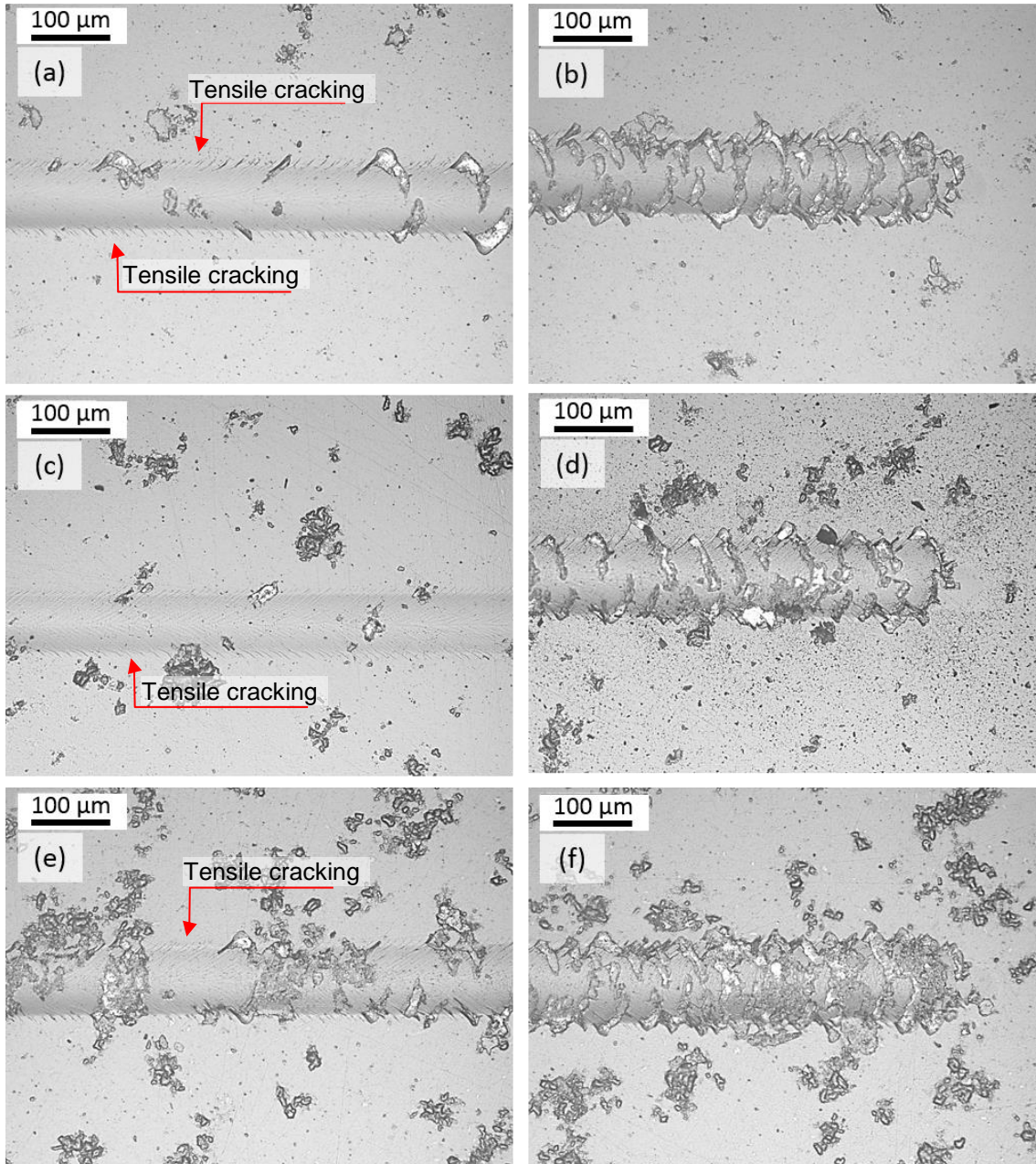
Figure 6.31 Higher magnification of optical micrographs at (a) A, (b) B, (c) C, (d) D, (e) E and (f) F areas in Figure 6.30.
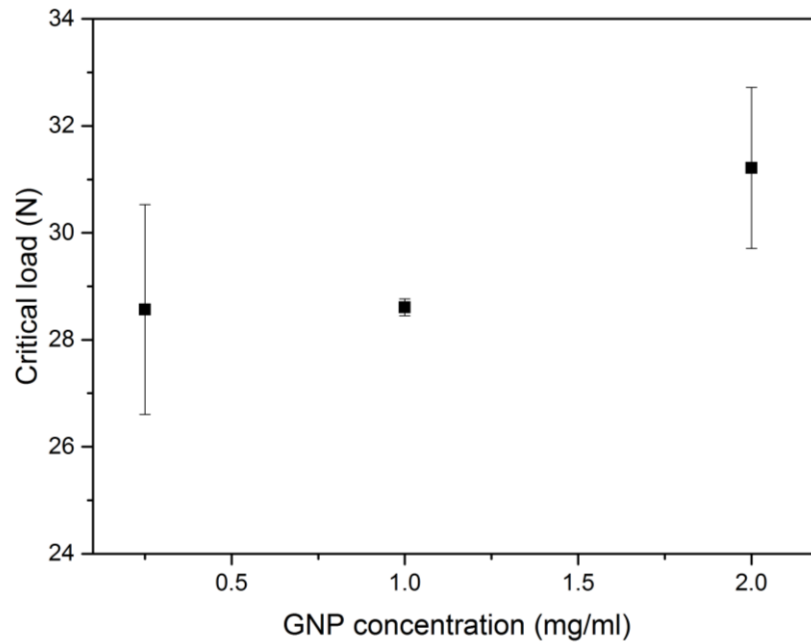
Figure 6.32 Critical load of DLC-GNP multilayer nanocomposite coating as a function of GNP concentration
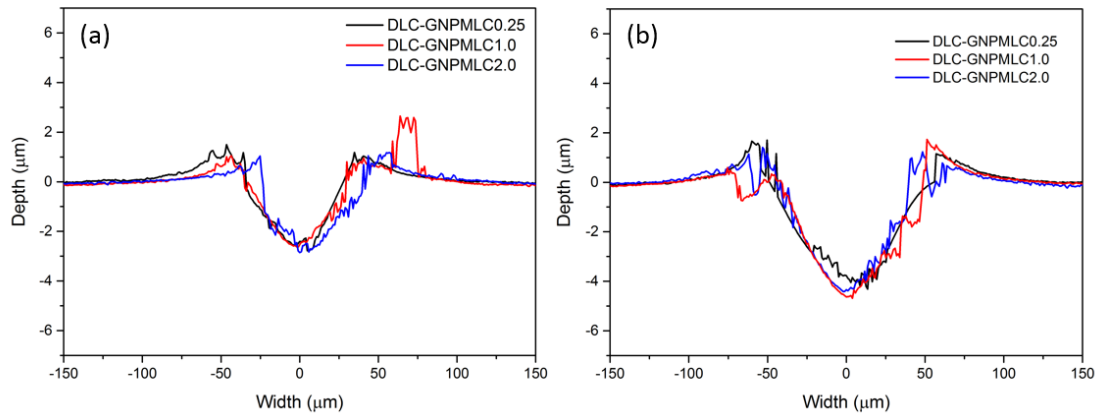
Figure 6.33 Scratch depth at (a) L_{C1} and (b) end of scratch for multilayer DLC-GNP at GNP concentration of 0.25, 1.0 and 2.0 mg/mL

6.4.3 Raman analysis

Raman analysis was carried out on multilayer DLC-GNP nanocomposite coating to investigate how changing the GNP concentration could change the chemical structure of the coating. Figure 6.34 presents the Raman spectra of multilayer DLC-GNPMLC0.25, DLC-GNPMLC1.0 and DLC-GNPMLC2.0.   All spectra show the typical shape of DLC-GNP composite obtained before, with signature broad G-peak and shoulder of D-peak. The position of D- and G-

244

peaks and its I_D/I_G ratio extracted from three different areas of the coating are summarized in Table 6.8.
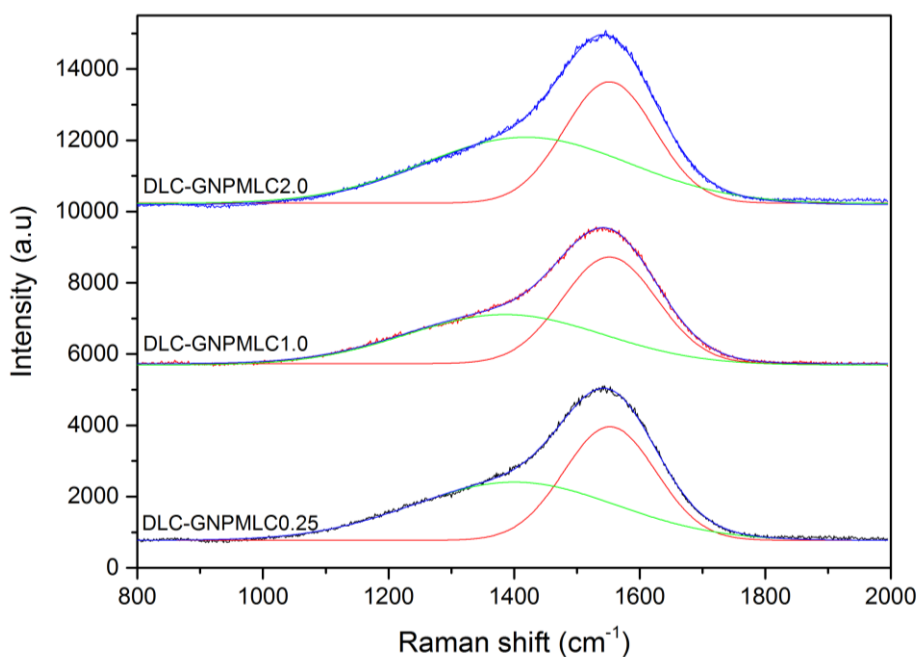
Figure 6.34 Representative Raman spectra of multilayer DLC-GNP nanocomposite coatings with different GNP concentration of 0.25, 1.0 and 2.0 mg/mL respectively

Table 6.8 Position and integrated intensity I_D/I_G of the main peaks in Raman spectra of multilayer DLC-GNP with different GNP concentration

Sample	D-peak position (cm^{-1})	G-peak position (cm^{-1})	I_D/I_G
DLC-GNPMLC0.25	1364-1428	1550-1553	0.35-0.54
DLC-GNPMLC1.0	1365-1414	1547-1552	0.43-0.59
DLC-GNPMLC2.0	1382-1413	1547-1551	0.47-0.52

A plot of GNP concentration as a function of variation of I_D/I_G ratio is presented in Figure 6.35. As can be seen, the range of I_D/I_G ratio is shifted to the higher range as the GNP concentration was increased from 0.25 to 2.0 mg/mL. This may indicate an increase of sp^2 bonds in the nanocomposite.
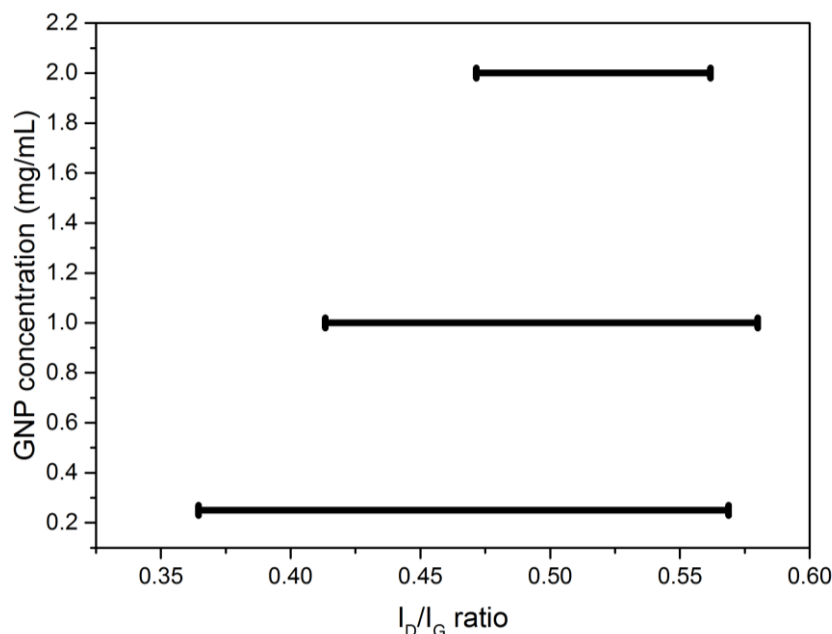
Figure 6.35 The range of I_D/I_G ratio for multilayer DLC-GNP with different GNP concentration of 0.25, 1.0 and 2.0 mg/mL

6.4.4 Tribological properties of multilayer DLC-GNP nanocomposite coating

6.4.4.1 Friction evaluation

Figure 6.36 shows how CoF changed during the three hours test in base oil for coating DLC-GNPMLC0.25, DLC-GNPMLC1.0 and DLC-GNPMLC2.0 respectively. The CoF appears to be more stable than the other coating of DLC-GNP tested previously. For DLC-GNPMLC0.25, the CoF increased drastically to about 0.10 in the first few minutes of the test, before remaining at that level unchanged for the duration of the test. DLC-GNPMLC0.25 exhibit the highest CoF values compared to the other samples. As for sample DLC-GNPMLC1.0, the CoF begins to increase slowly after 80 minutes of the test. The CoF for DLC-GNPMLC1.0 did not reach a steady state condition in three hours test. The CoF trend for sample DLC-GNPMLC2.0 is almost similar to DLC-GNPMLC1.0 in the first 80 minutes of the test before reducing to 0.08.

The average CoF in the last two hours of test is shown in Figure 6.37. As expected, sample DLC-GNPMLC0.25 has the highest average CoF of approximately 0.12. The CoF reduced as GNP concentration increased. Sample DLC-GNPMLC2.0 recorded the lowest CoF at about 0.08.
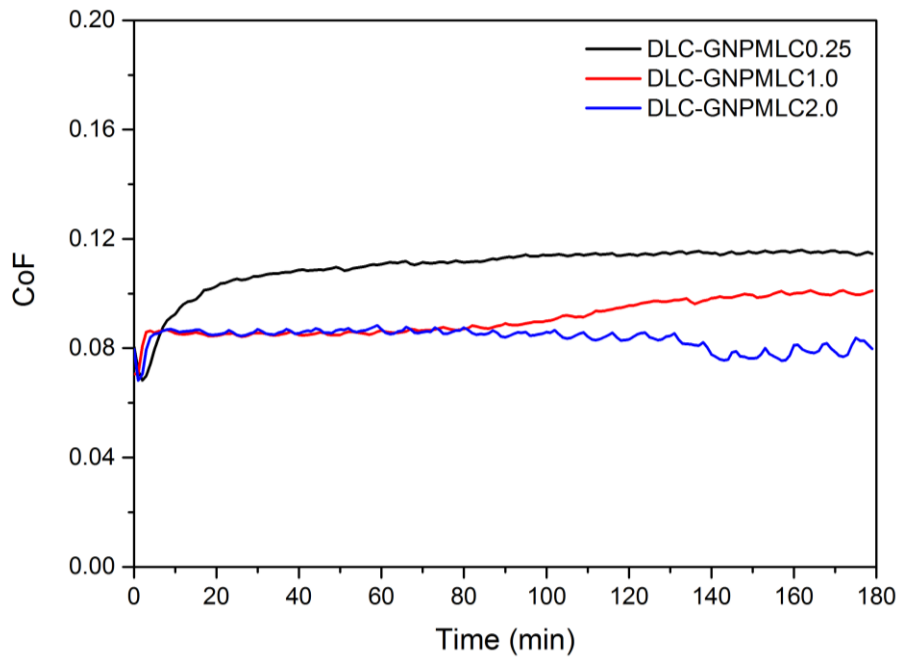
Figure 6.36 Representative CoF by a function of time for sample DLC-GNPMLC0.25, DLC-GNPMLC1.0 and DLC-GNPMLC2.0 tested for three hours in base oil
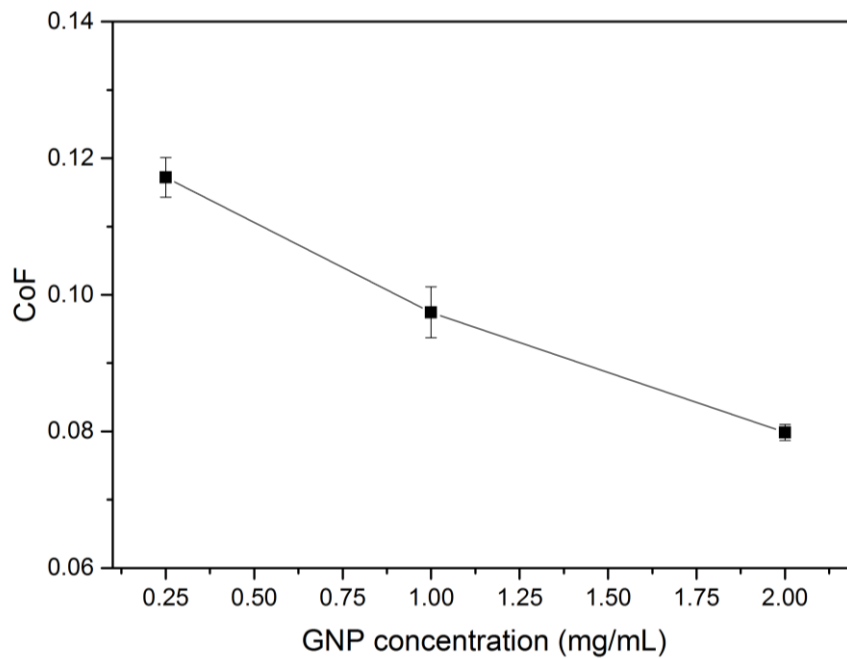
Figure 6.37 Average CoF for multilayer DLC-GNP samples measured in the last two hours of the test by a function of GNP concentration. The error bars in the graph indicate standard deviation for three measurements

6.4.4.2 Observation of wear track of coating and wear scar of the counterpart

Figure 6.38 presents the optical micrographs of the wear track of multilayer DLC-GNP nanocomposite coatings deposited with GNP concentration between 0.25 to 2.0 mg/mL. The width of the wear tracks for sample DLC-GNPMLC0.25, DLC-GNPMLC1.0 and DLC-GNPMLC2.0 are measured to be 1.11, 1.20 and 1.25 mm respectively. The wear tracks of all samples in this section exhibit significantly narrow width of wear track compared to samples in Section 1.3 (DLC-GNPML1.5 and DLC-GNPML2.5). This suggests highly improved wear resistance with post-treatment of 180 minutes. No obvious machining mark can be seen in any of the three samples. Worn areas seem to be smoother than the unworn areas from the colour difference of said areas. This can be observed easily especially in sample DLC-GNPMLC0.25 and DLC-GNPMLC1.0 in Figure 6.38(a) and (b). It is fairly hard to differentiate the worn and unworn area for sample DLC-GNPMLC2.0 (Figure 6.38(c)) due to the existence of more GNPs. The spots marked by the red arrows in sample Figure 6.38(a) and (b) showed wear that will later be investigated using WLI. This wear is similar to the one on wear track of sample DLC-GNPC0.25 in Figure 5.72 but with smaller size.
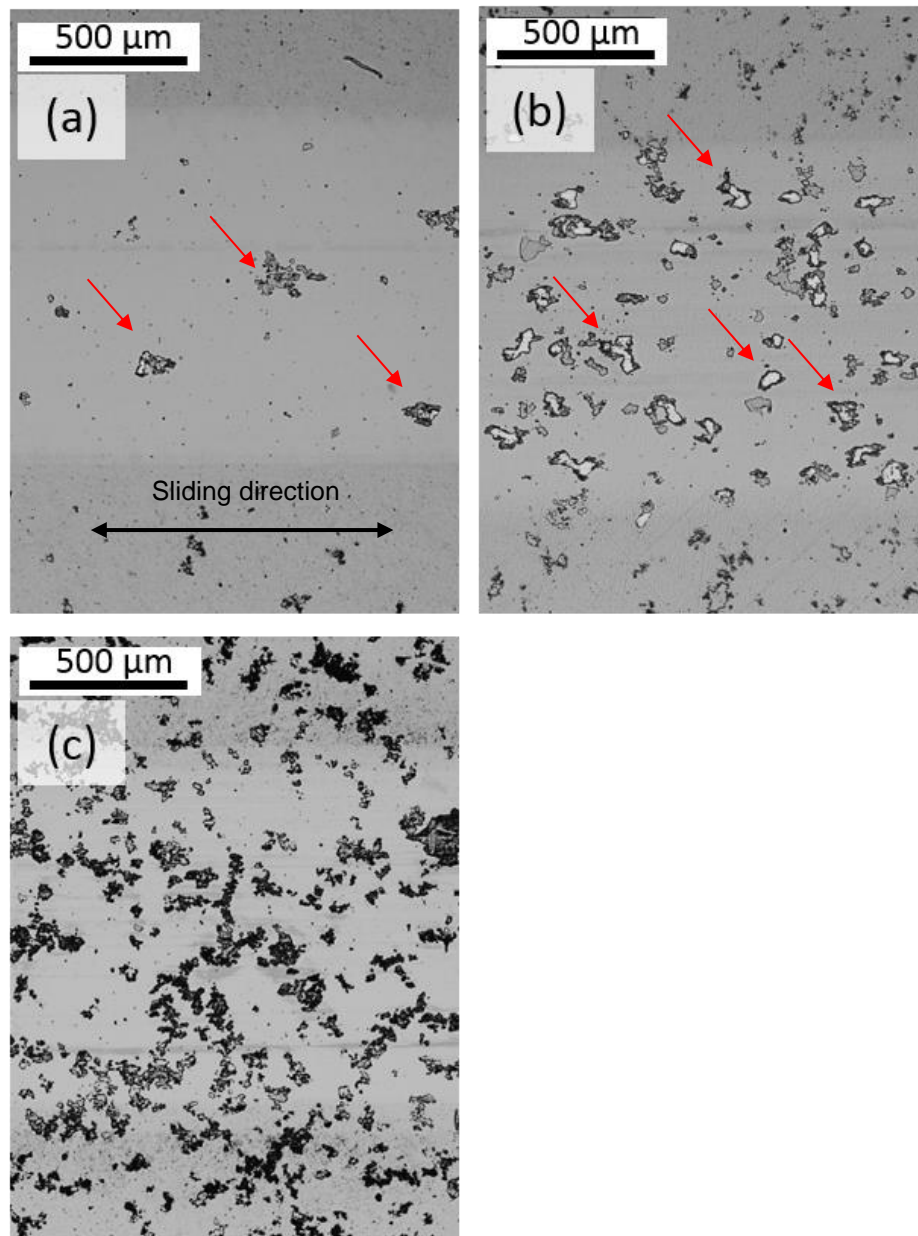
Figure 6.38 Optical micrographs of wear track of (a) DLC-GNPMLC0.25, (b) DLC-GNPMLC1.0 and (c) DLC-GNPMLC2.0 after three hours of test in base oil

The topography of wear scar for sample DLC-GNPMLC0.25, DLC-GNPMLC1.0 and DLC-GNPMLC2.0 are shown in Figure 6.39(a-c) respectively. All wear on the coatings are seen to have a polished effect where asperities on the surface are gradually removed by the sliding process. It can be seen that the spots marked by the red arrow in sample DLC-GNPMLC0.25 and DLC-GNPMLC1.0 (Figure 6.38(a) and (b)), are deep and narrow "spot-wear" that resulted from the act of coating replenishment during the test. Wear track of sample DLC-

GNPMLC1.0 has wider size of spot-wear compared to DLC-GNPMLC0.25 in the range of 0.01 to 0.05 µm. On the other hand, wear track for sample DLC-GNPMLC2.0 in Figure 6.39(c) has more spot-wear than other wear tracks but with slightly smaller spot size, in the range of 0.07-0.09 µm.
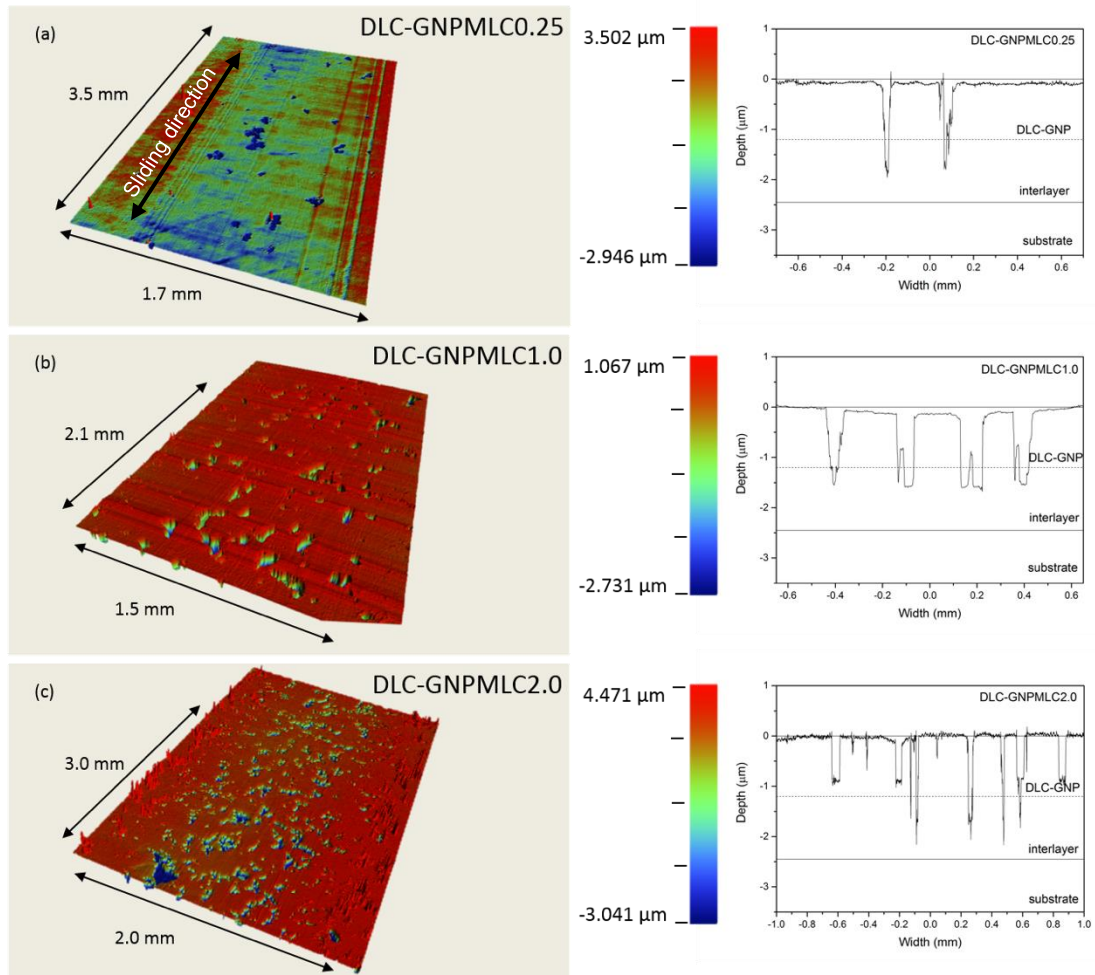
Figure 6.39 Surface topography and corresponding cross-section profiles of wear tracks for (a) DLC-GNPMLC0.25, (b) DLC-GNPMLC1.0 and (c) DLC-GNPMLC2.0

The wear scars on the counterpart of the cast iron pin are presented in Figure 6.40. The wear damages of all counterparts have fine scratches and are comparatively smaller than the wear scars observed previously in this work. All the wear scars have almost similar size. Micro cavity formation and plowing can also be seen in several areas in all of the wear scars.
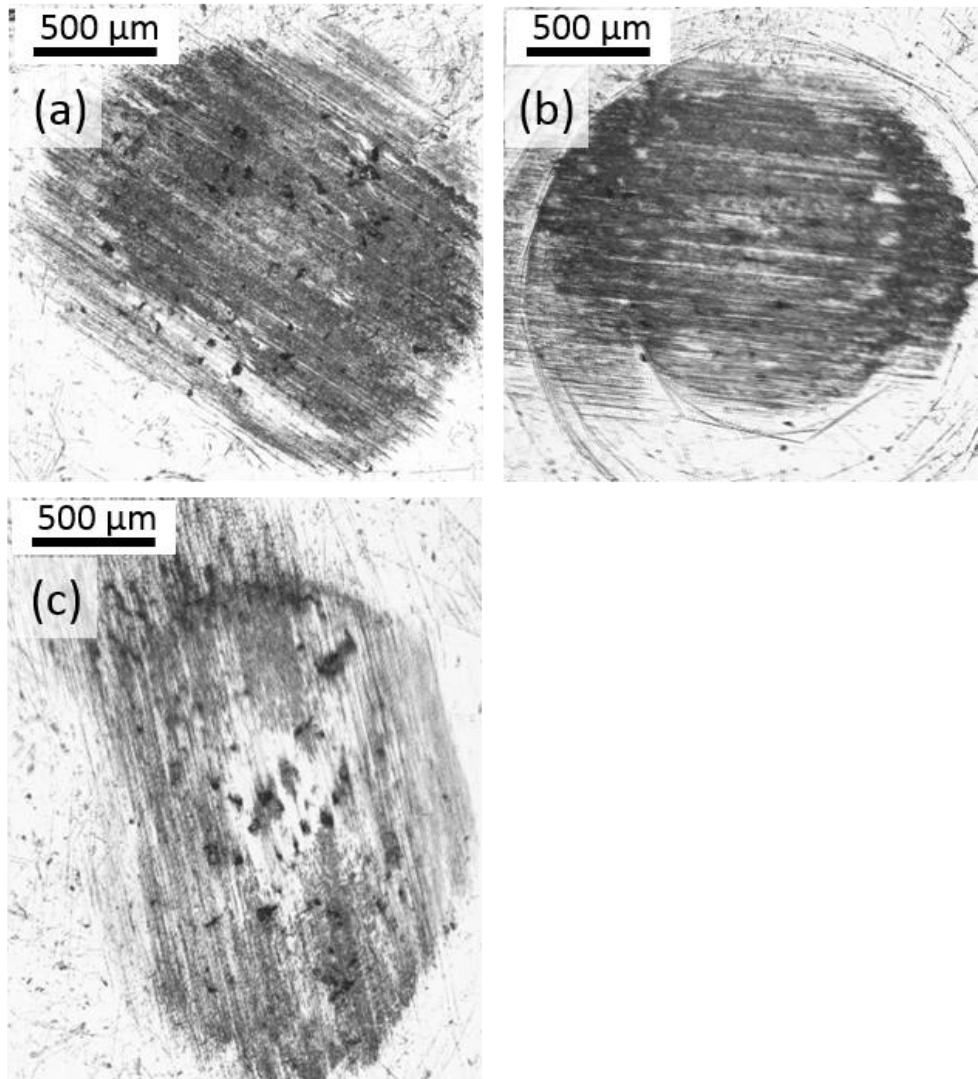
Figure 6.40 Optical micrographs of counterpart wear scar of (a) DLC-
GNPMLC0.25, (b) DLC-GNPMLC1.0 and (c) DLC-GNPMLC2.0
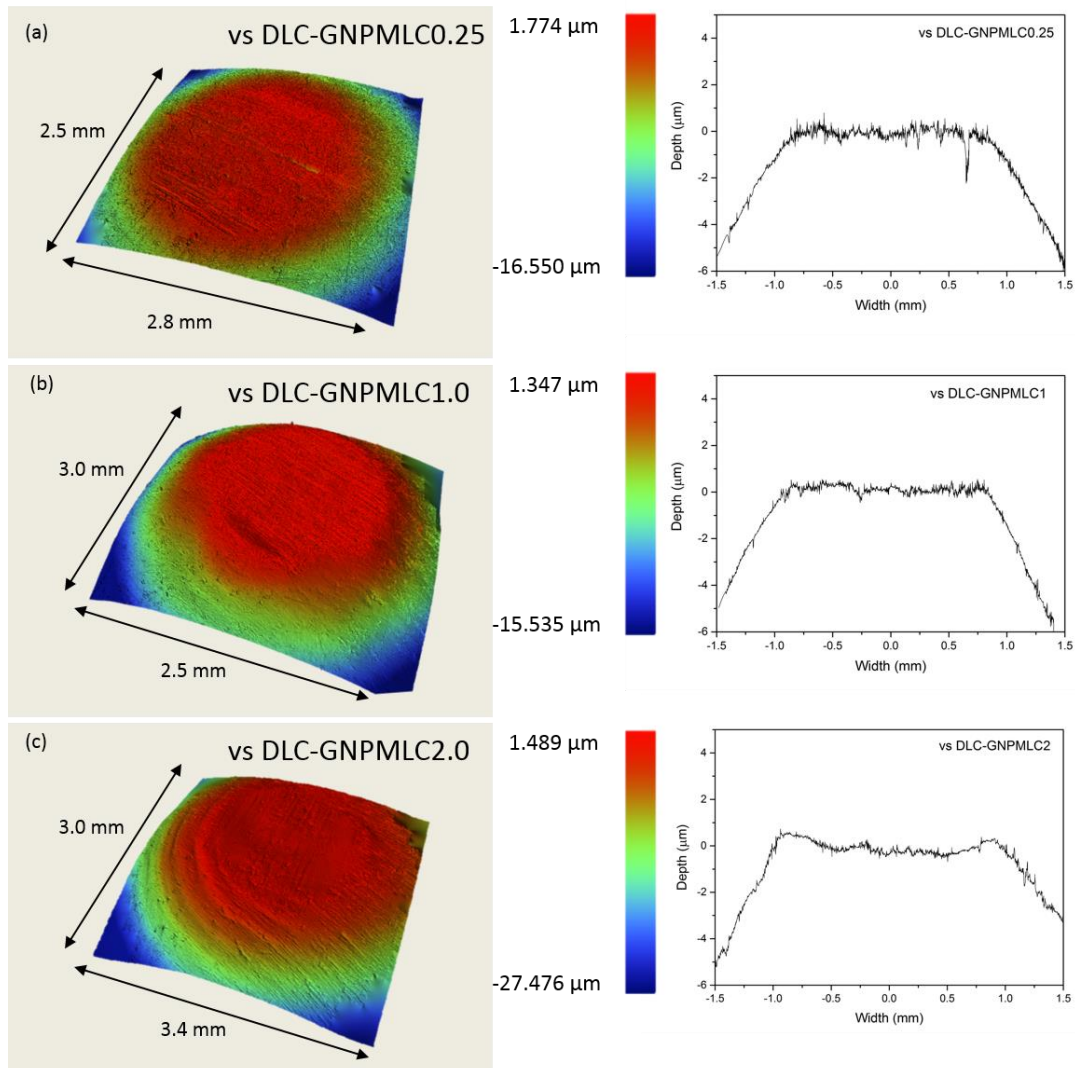
Figure 6.41 Surface topography and the corresponding cross-section profiles of the counterpart wear scar for (a) DLC-GNPMLC0.25, (b) DLC-GNPMLC1.0 and (c) DLC-GNPMLC2.0

6.4.4.3 Analysis of wear track of multilayer DLC-GNP

Wear rate and wear depth, of sample DLC-GNPMLC0.25, DLC-GNPMLC1.0 and DLC-GNPMLC2.0 are presented in Figure 6.42. The wear volume of each coating was determined from wear track analysis with WLI. As can be seen in the figure, sample DLC-GNPMLC0.25 exhibits the lowest wear rate compared to other two samples. There is no difference in wear rate can be seen for sample DLC-GNPMLC1.0 and DLC-GNPMLC2.0. No significant difference can be observed for the wear depth of all samples. Measuring wear volume of all the samples was challenging as the overall wear is fairly small with spot-wear

in a few places. Measurement of the wear volume may underestimate the trivial wear on the surface of the wear track, but more on measuring the wear of the spot-wears that relatively have a more substantial volume of coating replenishment.
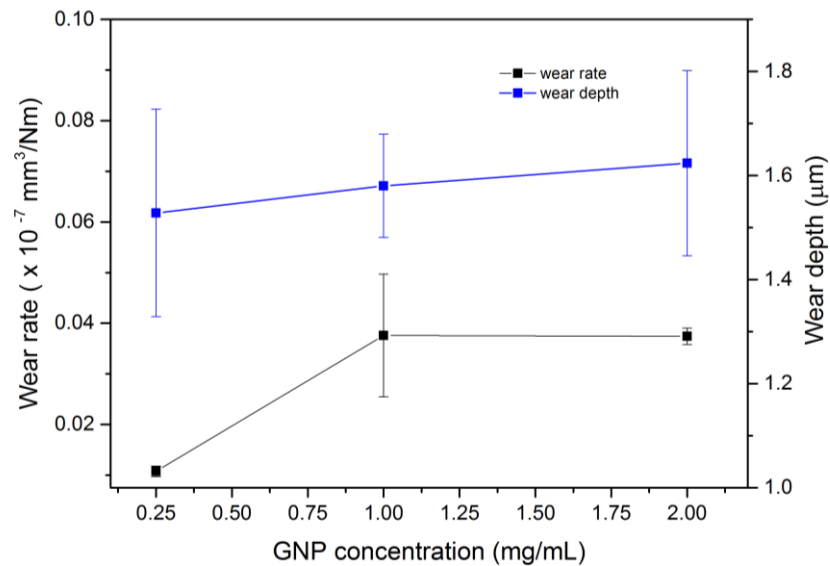
Figure 6.42 Wear rate and depth of wear track of multilayer DLC-GNP nanocomposite coatings at GNP concentration of 0.25, 1.0 and 2.0 mg/mL. The error bars in the graph indicate standard deviation for three measurements

Figure 6.43 displays the correlation between the CoF and wear rate of multilayer DLC-GNP with different GNP concentration. Despite having the highest CoF, the wear track of DLC-GNPMLC0.25 has the lowest wear rate of all. The wear track of sample DLC-GNPMLC2.0 had an almost similar wear rate with DLC-GNPMLC1.0 but achieved the lower CoF.
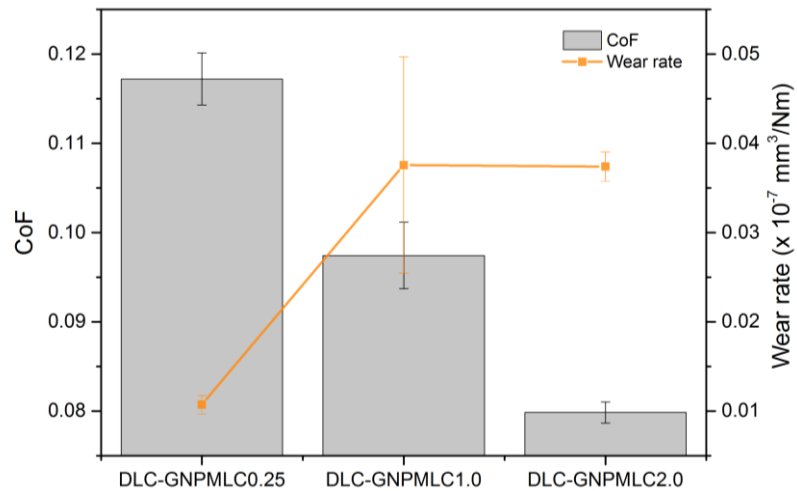
Figure 6.43 CoF and the wear rate of multilayer DLC-GNP nanocomposite coating at different GNP concentration. The error bars in the graph indicate standard deviation for three measurements

6.4.4.4   Analysis of wear scar of the counterpart

The wear rate and the wear scar diameter of the counterpart of sample DLC-GNPMLC0.25, DLC-GNPMLC1.0 and DLC-GNPMLC2.0 are shown in Figure 6.43. As seen in the graph, the wear rate of the counterparts is not in accord with the wear rate of the coatings. While the wear rate of DLC-GNPMLC0.25 was very low compared to the other coatings, the wear rate of its counterpart was almost the same with counterpart DLC-GNPMLC0.5.
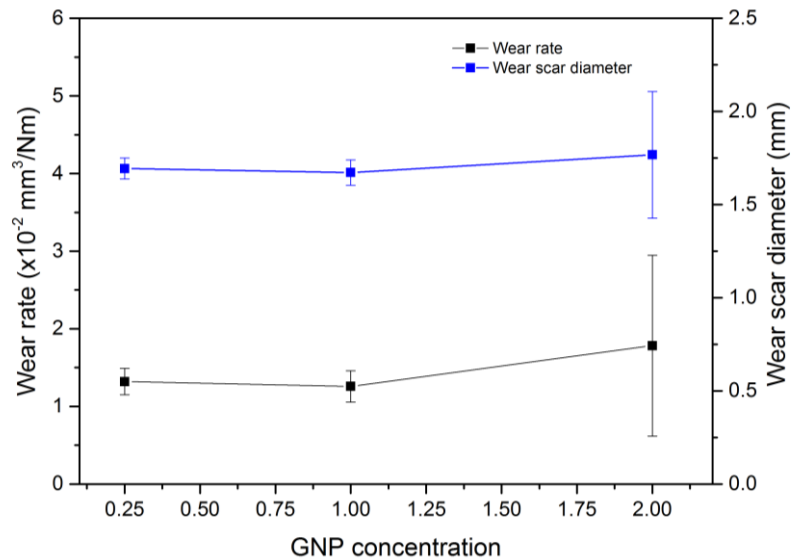
Figure 6.44 Wear rate of cast iron counterpart pins as a function of GNP concentration after sliding against multilayer DLC-GNP with different GNP concentration coating for three hours test in base oil. The error bars in the graph indicate standard deviation for three measurements

6.4.4.5 Raman analysis of wear

Figure 6.45 shows the Raman spectra collected from two different areas within the wear tracks of multilayer DLC-GNP nanocomposite composite with different GNP concentration from 0.25 to 2.0 mg/mL. All spectra were deconvoluted using Gaussian and Lorentz functions. Raman spectra at both areas in wear track of sample DLC-GNPMLC0.25 are similar to that of DLC-GNP nanocomposite coating before test (Figure 6.45(a)). While for wear track of samples DLC-GNPMLC1.0 and DLC-GNPMLC2.0 (Figure 6.45(b) and (c)), one of the wear area show different shape of Raman spectra with D and G-peaks having blue and red shift which possibly belongs to disordered carbon structure.

The details of D- and G-peaks position, as well as the I_D/I_G ratio, is tabulated in Table 6.9. The ratio of the other wear track areas in DLC-GNPMLC1.0 and DLC-GNPMLC2.0 area lower as compared to as-prepared coatings.

255
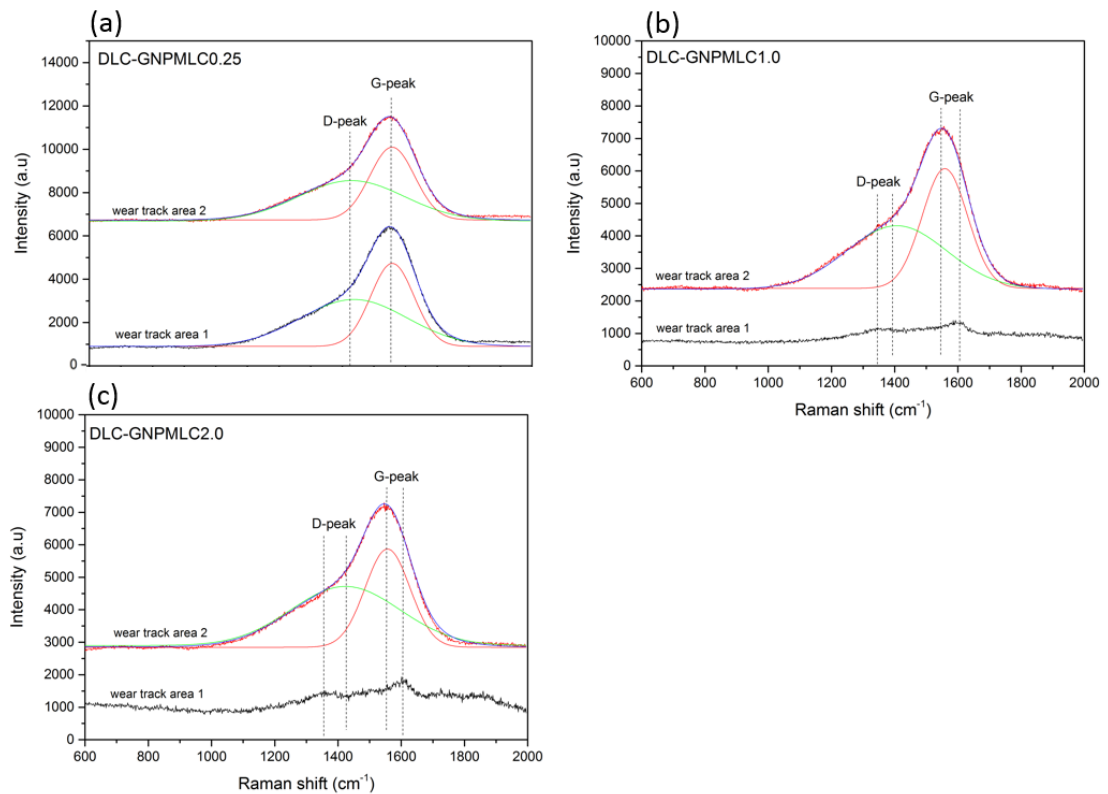
Figure 6.45 Raman spectra collected within the wear track of (a) DLC-GNPMLC0.25, (b) DLC-GNPMLC1.0 and (c) DLC-GNPMLC2.0

Table 6.9 Position and integrated intensity I_D/I_G of the main peaks in Raman spectra within wear tracks of multilayer DLC-GNP nanocomposite coating with different GNP concentration

Sample	Area	D-peak position (cm^{-1})	G-peak position (cm^{-1})	I_D/I_G
DLC-GNPMLC0.25	Wear track area 1	1437	1558	0.57
	Wear track area 2	1429	1558	0.56
DLC-GNPMLC1.0	Wear track area 1	1352	1605	0.40
	Wear track area 2	1407	1559	0.53
DLC-GNPMLC2.0	Wear track area 1	1352	1605	0.40
	Wear track area 2	1424	1557	0.60

Figure 6.46 shows the I_D/I_G ratio on the wear track of multilayer DLC-GNP nanocomposite coating at different GNP concentration. The shaded area represents the range of I_D/I_G ratio before the test. As shown, the I_D/I_G ratio of all

wear tracks lies almost between the same region as the I_D/I_G ratio of all the coatings before the test.
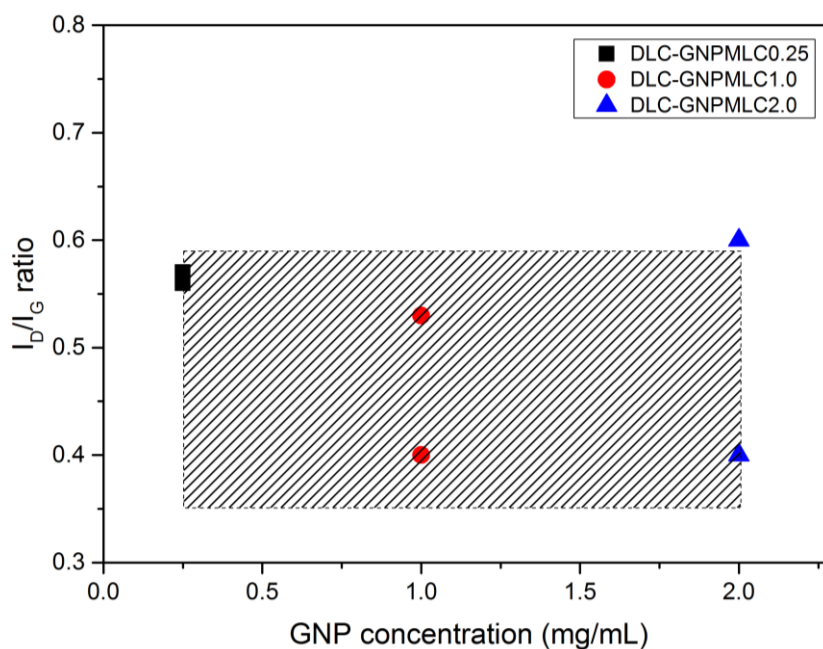
Figure 6.46 I_D/I_G ratio of wear track as a function of DLC deposition time for multilayer DLC-GNP with GNP concentration of 0.25, 1.0 and 2.0 mg/mL

The Raman spectra on the wear scar of the counterparts for samples DLCGNPMLC0.25, DLC-GNPMLC1.0 and DLC-GNPMLC2.0 are presented in Figure 6.47. Almost similar to other spectra of wear scar in the other section, all of the spectra, showed two dominant peaks of D and G-peaks with a weak peak of Fe-oxide that appears in some spectra. The appearance of some of the spectra similar to the spectra of as-prepared DLC-GNP coating, while some resemble highly disordered graphite. The outcomes show the formation of transfer layer of the coating. The position and measured I_D/I_G ratio are summarised in Table 6.10.
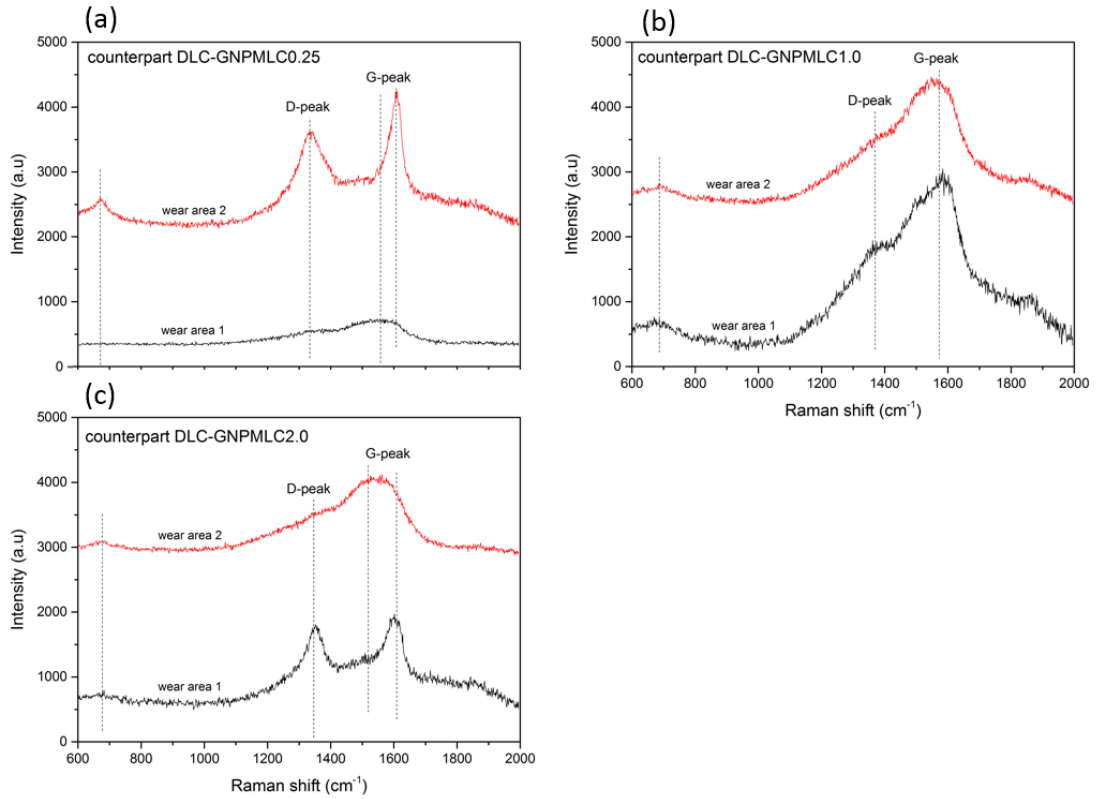
Figure 6.47 Raman spectra collected within the wear scar of counterpart (a) DLC-GNPMLC0.25, (b) DLC-GNPMLC1.0 and (c) DLC-GNPMLC2.0

Table 6.10 Position and integrated intensity I_D/I_G of the main peaks in Raman spectra of wear scars of multilayer DLC-GNP nanocomposite coating at different GNP concentration

Sample	Area	D-peak position (cm^{-1})	G-peak position (cm^{-1})	Fe-oxide position (cm^{-1})	I_D/I_G
DLC-GNPMLC0.25	Wear area 1	1426	1565	-	0.95
	Wear area 2	1344	1603	663	0.80
DLC-GNPMLC1.0	Wear area 1	1346	1557	627	0.30
	Wear area 2	1353	1552	652	0.28
DLC-GNPMLC2.0	Wear area 1	1350	1592	-	0.92
	Wear area 2	1377	1548	682	0.46

6.4.5 Summary of effect of GNP concentration on multilayer DLC-GNP nanocomposite coating

i.   The adhesion strength of the coating increased as the GNP concentration was increased. The ranking of adhesion strength is as follows; (highest) DLC-GNPMLC2.0 > DLC-GNPC1.0 ≈ DLC-GNPMLC0.25. The highest adhesion strength was achieved for sample DLC-GNPML2.0 (GNP vol% = 0.44%)

ii. The surface roughness of multilayer DLC-GNP samples was much higher compared to single-layer DLC-GNP with the same GNP concentration.

iii. Post-treatment of 180 minutes significantly improved the adhesion strength of multilayer DLC-GNP nanocomposite coating.

iv. CoF improves as the GNP concentration increased but slightly reduced the wear resistance of the coating.

Chapter 7
Discussion

7.1   Overview

This thesis aims was to develop DLC-GNP nanocomposite coatings with low friction and good wear resistance. The development involved optimisation of spin-coated GNP, preparation of single-layer DLC-GNP and finally deposition of double-layer DLC-GNP nanocomposite coating. In general, as can be seen in Figure 7.1, the as-prepared DLC-GNP nanocomposite coatings of single and double-layer have a wide range of tribological behaviour. Their properties significantly depend upon their method of preparation, GNP concentration, coating thickness and the number of coating layers. Using the tribological performance of pure DLC (produced in this work) as a reference, the tribological behaviour of the nanocomposite coatings can be divided into coatings having high wear/low CoF, high wear/high CoF, low wear/low CoF and low wear/high CoF. Most of the single-layer DLC-GNP coatings lies in the high wear/low CoF group. Only multilayer DLC-GNP coatings are in the low wear/low CoF group. Half of the single-layer DLC-GNP coatings lies in the high wear/low CoF, and the other half were in the high wear/high CoF. The most promising group of low wear/low CoF, on the other hand, is occupied only by the multilayer DLC-GNP coatings. The next sections of this chapter discuss the experimental findings on the physical structure, chemical bonding, and how the properties relate to mechanical and tribological performance. The proposed tribological mechanism of the nanocomposite coating is also discussed.
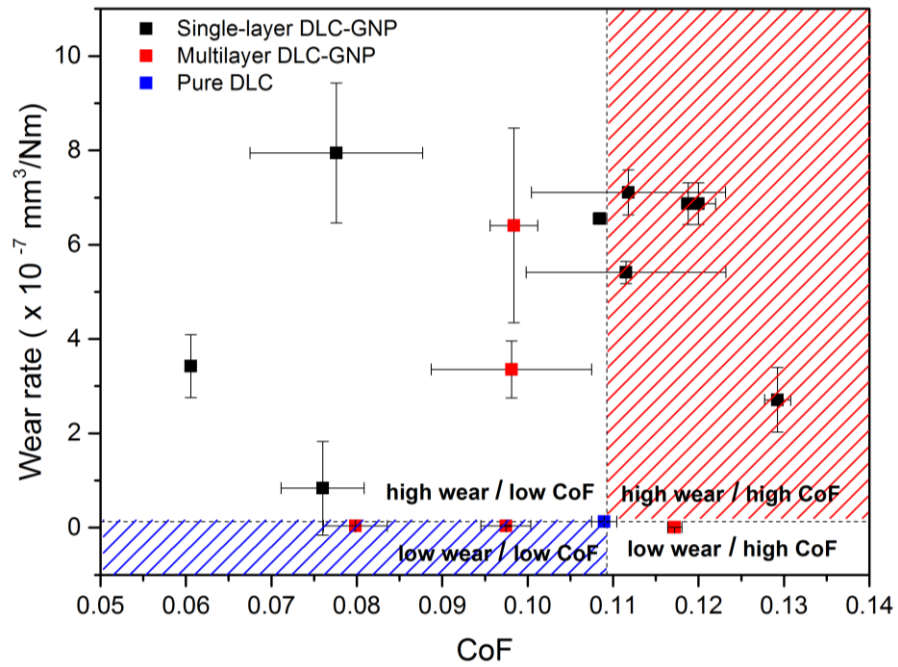
Figure 7.1 The wear rate and CoF of single and multilayer DLC-GNP nanocomposite coating

7.2 Structure and Mechanical Properties of DLC-GNP Nanocomposite Coating

7.2.1 Fabrication and structure of DLC-GNP nanocomposite coating

Figure 7.2 is a schematic representation of how the single and double-layer DLC-GNP nanocomposite coatings were designed and fabricated. All the nanocomposite coatings are composed of a Cr/WC-W:C:H interlayer, spin-coated GNP and DLC film.
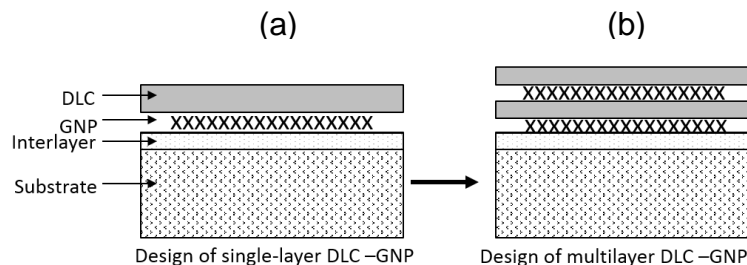
Figure 7.2 Coating model of (a) single layer DLC-GNP and (b) multilayer DLC-GNP nanocomposite coating

The fact that GNP can still be observed after DLC deposition unveils that the DLC film deposited using PECVD in this work is almost transparent and dark in colour. The cross-section view also suggests that DLC film was deposited on GNP and the bonding between DLC and GNP is not just a simple physical bonding. In work published by Tsai and Jeng [190] on DLC and Carbon Nanotube (CNT) composite coating, it was reported that DLC was fully deposited on each tip of vertically aligned CNT, and there is a 3.6 Å intermediate graphitic shell developed between DLC and the CNT. Ren et al. [191] have also discussed the formation of DLC on CNT which is due to "subplantation" effect. Zanin et al. [127] suggested that DLC film has chemically and physically covered CNT tips. It is believed that due to hexagonal lattice structure in DLC and GNP, the formation of chemical bonding between DLC and GNP is possible.

It is therefore suggested that the bonding characteristic that forms single and multilayer DLC-GNP nanocomposite coatings is as shown in Figure 7.3. Due to the GNP dispersion on surface and DLC deposition on the interlayer, the bonding that exists in multilayer DLC-GNP can be divided as follows:

i. interlayer-1st layer of GNP,

ii. interlayer-1st layer DLC,

iii. 1st layer of GNP-1st layer DLC,

iv. 1st layer DLC-2nd layer DLC and

v. 1st layer DLC-2nd layer GNP.

The bonding between spin-coated GNP and the interlayer (Figure 7.3(a)) and DLC-spin coated GNP (Figure 7.3(c)), are merely on Van der Waals bonding. The post-treatment improved the adhesion of spin-coated GNP on the interlayer and DLC film but did not create any chemical bonding between the layers.

In the multilayer DLC-GNP, the DLC film is deposited on the interlayer (Figure 7.3(e)), GNP and on DLC film itself. It is supposed that there is a bonding layer formed when DLC film was deposited using PECVD method. The carbon atoms

were transported to the surface and penetrate into the surface to form the bonding layer, and grow to a certain thickness. DLC is amorphous and has no grain boundary, it nucleates a new phase and grows further above each phase [192]. The bonding between deposited DLC film on GNP is believed to be C-C bonding. As for deposition of DLC on DLC film in Figure 7.3(d), the deposition of DLC is most likely to be the same process of DLC growth. This may explain the reason why the barrier between the two DLC layers was hardly seen. The topmost layer of the interlayer is composed of W:C:H. It is therefore, suggested that the bonding between the interlayer and DLC film is comprised mainly of C-C bonding. All of these C-C bondings in the DLC-GNP nanocomposite coating accommodate strong bonding between each layer.

The thickness of the coating increased with DLC deposition time for both pure DLC and DLC-GNP nanocomposite coating. The deposition rate was calculated to be approximately 7.3 nm/min for DLC-GNP nanocomposite coating, just slightly lower than the pure DLC. Uysul et al. [193] described that higher surface roughness of deposited GNP had changed the nucleation and growth mechanism of Ag matrix in the preparation of Ag-GNP composite coating. The larger surface area that has been created by the spin-coated GNP has increased the surface area of the whole surface. Therefore there was a larger area to be deposited for DLC film compared to a surface without spin-coated GNP. For this reason, the deposition rate on spin-coated GNP is calculated to be marginally lower than pure DLC.

The cross-section of multilayer DLC-GNP in Section 6.3 also reveals the existence of GNP in between DLC film and is mainly in the form of corrugated GNP. Due to the condition of GNP, the surface roughness has increased tremendously. The arrangement and orientation of GNP that has been seen from the cross-section are believed to be due to the spontaneous curl of GNP to form a convex shape. This spontaneous curling of GNP has been observed by numerous works involving graphene sheets [194, 195]. It is common for a tough material like graphene to wrinkle and curl as an outcome of high intrinsic stress [196-198]. Yamaletdinov and Pershin [198] named the curled graphene in such shape as graphene nanoribbon.
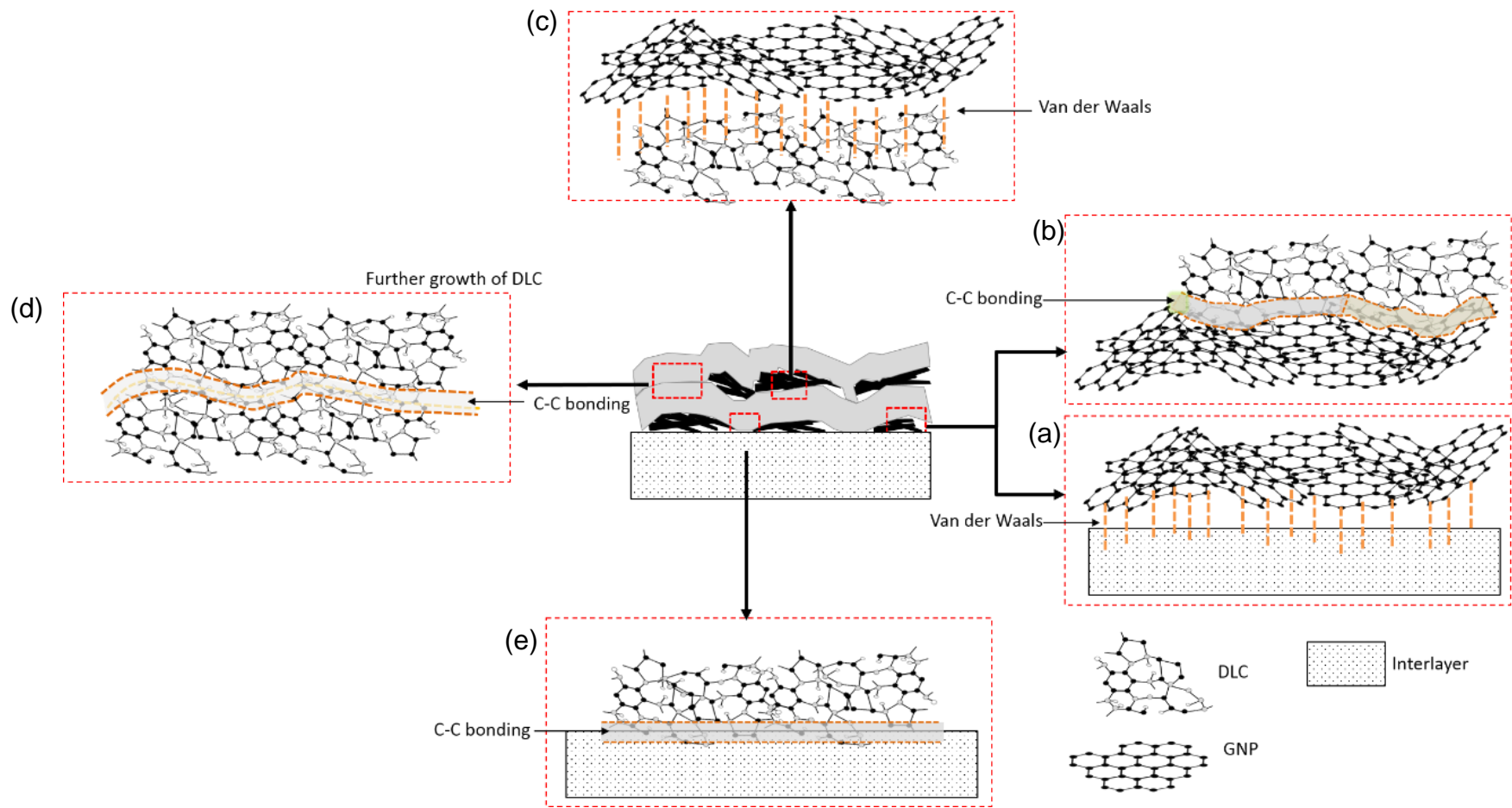
Figure 7.3 Schematic diagram showing the bonding formation between interlayer and GNP; and GNP and DLC for single-layer DLC-GNP nanocomposite coating

Figure 7.4 depicts the condition of GNP after spin-coating, onto the formation of curled GNP and finally DLC deposition in PECVD. Spin-coated GNP is believed to be in a crumpled condition. As explained earlier in Chapter 4 and 5, optical microscopy and surface roughness results showed that the darker areas of the GNP islands are higher than the bright GNP islands thus belong to crumpled GNP. During the process of post-treatment, the crumpled spin-coated GNP were pressed using the Kapton tape heated at 200°C temperature for a specific duration. This process creates and ironing-effect thus produced flat wrinkled and overlapping GNP on the interlayer. It is supposed that during the heating process in the PECVD chamber that the graphene curled [199]. As there is a high possibility of some solvent and moisture being left in the GNP, evaporation may occur during heating in the PECVD chamber before DLC film deposition.

It is proposed that this phenomenon occurred in both single and multilayer DLC-GNP regardless of the thickness or DLC deposition time which in turn increased the final thickness of the coating. The effect is more noticeable for multilayer DLC-GNP as it occurred twice for both deposition processes.
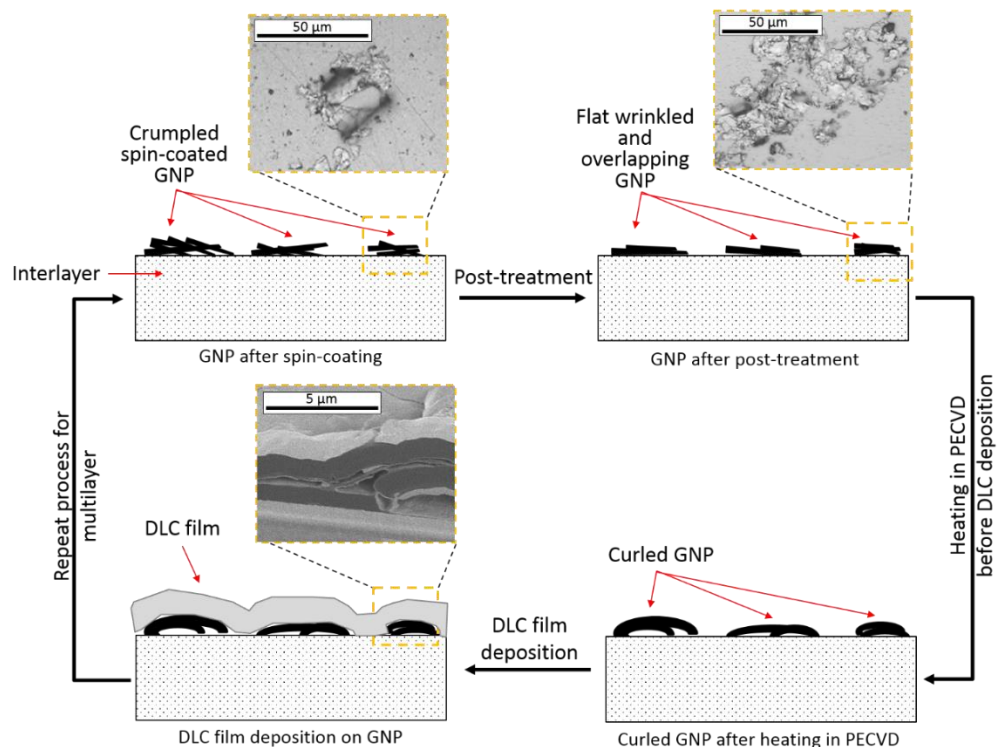
Figure 7.4 Schematic representation of the process flow of spin-coated GNP and DLC deposition of DLC on GNP and the corresponding optical and SEM micrographs

7.2.2 Scratch failure and adhesion strength of DLC-GNP nanocomposite coating

Figure 7.5 summarises the critical load value as a function of coating thickness for single and multilayer DLC-GNP nanocomposite coating. In general, the adhesion strength of the coating increases with coating thickness up to ~ 1.7 μm (single-layer DLC-GNP) but decreases when the thickness is more (multilayer DLC-GNP). This is in accord with many findings that reported similar results where a higher load is needed to break through the thicker coating thus improving the adhesion, but as thickness increases, the adhesion strength can also be seen to reduce due to the weakening of the structure from internal stresses [200, 201]. Nevertheless, the coating thickness is not the only or dominant factor that influences the adhesion strength. In this work, the post-treatment, GNP concentration and coating structure are also the factors that determined adhesion strength of the coatings.
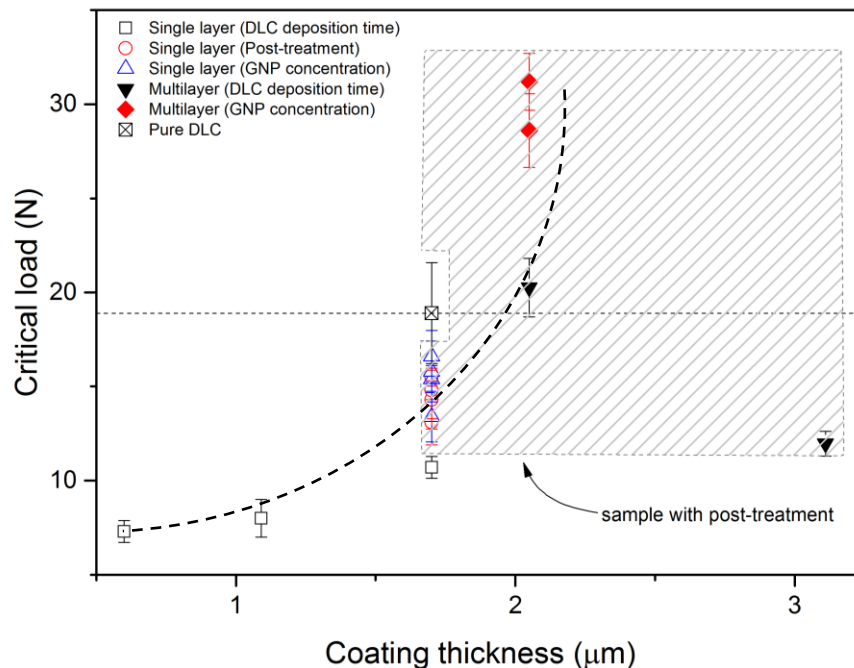
Figure 7.5 Relationship between critical load with coating thickness of single-layer and multilayer DLC-GNP nanocomposite coating

When coating thickness is the dominant factor, thicker coating established higher critical load compared to thinner coating. However, it is still low as compared to the same thickness of pure DLC coating. It can also be said that

incorporating GNP in the matrix causes deterioration to the whole coating structure. Incorporation of a new element for a composite coating may also weaken the adhesion strength if it failed to chemically or physically bond, especially when the added element is in agglomerated condition [32, 202].

Multilayer DLC-GNP has shown higher adhesion strength than single layer DLC-GNP. The critical load value has improved more than 300% than the lowest critical load recorded with single-layer DLC-GNP with a thickness of 0.60 μm without post-treatment process. Many works have reported an increase of adhesion strength of multilayer DLC compared to single layer [66]. Cui et al. [203] found that deposition of DLC film with a multilayer structure reduced tensile and compressive stresses between the film and substrate which improved the adhesion strength of the coating. Cho et al. [205] also reported an increase of critical load for double-layer DLC by almost 50% compared to a single-layer.

Weiss [204] suggests that adhesion mechanism can be divided into mechanical interlocking, physical and chemical bonding. Figure 7.6 shows various mechanisms in mechanical interlocking, physical and chemical bonding. As has been discussed earlier in Section 7.2.2, due to high surface energy of GNP, it is believed that the adhesion between GNP and the surface was a physical bonding of Van der Waals forces. Van der Waals bonding is not capable of creating strong adhesion between GNP and the surface. The spin-coated GNP was easily washed away from the surface with simple sonication. This is the reason why the DLC-GNP nanocomposite coatings that have been prepared with only spin-coated GNP without post-treatment have weak adhesion strength.

However, after post-treatment, the interfacial strength between the GNP and substrate become stronger. The critical load value increases when the post-treatment is applied to the coating system. The formation of bonding that creates the adhesion strength of the whole composite system has been explained earlier in Section 1.2.1. Few works also reported an improvement of adhesion strength with heat [137].
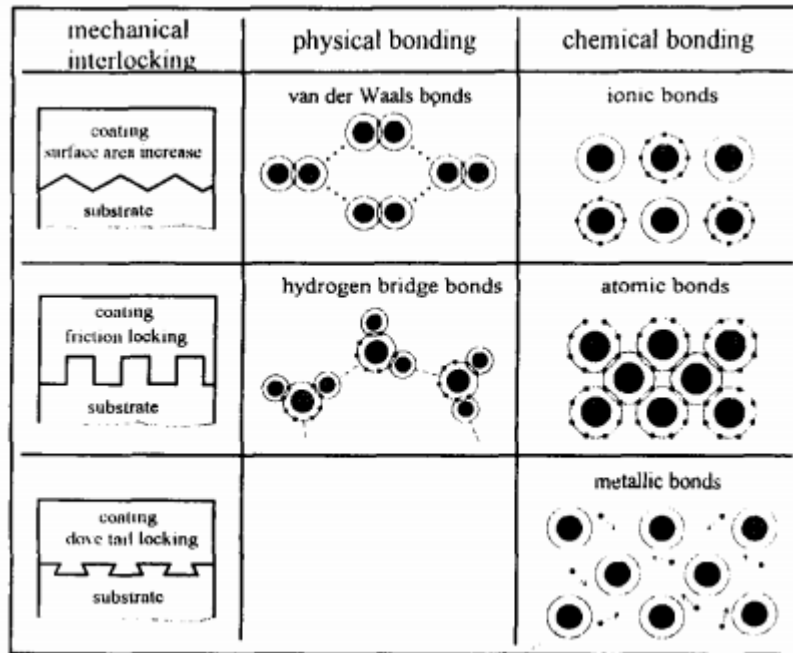
Figure 7.6 Schematic of physical and chemical bonding mechanism [204]

Figure 7.7 was plotted to establish whether the GNP amount influences the adhesion strength of the coating. All coatings shown in Figure 7.7 have been through the same post-treatment process of 180 minutes. Interestingly, both single and multilayer DLC-GNP nanocomposite coatings have almost similar trend of adhesion strength increment when the GNP is above ~ 0.025 vol%. For the single-layer DLC-GNP coating having GNP lower than 0.025 vol% there is only a slight difference in adhesion as compared to a pure DLC. This is due to a very low content of GNP in the nanocomposite coating. It is also an indication that GNP does contribute to the improvement of adhesion strength for both single and multilayer DLC-GNP nanocomposite coatings.
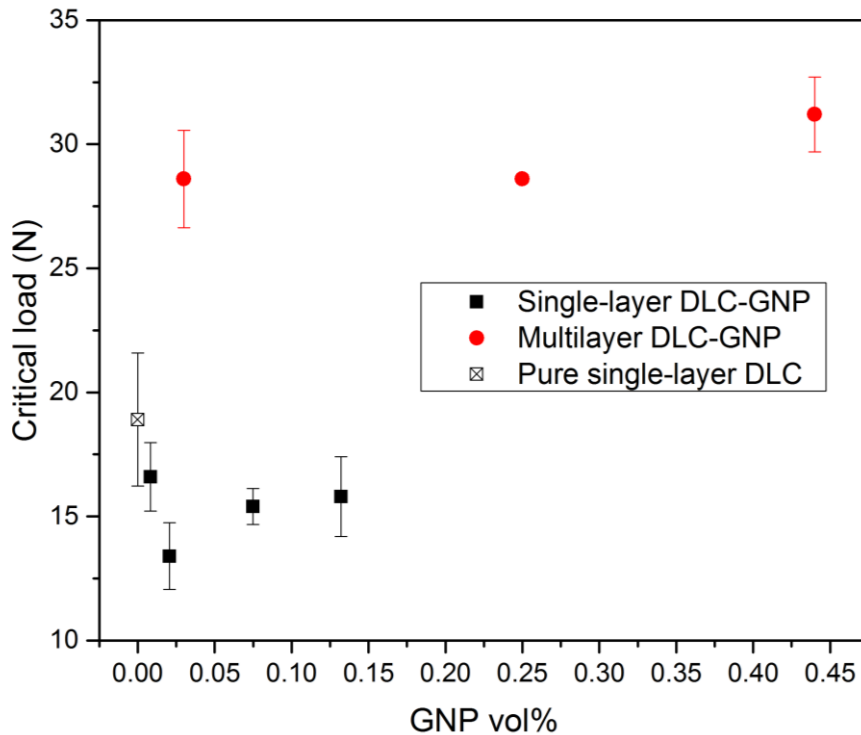
Figure 7.7 Critical load of single and multilayer DLC-GNP nanocomposite coatings as a function of GNP vol%

The scratch depth has also been used to predict the toughness of coatings. Figure 7.8 shows the scratch depth at L_{C1} and the deepest depth of the scratch for single and multilayer DLC-GNP nanocomposite coating. The scratch depth for pure DLC marked in black is used as a reference. The green shaded area represents the single-layer, while the red shaded area is the multilayer DLC-GNP nanocomposite coating. It is also divided into three different thickness of 1.70, 2.05 and 3.11 µm. Most of the adhesion failure (L_{C1}) occurred at the point when the penetration reached the interface between the adhesion layer and substrate as shown in Figure 7.9. It is also worth noting that the maximum penetration depth reduced as the adhesion strength improved. The result might be associated with the hardness and toughness of the coating where coatings with higher hardness and toughness will have lesser penetration depth. A coating which is tougher and harder have better adhesion strength. Sample multilayer DLC-GNP deposited with 2.5 hours of DLC that has the lowest critical load of all, have the deepest maximum depth. Meanwhile, multilayer DLC-GNP deposited with 1.5-hour deposition of DLC and post-treated for three hours has less penetration. The results show an

improvement of coating's toughness for coating having post-treatment 180 minutes and a multilayer structure.
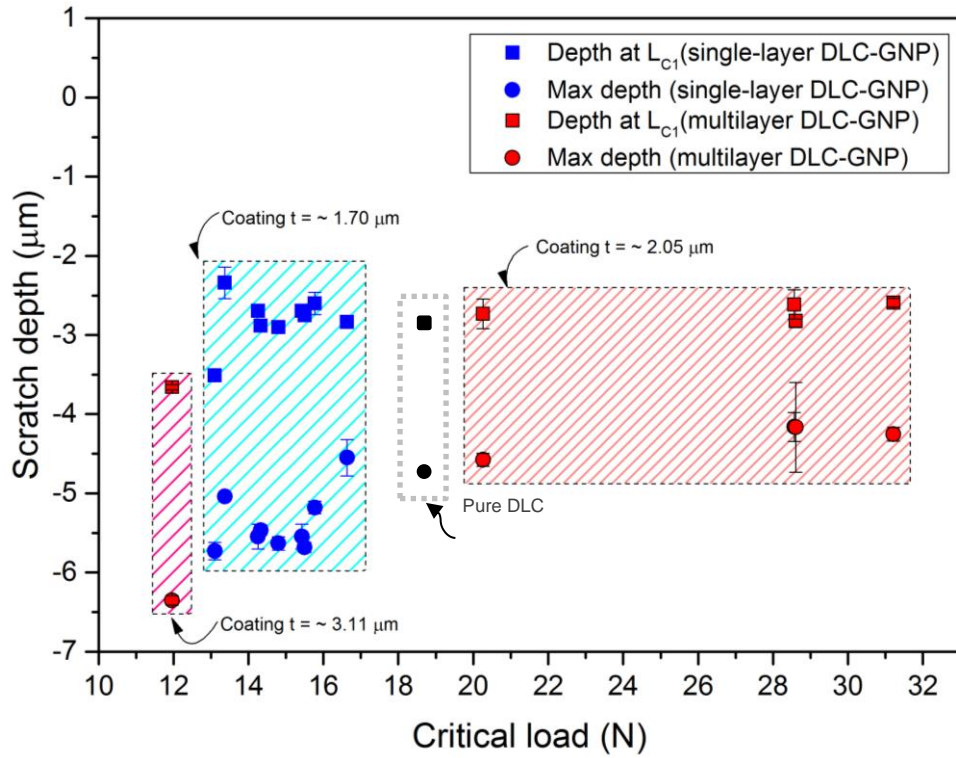
Figure 7.8 Relationship between scratch depth and critical load for single-layer and multilayer DLC-GNP nanocomposite coating
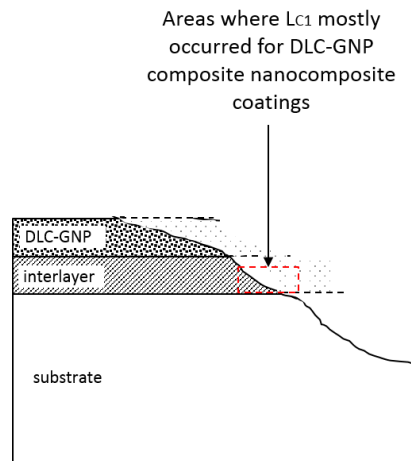
Figure 7.9 Schematic of scratch depth showing adhesion failure L_{C1} occurrence

7.3 Chemical Structural of Spin-coated GNP and DLC-GNP Nanocomposite Coating

7.3.1 Raman spectra of spin-coated GNP

Raman spectra of spin-coated GNP are also analysed to investigate the effect of each experimental parameter on GNP bonding structure; this may also change the chemical structure of DLC-GNP nanocomposite coating. In this work, I_G/I_{2D} ratio was used to characterise spin-coated GNP. The I_G/I_{2D} or I_{2D}/I_G ratios are widely used to determine the structure or number of layers of graphene [206-210]. Analyzing Raman spectra of GNP is more challenging than graphene film as there might be numerous of different types of GNP existing in the GNP suspension.

Single layer graphene will typically exhibit I_G/I_{2D} ratio of approximately ~0.2 [159[166], whereas I_G/I_{2D} ratio of all samples in this work was calculated to be ~2-3. Regardless of the dispersion method, post-treatment and the concentration, the values of I_G/I_{2D} and shape of spectra for all tested GNP verified that it is multilayer type of GNP. A very broad 2D-peak also confirms that all the GNP in the suspensions are multilayer graphene which is consistent with the shape of the 2D peak reported previously [34, 211, 212]. The shape of the Raman spectra obtained in this work are similar to five layer spectra recorded by Calizo [166]. The low and occasionally invisible D-peak obtained from all samples suggest a lower level of GNP defects [167]. The existence of D-peak is commonly ascribed to the quality of graphene layer [213]. Both D- and 2D-peaks are sp^2 domains which are attributed to disorder and imperfection of the carbon crystallites [214].

A huge range of I_G/I_{2D} ratios were measured for all GNP samples. One possible reason is because the orientation and the condition of GNP. The condition whether the GNP is lying flat on a surface or in folded condition can influence the measured values of I_G/I_{2D} ratios [215]. Due to this reason, using one value or a mean value of I_G/I_{2D} as a characteristic value might not represent the real chemical structure of the whole GNP of one sample. Therefore it would be more appropriate that GNP or any other graphene dispersion be presented in a

range value if comparison needs to be carried out between a different sample of GNP.

One interesting finding from Raman spectra of GNP is the difference of intensity between darker and brighter area on the sample. Although the range of I_G/I_{2D} Raman spectra showed that no distinct trend when post-treatment was applied on the GNP, the intensity of main peaks seem to be dramatically increased even when 30 minutes post-treatment was applied to GNP as compared to GNP without post-treatment. The results obtained from post-treated GNP can be explained by the results obtained in Section 4.4 on GNP dispersion. Results in Section 4.4 showed that dark areas of spin-coated GNP belong to crumpled and not well-oriented overlapping of GNP with higher surface roughness. Bright areas that have high peak intensity are more oriented GNP that is closely overlapping with each other with low surface roughness. For this reason, it can also be suggested that higher intensity of peaks for post-treated samples is due to the well-oriented arrangement of GNP that are close to each other after the post-treatment process.

While the increase of G-peak in graphene usually relates to the increase in number of layers, there also evidence that it can also be associated with the orientation of the GNP itself. Higher intensity of G and 2D-peaks indicates more C-C bonding has been detected. Li et al. [231] also have discussed how the orientation and good dispersion of graphene oxide in polymer-based composite give strong G-peak in the Raman spectra.

7.3.2 The sp^2 and sp^3 content in DLC and DLC-GNP nanocomposite coating

In this work, the microstructure of the DLC-GNP nanocomposite coating was investigated using Raman spectra and XPS analyses. Raman analysis will be focusing on the value of I_D/I_G ratio measured on each coating. Analysis of the XPS data, on the other hand, will be discussed directly in relation to the measured sp^2 and sp^3 content obtained from the C1s peak.

All Raman spectra of DLC-GNP samples in this work showed main D- and G-peaks. It is well-known that the I_D/I_G ratio can relate to the amount of sp^3 in the

coating. I_D/I_G value has been reported to correlate closely with four-fold coordinated structures (sp^3) content [186]. A change of I_D/I_G ratio correlates closely with the variation of the sp^2/sp^3 ratio [190]. Since it is indirectly related to sp^2/sp^3 value, the value of I_D/I_G ratio can also provide information about the quality and hardness of the coating [216]. Due to a close relationship between I_D/I_G ratio to the sp^2/sp^3 value, focus on discussion will be on the I_D/I_G value to study the chemical structure and estimate the mechanical properties of DLC-GNP nanocomposite coating.

The two main results from Raman spectra analysis of the DLC-GNP nanocomposite coatings are: 1) The shape of the spectrum and the position of D- and G-peaks are similar to pure DLC, and 2) The I_D/I_G ratios of DLC-GNP nanocomposite coatings vary in wide range. These results shall be discussed in this section.

Addition of GNP in the DLC matrix does not shift position of both D- and G-peak when compared to pure DLC film. The 2D-peak of GNP also did not appear in any spectra of DLC-GNP both single and multilayer. Comparing the results with the other reported DLC-based composites, there are two different outcomes from the previous works. Some the composites have a shift of peak, and change of spectrum's shape, while others found almost unchanged shape or shift of peak when new element is added to DLC matrix [217, 218].

One of the possible reason is that the position of D- and G-peaks of DLC being overlapping with D and G-peaks of GNP. The second possible reason is the penetration depth of Raman laser might be low that it did not reach the GNP underneath DLC film. Nevertheless, the second reason seems to be in doubt. The measurement of I_D/I_G ratio showed that there is an immense difference between the value of pure DLC and DLC-GNP nanocomposite coating which is also the second main result of the Raman spectra analysis of DLC-GNP nanocomposite coating.

Analysis of I_D/I_G ratio of pure DLC and DLC-GNP nanocomposite coating revealed that DLC-GNP nanocomposite coating has a wide range of I_D/I_G ratio value compared to pure DLC. If the Raman laser only penetrates a few nanometers into the coating, it might only be showing the spectra from DLC

273

which should be the same as the pure DLC. Raman spectra analysed in this work were taken from areas with and without GNP. It is quite clear that the reason for wide range of I_D/I_G ratio for DLC-GNP samples was due to the arrangement and orientation of the GNP in the coating. Chen et al. [219] also reported an irregular dependence of I_D/I_G with the incorporation of silver in a-C:H matrix.

The average value of I_D/I_G ratio for single and multilayer DLC-GNP nanocomposite coating is shown in Figure 7.10. The black colour columns represent the I_D/I_G ratio of the single-layer DLC-GNP, while red columns serve the multilayer DLC-GNP. The horizontal line in the graph indicates the recorded I_D/I_G ratio of pure DLC with 1.7 µm thickness. It can be seen from Figure 7.6, that I_D/I_G ratio has an irregular dependence on the structure of DLC-GNP. This again might be attributed to the distribution of GNP in the composite especially when the amount of GNP is large. It can be confirmed by the small standard deviation of only sample DLC-GNP0.25 which has a low concentration of GNP.
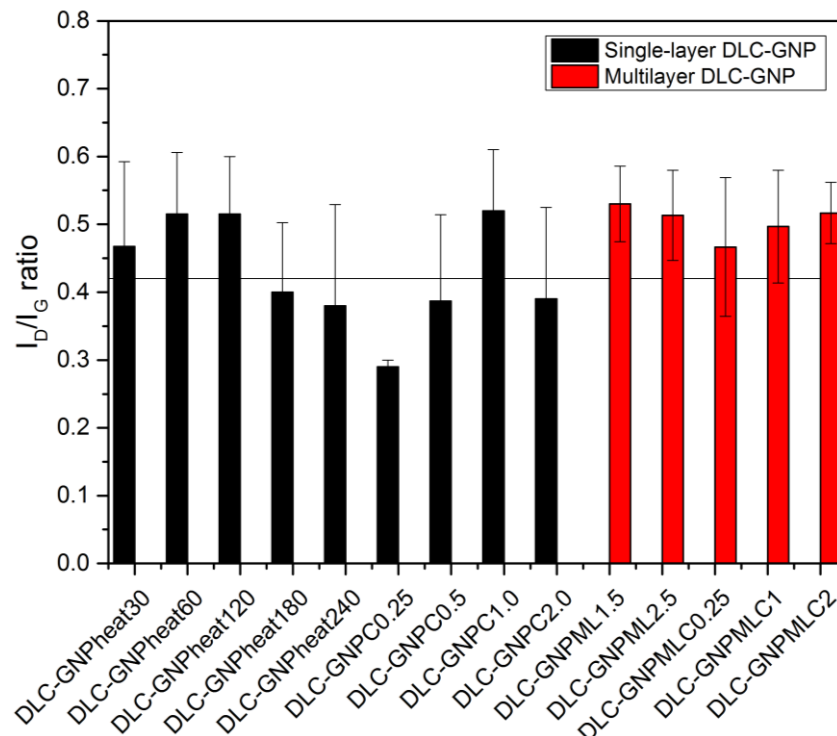
Figure 7.10 I_D/I_G ratio of single and multilayer DLC-GNP nanocomposite coatings. The error bars in the graph indicate standard deviation for three measurements

Generally, it can be seen that most of the I_D/I_G ratio of the nanocomposite coating is higher than the pure DLC. The I_D/I_G ratio of multilayer coatings are roughly higher than the single-layer coatings. There is also a trend of I_D/I_G increase as the GNP increased for both single and multilayer DLC-GNP nanocomposite coating except for sample DLC-GNPC2.0 that may be due to the reason explained above on inhomogeneity of high GNP samples. Commonly, the lower the ratio of I_D/I_G the higher amount of sp^3 bonding there is, and contrarily higher I_D/I_G describes higher sp^2 bond [178]. Unlike DLC, GNP is composed of only sp^2 bonding. It is possible that the Raman spectra might have detected the sp^2 bonding from GNP when the concentration of GNP is high enough. This is in agreement with the finding of Zanin et al. [127] on DLC and Carbon-Nanotube (CNT) composite where the I_D/I_G increase upon addition of CNT from 0.28 to 0.52. The increase of sp^2 is usually ascribed to the reduction of hardness [220]. The value of I_D/I_G ratio measured for pure DLC and all DLC-GNP nanocomposite coatings lies between ~0.3 – 0.6. This represents sp^3 content of approximately ~35 -70% [32, 127].

According to Raman analysis, it is also noticeable that when the amount of GNP in the composite is low (0.25 mg/mL), the sp^3 bonding is noticeably higher than the pure DLC (low I_D/I_G ratio). Reduction of I_D/I_G ratio is also observed when the post-treatment is above 180 minutes. These may relate to the homogeneous distribution of GNP when the concentration is low and when the duration of post-treatment is effective.

In this work, XPS analysis was conducted for pure DLC and multilayer DLC-GNPML1.5 nanocomposite coatings. Therefore, discussion on sp^3 content using Raman and XPS analyses is carried out for those two coatings. Table 7.1 compares the estimated and the calculated values of sp^3 content from Raman and XPS analysis. There is a significant difference between the value estimated using I_D/I_G ratio and the value measured using XPS analysis. However, both analyses showed an apparent reduction of sp^3 content in all measured areas for nanocomposite coating compared to the pure DLC coating. This is an evidence of the existence of different bonding in DLC-GNP nanocomposite coating compared to pure DLC. The outmost DLC layer deposited on GNP is more graphitic in nature than the pure DLC coating. As

mentioned earlier in Section 7.2.1, the formation of DLC film on GNP may have been through subplantation mechanism. The subplantation would promote formation of high sp^3 content and a sub-surface layer that is rich in sp^2 [191, 221]. XPS analysis relates to the top surface layer of coating rather than the entire coating thickness like Raman analysis which is the reason of high sp^2 content recorded for the coating. These results also explain the discrepancy between the sp^3 content values estimated from Raman analysis and measured from the XPS.

Table 7.1 Comparison of sp^3 content in pure DLC and DLC-GNPML1.5 estimated and measured by Raman and XPS analyses

Sample	sp^3 content (%)	
	Raman	XPS
Pure DLC	~ 45-55	74.0
DLC-GNPML1.5 (area with, without GNP)	~35-45	24.3, 32.1

7.4 Tribological Performance of DLC-GNP Nanocomposite Coating

7.4.1 Friction behaviour of DLC-GNP nanocomposite coating

7.4.1.1 Effect of GNP on friction behaviour

Graphene has been reported to be an excellent solid lubricant that is capable of reducing friction in many graphene-based composite coating [222]. However, an appropriate amount of and favourable conditions for graphene are needed to optimise its performance. Results showed that incorporation of GNP in the DLC matrix does influence the friction behaviour of the DLC-GNP nanocomposite coating. To date, the lowest CoF recorded in this work is 0.06 by single-layer DLC-GNP (0.11 vol%) with 180 minutes of post-treatment process and DLC deposition for 240 minutes. It is lower than the CoF recorded by pure DLC with almost the same thickness of about 0.11. The second lowest CoF was multilayer DLC-GNP with 180 minutes post-treatment deposited with 90 minutes of DLC film for each layer.

The amount of GNP also plays a crucial role in determining the friction behaviour. Figure 7.11 represents the CoF of both single and multilayer DLC-GNP nanocomposite coating as a function of GNP vol%. Note the samples of single-layer DLC-GNP were post-treated for only one hour hence they experience higher values of CoF for most of the coating. The trend shows a reduction of CoF as the GNP vol% was increased for both types of coatings. This indicates that GNP amount in the composite may have contributed to reducing the CoF of the system. Zhang et al. [223] reported that overlapped and thicker graphene sheets are more favourable for shearing to form nano bearing effect between the coating and counterpart. In a separate study performed by Meyer [224], it was found that thicker GNP hinders puckering from occurring due to larger bending stiffness of the sheet. On the one hand, as can be seen in Figure 7.11, single-layer DLC-GNP coatinghaving a really low concentration of GNP (0.008 vol%), also recorded very low CoF. The concentration of GNP used on this coating was 0.25 mg/mL. One of the reason is, at low concentration of GNP, GNP is in less aggregation condition. Spin-coated GNP at this concentration may have an excellent dispersibility on the surface, promoting low-shear mechanism.
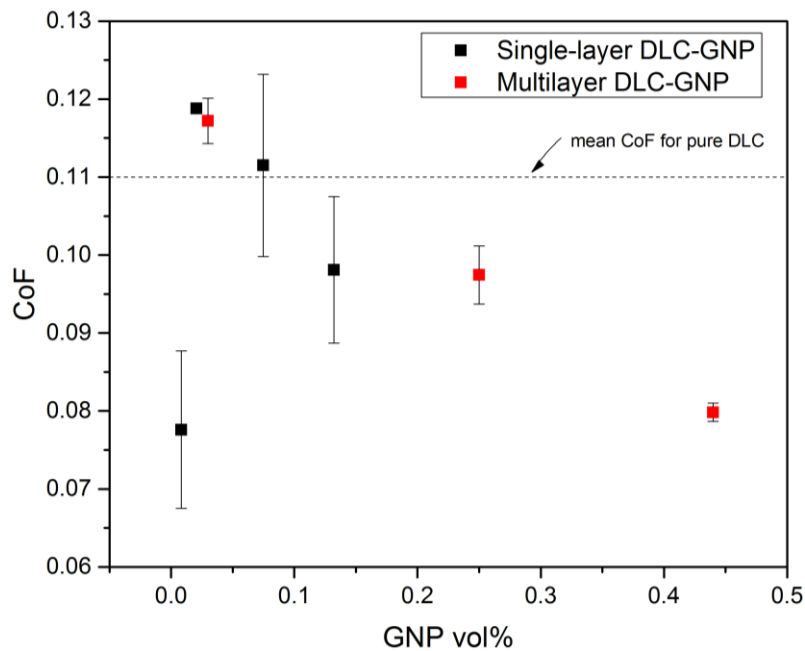
Figure 7.11 CoF of DLC-GNP nanocomposite coatings as a function of GNP vol%

7.4.1.2 Effect of adhesion strength on friction behaviour

Figure 7.12 presents the measured average CoF as a function of critical load for all single and multilayer DLC-GNP nanocomposite coating. As we can see in the plot, there is no clear and direct correlation between CoF and critical load. If we look at the performance of single-layer DLC-GNP samples, many of the samples with stronger adhesive strength exhibit high CoF. The multilayer DLC-GNP coatings also have almost the same condition where adhesive strength did not influence its frictional behaviour.

If we assume that a CoF above 0.10 is high, we can see that almost all of the multilayer DLC-GNP samples demonstrate CoF below 0.10. Whereas for single-layer samples, almost 70% of the samples have CoF more than 0.10. As a reference pure DLC recorded average CoF of 0.11. The lowest CoF recorded in this work is with sample DLC-GNPheat180 of ~0.06. A few other coatings that have heat-treated also have CoF below than 0.1.
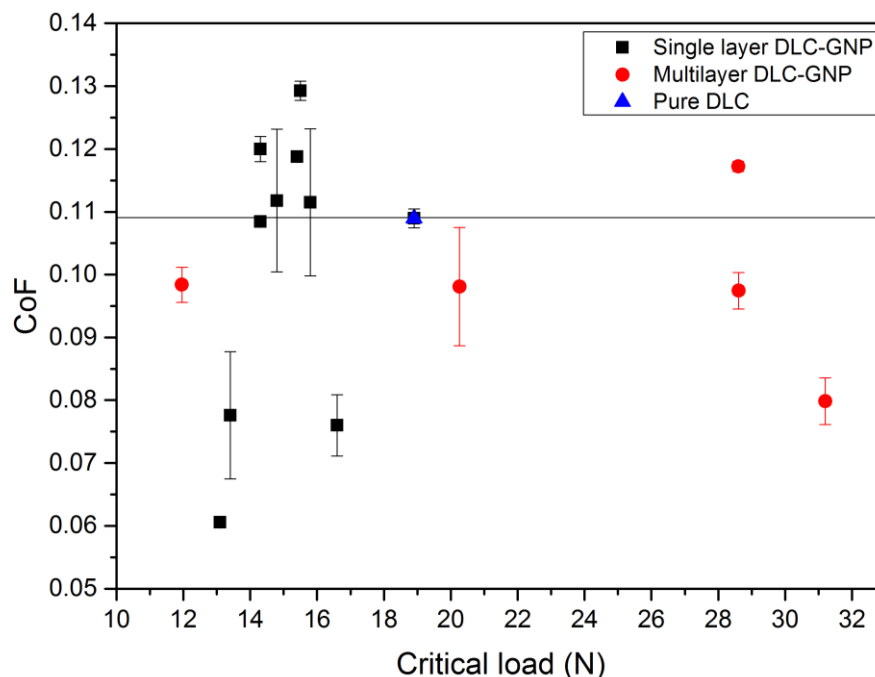
Figure 7.12 Coefficient of friction (CoF) as a function of critical load of single and multilayer DLC-GNP nanocomposite coatings

7.4.1.3 The relationship between friction behaviour and I_D/I_G ratio of the coating and wear

In this work, Raman analysis of wear specifically the I_D/I_G ratio has been employed to investigate the tribological behaviour of DLC-GNP nanocomposite coating. An increase in I_D/I_G ratio is commonly related to an increase in number of sp_2 clusters which also ascribed to graphitisation. Liu et al. [225] proposed that graphitisation is related to frictional energy, followed by hydrogen atom release stage and finally shear deformation that converts the $(111)_{DLC}$ into hexagonal $(0002)_{GR}$ planes enabling the nucleation of graphite.

The distribution of average CoF as a function of $\Delta(I_D/I_G)$ is displayed in Figure 7.13. The $\Delta(I_D/I_G)$ represents the change of I_D/I_G ratio after (inside the wear track) and before testing. As can be seen, most of the coatings have the increased I_D/I_G ratio which interprets that graphitisation occurred. Compared to DLC-GNP nanocomposite coatings, pure DLC has the least change of I_D/I_G ratio.

Many works suggested that DLC graphitisation is due to relaxation of sp^3 bonds during sliding and the one responsible for the reduction of friction [226, 227]. However, in this work, graphitisation may not be the factor in friction reduction in the 3-hour test. No specific trend can be observed based on the change of I_D/I_G ratio for all coatings. One of the possible reasons is due to the variation of I_D/I_G ratio on the wear tracks. It is evident that the I_D/I_G ratio of most of multilayer DLC-GNP coatings did not change much as compared to the single-layer DLC-GNP coatings after the sliding test.
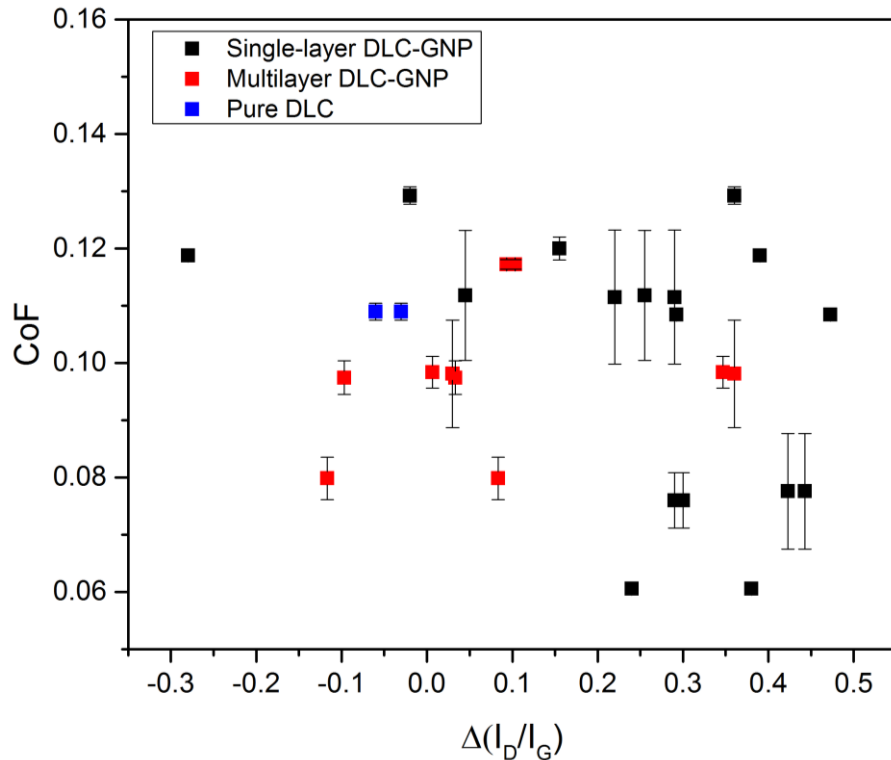
Figure 7.13 CoF as a function of Δ (I_D/I_G) for single and multilayer DLC-GNP nanocomposite coatings

7.4.2 Wear behaviour of DLC-GNP nanocomposite coating

7.4.2.1 Effect of adhesion strength on wear behaviour

The principal of wear is when contact stress exceeds the yield stress of substrate; the wear will increase due to plastic deformation and fracture of the coated material [228]. The wear rate as a function of critical load is plotted in Figure 2.11. From the graph, it is obvious that the wear rate reduced as the critical load increased. The multilayer coating samples which go through 180 minutes of post-treatment did not suffer adhesive wear. It has also been discussed earlier that the incorporation of GNP without any post-treatment has deteriorated the adhesion strength of the composite coating. It is evident that GNP adhesion on the surface plays a crucial role in the wear behaviour of DLC-GNP nanocomposite coating. When GNP does not adhere well to the surface, the adhesion strength of the DLC-GNP coating become weak. As a result, complete delamination of coating occurred.
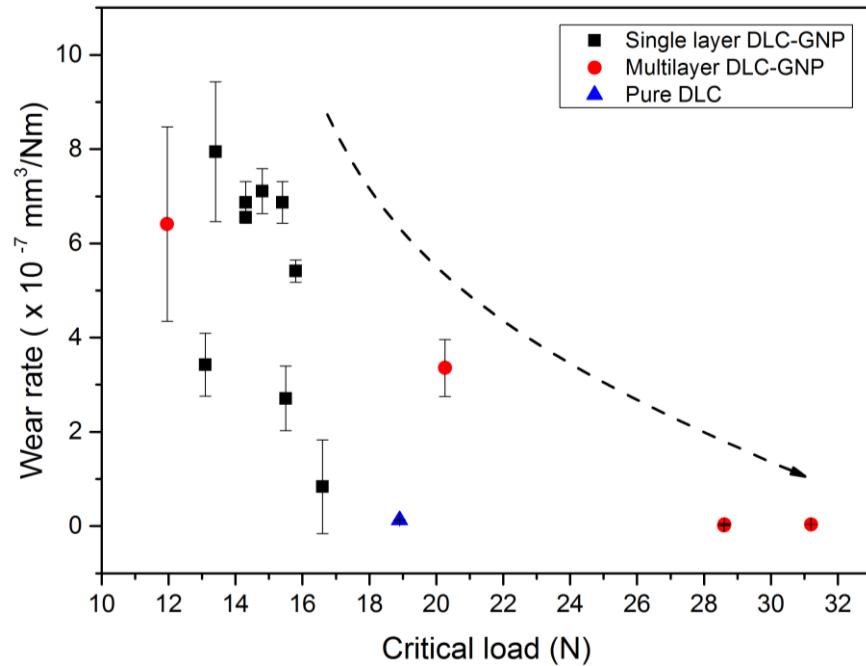
Figure 7.14 Wear rate as a function of critical load for single and multilayer DLC-GNP nanocomposite coating

7.4.2.2 The relationship between wear rate and I_D/I_G ratio of the coating and wear track

Raman analyses of wear tracks on samples as well as on the wear scars of the counterparts can give useful information for predicting the wear mechanism of DLC-GNP nanocomposite coating in base oil. The wear rate of the counterparts was studied using an optical microscope to observe the wear morphology, WLI to investigate the wear volume and Raman microscopy to characterise the structure change of the surface after the test. It is evident from the Raman spectra analysis that there is a mixture of surface transformations occurring after the sliding test. Some spectra coincide with that of graphite while some remained the same peaks of the as-produced DLC-GNP coating.

Figure 7.15 shows the correlation between wear rate of DLC-GNP nanocomposite coating and the different of I_D/I_G ratio after (inside wear track) and before the 3-hour test sliding test ($\Delta(I_D/I_G)$). As can be seen, most of the I_D/I_G of wear tracks were higher than the as-prepared DLC-GNP coating which

shows the existence of more graphitic structure (sp^2) [186]. Graphitisation of coatings after sliding test has been discussed earlier in Section 7.4.1. Most of the coatings that have severe wear (high wear rate) have high changes of I_D/I_G on their wear tracks. In contrast, coatings with less wear inside the square dotted area, have the least changes of I_D/I_G. The results indicate that graphitisation of the nanocomposite coating reduces the wear resistance of the coating. Many works reported the increment of I_D/I_G ratio in wear track area [216, 229]. Zhou and group [196, 230] also reported a pre-graphitisation condition on wear track of Ti-DLC coating, where the wear track has similar spectra but with a lower intensity of Raman spectra compare to before sliding test. Ghosh et al. [216] also reported that an increase of I_D/I_G indicates the severity of the coating wear.

Various coating structure changes can happen in different areas on one wear track of a coating. Graphitisation of coating during sliding represents the wear of coating but not the friction value. Generally, it can be suggested that the rise of I_D/I_G of the wear track indicates the wear rate of the coating.
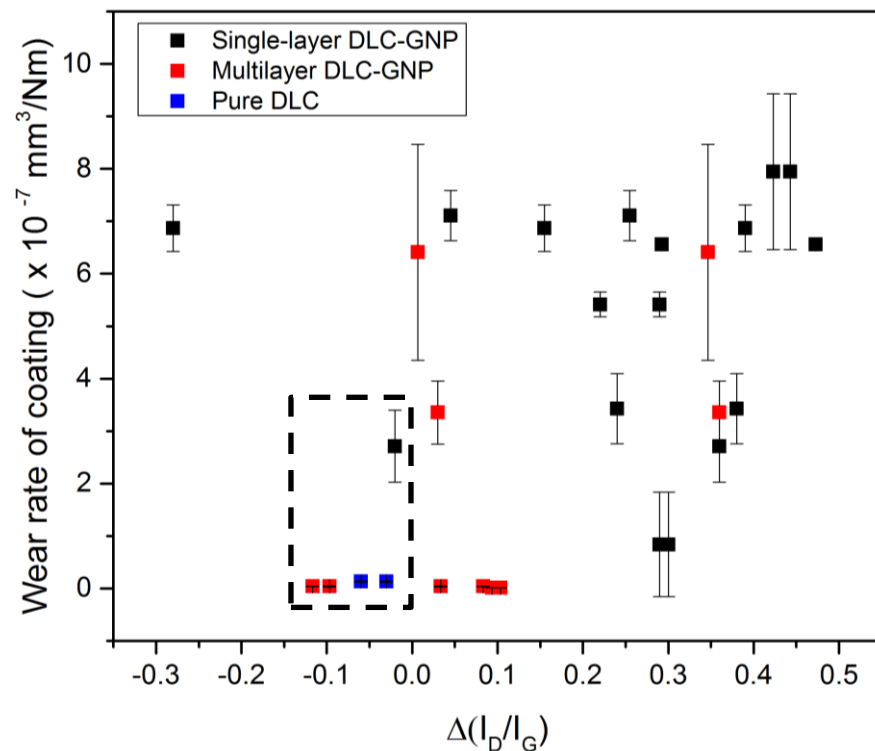
Figure 7.15 Wear rate of the nanocomposite coating as a function of $\Delta(I_D/I_G)$

7.4.3 Proposed wear and frictional mechanism of DLC-GNP nanocomposite coating

The results of CoF and wear of DLC-GNP coating imply that post-treatment does improve the friction and wear performance of the coating. It demonstrates that in order to benefit the excellent tribological properties of GNP in DLC-GNP nanocomposite coating, the distribution and adhesion of GNP are very important. The mechanism governing the tribological behaviour of the coatings that have gone through post-treatment process is proposed. Figure 7.16 shows the schematic illustration of the friction mechanism of post-treated coatings for 180 minutes and the micrographs of wear scar and wear track on the counterpart and coating. Durability test also demonstrates that the wear track still has a columnar structure even after the 24-hour test. The wear volume increased after six hours and remained almost the same. In hindsight, this columnar structure has promoted the reduction of CoF and wear rate of coating.
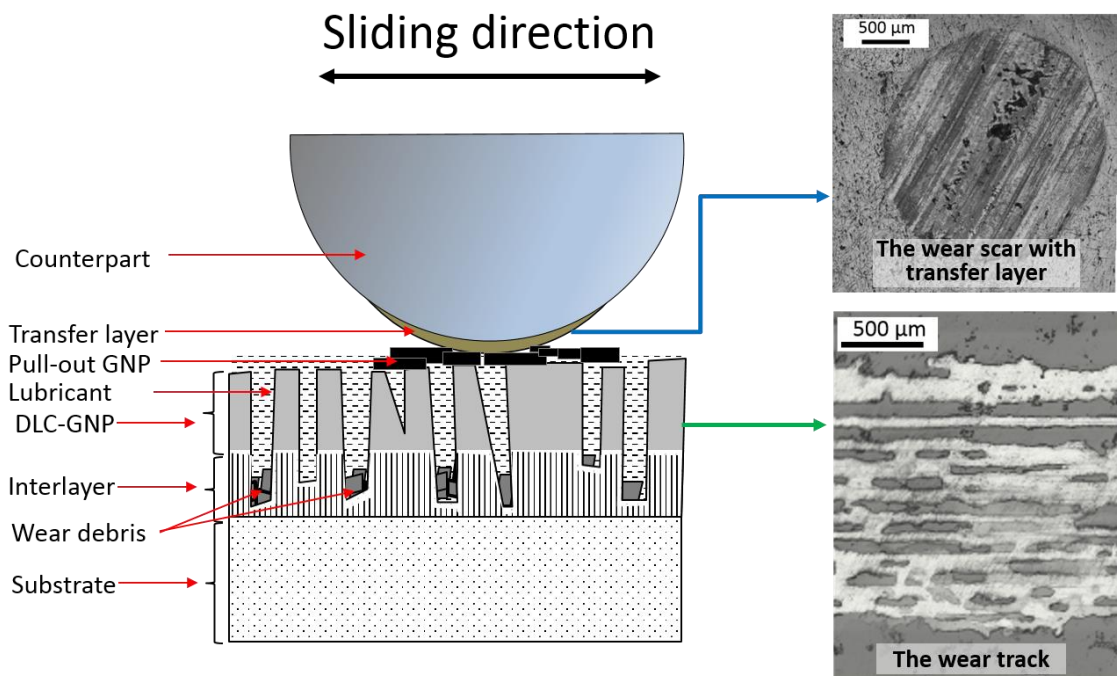
Figure 7.16 Schematic illustration of friction and wear behaviour of sample DLC-GNPheat180 nanocomposite coating and the corresponding micrograph of wear scar on counterpart and wear track on the coating

In general, DLC-GNP nanocomposite coatings have a rougher surface compared to pure DLC. This is due to the existence of GNP cluster on the surface when GNPs were incorporated in the coatings. It is likely that the coating was worn through when the GNP clusters were sheared and deformed to the columnar structure during the running-in period. Figure 7.17 shows the running-in CoF measured for coatings post-treated for 30 to 240 minutes. Coatings of DLC-GNPheat180 and DLC-GNPheat240 that have the columnar wear structure are marked in the dotted square in the graph. As can be seen in the figure, the wear rate increased with the rised of the running-in CoF.

Figure 7.18 shows the schematic of wear mechanism during the running-in period that deformed the coating to the feature in Figure 7.16. A rough coating is commonly subjected to polishing and abrasive wear during the running-in period [231]. The polishing and ploughing wear has made the embedded GNPs were pulled out from the coating and subsequently act as a slider between counterpart and coating as shown earlier in Figure 7.16.

It can be suggested that the polishing wear has made the asperity of coating, which is mainly at the area where GNP exist, being polished out. When the adhesion strength of GNP is high (180 minutes post-treatment), the DLC and the GNP were removed together with the interlayer. The valley area of the coating remained intact on the substrate. The wear activity during the running-in period for rough DLC-GNP coating, has benefited in formation of the columnar wear that may not be obtained when the surface is smooth. The coatings with the columnar wear have a decreasing trend of CoF after the running-in period. The columnar wear may be related to what has been reported by Sonderby et al. [232] in which amorphous DLC could replicate the columnar structure of Cr interlayer. It is therefore possible that the DLC film may also fractured in columnar structure imitating the structure of the interlayer that was removed together during the running-in period.
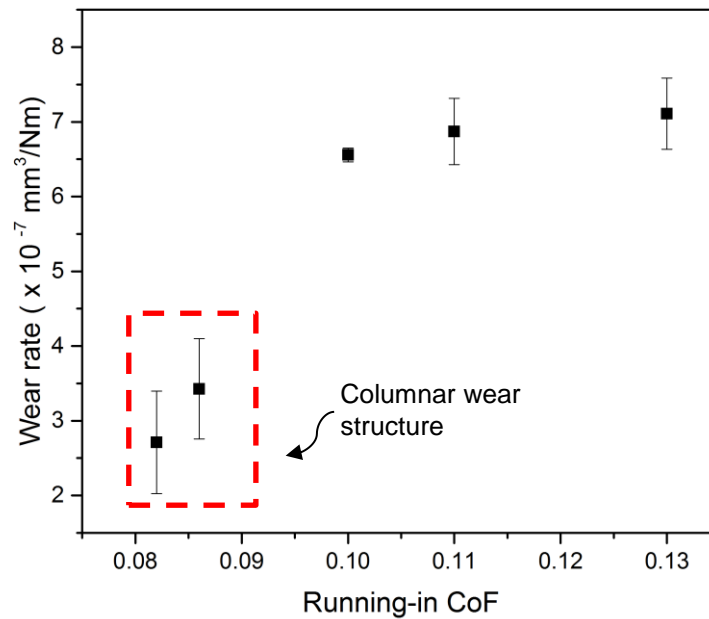
Figure 7.17 The wear rate as a function of running-on CoF for post-treated DLC-GNP nanocomposite coating

The spontaneous formation of the worn texture as in figure can act as a reservoir to trap the wear debris thus preventing further abrasive wear. Extended sliding tests to six hours on the coatings proved that the tribofilms might have been continuously replaced by the GNP that exist in the wear features thus reduced the CoF to 0.05. The CoF slightly increased when the test was further extended to 12 hours and remained almost the same until 24 hours. Interestingly columnar wear remained even after the 24-hour test. It has also been verified by the small wear observed on the counterpart for this sample and formation of tribofilm documented from Raman spectra [233]. These results demonstrate the beneficial contribution of GNP in promoting low friction and low wear. As mentioned earlier, this columnar wear structure remained even after the 24-hour test. This nanocomposite coating has the potential to be developed as a new functionalized tribological coating that creates a columnar structure in the initial stages of wear and is able to maintain the structure for low friction and wear.
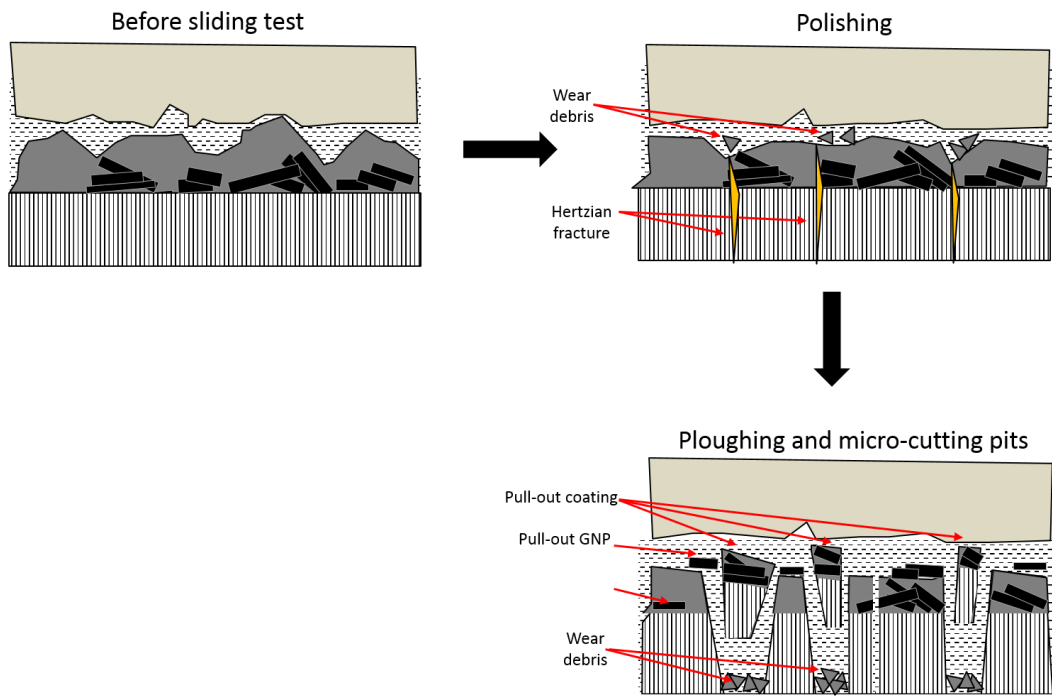
Figure 7.18 Schematic representation of wear occurred during the running-in period and the columnar wear formation

Chapter 8

Conclusions and Future Work

Single and multilayer DLC-GNP nanocomposite coating have been fabricated with a combination of spin-coating and PECVD methods. With the improvement of the method of deposition, post-treatment and coating structure, DLC-GNP nanocomposite coatings with the enhancement of the mechanical and tribological properties have been obtained. This chapter will list the main findings of this work with recommendations on possible plans for future work.

8.1   Conclusions

The major findings of this thesis are concluded as follows:

8.1.1   Adhesion strength of DLC-GNP nanocomposite coating

- Post-treatment of 180 minutes has significantly improved the adhesion of GNP thus improving the adhesion strength of the nanocomposite coating.

- The adhesion strength of DLC-GNP nanocomposite coatings from the combination of bonding strength between the substrate-GNP and GNP-DLC interfaces. The bonding for substrate-GNP and GNP-DLC interfaces is physical bonding of Van der Waals and formation of bonding layer during deposition of DLC respectively.

- Deposition of multilayer DLC-GNP coating has significantly increased the adhesion strength almost doubling that of the single-layer DLC-GNP processed in the same condition. The highest adhesion strength was achieved by multilayer DLC-GNPML2.0 with the highest content of GNP of all samples, (0.44 vol%) at critical load of ~ 31 N.

8.1.2   Mechanical properties

- DLC-GNP nanocomposite coatings have a wide range value of nanohardnesses and elastic modulus depending on the area with and without GNP.

- Combinations of post-treatment at 180 minutes and multilayer structure with deposition time of 1.5 hours for each layer, contribute to adhesion strength of DLC-GNP nanocomposite coatings.

8.1.3 Tribological performance of DLC-GNP nanocomposite coating

- The normal load used in this work was 281 N and the measured Hertzian contact stress was 750 MPa which corresponds to the tribological conditions at the cam/ tapped interface. The DLC-GNP nanocomposite coatings, showed high potential to be applied in this type of highly loaded contacts.

- Post-treatment of 180 minutes is beneficial in improving the tribological performance.

- Weak adhesion strength of DLC-GNP nanocomposite coating contributes to low tribological performance.

- High GNP concentration in coating (vol%) reduces the CoF by contributing to the low-shear effect. However, at low concentration, GNP in DLC-GNP has less aggregation and is more dispersed, thus may also contribute to low CoF.

- The lowest wear rate achieved with a multilayer DLC-GNP coating was 0.003×10^{-7} mm^3/Nm at GNP vol% of 0.03%.

- The columnar structure obtained for a coating having 180 minutes post-treatment, contributes to low CoF as low as 0.06. The structure is capable to continuously provide GNP that act as a low-shear film in the system, thus reducing the CoF.

- The micrographs of the wear scars show formation of carbon-rich wear debris in all counterparts of pure DLC, single and multilayer DLC-GNP

nanocomposite coatings. High I_D/I_G values within the wear scars of the DLC-GNP nanocomposite coatings indicate that the adhered debris is a layer composed of graphitic carbon debris.

- Graphitisation plays a great role in wear loss of DLC-GNP nanocomposite coating. Higher graphitisation of coatings after sliding test indicate higher wear on the coating.

8.2   Future Work

Preparation of DLC-GNP nanocomposite coating with post-treatment for 180 minutes showed an interesting result with strong adhesion and low coefficient of friction (CoF). Multilayer DLC-GNP nanocomposite coating on the other hand efficiently improved the adhesion strength and wear rate. With a combination of post-treatment and a multilayer structure, it is believed that the nanocomposite coating can be further improved to provide better structure, toughness, and lower friction and lower wear rate. In order to improve the mechanical and tribological properties of the coating and make it useful for practical applications, the following further investigations are recommended:

1. To include centrifugation method in the dispersion of GNP. Centrifugation is a method that has been widely used for producing a well dispersed GNP suspension [234, 235]. Using centrifugation method, selection of GNP is possible where aggregated GNP can be eliminated from the dispersion and leaving only the dispersed GNP. Centrifugation can be done after the process of dispersing GNP in a solvent using ultrasonication. Dispersion of GNP influences the dispersion of spin-coated GNP. Better dispersion of GNP provides less aggregation of GNP thus improving the wear performance of the composite.

2. It is worthwhile to increase the number of layers in multilayer DLC-GNP nanocomposite coating and investigate the mechanical and tribological properties. It could be achieved by attempting to reduce the thickness of one layer of DLC film, whilst adding layers in the composite. The

multilayer structure is capable of maintaining less thickness but at the same time improving adhesion and tribological performance.

3. In order to further reveal the potential of the coating, the sliding duration of reciprocating test should be increased to 6 and 12-hour time periods. In the current work, the sliding duration for all test has been fixed to three hours only. It would be interesting to investigate the friction and wear change during the long time scale test.

4. In this work, base oil Group III has been used to study the tribological properties of all coatings in this work. DLC has also been reported to work effectively in fully formulated lubricant containing additives such as zinc dialkyldithiophosphate (ZDDP) and MoDTC [69]. Ionic liquids have also been reported to have good interaction with DLC and graphene. However most published works are using graphene as an additive in the ionic liquid [236, 237]. In order to investigate the use of the DLC-GNP coating in various applications, it could be of great technical interest to investigate its performance with other potential lubricants as well.

References

1. Won, M.-S., O.V. Penkov, and D.-E. Kim, *Durability and degradation mechanism of graphene coatings deposited on Cu substrates under dry contact sliding.* Carbon, 2013. **54**: p. 472-481.
2. Chu, S. and A. Majumdar, *Opportunities and challenges for a sustainable energy future.* Nature, 2012. **488**(7411): p. 294-303.
3. Patterson, M.G., *What is energy efficiency? Concepts, indicators and methodological issues.* Energy Policy, 1996. **24**(5): p. 377-390.
4. Holmberg, K., P. Andersson, and A. Erdemir, *Global energy consumption due to friction in passenger cars.* Tribology International, 2012. **47**: p. 221-234.
5. Holmberg, K., P. Andersson, N.-O. Nylund, K. Makela, and A. Erdemir, *Global energy consumption due to friction in trucks and buses.* Tribology International, 2014. **78**: p. 94-114.
6. Holmberg, K., R. Siilasto, T. Laitinen, P. Andersson, and A. Jasberg, *Global energy consumption due to friction in paper machines.* Tribology International, 2013. **62**: p. 58-77.
7. Hermann, M., T. Pentek, and B. Otto. *Design principles for industrie 4.0 scenarios.* in *System Sciences (HICSS), 2016 49th Hawaii International Conference on.* 2016. IEEE.
8. Matthews, A., S. Franklin, and K. Holmberg, *Tribological coatings: contact mechanisms and selection.* Journal of Physics D: Applied Physics, 2007. **40**(18): p. 5463-5475.
9. Holmberg, K., H. Ronkainen, and A. Matthews, *Tribology of thin coatings.* Ceramics International, 2000. **26**(7): p. 787-795.
10. Salvadori, M.C., D.R. Martins, and M. Cattani, *DLC coating roughness as a function of film thickness.* Surface & Coatings Technology, 2006. **200**(16-17): p. 5119-5122.
11. Ohana, T., M. Suzuki, T. Nakamura, A. Tanaka, and Y. Koga, *Tribological properties of DLC films deposited on steel substrate with various surface roughness.* Diamond and Related Materials, 2004. **13**(11-12): p. 2211-2215.
12. Waseem, B., S. Alam, M. Irfan, M. Shahid, B.D. Soomro, S. Hashim, and R. Iqbal, *Optimization and characterization of adhesion properties of DLC coatings on different substrates*, in *13th International Symposium on Advanced Materials*, S. Qaisar, A.N. Khan, and E.A. Mukhtar, Editors. 2014.
13. Zhang, S., D. Sun, Y.Q. Fu, and H.J. Du, *Recent advances of superhard nanocomposite coatings: a review.* Surface & Coatings Technology, 2003. **167**(2-3): p. 113-119.
14. Hogmark, S., S. Jacobson, and M. Larsson, *Design and evaluation of tribological coatings.* Wear, 2000. **246**(1-2): p. 20-33.
15. Leyland, A. and A. Matthews, *On the significance of the H/E ratio in wear control: a nanocomposite coating approach to optimised tribological behaviour.* Wear, 2000. **246**(1-2): p. 1-11.

16. Dwivedi, N. and S. Kumar, *Nanoindentation testing on copper/diamond-like carbon bi-layer films.* Current Applied Physics, 2012. **12**(1): p. 247-253.

17. Blazek, J., J. Musil, P. Stupka, R. Cerstvy, and J. Houska, *Properties of nanocrystalline Al-Cu-O films reactively sputtered by DC pulse dual magnetron.* Applied Surface Science, 2011. **258**(5): p. 1762-1767.

18. Musil, J., *Hard nanocomposite coatings: Thermal stability, oxidation resistance and toughness.* Surface & Coatings Technology, 2012. **207**: p. 50-65.

19. Musil, J., P. Novak, R. Cerstvy, and Z. Soukup, *Tribological and mechanical properties of nanocrystalline-TiC/a-C nanocomposite thin films.* Journal of Vacuum Science & Technology A, 2010. **28**(2): p. 244-249.

20. Chen, X., Z. Peng, X. Yu, Z. Fu, W. Yue, and C. Wang, *Microstructure and tribological performance of self-lubricating diamond/tetrahedral amorphous carbon composite film.* Applied Surface Science, 2011. **257**(8): p. 3180-3186.

21. Sarmadi, H., A.H. Kokabi, and S.M. Seyed Reihani, *Friction and wear performance of copper–graphite surface composites fabricated by friction stir processing (FSP).* Wear, 2013. **304**(1-2): p. 1-12.

22. Bewilogua, K. and D. Hofmann, *History of diamond-like carbon films - From first experiments to worldwide applications.* Surface & Coatings Technology, 2014. **242**: p. 214-225.

23. Santra, T., T. Bhattacharyya, P. Patel, F. Tseng, and T. Barik, *Diamond, diamond-like carbon (DLC) and diamond-like nanocomposite (DLN) thin films for MEMS applications*, in *Microelectromechanical Systems and Devices.* 2012, InTech.

24. Deaquino-Lara, R., N. Soltani, A. Bahrami, E. Gutiérrez-Castañeda, E. García-Sánchez, and M.A.L. Hernandez-Rodríguez, *Tribological characterization of Al7075–graphite composites fabricated by mechanical alloying and hot extrusion.* Materials & Design, 2015. **67**: p. 224-231.

25. Omrani, E., A.D. Moghadam, P.L. Menezes, and P.K. Rohatgi, *Influences of graphite reinforcement on the tribological properties of self-lubricating aluminum matrix composites for green tribology, sustainability, and energy efficiency—a review.* The International Journal of Advanced Manufacturing Technology, 2015.

26. Matthews, A., A. Leyland, K. Holmberg, and H. Ronkainen, *Design aspects for advanced tribological surface coatings.* Surface & Coatings Technology, 1998. **100**(1-3): p. 1-6.

27. Sainio, S., T. Palomäki, S. Rhode, M. Kauppila, O. Pitkänen, T. Selkälä, G. Toth, M. Moram, K. Kordas, J. Koskinen, and T. Laurila, *Carbon nanotube (CNT) forest grown on diamond-like carbon (DLC) thin films significantly improves electrochemical sensitivity and selectivity towards dopamine.* Sensors and Actuators B: Chemical, 2015. **211**: p. 177-186.

28. Zhao, F., A. Afandi, and R.B. Jackman, *Graphene diamond-like carbon films heterostructure.* Applied Physics Letters, 2015. **106**(10).

29. Nakazawa, H., R. Kamata, S. Miura, and S. Okuno, *Effects of frequency of pulsed substrate bias on structure and properties of silicon-doped*

diamond-like carbon films by plasma deposition. Thin Solid Films, 2015. **574**: p. 93-98.

30. Eastman, *Technical Data Sheet N-Methyl-2-Pyrrolidone (NMP).* 2015.
31. Gayathri, S., N. Kumar, R. Krishnan, T.R. Ravindran, S. Amirthapandian, S. Dash, A.K. Tyagi, and M. Sridharan, *Influence of transition metal doping on the tribological properties of pulsed laser deposited DLC films.* Ceramics International, 2015. **41**(1): p. 1797-1805.
32. Zanin, H., P.W. May, A.O. Lobo, E. Saito, J.P.B. Machado, G. Martins, V.J. Trava-Airoldi, and E.J. Corat, *Effect of Multi-Walled Carbon Nanotubes Incorporation on the Structure, Optical and Electrochemical Properties of Diamond-Like Carbon Thin Films.* Journal of the Electrochemical Society, 2014. **161**(5): p. H290-H295.
33. Yang, L., A. Neville, A. Brown, P. Ransom, and A. Morina, *Friction reduction mechanisms in boundary lubricated W-doped DLC coatings.* Tribology International, 2014. **70**: p. 26-33.
34. Liu, X., J. Pu, L. Wang, and Q. Xue, *Novel DLC/ionic liquid/graphene nanocomposite coatings towards high-vacuum related space applications.* Journal of Materials Chemistry A, 2013. **1**(11): p. 3797-3809.
35. Tinchev, S.S., *Surface modification of diamond-like carbon films to graphene under low energy ion beam irradiation.* Applied Surface Science, 2012. **258**(7): p. 2931-2934.
36. Wei, C., C.-I. Wang, F.-C. Tai, K. Ting, and R.-C. Chang, *The effect of CNT content on the surface and mechanical properties of CNTs doped diamond like carbon films.* Diamond and Related Materials, 2010. **19**(5-6): p. 562-566.
37. Wang, Y., L. Wang, G. Zhang, S.C. Wang, R.J.K. Wood, and Q. Xue, *Effect of bias voltage on microstructure and properties of Ti-doped graphite-like carbon films synthesized by magnetron sputtering.* Surface and Coatings Technology, 2010. **205**(3): p. 793-800.
38. Choi, E.C., Y.S. Park, and B. Hong, *Synthesis of carbon nanotubes on diamond-like carbon by the hot filament plasma-enhanced chemical vapor deposition method.* Micron, 2009. **40**(5-6): p. 612-6.
39. Hu, H., G. Chen, and J. Zhang, *Facile synthesis of CNTs-doped diamond-like carbon film by electrodeposition.* Surface and Coatings Technology, 2008. **202**(24): p. 5943-5946.
40. Kinoshita, H., I. Ippei, H. Sakai, and N. Ohmae, *Synthesis and mechanical properties carbon nanotube/diamond-like carbon composite films.* Diamond and Related Materials, 2007. **16**(11): p. 1940-1944.
41. Aisenber.S and R. Chabot, *Ion-Beam Deposition Of Thin Films Of Diamondlike Carbon.* Journal of Applied Physics, 1971. **42**(7): p. 2953-&.
42. Grill, A., *Diamond-like carbon: state of the art.* Diamond and Related Materials, 1999. **8**(2-5): p. 428-434.
43. Robertson, J., *Diamond-like amorphous carbon.* Materials Science & Engineering R-Reports, 2002. **37**(4-6): p. 129-281.
44. Erdemir, A. and C. Donnet, *Tribology of diamond-like carbon films: recent progress and future prospects.* Journal of Physics D-Applied Physics, 2006. **39**(18): p. R311-R327.

45.   Voevodin, A.A., J.P. O'Neill, and J.S. Zabinski, *WC/DLC/WS2 nanocomposite coatings for aerospace tribology.* Tribology Letters, 1999. **6**(2): p. 75-78.
46.   Kano, M., *Overview of DLC-Coated Engine Components*, in *Coating Technology for Vehicle Applications.* 2015, Springer. p. 37-62.
47.   Hong, Y.-S., S.-R. Lee, J.-H. Kim, and S.-Y. Lee, *Application of a DLC-Coating for improving hydrostatic piston shoe bearing performance under mixed friction conditions.* International Journal of Precision Engineering and Manufacturing, 2015. **16**(2): p. 335-341.
48.   Zhang, T., Q. Deng, B. Liu, B. Wu, F. Jing, Y. Leng, and N. Huang, *Wear and corrosion properties of diamond like carbon (DLC) coating on stainless steel, CoCrMo and Ti6Al4V substrates.* Surface and Coatings Technology, 2015. **273**: p. 12-19.
49.   Banerjee, A. and D. Das. *Fabrication of highly transparent diamond-like carbon anti-reflecting coating for Si solar cell application.* in *AIP Conference Proceedings.* 2014.
50.   Ghosh, B., D. Ghosh, A. Ghosh, S. Hussain, R. Bhar, and A. Pal, *Electrodeposited diamond-like carbon (DLC) films on n-Si (100) substrates for photovoltaic application.* Materials Science in Semiconductor Processing, 2014. **25**: p. 130-136.
51.   Depner-Miller, U., J. Ellermeier, H. Scheerer, M. Oechsner, K. Bobzin, N. Bagcivan, T. Brögelmann, R. Weiss, K. Durst, and C. Schmid, *Influence of application technology on the erosion resistance of DLC coatings.* Surface and Coatings Technology, 2013. **237**: p. 284-291.
52.   Hu, Z., A. Schubnov, and F. Vollertsen, *Tribological behaviour of DLC-films and their application in micro deep drawing.* Journal of Materials Processing Technology, 2012. **212**(3): p. 647-652.
53.   Morshed, M.M., B.P. McNamara, D.C. Cameron, and M.S.J. Hashmi, *Effect of surface treatment on the adhesion of DLC film on 316L stainless steel.* Surface & Coatings Technology, 2003. **163**: p. 541-545.
54.   Marciano, F.R., L.F. Bonetti, R.S. Pessoa, J.S. Marcuzzo, M. Massi, L.V. Santos, and V. Trava-Airoldi, *The improvement of DLC film lifetime using silver nanoparticles for use on space devices.* Diamond and Related Materials, 2008. **17**(7-10): p. 1674-1679.
55.   Litovchenko, V. and N. Klyui, *Solar cells based on DLC film–Si structures for space application.* Solar energy materials and solar cells, 2001. **68**(1): p. 55-70.
56.   Kleps, I., A. Angelescu, N. Samfirescu, A. Gil, and A. Correia, *Study of porous silicon, silicon carbide and DLC coated field emitters for pressure sensor application.* Solid-State Electronics, 2001. **45**(6): p. 997-1001.
57.   Baranov, A., A. Varfolomeev, A. Nefedov, M. Anderle, L. Calliari, G. Speranza, and N. Landini, *Development of DLC film technology for electronic application.* Diamond and Related Materials, 2000. **9**(3): p. 649-653.
58.   Arnoldussen, T.C. and E.-M. Rossi, *Materials for magnetic recording.* Annual Review of Materials Science, 1985. **15**(1): p. 379-409.
59.   Puchi-Cabrera, E.S., M.H. Staia, E.A. Ochoa-Perez, D.G. Teer, Y.Y. Santana-Mendez, J.G. La Barbera-Sosa, D. Chicot, and J. Lesage, *Fatigue behavior of a 316L stainless steel coated with a DLC film deposited by PVD magnetron sputter ion plating.* Materials Science and

Engineering a-Structural Materials Properties Microstructure and Processing, 2010. **527**(3): p. 498-508.

60. Al Mahmud, K.A.H., M.A. Kalam, H.H. Masjuki, H.M. Mobarak, and N.W.M. Zulkifli, *An updated overview of diamond-like carbon coating in tribology.* Critical Reviews in Solid State and Materials Sciences, 2015. **40**(2): p. 90-118.

61. Xiao, Y., W. Shi, J. Luo, and Y. Liao, *The tribological performance of TiN, WC/C and DLC coatings measured by the four-ball test.* Ceramics International, 2014. **40**(5): p. 6919-6925.

62. Kovacı, H., Ö. Baran, Ö. Bayrak, A.F. Yetim, and A. Çelik, *Influence of plasma nitriding treatment on the adhesion of DLC films deposited on AISI 4140 steel by PVD magnetron sputtering.* Journal of Adhesion Science and Technology, 2017. **31**(18): p. 2015-2027.

63. Bouzakis, K., A. Asimakopoulos, M. Batsioloas, N. Ene, F. Dimofte, R. Handschuh, and T. Krantz, *Characterization of DLC PVD coatings properties on wave bearings of aero-transmissions.* Laboratory for Machine Tools and Manufacturing Engineering, 2008: p. 339-348.

64. Tillmann, W., E. Vogli, and F. Hoffmann, *Low-friction diamond-like carbon (DLC)-layers for humid environment.* Thin Solid Films, 2007. **516**(2): p. 262-266.

65. Wojciechowski, K., R. Zybala, R. Mania, and J. Morgiel, *DLC layers prepared by the PVD magnetron sputtering technique.* Journal of Achievements in Materials and Manufacturing Engineering, 2009. **37**(2): p. 726-729.

66. Voevodin, A., S. Walck, and J. Zabinski, *Architecture of multilayer nanocomposite coatings with super-hard diamond-like carbon layers for wear protection at high contact loads.* Wear, 1997. **203**: p. 516-527.

67. Hampden-Smith, M.J. and T.T. Kodas, *Chemical Vapor Deposition of Metals: Part 1. An Overview of CVD Processes.* Chemical Vapor Deposition, 1995. **1**(1): p. 8-23.

68. Win, K.N., A. Neville, I. Kolev, and H. Zhao, *Effects of substrate bias on tribological properties of diamond-like carbon thin films deposited via microwave excited plasma enhanced chemical vapour deposition.* Journal of Tribology, 2016. **138**(3).

69. Austin, L.B., *Evaluation and Optimisation of Diamond-Like Carbon for Tribological Application*, in *School of Mechanical Engineering*. 2014, University of Leeds. p. 224.

70. Bonetti, L.F., G. Capote, L.V. Santos, E.J. Corat, and V.J. Trava-Airoldi, *Adhesion studies of diamond-like carbon films deposited on Ti6Al4V substrate with a silicon interlayer.* Thin Solid Films, 2006. **515**(1): p. 375-379.

71. Wei, C. and J.-Y. Yen, *Effect of film thickness and interlayer on the adhesion strength of diamond like carbon films on different substrates.* Diamond and Related Materials, 2007. **16**(4-7): p. 1325-1330.

72. Fedosenko, G., A. Schwabedissen, J. Engemann, E. Braca, L. Valentini, and J. Kenny, *Pulsed PECVD deposition of diamond-like carbon films.* Diamond and related materials, 2002. **11**(3): p. 1047-1052.

73. Piazza, F., D. Grambole, D. Schneider, C. Casiraghi, A. Ferrari, and J. Robertson, *Protective diamond-like carbon coatings for future optical storage disks.* Diamond and related materials, 2005. **14**(3): p. 994-999.

74.   Pappas, D.L., K.L. Saenger, J. Bruley, W. Krakow, J.J. Cuomo, T. Gu, and R.W. Collins, *Pulsed laser deposition of diamond-like carbon films.* Journal of applied physics, 1992. **71**(11): p. 5675-5684.

75.   Voevodin, A., M. Donley, and J. Zabinski, *Pulsed laser deposition of diamond-like carbon wear protective coatings: a review.* Surface and Coatings Technology, 1997. **92**(1): p. 42-49.

76.   Takikawa, H., K. Izumi, R. Miyano, and T. Sakakibara, *DLC thin film preparation by cathodic arc deposition with a super droplet-free system.* Surface and Coatings Technology, 2003. **163**: p. 368-373.

77.   Wu, J.-B., J.-J. Chang, M.-Y. Li, M.-S. Leu, and A.-K. Li, *Characterization of diamond-like carbon coatings prepared by pulsed bias cathodic vacuum arc deposition.* Thin Solid Films, 2007. **516**(2): p. 243-247.

78.   Wasy, A., G. Balakrishnan, S. Lee, J. Kim, D. Kim, T. Kim, and J. Song, *Argon plasma treatment on metal substrates and effects on diamond-like carbon (DLC) coating properties.* Crystal Research and Technology, 2014. **49**(1): p. 55-62.

79.   Depla, D., S. Mahieu, and J.E. Green, *<Depla et al 2009.pdf>*. 3rd ed. Handbook of Deposition Technologies for Films and Coatings 2009: Elservier.

80.   Bharathy, P.V., D. Nataraj, P.K. Chu, H. Wang, Q. Yang, M.S.R.N. Kiran, J. Silvestre-Albero, and D. Mangalaraj, *Effect of titanium incorporation on the structural, mechanical and biocompatible properties of DLC thin films prepared by reactive-biased target ion beam deposition method.* Applied Surface Science, 2010. **257**(1): p. 143-150.

81.   Dai, W., P. Ke, M.-W. Moon, K.-R. Lee, and A. Wang, *Investigation of the microstructure, mechanical properties and tribological behaviors of Ti-containing diamond-like carbon films fabricated by a hybrid ion beam method.* Thin Solid Films, 2012. **520**(19): p. 6057-6063.

82.   Gao, K., L. Zhang, J. Wang, B. Zhang, and J. Zhang, *Further improving the mechanical and tribological properties of low content Ti-doped DLC film by W incorporating.* Applied Surface Science, 2015. **353**: p. 522-529.

83.   Wei, Q., A.K. Sharma, J. Sankar, and J. Narayan, *Mechanical properties of diamond-like carbon composite thin films prepared by pulsed laser deposition.* Composites Part B-Engineering, 1999. **30**(7): p. 675-684.

84.   Lin, L.-Y., D.-E. Kim, W.-K. Kim, and S.-C. Jun, *Friction and wear characteristics of multi-layer graphene films investigated by atomic force microscopy.* Surface and Coatings Technology, 2011. **205**(20): p. 4864-4869.

85.   Kim, K.-S., H.-J. Lee, C. Lee, S.-K. Lee, H. Jang, J.-H. Ahn, J.-H. Kim, and H.-J. Lee, *Chemical Vapor Deposition-Grown Graphene: The Thinnest Solid Lubricant.* Acs Nano, 2011. **5**(6): p. 5107-5114.

86.   Hong, J., M.K. Park, E.J. Lee, D. Lee, D.S. Hwang, and S. Ryu, *Origin of New Broad Raman D and G Peaks in Annealed Graphene.* Scientific Reports, 2013. **3**.

87.   Geim, A., *Graphene prehistory.* Physica Scripta, 2012. **2012**(T146): p. 014003.

88.	Warner, J.H., F. Schaffel, A. Bachmatiuk, and M.H. Rummeli, *Graphene: Fundamentals and Emergent Applications*. Graphene: Fundamentals and Emergent Applications. 2013. 1-450.

89.	Novoselov, K.S., A.K. Geim, S.V. Morozov, D. Jiang, Y. Zhang, S.V. Dubonos, I.V. Grigorieva, and A.A. Firsov, *Electric field effect in atomically thin carbon films.* Science, 2004. **306**(5696): p. 666-669.

90.	de Andres, P.L., R. Ramirez, and J.A. Verges, *Strong covalent bonding between two graphene layers.* Physical Review B, 2008. **77**(4).

91.	Lee, C., X. Wei, Q. Li, R. Carpick, J.W. Kysar, and J. Hone, *Elastic and frictional properties of graphene.* physica status solidi (b), 2009. **246**(11-12): p. 2562-2567.

92.	Bianco, A., H.-M. Cheng, T. Enoki, Y. Gogotsi, R.H. Hurt, N. Koratkar, T. Kyotani, M. Monthioux, C.R. Park, J.M.D. Tascon, and J. Zhang, *All in the graphene family – A recommended nomenclature for two-dimensional carbon materials.* Carbon, 2013. **65**(Supplement C): p. 1-6.

93.	Koenig, S.P., N.G. Boddeti, M.L. Dunn, and J.S. Bunch, *Ultrastrong adhesion of graphene membranes.* Nat Nanotechnol, 2011. **6**(9): p. 543-6.

94.	Suk, J.W., R.D. Piner, J. An, and R.S. Ruoff, *Mechanical Properties of Mono layer Graphene Oxide.* Acs Nano, 2010. **4**(11): p. 6557-6564.

95.	Novoselov, K.S., V.I. Fal'ko, L. Colombo, P.R. Gellert, M.G. Schwab, and K. Kim, *A roadmap for graphene.* Nature, 2012. **490**(7419): p. 192-200.

96.	Song, X., J. Liu, L. Yu, J. Yang, L. Fang, H. Shi, C. Du, and D. Wei, *Direct versatile PECVD growth of graphene nanowalls on multiple substrates.* Materials Letters, 2014. **137**: p. 25-28.

97.	Li, X., Y. Zhu, W. Cai, M. Borysiak, B. Han, D. Chen, R.D. Piner, L. Colombo, and R.S. Ruoff, *Transfer of Large-Area Graphene Films for High-Performance Transparent Conductive Electrodes.* Nano Letters, 2009. **9**(12): p. 4359-4363.

98.	Virojanadara, C., R. Yakimova, A.A. Zakharov, and L.I. Johansson, *Large homogeneous mono-/bi-layer graphene on 6H-SiC(0001) and buffer layer elimination.* Journal of Physics D-Applied Physics, 2010. **43**(37).

99.	Wu, Y., G. Yu, H. Wang, B. Wang, Z. Chen, Y. Zhang, B. Wang, X. Shi, X. Xie, Z. Jin, and X. Liu, *Synthesis of large-area graphene on molybdenum foils by chemical vapor deposition.* Carbon, 2012. **50**(14): p. 5226-5231.

100.	Dao, T.D. and H.M. Jeong, *Graphene prepared by thermal reduction-exfoliation of graphite oxide: Effect of raw graphite particle size on the properties of graphite oxide and graphene.* Materials Research Bulletin, 2015. **70**: p. 651-657.

101.	Hiramatsu, M., H. Kondo, and M. Hori, *Graphene Nanowalls, New Progress on Graphene Research*. Nanotechnology and Nanomaterials. 2014: InTech.

102.	Hiramatsu, M., M. Naito, H. Kondo, and M. Hori, *Fabrication of Graphene-Based Films Using Microwave-Plasma-Enhanced Chemical Vapor Deposition.* Japanese Journal of Applied Physics, 2013. **52**(1).

103. Wang, Z., M. Shoji, and H. Ogata, *Carbon nanosheets by microwave plasma enhanced chemical vapor deposition in CH4-Ar system.* Applied Surface Science, 2011. **257**(21): p. 9082-9085.

104. Filleter, T., J.L. McChesney, A. Bostwick, E. Rotenberg, K.V. Emtsev, T. Seyller, K. Horn, and R. Bennewitz, *Friction and Dissipation in Epitaxial Graphene Films.* Physical Review Letters, 2009. **102**(8).

105. Tung, V.C., M.J. Allen, Y. Yang, and R.B. Kaner, *High-throughput solution processing of large-scale graphene.* Nature Nanotechnology, 2009. **4**(1): p. 25-29.

106. BCC Research. *Graphene: Technologies, Applications and Markets.* 2012 [cited 2012 16/03/2016]; Available from: http://www.bccresearch.com/pressroom/avm/global-market-graphene-based-products-reach-$986.7-million-2022.

107. Mo, M., W. Zhao, Z. Chen, Q. Yu, Z. Zeng, X. Wu, and Q. Xue, *Excellent tribological and anti-corrosion performance of polyurethane composite coatings reinforced with functionalized graphene and graphene oxide nanosheets.* Rsc Advances, 2015. **5**(70): p. 56486-56497.

108. Bhargava, S., N. Koratkar, and T.A. Blanchet, *Effect of Platelet Thickness on Wear of Graphene-Polytetrafluoroethylene (PTFE) Composites.* Tribology Letters, 2015. **59**(1).

109. Shen, X.-J., X.-Q. Pei, Y. Liu, and S.-Y. Fu, *Tribological performance of carbon nanotube-graphene oxide hybrid/epoxy composites.* Composites Part B-Engineering, 2014. **57**: p. 120-125.

110. Pu, J., S. Wan, W. Zhao, Y. Mo, X. Zhang, L. Wang, and Q. Xue, *Preparation and Tribological Study of Functionalized Graphene-IL Nanocomposite Ultrathin Lubrication Films on Si Substrates.* Journal of Physical Chemistry C, 2011. **115**(27): p. 13275-13284.

111. Tabandeh-Khorshid, M., E. Omrani, P.L. Menezes, and P.K. Rohatgi, *Tribological performance of self-lubricating aluminum matrix nanocomposites: role of graphene nanoplatelets.* Engineering Science and Technology, an International Journal, 2016. **19**(1): p. 463-469.

112. Liu, J., U. Khan, J. Coleman, B. Fernandez, P. Rodriguez, S. Naher, and D. Brabazon, *Graphene oxide and graphene nanosheet reinforced aluminium matrix composites: Powder synthesis and prepared composite characteristics.* Materials & Design, 2016. **94**: p. 87-94.

113. Yazdani, B., F. Xu, I. Ahmad, X. Hou, Y. Xia, and Y. Zhu, *Tribological performance of Graphene/Carbon nanotube hybrid reinforced Al2O3 composites.* Scientific Reports, 2015. **5**: p. 11579.

114. Xu, Z., X. Shi, W. Zhai, J. Yao, S. Song, and Q. Zhang, *Preparation and tribological properties of TiAl matrix composites reinforced by multilayer graphene.* Carbon, 2014. **67**: p. 168-177.

115. Porwal, H., P. Tatarko, R. Saggar, S. Grasso, M. Kumar Mani, I. Dlouhý, J. Dusza, and M.J. Reece, *Tribological properties of silica–graphene nano-platelet composites.* Ceramics International, 2014. **40**(8, Part A): p. 12067-12074.

116. Gao, X., H. Yue, E. Guo, S. Zhang, L. Yao, X. Lin, B. Wang, and E. Guan, *Tribological properties of copper matrix composites reinforced with homogeneously dispersed graphene nanosheets.* Journal of Materials Science & Technology, 2018.

117. Zhamu, A.C., OH, US), Jang, Bor Z. (Centerville, OH, US), *Nano graphene-modified lubricant.* 2011: United States.

118. Eswaraiah, V., V. Sankaranarayanan, and S. Ramaprabhu, *Graphene-based engine oil nanofluids for tribological applications.* ACS Appl Mater Interfaces, 2011. **3**(11): p. 4221-7.

119. Khare, V., M.Q. Pham, N. Kumari, H.S. Yoon, C.S. Kim, J.I. Park, and S.H. Ahn, *Graphene-ionic liquid based hybrid nanomaterials as novel lubricant for low friction and wear.* ACS Appl Mater Interfaces, 2013. **5**(10): p. 4063-75.

120. Lin, J., L. Wang, and G. Chen, *Modification of Graphene Platelets and their Tribological Properties as a Lubricant Additive.* Tribology Letters, 2011. **41**(1): p. 209-215.

121. Li, Q., C. Lee, R.W. Carpick, and J. Hone, *Substrate effect on thickness-dependent friction on graphene.* physica status solidi (b), 2010. **247**(11-12): p. 2909-2914.

122. Chen, H. and T. Filleter, *Effect of structure on the tribology of ultrathin graphene and graphene oxide films.* Nanotechnology, 2015. **26**(13): p. 135702.

123. Berman, D., S.A. Deshmukh, S.K.R.S. Sankaranarayanan, A. Erdemir, and A.V. Sumant, *Macroscale superlubricity enabled by graphene nanoscroll formation.* Science, 2015. **348**(6239): p. 1118-1122.

124. Bociąga, D., W. Jakubowski, P. Komorowski, A. Sobczyk-Guzenda, A. Jędrzejczak, D. Batory, and A. Olejnik, *Surface characterization and biological evaluation of silver-incorporated DLC coatings fabricated by hybrid RF PACVD/MS method.* Materials Science and Engineering C, 2016. **63**: p. 462–474.

125. Paul, R., S. Hussain, and A.K. Pal, *Characterization of nanocrystalline gold/DLC composite films synthesized by plasma CVD technique.* Applied Surface Science, 2009. **255**(18): p. 8076-8083.

126. Casiraghi, C., F. Piazza, A.C. Ferrari, D. Grambole, and J. Robertson, *Bonding in hydrogenated diamond-like carbon by Raman spectroscopy.* Diamond and Related Materials, 2005. **14**(3-7): p. 1098-1102.

127. Zanin, H., P.W. May, M.H.M.O. Hamanaka, and E.J. Corat, *Field Emission from Hybrid Diamond-like Carbon and Carbon Nanotube Composite Structures.* Acs Applied Materials & Interfaces, 2013. **5**(23): p. 12238-12243.

128. Huang, Q., S. Tian, D. Zeng, X. Wang, W. Song, Y. Li, W. Xiao, and C. Xie, *Enhanced photocatalytic activity of chemically bonded TiO2/graphene composites based on the effective interfacial charge transfer through the C–Ti bond.* Acs Catalysis, 2013. **3**(7): p. 1477-1485.

129. Mori, H. and H. Tachikawa, *Increased adhesion of diamond-like carbon-Si coatings and its tribological properties.* Surface & Coatings Technology, 2002. **149**(2-3): p. 225-230.

130. Wang, C.T., A. Escudeiro, T. Polcar, A. Cavaleiro, R.J.K. Wood, N. Gao, and T.G. Langdon, *Indentation and scratch testing of DLC-Zr coatings on ultrafine-grained titanium processed by high-pressure torsion.* Wear, 2013. **306**(1-2): p. 304-310.

131. Xu, Z.H. and D. Rowcliffe, *Nanoindentation on diamond-like carbon and alumina coatings.* Surface & Coatings Technology, 2002. **161**(1): p. 44-51.

132. Chockalingam, S., R. Tripathi, and O. Panwar, *Nanoindentation Study of Mechanical Properties of Diamond Like Carbon Coatings*, in *Physics of Semiconductor Devices*. 2014, Springer. p. 741-743.

133. Dwivedi, N., S. Kumar, and H.K. Malik, *Nanoindentation measurements on modified diamond-like carbon thin films.* Applied Surface Science, 2011. **257**(23): p. 9953-9959.

134. Material, A., *Products - Graphene Nanoplatelets.* 2016.

135. Johnson, D.W., B.P. Dobson, and K.S. Coleman, *A manufacturing perspective on graphene dispersions.* Current Opinion in Colloid & Interface Science, 2015. **20**(5–6): p. 367-382.

136. Zhao, W., F. Wu, H. Wu, and G. Chen, *Preparation of colloidal dispersions of graphene sheets in organic solvents by using ball milling.* Journal of Nanomaterials, 2010. **2010**: p. 6.

137. Wei, J., M.S. Saharudin, T. Vo, and F. Inam, *N, N-Dimethylformamide (DMF) usage in epoxy/graphene nanocomposites: problems associated with reaggregation.* Polymers, 2017. **9**(6): p. 193.

138. Hernandez, Y., V. Nicolosi, M. Lotya, F.M. Blighe, Z. Sun, S. De, I.T. McGovern, B. Holland, M. Byrne, Y.K. Gun'Ko, J.J. Boland, P. Niraj, G. Duesberg, S. Krishnamurthy, R. Goodhue, J. Hutchison, V. Scardaci, A.C. Ferrari, and J.N. Coleman, *High-yield production of graphene by liquid-phase exfoliation of graphite.* Nat Nano, 2008. **3**(9): p. 563-568.

139. Harreus, A.L., *2-Pyrrolidone.* Ullmann's Encyclopedia of Industrial Chemistry, 1993.

140. Khan, U., H. Porwal, A. O'Neill, K. Nawaz, P. May, and J.N. Coleman, *Solvent-Exfoliated Graphene at Extremely High Concentration.* Langmuir, 2011. **27**(15): p. 9077-9082.

141. Kuila, T., S. Bose, A.K. Mishra, P. Khanra, N.H. Kim, and J.H. Lee, *Chemical functionalization of graphene and its applications.* Progress in Materials Science, 2012. **57**(7): p. 1061-1105.

142. Blanch, A.J., C.E. Lenehan, and J.S. Quinton, *Optimizing Surfactant Concentrations for Dispersion of Single-Walled Carbon Nanotubes in Aqueous Solution.* The Journal of Physical Chemistry B, 2010. **114**(30): p. 9805-9811.

143. Perumal, S., H.M. Lee, and I.W. Cheong, *High-concentration graphene dispersion stabilized by block copolymers in ethanol.* Journal of Colloid and Interface Science, 2017. **497**: p. 359-367.

144. Jaybhaye, S., M. Sharon, A. Ansaldo, D. Ricci, L. Singh, and E.D. Zitti. *Taguchi methodology to grow single-walled carbon nanotubes on silicon wafer.* in *2009 9th IEEE Conference on Nanotechnology (IEEE-NANO).* 2009.

145. Evtukh, A.A., H. Hartnagel, V.G. Litovchenko, M.O. Semenenko, and O. Yilmazoglu, *Enhancement of electron field emission stability by nitrogen-doped diamond-like carbon film coating.* Semiconductor Science and Technology, 2004. **19**(7): p. 923.

146. Pavlicek, P. and O. Hybl, *White-light interferometry on rough surfaces - measurement uncertainty caused by surface roughness.* Applied Optics, 2008. **47**(16): p. 2941-2949.

147. Robertson, J., *Properties of diamond-like carbon.* Surface and Coatings Technology, 1992. **50**(3): p. 185-203.

148. Paterson, M.J., K.G. Orrman-Rossiter, D.K. Sood, and S.K. Bhargava, *Structural investigation of low energy ion beam deposited diamond-like films.* Diamond and Related Materials, 1993. **2**(11): p. 1439-1444.

149. Moulder, J.F., W.F. Stickle, P.E. Sobol, and K.D. Bomben, *Handbook of X-ray photoelectron spectroscopy: a reference book of standard spectra for identification and interpretation of XPS data.* 1992: Perkin-Elmer Eden Prairie, MN.

150. Chu, P.K. and L. Li, *Characterization of amorphous and nanocrystalline carbon films.* Materials Chemistry and Physics, 2006. **96**(2-3): p. 253-277.

151. Broitman, E., *Indentation hardness measurements at macro-, micro-, and nanoscale: a critical overview.* Tribology Letters, 2017. **65**(1): p. 23.

152. Oliver, W.C. and G.M. Pharr, *Measurement of hardness and elastic modulus by instrumented indentation: Advances in understanding and refinements to methodology.* Journal of Materials Research, 2004. **19**(1): p. 3-20.

153. Chalker, P.R., S.J. Bull, and D.S. Rickerby, *A Review Of The Methods For The Evaluation Of Coating-Substrate Adhesion.* Materials Science and Engineering a-Structural Materials Properties Microstructure and Processing, 1991. **140**: p. 583-592.

154. Rickerby, D.S., *A Review Of The Methods For The Measurement Of Coating Substrate Adhesion.* Surface & Coatings Technology, 1988. **36**(1-2): p. 541-557.

155. Bull, S.J., *Failure Modes In Scratch Adhesion Testing.* Surface & Coatings Technology, 1991. **50**(1): p. 25-32.

156. Valli, J., U. Makela, A. Matthews, and V. Murawa, *TiN Coating Adhesion Studies Using The Scratch Test Method.* Journal of Vacuum Science & Technology a-Vacuum Surfaces and Films, 1985. **3**(6): p. 2411-2414.

157. Bull, S.J. and E.G. Berasetegui, *An overview of the potential of quantitative coating adhesion measurement by scratch.* Tribology International, 2006. **39**(2): p. 99-114.

158. Qu, J. and J.J. Truhan, *An efficient method for accurately determining wear volumes of sliders with non-flat wear scars and compound curvatures.* Wear, 2006. **261**(7): p. 848-855.

159. Fan, W., L. Zhang, and T. Liu, *Strategies for the Hybridization of CNTs with Graphene*, in *Graphene-Carbon Nanotube Hybrids for Energy and Environmental Applications.* 2017, Springer. p. 21-51.

160. Das, A., B. Chakraborty, and A. Sood, *Raman spectroscopy of graphene on different substrates and influence of defects.* Bulletin of Materials Science, 2008. **31**(3): p. 579-584.

161. Hernandez, Y., M. Lotya, D. Rickard, S.D. Bergin, and J.N. Coleman, *Measurement of Multicomponent Solubility Parameters for Graphene Facilitates Solvent Discovery.* Langmuir, 2010. **26**(5): p. 3208-3213.

162. Giordani, S., S.D. Bergin, V. Nicolosi, S. Lebedkin, M.M. Kappes, W.J. Blau, and J.N. Coleman, *Debundling of Single-Walled Nanotubes by Dilution: Observation of Large Populations of Individual Nanotubes in Amide Solvent Dispersions.* The Journal of Physical Chemistry B, 2006. **110**(32): p. 15708-15718.

163. Samoilov, V.M., A.V. Nikolaeva, E.A. Danilov, G.A. Erpuleva, N.N. Trofimova, S.S. Abramchuk, and K.V. Ponkratov, *Preparation of*

aqueous graphene suspensions by ultrasonication in the presence of a fluorine-containing surfactant. Inorganic Materials, 2015. **51**(2): p. 98-105.

164. Wang, Y., M. Mortimer, C.H. Chang, and P.A. Holden, *Alginic Acid-Aided Dispersion of Carbon Nanotubes, Graphene, and Boron Nitride Nanomaterials for Microbial Toxicity Testing.* Nanomaterials, 2018. **8**(2): p. 76.

165. Gong, L., I.A. Kinloch, R.J. Young, I. Riaz, R. Jalil, and K.S. Novoselov, *Interfacial stress transfer in a graphene monolayer nanocomposite.* Advanced Materials, 2010. **22**(24): p. 2694-2697.

166. Calizo, I., I. Bejenari, M. Rahman, G. Liu, and A.A. Balandin, *Ultraviolet Raman microscopy of single and multilayer graphene.* Journal of Applied Physics, 2009. **106**(4).

167. Ferrari, A.C., *Raman spectroscopy of graphene and graphite: disorder, electron–phonon coupling, doping and nonadiabatic effects.* Solid state communications, 2007. **143**(1): p. 47-57.

168. Björling, M., R. Larsson, and P. Marklund, *The Effect of DLC Coating Thickness on Elstohydrodynamic Friction.* Tribology Letters, 2014. **55**(2): p. 353-362.

169. Villiger, P., C. Sprecher, and J.A. Peters, *Parameter optimisation of Ti-DLC coatings using statistically based methods.* Surface and Coatings Technology, 1999. **116-119**: p. 585-590.

170. Salvadori, M.C., D.R. Martins, and M. Cattani, *DLC coating roughness as a function of film thickness.* Surface and Coatings Technology, 2006. **200**(16): p. 5119-5122.

171. Haque, T., A. Morina, A. Neville, R. Kapadia, and S. Arrowsmith, *Effect of oil additives on the durability of hydrogenated DLC coating under boundary lubrication conditions.* Wear, 2009. **266**(1-2): p. 147-157.

172. Moder, J., F. Grün, F. Summer, T. Gasperlmair, and M. Andritschky, *Effect of temperature on wear and tribofilm formation in highly loaded DLC-steel line contacts.* Tribology International, 2018.

173. Nelson, N., R. Rakowski, J. Franks, P. Woolliams, P. Weaver, and B. Jones, *The effect of substrate geometry and surface orientation on the film structure of DLC deposited using PECVD.* Surface and Coatings Technology, 2014. **254**: p. 73-78.

174. Chen, Z., X. Ren, L. Ren, T. Wang, X. Qi, and Y. Yang, *Improving the Tribological Properties of Spark-Anodized Titanium by Magnetron Sputtered Diamond-Like Carbon.* Coatings, 2018. **8**(2): p. 83.

175. Tai, F. and S. Tyan, *Correlation between ID∕IG Ratio from Visible Raman Spectra and sp2/sp3 Ratio from XPS Spectra of Annealed Hydrogenated DLC Film.* Materials transactions, 2006. **47**(7): p. 1847-1852.

176. Solis, J., H. Zhao, C. Wang, J.A. Verduzco, A.S. Bueno, and A. Neville, *Tribological performance of an H-DLC coating prepared by PECVD.* Applied Surface Science, 2016. **383**(Supplement C): p. 222-232.

177. Schwan, J., S. Ulrich, V. Batori, H. Ehrhardt, and S. Silva, *Raman spectroscopy on amorphous carbon films.* Journal of Applied Physics, 1996. **80**(1): p. 440-447.

178. Zavaleyev, V., J. Walkowicz, M. Sawczak, M. Klein, D. Moszyński, R. Chodun, and K. Zdunek, *Determination of sp³ fraction in ta-C coating*

using XPS and Raman spectroscopy. Вопросы атомной науки и техники, 2016.

179. Tsai, P.C. and Y.R. Jeng, *Effects of nanotube size and roof-layer coating on viscoelastic properties of hybrid diamond-like carbon and carbon nanotube composites.* Carbon, 2015. **86**: p. 163-173.

180. Zhu, H., A. Liu, F. Shan, W. Yang, C. Barrow, and J. Liu, *Direct transfer of graphene and application in low-voltage hybrid transistors.* RSC advances, 2017. **7**(4): p. 2172-2179.

181. Wang, Y., Z. Ni, Z. Shen, H. Wang, and Y. Wu, *Interference enhancement of Raman signal of graphene.* arXiv preprint arXiv:0801.4595, 2008.

182. Hovsepian, P.E., P. Mandal, A.P. Ehiasarian, G. Sáfrán, R. Tietema, and D. Doerwald, *Friction and wear behaviour of Mo–W doped carbon-based coating during boundary lubricated sliding.* Applied Surface Science, 2016. **366**: p. 260-274.

183. Sheeja, D., B. Tay, S. Lau, and X. Shi, *Tribological properties and adhesive strength of DLC coatings prepared under different substrate bias voltages.* Wear, 2001. **249**(5-6): p. 433-439.

184. Han, X., Y. Chen, H. Zhu, C. Preston, J. Wan, Z. Fang, and L. Hu, *Scalable, printable, surfactant-free graphene ink directly from graphite.* Nanotechnology, 2013. **24**(20): p. 205304.

185. Lotya, M., P.J. King, U. Khan, S. De, and J.N. Coleman, *High-concentration, surfactant-stabilized graphene dispersions.* ACS nano, 2010. **4**(6): p. 3155-3162.

186. Zhang, S., X. Zeng, H. Xie, and P. Hing, *A phenomenological approach for the I d/I g ratio and sp 3 fraction of magnetron sputtered aC films.* Surface and Coatings Technology, 2000. **123**(2): p. 256-260.

187. Cranford, S., D. Sen, and M.J. Buehler, *Meso-origami: folding multilayer graphene sheets.* Applied physics letters, 2009. **95**(12): p. 123121.

188. Mobarak, H.M., H.H. Masjuki, E.N. Mohamad, S.M.A. Rahman, K.A.H.A. Mahmud, M. Habibullah, and S. Salauddin, *Effect of DLC Coating on Tribological Behavior of Cylinder Liner-piston Ring Material Combination When Lubricated with Jatropha Oil.* Procedia Engineering, 2014. **90**: p. 733-739.

189. Tasdemir, H.A., T. Tokoroyama, H. Kousaka, N. Umehara, and Y. Mabuchi, *Friction and Wear Performance of Boundary-lubricated DLC/DLC Contacts in Synthetic base Oil.* Procedia Engineering, 2013. **68**: p. 518-524.

190. Tsai, P.-C. and Y.-R. Jeng, *Effects of nanotube size and roof-layer coating on viscoelastic properties of hybrid diamond-like carbon and carbon nanotube composites.* Carbon, 2015. **86**: p. 163-173.

191. Ren, W., A. Iyer, J. Koskinen, A. Kaskela, E.I. Kauppinen, K. Avchaciov, and K. Nordlund, *Conditions for forming composite carbon nanotube-diamond like carbon material that retain the good properties of both materials.* Journal of Applied Physics, 2015. **118**(19): p. 194306.

192. Ramamoorthy, B. and B.C. Yeldose, *An investigation into the adhesion strength of diamond like carbon multilayer coating (DLC/TiN/Ti/Cu/Ni).* Intelligent Information Management, 2009. **1**(03): p. 179.

193. Uysal, M., H. Akbulut, M. Tokur, H. Algül, and T. Çetinkaya, *Structural and sliding wear properties of Ag/Graphene/WC hybrid nanocomposites*

produced by electroless co-deposition. Journal of Alloys and Compounds, 2016. **654**: p. 185-195.

194. Zhao, W., F. Wu, H. Wu, and G. Chen, *Preparation of Colloidal Dispersions of Graphene Sheets in Organic Solvents by Using Ball Milling.* Journal of Nanomaterials, 2010.

195. Deng, S. and V. Berry, *Wrinkled, rippled and crumpled graphene: an overview of formation mechanism, electronic properties, and applications.* Materials Today, 2016. **19**(4): p. 197-212.

196. Zhao, F., H. Li, L. Ji, Y. Wang, H. Zhou, and J. Chen, *Ti-DLC films with superior friction performance.* Diamond and Related materials, 2010. **19**(4): p. 342-349.

197. Leng, Y., W. Wang, L. Zhang, F. Zabihi, and Y. Zhao, *Fabrication and photocatalytical enhancement of ZnO-graphene hybrid using a continuous solvothermal technique.* The Journal of Supercritical Fluids, 2014. **91**: p. 61-67.

198. Yamaletdinov, R.D. and Y.V. Pershin, *Finding stable graphene conformations from pull and release experiments with molecular dynamics.* Scientific reports, 2017. **7**: p. 42356.

199. Cao, Y., R.L. Flores, and Y.-Q. Xu, *Curling graphene ribbons through thermal annealing.* Applied Physics Letters, 2013. **103**(18): p. 183103.

200. Sheeja, D., B. Tay, S. Lau, K. Leong, and C. Lee, *An empirical relation for critical load of DLC coatings prepared on silicon substrates.* International Journal of Modern Physics B, 2002. **16**(06n07): p. 958-962.

201. Sheeja, D., B.K. Tay, K.W. Leong, and C.H. Lee, *Effect of film thickness on the stress and adhesion of diamond-like carbon coatings.* Diamond and Related Materials, 2002. **11**(9): p. 1643-1647.

202. García, M., J. Marchese, and N. Ochoa, *Effect of the particle size and particle agglomeration on composite membrane performance.* Journal of applied polymer science, 2010. **118**(4): p. 2417-2424.

203. Cui, M., J. Pu, J. Liang, L. Wang, G. Zhang, and Q. Xue, *Corrosion and tribocorrosion performance of multilayer diamond-like carbon film in NaCl solution.* RSC Advances, 2015. **5**(127): p. 104829-104840.

204. Weiss, H., *Adhesion of advanced overlay coatings: mechanisms and quantitative assessment.* Surface and Coatings Technology, 1995. **71**(2): p. 201-207.

205. Cho, Y.H., W.S. Choi, Y.S. Park, H.J. Cho, and B. Hong, *Study of the tribological properties of DLC double-layer films grown by using plasma enhanced chemical-vapor deposition and closed-field unbalanced magnetron sputtering.* JOURNAL-KOREAN PHYSICAL SOCIETY, 2007. **51**(3): p. 1129.

206. No, Y.-S., H.K. Choi, J.-S. Kim, H. Kim, Y.-J. Yu, C.-G. Choi, and J.S. Choi, *Layer number identification of CVD-grown multilayer graphene using Si peak analysis.* Scientific Reports, 2018. **8**(1): p. 571.

207. Yoon, D., H. Moon, Y.-W. Son, J.S. Choi, B.H. Park, Y.H. Cha, Y.D. Kim, and H. Cheong, *Interference effect on Raman spectrum of graphene on SiO 2/Si.* Physical Review B, 2009. **80**(12): p. 125422.

208. Wu, Y., B. Wang, Y. Ma, Y. Huang, N. Li, F. Zhang, and Y. Chen, *Efficient and large-scale synthesis of few-layered graphene using an arc-discharge method and conductivity studies of the resulting films.* Nano Research, 2010. **3**(9): p. 661-669.

209. Chen, J., W. Shi, Z. Gao, T. Wang, S. Wang, L. Dong, Q. Yang, and C. Xiong, *Facile preparation of pristine graphene using urea/glycerol as efficient stripping agents.* Nano Research, 2018. **11**(2): p. 820-830.

210. Kalisz, M., M. Grobelny, M. Mazur, M. Zdrojek, D. Wojcieszak, M. Świniarski, J. Judek, and D. Kaczmarek, *Comparison of mechanical and corrosion properties of graphene monolayer on Ti–Al–V and nanometric Nb2O5 layer on Ti–Al–V alloy for dental implants applications.* Thin Solid Films, 2015. **589**: p. 356-363.

211. Heeg, S., R. Fernandez-Garcia, A. Oikonomou, F. Schedin, R. Narula, S.A. Maier, A. Vijayaraghavan, and S. Reich, *Polarized plasmonic enhancement by Au nanostructures probed through Raman scattering of suspended graphene.* Nano letters, 2012. **13**(1): p. 301-308.

212. Shin, Y., E. Prestat, K.-G. Zhou, P. Gorgojo, K. Althumayri, W. Harrison, P.M. Budd, S.J. Haigh, and C. Casiraghi, *Synthesis and characterization of composite membranes made of graphene and polymers of intrinsic microporosity.* Carbon, 2016. **102**: p. 357-366.

213. Geng, D., S. Yang, Y. Zhang, J. Yang, J. Liu, R. Li, T.-K. Sham, X. Sun, S. Ye, and S. Knights, *Nitrogen doping effects on the structure of graphene.* Applied Surface Science, 2011. **257**(21): p. 9193-9198.

214. Antunes, E., A. Lobo, E. Corat, V. Trava-Airoldi, A. Martin, and C. Veríssimo, *Comparative study of first-and second-order Raman spectra of MWCNT at visible and infrared laser excitation.* Carbon, 2006. **44**(11): p. 2202-2211.

215. Çelik, Y., E. Flahaut, and E. Suvacı, *A comparative study on few-layer graphene production by exfoliation of different starting materials in a low boiling point solvent.* FlatChem, 2017. **1**: p. 74-88.

216. Ghosh, S., D. Choudhury, T. Roy, A.B. Mamat, H. Masjuki, and B. Pingguan-Murphy, *Tribological investigation of diamond-like carbon coated micro-dimpled surface under bovine serum and osteoarthritis oriented synovial fluid.* Science and technology of advanced materials, 2015. **16**(3): p. 035002.

217. Sonoda, T., S. Nakao, and M. Ikeyama, *Deposition of Ti/C nano-composite DLC films by magnetron DC sputtering with dual targets.* Vacuum, 2009. **84**(5): p. 666-668.

218. Czyzniewski, A., *Mechanical and Tribological Properties of Cr-DLC Coatings Deposited by ARC-MAG-RF PACVD Hybrid Method.* Plasma Processes and Polymers, 2007. **4**(S1).

219. Chen, S.-Y., K.-L. Ou, W.-C. Huang, K.-T. Chu, and S.-F. Ou, *Phase transformation of diamond-like carbon/silver composite films by sputtering deposition.* Ceramics International, 2013. **39**(3): p. 2575-2580.

220. Tokuta, Y., M. Kawaguchi, A. Shimizu, and S. Sasaki, *Effects of Applied Heat and Stress on Structural Changes of DLC Film.* Tribology Online, 2012. **7**(3): p. 119-126.

221. Dey, R., M. Pandey, D. Bhattacharyya, D. Patil, and S. Kulkarni, *Diamond like carbon coatings deposited by microwave plasma CVD: XPS and ellipsometric studies.* Bulletin of Materials Science, 2007. **30**(6): p. 541-546.

222. Akbulut, H., G. Hatipoglu, H. Algul, M. Tokur, M. Kartal, M. Uysal, and T. Cetinkaya, *Co-deposition of Cu/WC/graphene hybrid nanocomposites*

produced by electrophoretic deposition. Surface and Coatings Technology, 2015. **284**: p. 344-352.

223. Zhang, Y., D. Zhang, X. Wei, S. Zhong, and J. Wang, *Enhanced Tribological Properties of Polymer Composite Coating Containing Graphene at Room and Elevated Temperatures.* Coatings, 2018. **8**(3): p. 91.

224. Meyer, J.C., A.K. Geim, M.I. Katsnelson, K.S. Novoselov, T.J. Booth, and S. Roth, *The structure of suspended graphene sheets.* Nature, 2007. **446**(7131): p. 60-3.

225. Liu, Y., A. Erdemir, and E.I. Meletis, *An investigation of the relationship between graphitization and frictional behavior of DLC coatings.* Surface & Coatings Technology, 1996. **86-7**(1-3): p. 564-568.

226. Erdemir, A., C. Bindal, G.R. Fenske, C. Zuiker, and P. Wilbur, *Characterization of transfer layers forming on surfaces sliding against diamond-like carbon.* Surface and Coatings Technology, 1996. **86-87**: p. 692-697.

227. Liu, Y., A. Erdemir, and E.I. Meletis, *A study of the wear mechanism of diamond-like carbon films.* Surface and Coatings Technology, 1996. **82**(1): p. 48-56.

228. Takadoum, J. and H.H. Bennani, *Influence of substrate roughness and coating thickness on adhesion, friction and wear of TiN films.* Surface and Coatings Technology, 1997. **96**(2): p. 272-282.

229. Li, X., T. Sawaki, H. Kousaka, M. Murashima, and N. Umehara, *Effect of mating materials on wear properties of amorphous hydrogenated carbon (aC: H) coating and tetrahedral amorphous carbon (ta-C) coating in base oil boundary lubrication condition.* Jurnal Tribologi, 2017. **15**: p. 1-20.

230. Scharf, T. and I. Singer, *Role of the transfer film on the friction and wear of metal carbide reinforced amorphous carbon coatings during run-in.* Tribology Letters, 2009. **36**(1): p. 43-53.

231. Shaha, K., Y. Pei, D. Martinez-Martinez, and J.T.M. De Hosson, *Influence of surface roughness on the transfer film formation and frictional behavior of TiC/aC nanocomposite coatings.* Tribology letters, 2011. **41**(1): p. 97-101.

232. Sønderby, S., A.N. Berthelsen, K.P. Almtoft, B.H. Christensen, L.P. Nielsen, and J. Bøttiger, *Optimization of the mechanical properties of magnetron sputtered diamond-like carbon coatings.* Diamond and Related Materials, 2011. **20**(5): p. 682-686.

233. Kosarieh, S., A. Morina, E. Lainé, J. Flemming, and A. Neville, *Tribological performance and tribochemical processes in a DLC/steel system when lubricated in a fully formulated oil and base oil.* Surface and Coatings Technology, 2013. **217**: p. 1-12.

234. Petro, R., P. Borodulin, T. Schlesinger, and M. Schlesinger, *Liquid Exfoliated Graphene: A Practical Method for Increasing Loading and Producing Thin Films.* ECS Journal of Solid State Science and Technology, 2016. **5**(2): p. P36-P40.

235. Green, A.A. and M.C. Hersam, *Emerging methods for producing monodisperse graphene dispersions.* The journal of physical chemistry letters, 2009. **1**(2): p. 544-549.

236. Sanes, J., M.-D. Avilés, N. Saurín, T. Espinosa, F.-J. Carrión, and M.-D. Bermúdez, *Synergy between graphene and ionic liquid lubricant additives.* Tribology International, 2017. **116**: p. 371-382.

237. Gusain, R., H.P. Mungse, N. Kumar, T. Ravindran, R. Pandian, H. Sugimura, and O.P. Khatri, *Covalently attached graphene–ionic liquid hybrid nanomaterials: synthesis, characterization and tribological application.* Journal of Materials Chemistry A, 2016. **4**(3): p. 926-937.

Appendix A Greyscale measurement using ImageJ

1. Open file.

2. Select line option.
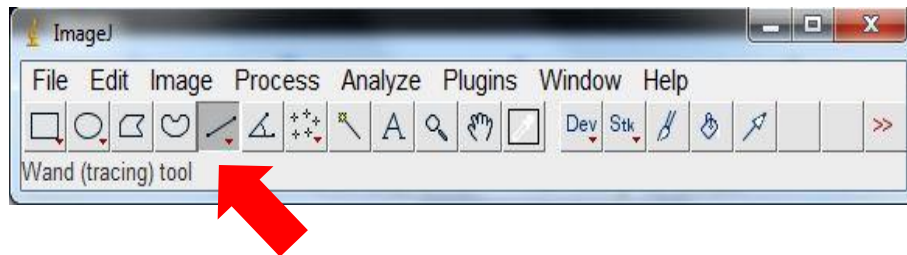
3. Draw line at the above part of the dispersion.
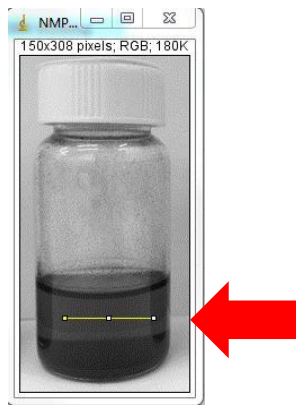
4. Select "Plot Profile" from the "Analyze" section of the top list
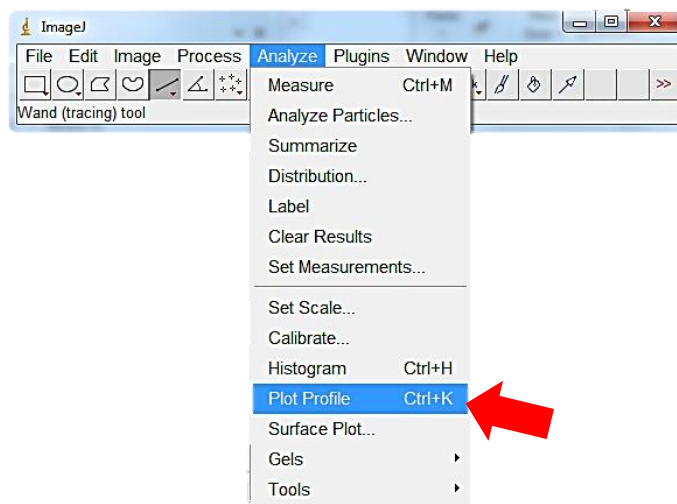
5. A plot of the greyscale profile at the selected line will appear as in figure. Select "List" from the plot.
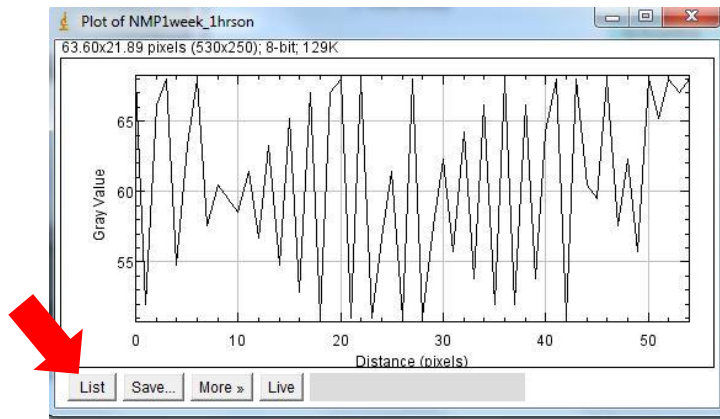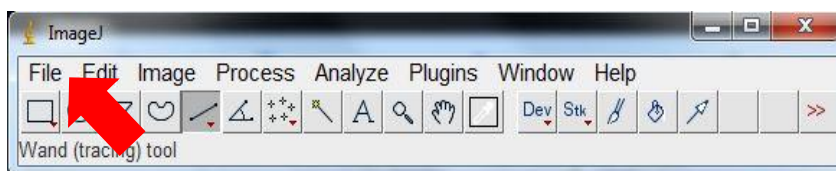

6. A list of greyscale value measured from the line that has been drawn will appear. Measurement was repeated for at least three times at different areas.

Appendix B Measurement of coverage and size of GNP island using ImageJ software
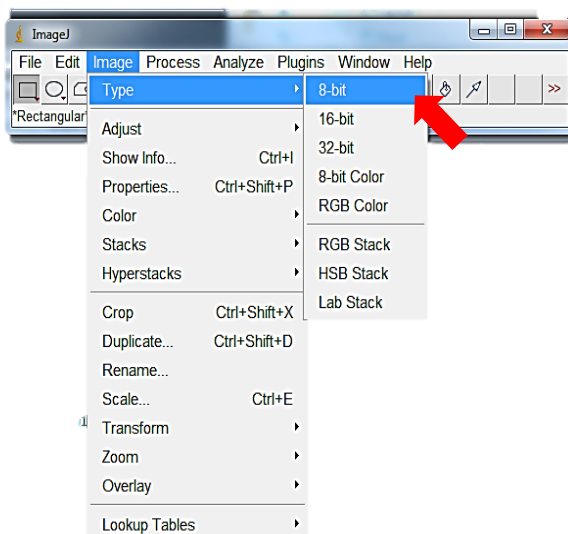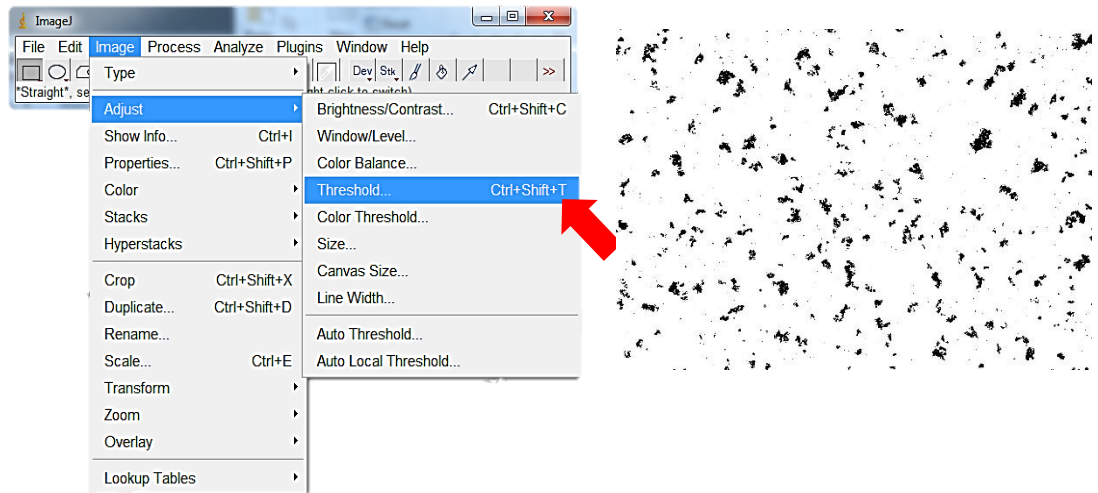
1. Open image by selecting the "File".

2. Set scale using scale in image. Go to "Analyze" and select "Select Scale"
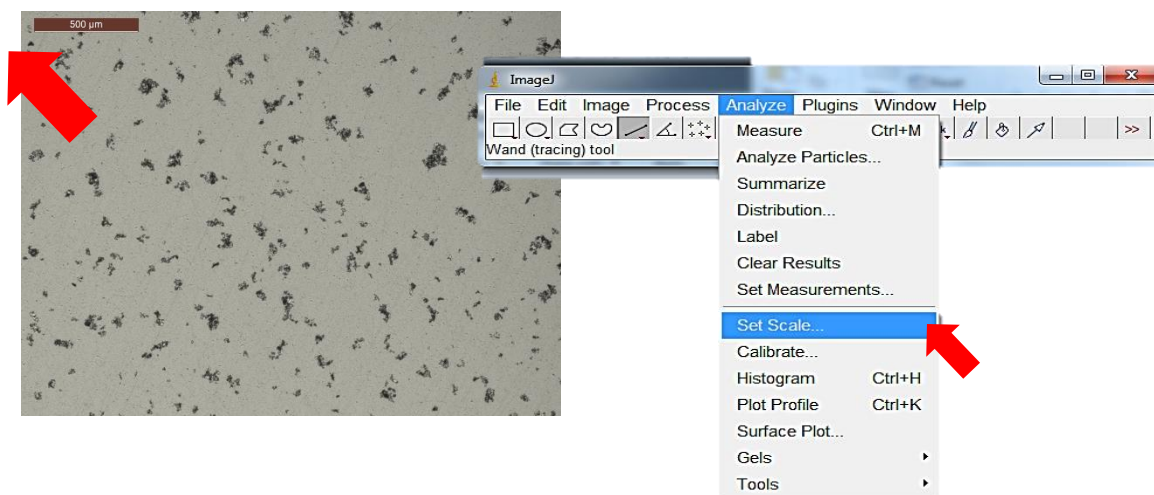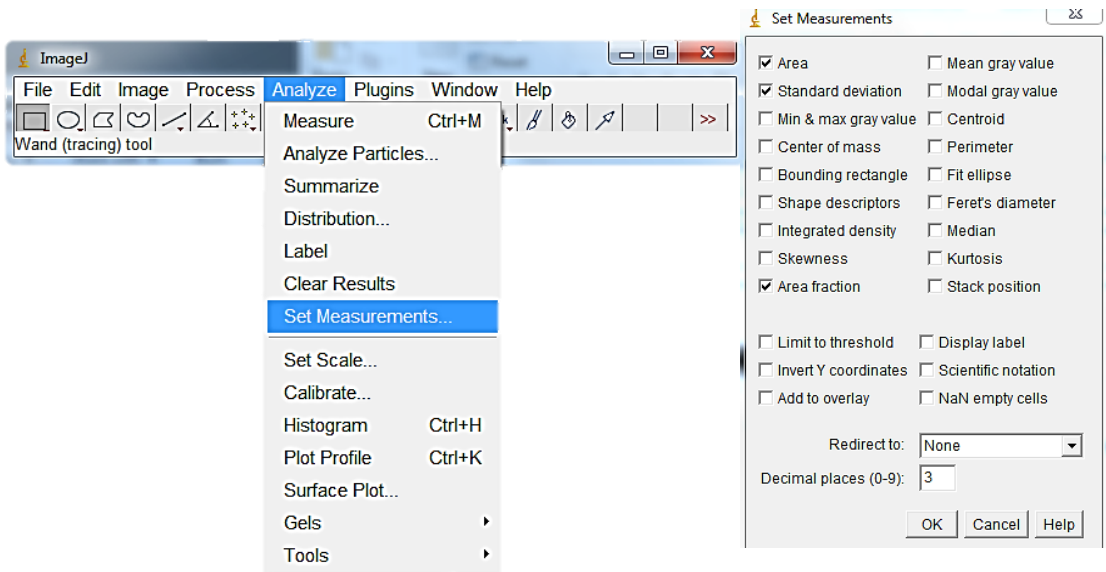

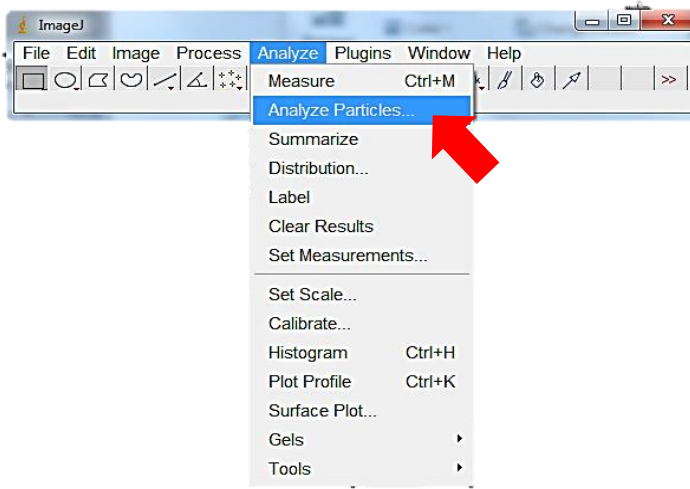3. Convert the image to 8-bit image from the "Image" option.

4. Go to "Image" and change the image to threshold image. Optical image will be converted to threshold image.

5. Go to "Analyze" and "Set Measurement"

6. Then select "Analyze Particles" in "Analyze" and results will appear showing the details of measurement and the summary of total area and average size of the island.

Appendix C Sedimentation test

C.1. GNP/DMF suspension
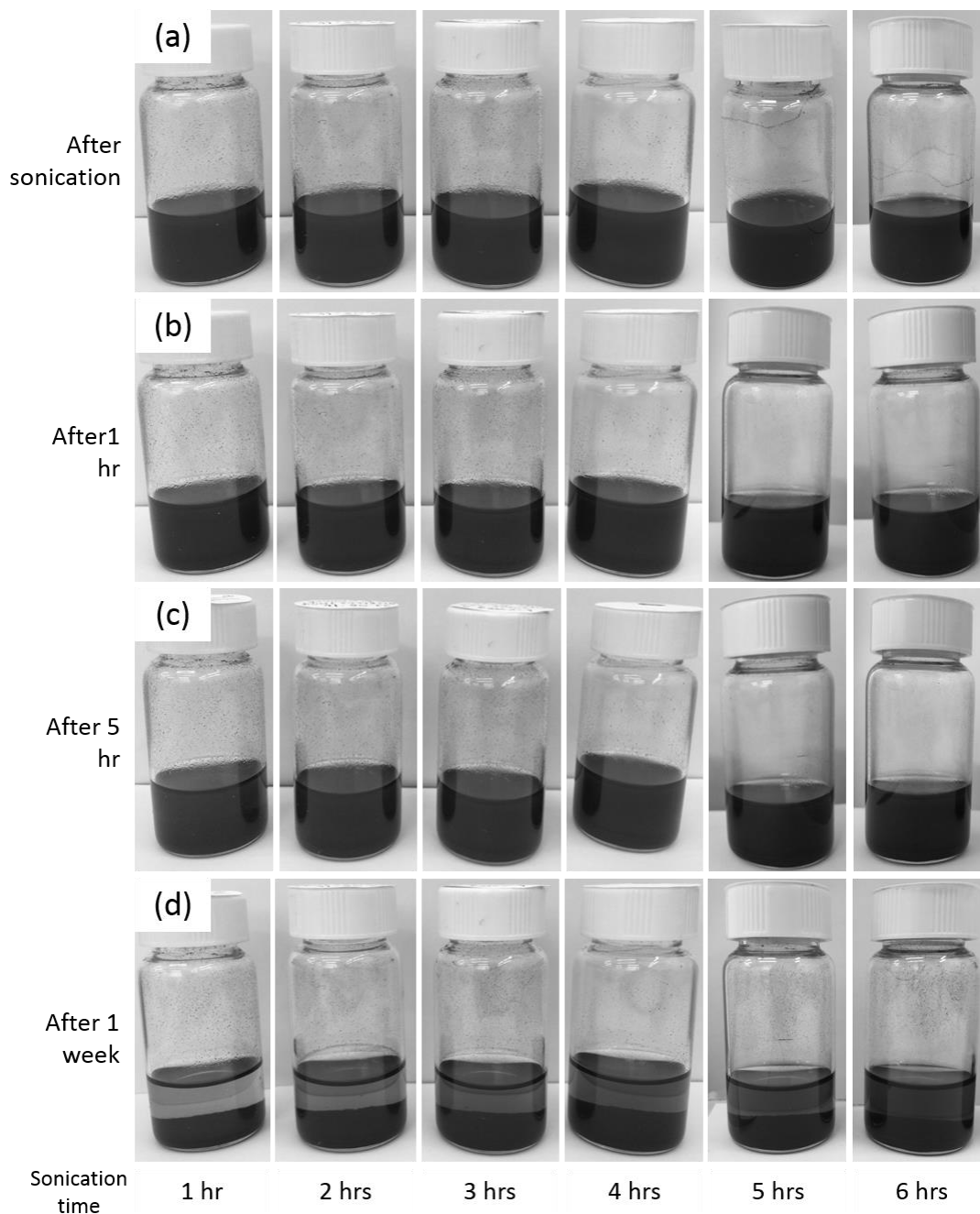
Figure C 1 Dispersion of GNP in DMF (GNP/DMF). The vials are photographs at (a) 0 hr, (b) 1 hour, (c) 5 hours and (d) 1 week after sonication. From left to right, GNP/DMF sonicated for 1, 2, 3, 4, 5 and 6 hours.

C.2. GNP/ethanol suspension
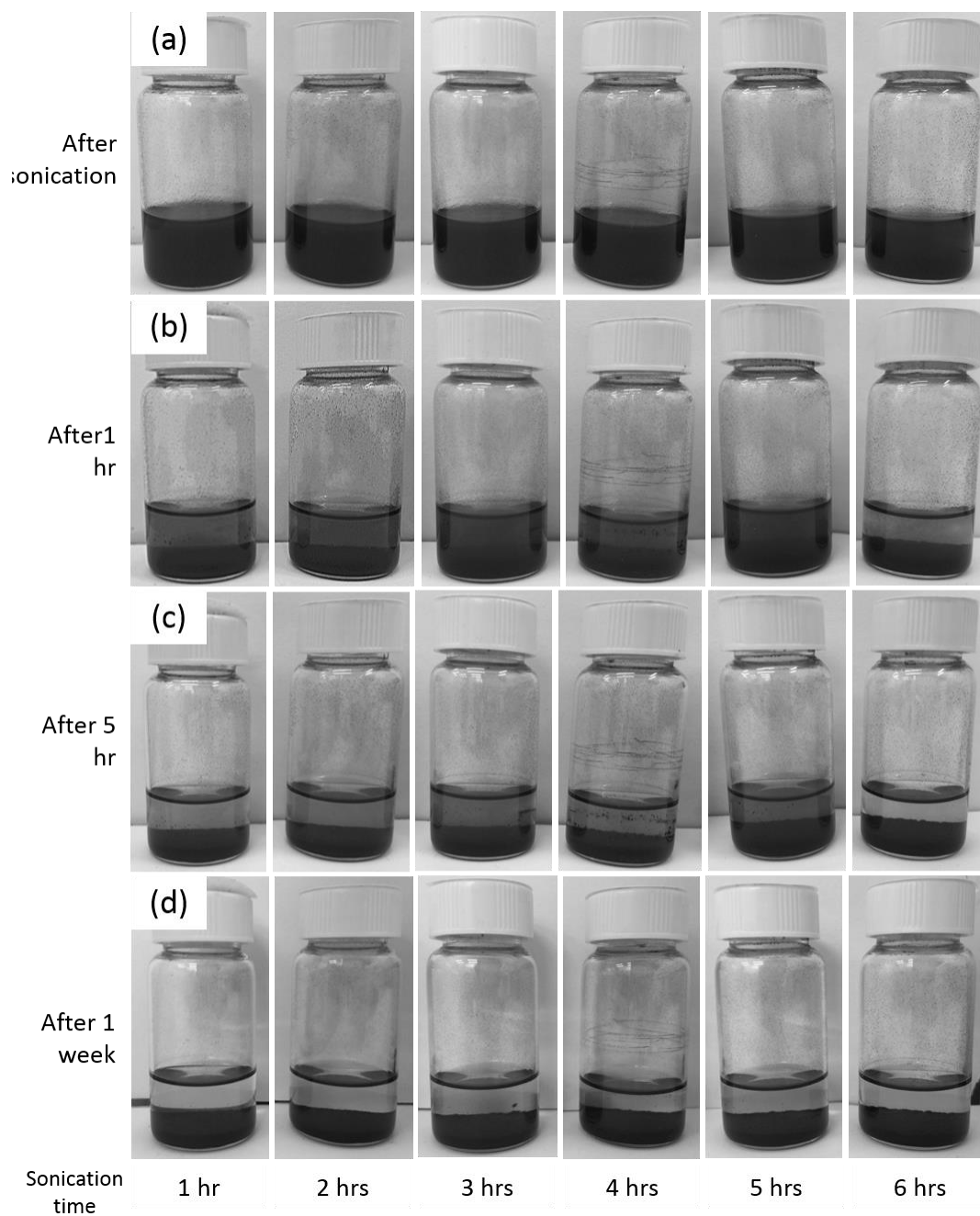
Figure C 2 Sedimentation test of GNP in ethanol (GNP/ethanol). The vials are photographs at (a) 0 hr, (b) 1 hour, (c) 5 hours and (d) 1 week after sonication. From left to right, GNP/ethanol sonicated for 1, 2, 3, 4, 5 and 6 hour

C.3. GNP/NMP suspension
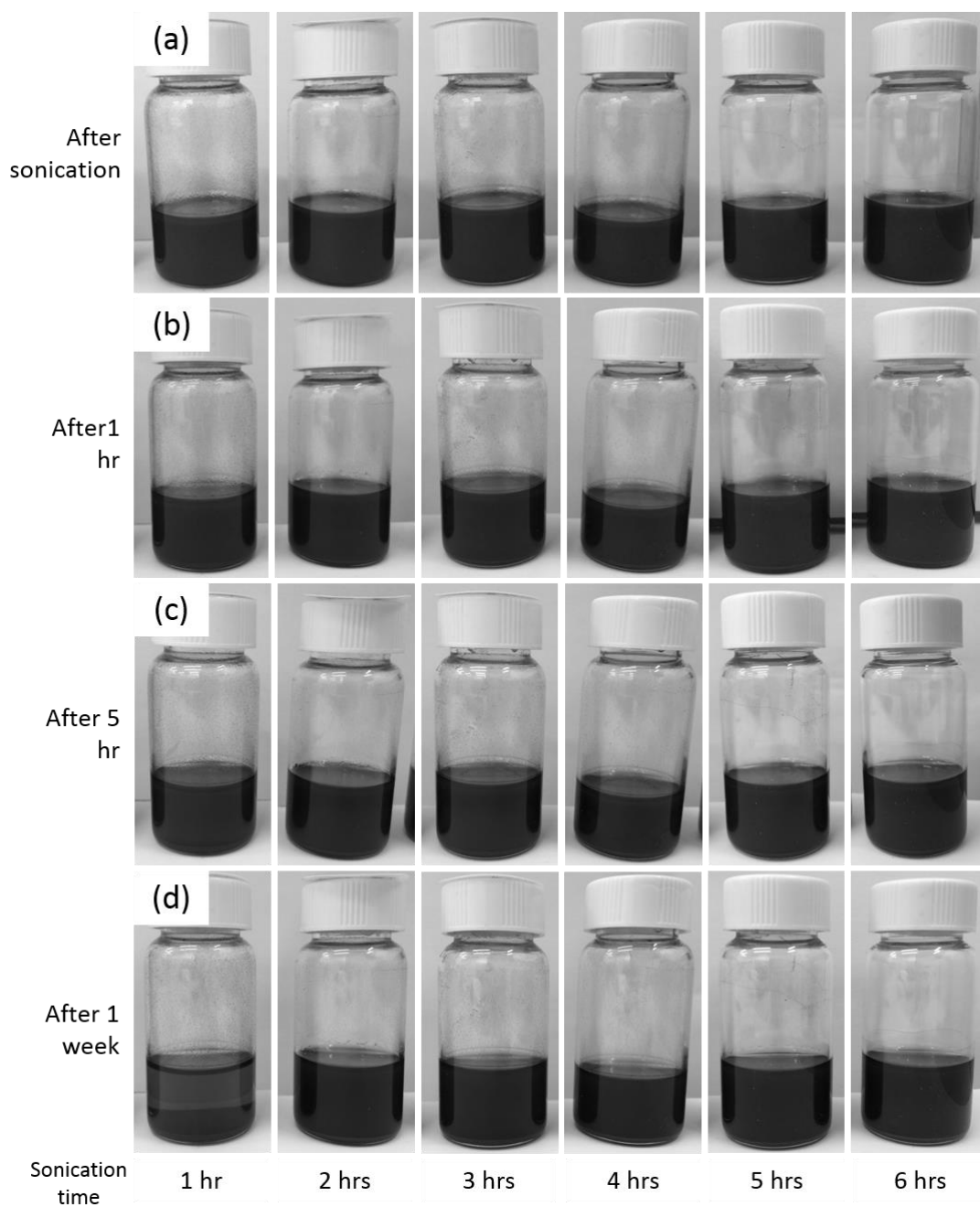
Figure C 3 Dispersion of GNP in NMP (GNP/NMP). The vials are photographs at (a) 0 hr, (b) 1 hour, (c) 5 hours and (d) 1 week after sonication. From left to right, GNP/NMP sonicated for 1, 2, 3, 4, 5 and 6 hours

Appendix D Surface topography of spin-coated GNP in different types of solvent

D.1. GNP/DMF

Figure D 1 Profilometric images of GNP/DMF samples sonicated for one to six hours

D.2. GNP/ethanol

Figure D 2 Profilometric images of GNP/ethanol samples sonicated for one to six hours

D.3. GNP/NMP

GNP/NMP

Figure D 3 Profilometric images of GNP/NMP samples sonicated for one to six hours

Appendix E Experimental results and the corresponding responses using Taguchi Method

E.1. Graphene distribution

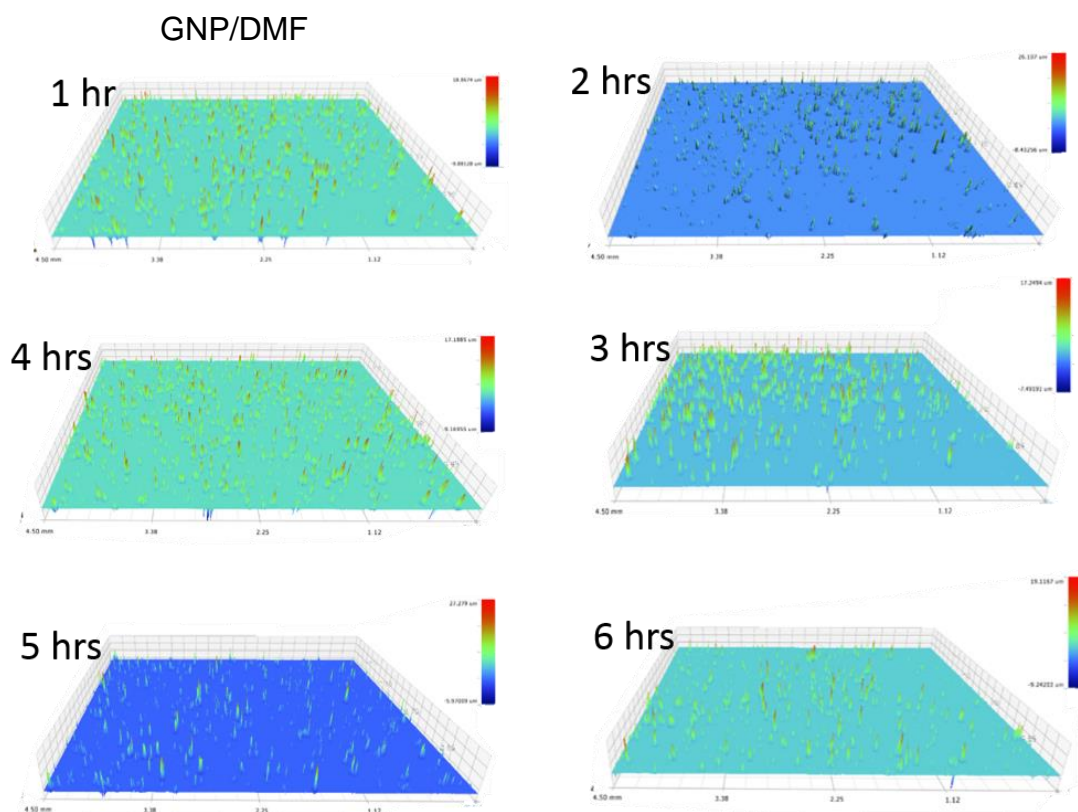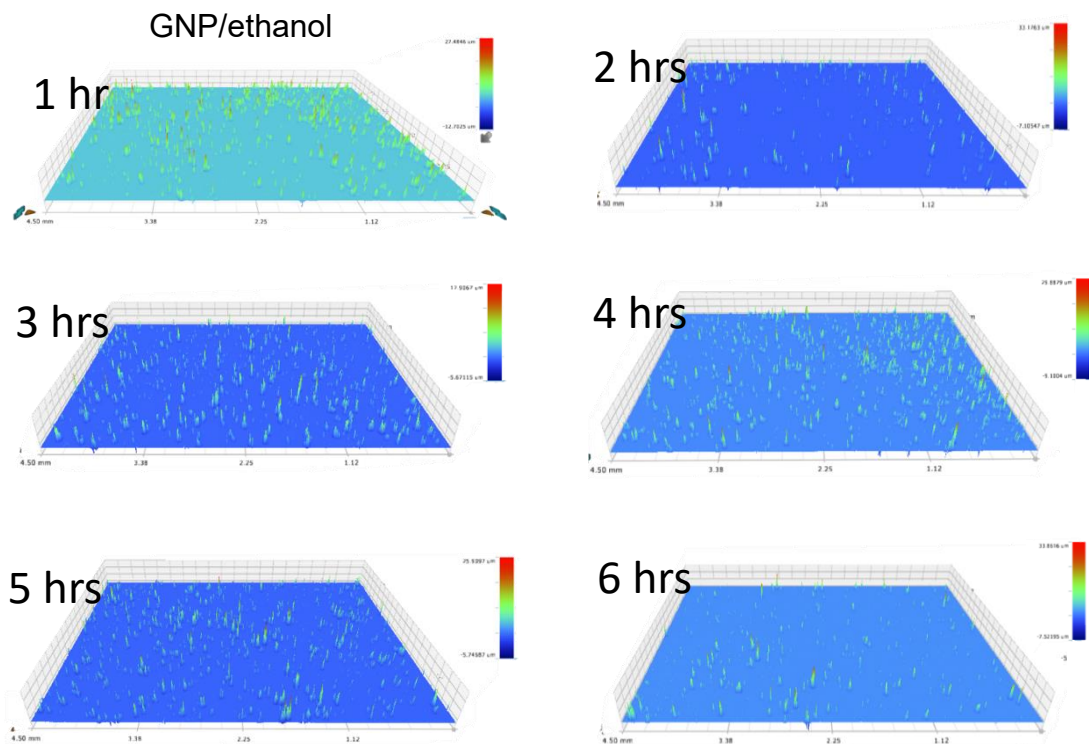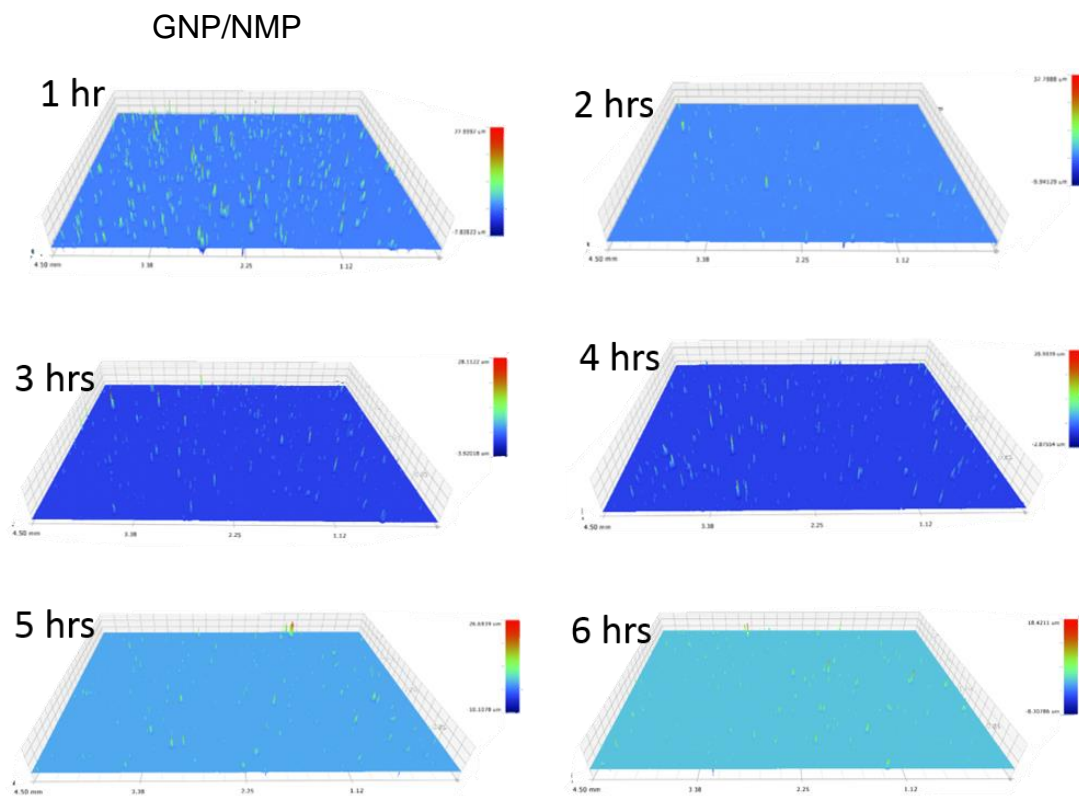| Ex No	Parameter and level				Measurements					Graphene distribution (%) Bigger is the better (S/N)		
	A	B	C		1	2	3	4	5	Mean	SD	S/N
1	1	1	1	$A_1B_1C_1$	-	-	-	-	-	N/A	N/A	N/A
2	1	2	2	$A_1B_2C_2$	-	-	-	-	-	N/A	N/A	N/A
3	1	3	3	$A_1B_3C_3$	-	-	-	-	-	N/A	N/A	N/A
4	2	1	3	$A_2B_1C_3$	11.365	9.615	8.675	8.649	5.672	8.80	2.07	18.16
5	2	2	1	$A_2B_2C_1$	7.624	6.273	7.252	3.157	7.438	6.35	1.86	14.44
6	2	3	2	$A_2B_3C_2$	13.363	13.43	13.608	14.997	5.868	12.25	3.63	20.00
7	3	1	2	$A_3B_1C_2$	4.764	5.746	6.578	6.8	7.28	6.23	0.99	15.59
8	3	2	3	$A_3B_2C_3$	6.589	6.144	5.233	5.179	8.248	6.28	1.25	15.59
9	3	3	1	$A_3B_3C_1$	10.307	7.491	4.876	8.678	9.301	8.13	2.09	17.25
Y_{i1}	-	7.51	7.24	Mean response value at level 1						8.01		16.84
Y_{i2}	9.13	6.31	9.24	Mean response value at level 2								
Y_{i3}	6.88	10.19	7.54	Mean response value at level 3								
SD_{i1}	-	1.53	1.97	Mean SD value at level 1								
SD_{i1}	2.52	1.56	2.31	Mean SD value at level 2								
SD_{i1}	1.44	2.86	1.66	Mean SD value at level 3								
S/N_{i1}	N/A	16.88	15.84	Mean S/N value at level 1								
S/N_{i2}	17.53	15.01	17.79	Mean S/N value at level 2								
S/N_{i3}	16.14	18.62	16.88	Mean S/N value at level 3								
delta	1.39	3.61	1.95									

E.2. Surface roughness

Exp No	Parameters and levels				Measurements					Surface roughness (%) Smaller is the better (S/N)		
	A	B	C		1	2	3	4	5	Mean	SD	S/N
1	1	1	1	$A_1B_1C_1$	218.00	59.40	119.00	75.50	53.40	105.06	68.15	-41.69
2	1	2	2	$A_1B_2C_2$	54.10	351.00	399.00	145.00	206.00	231.02	143.12	-48.44
3	1	3	3	$A_1B_3C_3$	27.40	33.11	24.66	45.04	74.46	40.93	20.31	-33.02
4	2	1	3	$A_2B_1C_3$	21.36	25.5	17.95	19.69	17.3	20.360	3.280	-26.26
5	2	2	1	$A_2B_2C_1$	20.38	19.44	27.11	28.07	20.4	23.080	4.149	-27.38
6	2	3	2	$A_2B_3C_2$	65.27	59.19	59.23	68.75	27.4	55.968	16.485	-35.25
7	3	1	2	$A_3B_1C_2$	19.87	20.49	21.37	43.45	25.36	26.108	9.928	-28.81
8	3	2	3	$A_3B_2C_3$	43.500	47.800	33.500	34.500	33.200	38.500	6.719	-31.81
9	3	3	1	$A_3B_3C_1$	59.29	61.91	58.57	43.74	30.03	50.708	13.575	-34.34
Y_{i1}	125.67	50.51	59.62	Mean response value at level 1						65.75		-34.11
Y_{i2}	33.14	97.53	104.37	Mean response value at level 2								
Y_{i3}	38.44	49.20	33.26	Mean response value at level 3								
SD_{i1}	77.19	27.12	28.62	Mean SD value at level 1								
SD_{i1}	7.97	51.33	56.51	Mean SD value at level 2								
SD_{i1}	10.07	16.79	10.10	Mean SD value at level 3								
S/N_{i1}	-41.05	-32.25	-34.47	Mean S/N value at level 1								
S/N_{i2}	-29.63	-35.88	-37.50	Mean S/N value at level 2								
S/N_{i3}	-31.66	-34.21	-30.37	Mean S/N value at level 3								
Delta	11.42	3.62	7.13									